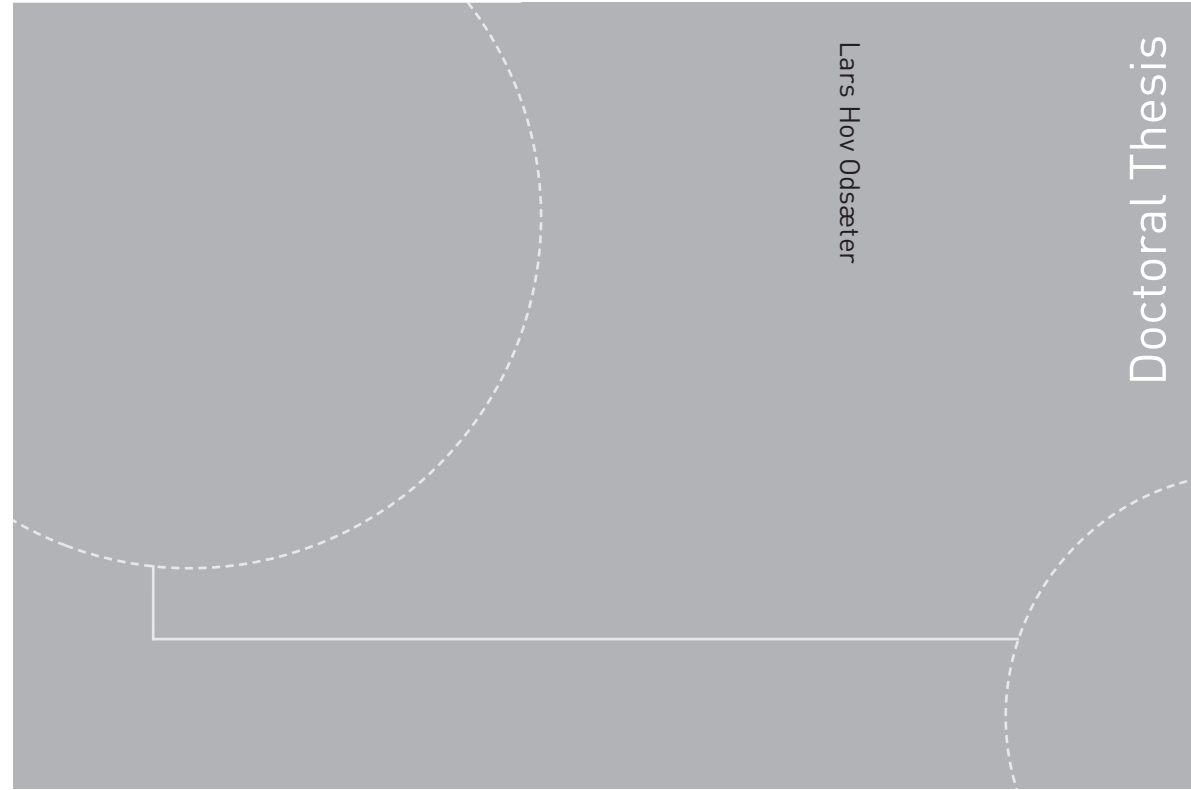


ISBN 978-82-326-3120-9 (printed version)  
ISBN 978-82-326-3121-6 (electronic version)  
ISSN 1503-8181



Doctoral theses at NTNU, 2018:165

Lars Hov Odsæter

# Reservoir Simulation in Heterogeneous and Fractured Reservoirs

Doctoral theses at NTNU, 2018:165

**NTNU**  
Norwegian University of  
Science and Technology  
Faculty of Information Technology  
and Electrical Engineering  
Department of Mathematical Sciences

 **NTNU**  
Norwegian University of  
Science and Technology

 NTNU

 **NTNU**  
Norwegian University of  
Science and Technology

Lars Hov Odsæter

# Reservoir Simulation in Heterogeneous and Fractured Reservoirs

Thesis for the degree of Philosophiae Doctor

Trondheim, June 2018

Norwegian University of Science and Technology  
Faculty of Information Technology  
and Electrical Engineering  
Department of Mathematical Sciences



Norwegian University of  
Science and Technology

**NTNU**

Norwegian University of Science and Technology

Thesis for the degree of Philosophiae Doctor

Faculty of Information Technology  
and Electrical Engineering  
Department of Mathematical Sciences

© Lars Hov Odsæter

ISBN 978-82-326-3120-9 (printed version)

ISBN 978-82-326-3121-6 (electronic version)

ISSN 1503-8181

Doctoral theses at NTNU, 2018:165



Printed by Skipnes Kommunikasjon as

## Preface

This thesis is submitted in partial fulfillment of the requirements for the degree of philosophiae doctor (PhD) at the Norwegian University of Science and Technology (NTNU), Trondheim, Norway. The thesis is organized in two parts. Part I gives an introduction to reservoir simulation in general, and to the main topics of this thesis in particular. Part II constitutes the main contributions in terms of scientific research papers.

Pursuing a PhD has been a long and tough journey, and there are many persons that have given me generous help and support on the way. First, I would like to thank Alf Birger Rustad, who has been my mentor for more than six years, dating back to my master's thesis. Alf is always available for a discussion, and I have appreciated his broad knowledge and honest opinion. Next, I would like to express my sincere gratitude to my supervisor Trond Kvamsdal, for his feedback, advice and inspiration, and for pushing me to deliver my best. I would also like to thank my co-supervisor Stein Krogstad for good discussions and valuable input. Moreover, thanks to my co-authors Carl Fredrik Berg, Mary F. Wheeler and Mats G. Larson, for great cooperation and fruitful discussions.

During the years as a PhD student I have enjoyed numerous coffee and lunch breaks with good friends and colleagues at the Department of Mathematical Sciences at NTNU. The first half of 2015 was spent at the Center for Subsurface Modeling at the University of Texas at Austin under supervision of Mary F. Wheeler. I was met with great hospitality, and the visit served as a valuable source of inspiration.

My research has been funded by VISTA, which is a basic research program funded by Statoil and conducted in close collaboration with The Norwegian Academy of Science and Letters. During the first years of the thesis I also enjoyed having a second office at Statoil's research center at Rotvoll in Trondheim, and I have appreciated help and support from numerous researchers at Statoil. Thanks also to the OPM community for help with implementations and access to an open-source reservoir simulator.

I would also like to thank my parents, Grethe and Knut, and my parents in law, Astrid and Anders, for their continued support, and for help with taking care of our children, so that both Ingrid and I could go to work.

Last, but not least, I would like to thank my family, Ingrid, Astrid and Johannes, for their unconditional love. Ingrid's support and patience during periods of frustration have been essential for the completion of this thesis.

Lars Hov Odsæter  
Trondheim, March 2018





# Contents

Preface . . . . .	i
List of research papers . . . . .	v
<b>Part I Background</b>	
1 Introduction . . . . .	3
1.1 Objectives of thesis . . . . .	3
1.2 Outline of thesis . . . . .	4
2 Flow and transport in porous media . . . . .	4
2.1 Scales of consideration . . . . .	5
2.2 Single-phase flow . . . . .	7
2.3 Multiphase flow . . . . .	8
3 Discretization . . . . .	11
3.1 Preliminaries . . . . .	12
3.2 Discretization schemes for the flow equation . . . . .	12
3.3 Discretization scheme for the transport equation . . . . .	16
3.4 Local conservation of mass . . . . .	17
4 Upscaling . . . . .	19
4.1 Single-phase upscaling . . . . .	20
4.2 Two-phase upscaling . . . . .	22
5 Flow and transport in fractured porous media . . . . .	23
5.1 Governing equations . . . . .	24
5.2 Discrete versus continuum fracture models . . . . .	25
5.3 Lower-dimensional discrete fracture-matrix models . . . . .	26
6 Summary of papers . . . . .	29
Paper I . . . . .	30
Paper II . . . . .	31
Paper III . . . . .	32
A Open-source simulation software . . . . .	34
Bibliography . . . . .	35
<b>Part II Research papers</b>	
Paper I: Rate dependency in steady-state upscaling . . . . .	51
Paper II: Postprocessing of non-conservative flux for compatibility with transport in heterogeneous media . . . . .	79
Paper III: A simple embedded discrete fracture-matrix model for a coupled flow and transport problems in porous media . . . . .	113



## List of research papers

**Paper I: Rate dependency in steady-state upscaling**

Odsæter, L.H., Berg, C.F., and Rustad, A.B.

*Transport in Porous Media*, 110(3):565–589, 2015

**Paper II: Postprocessing of non-conservative flux for compatibility with transport in heterogeneous media**

Odsæter, L.H., Wheeler, M.F., Kvamsdal, T., and Larson, M.G.

*Computer Methods in Applied Mechanics and Engineering*, 315:799–830, 2017

**Paper III: A simple embedded discrete fracture-matrix model for coupled flow and transport problems in porous media**

Odsæter, L.H., Kvamsdal, T., and Larson, M.G.

Preprint, submitted to *Computer Methods in Applied Mechanics and Engineering*, 2018



**Part I**

**Background**



# 1 Introduction

Reservoir simulation refers to the procedure of applying mathematical models and computational methods to predict the flow and transport of fluids and fluid components in porous media. Oil and gas companies use reservoir simulation as an engineering tool for decision making in reservoir management, e.g., for development of new fields or to increase the recovery of hydrocarbons from existing fields. Reservoir simulation is also used in other engineering disciplines, such as CO<sub>2</sub> storage and sequestration, groundwater flow, and nuclear waste disposal. A wide range of materials can be classified as porous, e.g., rock, soil, biological tissue, cements and ceramics, and the flow of fluids through these can be described by much of the same models as in a petroleum reservoir.

In a mathematics perspective reservoir simulation contains two main steps. The first, commonly referred to as *mathematical modeling*, is to model the physical processes of porous media flow by a set of differential equations and associated boundary conditions. Central in the modeling step is to determine what kind of assumptions that are appropriate for the specific problem at hand. This is a difficult task and require deep understanding of the physical processes. A wide range of models for fluid flow in porous media have been developed for different applications. The second step, *discretization*, is to reduce the infinite dimensional problems, governed by the mathematical model, to a finite dimensional problem that can be solved by computer methods. The geological models describing a reservoir are typically large and complex. Thus, efficient and robust numerical methods are needed to approximate the solution. The increase in computational power has been tremendous over the last decades, but maybe equally important to the overall efficiency is the development of mathematical methods.

A typical subsea reservoir is heterogeneous on many different length scales. The material properties may vary locally by many orders of magnitude, and the heterogeneities may form complex geometrical patterns. Such high ratios in material properties combined with complicated geometry are known to pose great challenges to the numerical methods. An extreme type of heterogeneity are fractures, which are thin surfaces with very high conductivity compared to the surrounding material. Fractures are often paramount to the fluid flow, since they serve as preferential paths. The fracture aperture (width) is typically orders of magnitude smaller than any other characteristic sizes in the domain of interest.

Basically there are two main ways to handle heterogeneity or fractures. The first alternative is to explicitly include them in the model. This is a feasible approach whenever the characteristic size of the geological feature is only a few orders of magnitude smaller than the global domain in consideration. However, one may have geological features that are present on a much smaller scale, but that still are of great importance to the global flow pattern. Even with the tremendous increase in computational power, it is infeasible to include such features explicitly into the global model. Hence, the second alternative to handle heterogeneity and fractures is by upscaling, also referred to as averaging or homogenization. The essence of upscaling is to find an effective (upscaled) value of the rock property in a heterogeneous bulk, such that the effective value captures the small scale influence on the larger scale. In the ideal situation this would reduce the model size, while still being able to approximate the global flow pattern accurately.

## 1.1 Objectives of thesis

This thesis addresses *simulation of fluid flow and transport in heterogeneous and fractured porous media*. The viewpoint will be from an applied mathematics perspective with the overall goal of contributing towards more *accurate, efficient and robust reservoir simulation software*.



The purpose of this thesis is to develop mathematical models and numerical methods that in turn can be used in simulation software. Moreover, we aim at delivering contributions that is of relevance to both industry and the mathematical community.

Motivated by the introductory discussion, we have identified three key tasks that are addressed in this thesis:

- (I) Study and validate steady-state upscaling of two-phase flow for representative heterogeneous reservoirs.
- (II) Develop a postprocessing method to calculate locally conservative fluxes in heterogeneous media.
- (III) Develop an embedded discrete fracture-matrix model for coupled flow and transport in fractured porous media.

## 1.2 Outline of thesis

This thesis consists of two parts. Part I, *Background*, introduces the main topics and the basic theory, while Part II, *Research papers*, constitutes the main contributions in terms of scientific research papers published in or submitted to peer-reviewed journals. The research papers are somehow compressed and focused towards a few issues. Hence, the main purpose of Part I is to serve as a complement to the individual papers by properly introducing the central topics, give additional details and put the contributions into a larger context. This will hopefully also motivate the choice of identified tasks in light of the main objective of the thesis.

After this introductory section of Part I, we proceed with a brief presentation of the fundamental theory of porous media flow in Section 2. This includes central concepts in reservoir simulation and a description of the most commonly used mathematical models. In Section 3, we introduce basic discretization schemes used in reservoir simulation. Moreover, the notion of local conservation of mass, which is a key concept for task (II) above, is discussed here. The next two sections, Section 4 and 5, are devoted to the main topics of this thesis: upscaling and flow in fractured porous media. We describe the basic theory and refer to key references among the great amount of literature. Finally, in Section 6, we give a summary of each research paper contained in Part II. We highlight the main contributions and comment on how they contribute to the main objectives of the thesis.

## 2 Flow and transport in porous media

This section introduces some of the fundamental theory of flow and transport in porous media. We only give a brief introduction to those concepts that are relevant for this thesis. For further details we refer to one of the many textbooks on porous media flow, e.g., [1–6], or [7, 8] for a more condensed version. Flow in fractured porous media is covered in Section 5, and is not considered here.

A porous media is a solid material containing interconnected pores (void space). The pores are usually filled with fluids, either liquid or gas. The *porosity* of a porous media is defined as the volume fraction of void space over the total volume. Another important property is the *permeability*, which is a measure of the ability of the material to allow fluids to pass through it. A subsea reservoir is typically built up of many thin layers of different porous rocks alternating in the vertical direction, see Fig. 2.1. Reservoirs can be highly heterogeneous and the rock properties may vary by many orders of magnitude. Local variations in permeability in the

range 1 mD to  $10^4$  mD ( $1 \text{ mD} = 9.87 \cdot 10^{-16} \text{ m}^2$ ) are not unusual. Such heterogeneities are present on many different length scales [8–12], and resolving these is one of the key challenges in reservoir simulation.

In general the governing equations for fluid flow and transport can be formulated as a set of conservation equations, one for each component present in the porous media. The number of different components can be very large, and hence it is common to group components with similar properties together and describe their movement with the same set of equations. The term *phase* is used for matter that has uniform physical properties. Usually, only three phases are considered: aqueous (w), oleic (o) and gaseous (g) phase. One or multiple component(s) constitute the phases. Before introducing the mathematical models for single-phase and multiphase flow (Section 2.2 and 2.3, respectively), we give a short introduction to the different scales of interest.

## 2.1 Scales of consideration

An important concept for the separation of scales is the notion of *representative elementary volumes* (REVs). A REV denotes a volume of the property field that is large enough to capture a representative amount of the heterogeneity [4], see Fig. 2.2. For practical purposes, one often speaks of an *appropriate volume*, which is a volume where the measured property is relatively insensitive to small changes in volume and location [11]. Identifying REVs is a challenging task, since they are property dependent and also vary from reservoir to reservoir. Nevertheless, if REVs can be identified, they can serve as a guideline to separate and identify natural length scales for modelling [8]. A central reference for REV is [4], while [11, 12] give more recent presentations.

The smallest scale of interest in reservoir simulation is the pore scale ( $\sim 10^{-3}$  m). This is where the actual flow takes place, and studies on the fundamentals of porous media flow are conducted on this scale. Flow models at larger scales can be seen as averaging of flow at the pore scale. A common strategy is to represent the porous media by a graph, see e.g., [13]. The next scale of interest is the core scale ( $\sim 10^{-2}$  m). Rock samples on the core scale from a reservoir are commonly used to determine rock and fluid parameters in a laboratory. We are now at a scale where the porous media can be viewed as a continuum and where Darcy’s law (defined below) is commonly accepted.

Information from the pore and core scale is used to populate geological models, which are three-dimensional representations of a reservoir, with rock and fluid properties, see Fig. 2.3 for a schematic illustration. The industry standard is to represent such models by a corner-point

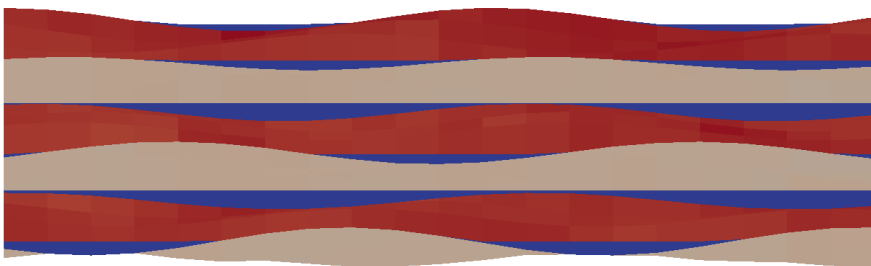


Fig. 2.1: Example of a section of a reservoir with alternating layers.

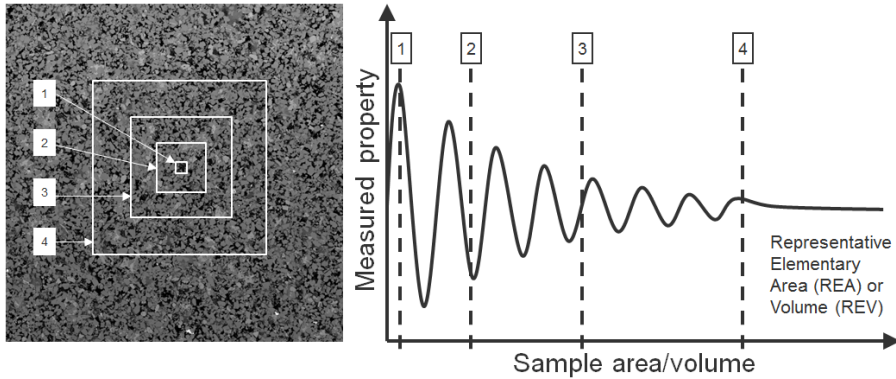


Fig. 2.2: Schematic illustration of representative elementary volume (REV) (after [12]). At small volumes (1), the measured property (e.g., porosity or permeability) is very sensitive to the size and position of the volume. As the volume increases (2 and 3), more of the texture is included and the variation in measured property is dampened. At a certain volume (4), referred to as a REV, enough of the texture is included so that the measured property is relatively insensitive to the position or further increase in volume.

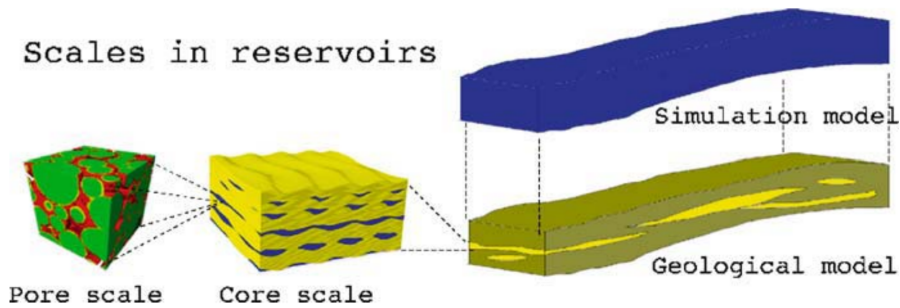


Fig. 2.3: Schematic figure of various scales and models in reservoir simulation (after [8, Fig. 3, p. 311]). Reprinted with permission from Springer Nature.

grid<sup>1</sup>, where the rock properties are represented by a constant value on each cell. Permeability may be given as a full tensor in order to represent cross-flow. A model is isotropic if the permeability can be expressed as a scalar. The size of a typical cell in a geological model is 10–50 m in the horizontal directions and 0.1–1 m in the vertical direction.

A full field reservoir can be on the scale of kilometers. Geological models typically contain far too many grid cells to run full field flow simulations directly on these models. This is due to limitations in memory and computing power of current computers. Field simulation is therefore performed on simulation models, which are also commonly represented on corner-point grids, but where the cell size is about 100 m in the horizontal direction and about 5 m in the vertical direction. Upscaling, which is a technique for transferring rock data from geological to simulation models, are covered in Section 4.

<sup>1</sup>See Section 3 for a brief introduction to corner-point grids.

## 2.2 Single-phase flow

The simplest model for fluid flow in porous media is single-phase flow, where only one phase is present. Single phase flow builds upon the general mass conservation equation

$$\frac{\partial(\phi\rho)}{\partial t} + \nabla \cdot (\rho\mathbf{u}) = \rho q. \quad (2.1)$$

Here  $\phi$  is the porosity,  $\rho$  is the fluid density,  $\mathbf{u}$  is the fluid velocity, and  $q$  is a source/sink term, typically modeling wells. The standard assumption on the fluid velocity is to apply Darcy's law,

$$\mathbf{u} = -\frac{\mathbf{K}}{\mu} (\nabla p - \rho g \nabla z), \quad (2.2)$$

where  $\mathbf{K}$  is the permeability tensor,  $\mu$  is the fluid viscosity,  $p$  is the fluid pressure,  $g$  is the gravitational acceleration and  $z$  is the depth. Eq. (2.1) and (2.2) constitutes the governing set of equations for single-phase flow.

The fluid pressure is commonly related to the fluid compressibility,  $c_f$ , through an equation of state,

$$c_f = \frac{1}{\rho} \left. \frac{\partial \rho}{\partial p} \right|_T \quad (2.3)$$

at a fixed temperature  $T$ . Assuming  $c_f$  constant over a certain range of pressure, we may write (2.3) as

$$\rho = \rho_0 e^{c_f(p-p_0)}, \quad (2.4)$$

where  $\rho_0$  is the density at a reference pressure  $p_0$ . Taylor expansion to the first order gives the approximation

$$\rho \approx \rho_0 (1 + c_f(p - p_0)). \quad (2.5)$$

Similarly, we may relate the porosity to the rock compressibility,  $c_r$ , defined as

$$c_r = \frac{1}{\phi} \frac{d\phi}{dp}. \quad (2.6)$$

After integration and Taylor expansion to the first order we arrive at the approximation

$$\phi \approx \phi_0 (1 + c_r(p - p_0)), \quad (2.7)$$

where  $\phi_0$  is the porosity at  $p_0$ .

Substituting Darcy's law (2.2) and the two approximations (2.5) and (2.7) into (2.1), and carrying out the time differentiation, we end up with the following equation for slightly compressible fluid and rock,

$$\phi \rho c_t \frac{\partial p}{\partial t} - \nabla \cdot \left( \frac{\rho}{\mu} \mathbf{K} (\nabla p - \rho g \nabla z) \right) = \rho q, \quad (2.8)$$

where  $c_t$  denotes the total compressibility,

$$c_t = c_f + \frac{\phi_0}{\phi} c_r. \quad (2.9)$$

Eq. (2.8) is parabolic in  $p$ .

If one further assumes incompressible fluid and rock, that is,  $c_r = c_f = 0$ , Eq. (2.8) reduces to the stationary elliptic problem

$$-\nabla \cdot \left( \frac{\mathbf{K}}{\mu} (\nabla p - \rho g \nabla z) \right) = q. \quad (2.10)$$

### 2.2.1 Transport of a component

The transport of a component, e.g., a solute, in a single fluid phase can be described by conservation of mass of the component,

$$\frac{\partial(\phi c \rho)}{\partial t} + \nabla \cdot (c \rho \mathbf{u} - \rho \mathbf{D} \nabla c) = \rho q c^*. \quad (2.11)$$

Here  $c$  is the concentration of the component,  $\mathbf{D}$  is the diffusion–dispersion tensor, and  $c^*$  is the upwind concentration at the source/sink, i.e.,

$$q c^* = \begin{cases} q c, & \text{if } q \leq 0, \\ q c_w, & \text{if } q > 0, \end{cases} \quad (2.12)$$

where  $c_w$  is the inflow concentration from the source. The diffusion–dispersion tensor  $\mathbf{D}$  is commonly expressed as

$$\mathbf{D}(\mathbf{u}) = \phi \left( d_m \mathbf{I} + |\mathbf{u}| \left( d_l \mathbf{E}(\mathbf{u}) + d_t \mathbf{E}^\perp(\mathbf{u}) \right) \right), \quad (2.13)$$

where  $d_m$  is the molecular diffusion coefficient,  $d_l$  and  $d_t$  are the longitudinal and transverse dispersion coefficients, respectively,  $\mathbf{E}(\mathbf{u}) = \frac{1}{|\mathbf{u}|^2} \mathbf{u} \mathbf{u}^T$ , and  $\mathbf{E}^\perp(\mathbf{u}) = \mathbf{I} - \mathbf{E}(\mathbf{u})$ , see e.g., [6].

Assuming incompressible fluid and rock, we end up with the following advection–diffusion equation

$$\phi \frac{\partial c}{\partial t} + \nabla \cdot (c \mathbf{u} - \mathbf{D} \nabla c) = q c^*. \quad (2.14)$$

A common application of this equation is tracer flow [14].

### 2.3 Multiphase flow

We consider next multiphase flow with multiple components. Denote by  $S_\alpha$  the phase saturation defined as the fraction of the void volume that is filled with phase  $\alpha$ ,  $\alpha \in \{w, o, g\}$ . Furthermore,  $c_{l\alpha}$  denotes the mass fraction of component  $l$  in phase  $\alpha$ . The sums of volume and mass fractions are equal to unity, i.e.,

$$\sum_{\alpha} S_{\alpha} = 1, \quad (2.15)$$

$$\sum_l c_{l\alpha} = 1, \quad \forall \alpha. \quad (2.16)$$

Mass is allowed to transfer between the phases, but each component is conserved. Hence, multiphase, multicomponent flow is governed by a set of conservation equations, one for each component  $l$ ,

$$\frac{\partial}{\partial t} \left( \phi \sum_{\alpha} c_{l\alpha} \rho_{\alpha} S_{\alpha} \right) + \nabla \cdot \left( \sum_{\alpha} c_{l\alpha} \rho_{\alpha} \mathbf{u}_{\alpha} \right) = \sum_{\alpha} c_{l\alpha} \rho_{\alpha} q_{\alpha}. \quad (2.17)$$

Subscript  $\alpha$  refers to a phase specific quantity, so that  $\rho_{\alpha}$  is the density of the phase,  $\mathbf{u}_{\alpha}$  is the phase velocity, and  $q_{\alpha}$  is the phase source.

To model the phase velocity, the most common approach is to extend Darcy’s law (2.2) to multiphase flow,

$$\mathbf{u}_{\alpha} = -\frac{\mathbf{K}_{\alpha}}{\mu_{\alpha}} (\nabla p_{\alpha} - \rho_{\alpha} g \nabla z), \quad (2.18)$$

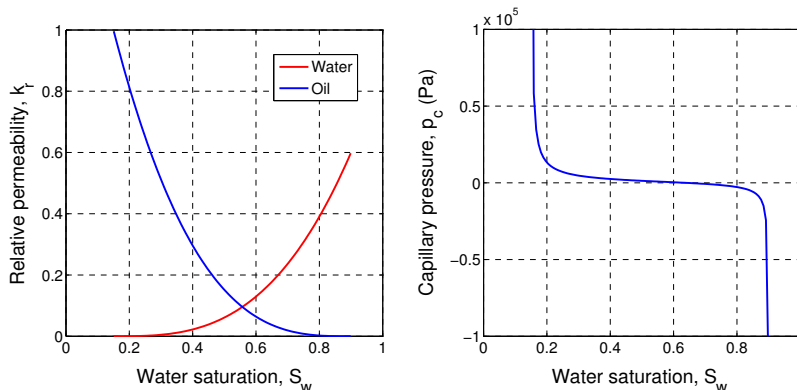


Fig. 2.4: Example of relative permeability and capillary pressure curves for a two-phase oil-water system.

where

$$\mathbf{K}_\alpha = k_{r\alpha} \mathbf{K} \quad (2.19)$$

is the phase permeability. The coefficient  $k_{r\alpha}$  is known as the relative permeability and models the reduced permeability of each phase due to the presence of the other phases. We will consider  $k_{r\alpha}$  as a known function of the phase saturations.

Another common assumption is that the differences between phase pressures are known functions of the phase saturations. These quantities are commonly referred to as capillary pressures, and are defined as

$$p_{cow} = p_o - p_w, \quad (2.20a)$$

$$p_{cgo} = p_g - p_o. \quad (2.20b)$$

One could also define a third capillary pressure, but this is not necessary since it can be expressed in terms of  $p_{cow}$  and  $p_{cgo}$ . Examples of relative permeability and capillary pressure curves are displayed in Fig. 2.4.

In the following sections, we consider two important multiphase flow models that are special cases of the general set of equations (2.15)–(2.18).

### 2.3.1 Immiscible two-phase flow

In this section we consider a two-phase flow model with one water phase ( $\alpha = w$ ) and one hydrocarbon phase ( $\alpha = o$ ). The water phase has a single component ( $l = w$ ), while the hydrocarbon phase consists of dissolved gas ( $l = g$ ) and a residual oil ( $l = o$ ). The fluids are immiscible and we assume that there is no mass transfer between the phases. Under these assumptions, the mass fractions  $c_{l\alpha}$  can be expressed as

$$\begin{aligned} c_{ww} &= 1, & c_{ow} &= 0, & c_{gw} &= 0, \\ c_{wo} &= 0, & c_{oo} &= \frac{m_o}{m_o + m_g}, & c_{go} &= \frac{m_g}{m_o + m_g}, \\ c_{wg} &= 0, & c_{og} &= 0, & c_{gg} &= 0, \end{aligned} \quad (2.21)$$

where  $m_g$  and  $m_o$  are the masses of oil and gas, respectively. The conservation equations (2.17) yields one equation for each component  $l$ ,  $l = w, o, g$ . Adding the equations for the oil and gas

components, we get one equation for each phase,

$$\frac{\partial(\phi\rho_\alpha S_\alpha)}{\partial t} + \nabla \cdot (\rho_\alpha \mathbf{u}_\alpha) = \rho_\alpha q_\alpha, \quad \alpha = o, w. \quad (2.22)$$

By inserting Darcy's law (2.18) into Eq. (2.22), we get the following equations for two-phase immiscible flow,

$$\frac{\partial(\phi\rho_\alpha S_\alpha)}{\partial t} - \nabla \cdot \left( \frac{\rho_\alpha k_{r\alpha}}{\mu_\alpha} \mathbf{K} (\nabla p_\alpha - \rho_\alpha g \nabla z) \right) = \rho_\alpha q_\alpha, \quad \alpha = o, w. \quad (2.23)$$

In addition, we have the closing conditions (2.15) and (2.20a).

Several alternative formulations of this set of equations have been derived. In the next section we consider the global pressure formulation.

### Global pressure formulation

For now, we assume incompressibility both for the rock and the fluids such that  $\frac{\partial\phi}{\partial t} = \frac{\partial\rho_\alpha}{\partial t} = 0$ , for  $\alpha = o, w$ . Then Eq. (2.23) reduces to

$$\phi \frac{\partial S_\alpha}{\partial t} + \nabla \cdot (\lambda_\alpha \mathbf{K} (\nabla p_\alpha - \rho_\alpha g \nabla z)) = q_\alpha, \quad \alpha = o, w, \quad (2.24)$$

where  $\lambda_\alpha = \frac{k_{r\alpha}}{\mu_\alpha}$  are the phase mobilities. Furthermore, define the fractional flow functions  $f_\alpha = \frac{\lambda_\alpha}{\lambda}$ . We follow the approach of [3] and introduce the global pressure

$$p = p_o - \hat{p}, \quad \hat{p}(S_w) = \int_1^{S_w} f_w(\xi) \frac{dp_{cow}}{d\xi}(\xi) d\xi. \quad (2.25)$$

From Darcy's law (2.18), we get that the global velocity is given as

$$\mathbf{u} = \mathbf{u}_o + \mathbf{u}_w = -\mathbf{K}\lambda (\nabla p - (\rho_w f_w + \rho_o f_o)g \nabla z) \quad (2.26)$$

with  $\lambda = \lambda_o + \lambda_w$ . Furthermore, by adding the two equations defined by (2.24) together, it follows that

$$\nabla \cdot \mathbf{u} = q, \quad (2.27)$$

where  $q = q_o + q_w$ . Moreover, the phase velocities can be expressed as

$$\mathbf{u}_w = f_w \mathbf{u} + \mathbf{K}\lambda_o f_w \nabla p_{cow} + \mathbf{K}\lambda_o f_w (\rho_w - \rho_o)g \nabla z, \quad (2.28)$$

$$\mathbf{u}_o = f_o \mathbf{u} - \mathbf{K}\lambda_w f_o \nabla p_{cow} + \mathbf{K}\lambda_w f_o (\rho_o - \rho_w)g \nabla z. \quad (2.29)$$

One can now rewrite (2.24) for  $\alpha = w$  into

$$\phi \frac{\partial S_w}{\partial t} + \nabla \cdot (\mathbf{K}\lambda_o f_w (\nabla p_{cow} - (\rho_o - \rho_w)g \nabla z) + f_w \mathbf{u}) = q_w. \quad (2.30)$$

Eq. (2.26), (2.27) and (2.30) constitute the global pressure formulation. Observe that the saturation equation (2.30) contains three different terms that represent different types of forces acting on the fluids. These are capillary forces ( $\mathbf{K}\lambda_o f_w \nabla p_{cow}$ ), gravitational forces ( $\mathbf{K}\lambda_o f_w (\rho_o - \rho_w)g \nabla z$ ), and viscous forces ( $f_w \mathbf{u}$ ). Eq. (2.27) is commonly referred to as the pressure equation and is elliptic in  $p$ , while Eq. (2.30) is in general parabolic in  $p$ , but with a hyperbolic nature when viscous or gravitational forces are dominant. An advantage of the global pressure formulation is that the pressure and saturation equations are weaker coupled compared to other formulations. This makes it better suitable for a sequential solution scheme.

### 2.3.2 The black oil model

The black oil model describes the simultaneous flow of three phases (water, oil and gas) and is one of the most common models in industrial reservoir simulators. The water phase still contains only pure water, and thus there are no mass transfer between the water phase and the other phases. The hydrocarbon components are divided into a gas component and a oil component at standard temperature and pressure. We allow for the gas component to be dissolved into the oil phase, but we do not consider oil to be vaporized into the gas phase. Hence, we have the following mass fractions,

$$\begin{aligned} c_{ww} &= 1, & c_{ow} &= 0, & c_{gw} &= 0, \\ c_{wo} &= 0, & c_{oo} &= (\text{PVT}), & c_{go} &= (\text{PVT}), \\ c_{wg} &= 0, & c_{og} &= 0, & c_{gg} &= 1, \end{aligned} \quad (2.31)$$

where we have indicated that  $c_{oo}$  and  $c_{go}$  need to be determined from PVT (Pressure–Volume–Temperature) models, which will not be further explained here. The conservation equations (2.17) for the three components can now be written as

$$\frac{\partial(\phi\rho_w S_w)}{\partial t} + \nabla \cdot (\rho_w \mathbf{u}_w) = \rho_w q_w, \quad (2.32)$$

$$\frac{\partial(\phi c_{oo} \rho_o S_o)}{\partial t} + \nabla \cdot (c_{oo} \rho_o \mathbf{u}_o) = c_{oo} \rho_o q_o, \quad (2.33)$$

$$\frac{\partial(\phi(c_{go} \rho_o S_o + \rho_g S_g))}{\partial t} + \nabla \cdot (c_{go} \rho_o \mathbf{u}_o + \rho_g \mathbf{u}_g) = c_{go} \rho_o q_o + \rho_g q_g. \quad (2.34)$$

The Darcy equations (2.18) is used as velocity model also for the black oil model. Furthermore, the closing conditions (2.15), (2.16) and (2.20) apply, where (2.16) reduces to the single condition  $c_{oo} + c_{go} = 1$ .

## 3 Discretization

In this section we introduce some of the most common discretization schemes used in classical reservoir simulation. The main purpose is to highlight their characteristics and describe their advantages and disadvantages. To keep the presentation simple we consider incompressible single-phase flow (2.10) coupled to the transport problem (2.14) for a single solute on a polyhedral domain  $\Omega \subset \mathbb{R}^d$ ,  $d = 2, 3$ . We refer to [6, 7, 15] for good reviews and discussions of discretization schemes for porous media flow.

We remark that *corner-point grids* [16] are the industry standard to represent geological and simulation models. A corner-point grid is built up of multiple vertical or inclined linear pillars. A constant number of points are defined on each pillar, and a corner-point cell is a hexahedron defined by four neighboring pillars and two neighboring points on each pillar. Corner-point grids are in general very flexible as they allow for degenerated cells where two or more points may coincide. Furthermore, the grid can be non-conforming, and cells may have zero volume. This flexibility allows for complex geological features to be represented, but pose great challenges to the numerical method, see [15] for further discussion. In the following, we will not restrict the presentation to discretization schemes on corner-point grids, but rather consider a general partition of the domain.



### 3.1 Preliminaries

Denote by  $\mathcal{K}_h$  a partition of  $\Omega$  into polyhedral cells (or elements)<sup>1</sup>  $K \in \mathcal{K}_h$ . We let  $K \in \mathcal{K}_h$  be open. The set of cell faces is denoted  $\mathcal{F}_h$ , which we further divide into interior faces,  $\mathcal{F}_{h,I}$ , and faces on the boundary,  $\mathcal{F}_{h,B}$ . Furthermore, let  $\mathbf{n}_K$  be the unit normal on  $\partial K$  pointing out of  $K$ . We also fix an orientation of every  $F \in \mathcal{F}_h$  and denote by  $\mathbf{n}_F$  the unit normal on  $F$ . Observe that  $\mathbf{n}_F$  either coincide with  $\mathbf{n}_K$  or points in the opposite direction, i.e.,  $\mathbf{n}_F = \pm \mathbf{n}_K|_F$  for  $F \in \partial K$ .

We will use the standard notation  $H^s(\omega)$  for the Sobolev space of order  $s$  on  $\omega$  with the special case  $L^2(\omega) = H^0(\omega)$ . For a function space  $V$ , we denote by  $V^d$  the space of  $d$ -dimensional vector functions with each component in  $V$ . In particular, we will make use of the following function spaces,

$$H^{\text{div}}(K) = \{\mathbf{v} \in (L^2(K))^d : \nabla \cdot \mathbf{v} \in L^2(K)\}, \quad (3.1)$$

$$H_0^{\text{div}}(\mathcal{K}_h) = \{\mathbf{v} \in H^{\text{div}}(\cup_{K \in \mathcal{K}_h} K) : \mathbf{v} \cdot \mathbf{n}|_{\partial\Omega} = 0\}, \quad (3.2)$$

$$H_0^{\text{div}}(\Omega) = H_0^{\text{div}}(\mathcal{K}_h) \cap H^{\text{div}}(\Omega). \quad (3.3)$$

Moreover, we denote by  $(\cdot, \cdot)_\omega$  the  $L^2$  inner product on  $\omega$ , and by  $(\cdot, \cdot)_{\mathcal{K}_h}$  the broken inner product, i.e.,

$$(u, v)_\omega = \int_\omega uv \, dx, \quad (3.4)$$

$$(u, v)_{\mathcal{K}_h} = \sum_{K \in \mathcal{K}_h} (u, v)_K, \quad (3.5)$$

$$(u, v)_{\mathcal{F}_h} = \sum_{F \in \mathcal{F}_h} (u, v)_F. \quad (3.6)$$

The set of piecewise constant functions on  $\mathcal{K}_h$  and  $\mathcal{F}_h$  are denoted  $P_0(\mathcal{K}_h)$  and  $P_0(\mathcal{F}_h)$ , respectively, while the set of continuous functions consisting of polynomials of order  $r > 0$  on each element in  $\mathcal{K}_h$  is denoted  $P_r(\mathcal{K}_h)$ . Moreover, we denote by  $[[\cdot]]$  and  $\{\{\cdot\}\}$  the jump and average operators, respectively, defined as

$$[[v]] = v_+ - v_-, \quad (3.7)$$

$$\{\{v\}\} = \frac{1}{2}(v_- + v_+), \quad (3.8)$$

where

$$v_\pm(\mathbf{x}) = \lim_{\epsilon \rightarrow 0^+} v(\mathbf{x} \pm \epsilon \mathbf{n}_F), \quad \mathbf{x} \in F. \quad (3.9)$$

### 3.2 Discretization schemes for the flow equation

The elliptic single-phase flow equation (2.10) is given by

$$-\nabla \cdot (\mathbf{K} \nabla p) = q, \quad \text{in } \Omega, \quad (3.10)$$

where we have neglected gravity and set  $\mu = 1$ . This equation can also be written in mixed form,

$$\nabla \cdot \mathbf{u} = q, \quad \text{in } \Omega, \quad (3.11a)$$

$$\mathbf{u} = -\mathbf{K} \nabla p, \quad \text{in } \Omega. \quad (3.11b)$$

<sup>1</sup>The terms cell and element will be used interchangeably throughout this thesis dependent on the context.

For simplicity, we consider homogeneous Neumann boundary conditions,

$$\mathbf{u} \cdot \mathbf{n} = 0, \quad \text{on } \partial\Omega, \quad (3.12)$$

also commonly referred to as no-flow conditions since no fluids are allowed to enter or leave the domain. To close the system, we add the extra constraint  $\int_{\Omega} p = 0$ , and we require  $\int_{\Omega} q = 0$  for the problem to be well-posed.

### 3.2.1 Cell-centered finite volume methods

We integrate Eq. (3.11a) over a cell  $K_i \in \mathcal{K}_h$  and apply the divergence theorem to obtain

$$\int_{\partial K_i} \mathbf{u} \cdot \mathbf{n}_{K_i} ds = \int_{K_i} q dx. \quad (3.13)$$

Finite volume methods are formulated by approximating the pressure  $p$  by a piecewise constant function  $p_h \in P_0(\mathcal{K}_h)$  and estimating the normal velocity  $\mathbf{u} \cdot \mathbf{n}$  across cell interfaces from a set of neighboring cell pressures. In the two-point flux approximation (TPFA) the normal velocity is approximated by the pressure in the two cells adjacent to the current interface.

Let  $u_{ij}$  be the integrated flux along an interface  $F_{ij} = \partial K_i \cap \partial K_j$ , i.e.,

$$u_{ij} = - \int_{F_{ij}} (\mathbf{K} \nabla p) \cdot \mathbf{n}_{ij} ds, \quad (3.14)$$

where  $\mathbf{n}_{ij}$  is the unit normal on  $F_{ij}$  pointing from  $K_i$  towards  $K_j$ . In the following, we will assume  $\mathcal{K}_h$  to be a regular hexahedral grid with gridlines aligned with the principal coordinate axes. Let  $F_{ij}$  be an interface between two neighboring cells in the  $x$ -directions so that  $\mathbf{n}_{ij} = (1, 0, 0)^T$ . Then the pressure gradient is approximated by the pressure drop in the two neighboring cells,

$$\left. \frac{\partial p}{\partial x} \right|_{F_{ij}} \approx \frac{2(p_{h,j} - p_{h,i})}{\Delta x_i + \Delta x_j}, \quad (3.15)$$

where  $p_{h,i} = p_h|_{K_i}$  and  $\Delta x_i$  is the cell dimension in the  $x$ -direction for cell  $K_i$ . Next, let  $u_{h,ij}$  be the finite volume approximation to  $u_{ij}$ . For TPFA we have

$$u_{h,ij} = - \frac{2(p_{h,j} - p_{h,i})}{\Delta x_i + \Delta x_j} \int_{F_{ij}} k_{ij} ds, \quad (3.16)$$

where  $k_{ij} = \mathbf{n}_{ij}^T \mathbf{K} \mathbf{n}_{ij}$  is the directional permeability. However, in most reservoir models,  $\mathbf{K}$  is a piecewise constant tensor, and hence not well-defined on the cell interfaces. Instead, the distance-weighted harmonic average is used, i.e.,

$$k_{ij} = (\Delta x_i + \Delta x_j) \left( \frac{\Delta x_i}{k_{i,ij}} + \frac{\Delta x_j}{k_{j,ij}} \right)^{-1}, \quad (3.17)$$

where  $k_{i,ij} = \mathbf{n}_{ij}^T \mathbf{K}_i \mathbf{n}_{ij}$ . We can now formulate the flux approximation (3.16) as

$$u_{h,ij} = t_{ij}(p_{h,i} - p_{h,j}), \quad (3.18)$$

where  $t_{ij}$  are known as the transmissibilities, defined as

$$t_{ij} = 2|F_{ij}| \left( \frac{\Delta x_i}{k_{i,ij}} + \frac{\Delta x_j}{k_{j,ij}} \right)^{-1}. \quad (3.19)$$

Summing over all neighboring cells, we get an approximation to  $\int_{\partial K_i} \mathbf{u} \cdot \mathbf{n}_{K_i}$ . By requiring (3.13) to hold for all  $K_i \in \mathcal{K}_h$ , we can formulate the TPFA method as follows.

**Definition 3.1** (TPFA). *Find  $p_h \in P_0(\mathcal{K}_h)$  such that*

$$\sum_j t_{ij}(p_{h,i} - p_{h,j}) = \int_{K_i} q \, dx, \quad \forall K_i \in \mathcal{K}_h. \quad (3.20)$$

The TPFA method can be extended to more general grids, including unstructured grids, and the formulation (3.20) still applies, but the calculation of the transmissibilities are dependent on the grid. The main drawback of TPFA is that it suffers from grid-orientation effects so that the solution depends on the geometry of the grid. More precisely, TPFA is only convergent on so-called  $\mathbf{K}$ -orthogonal grids. A grid is  $\mathbf{K}$ -orthogonal if every cell is a parallelepiped<sup>2</sup> and

$$\mathbf{n}_{ij} \cdot (\mathbf{K}\mathbf{n}_{ik}) = 0, \quad \forall K_i \in \mathcal{K}_h, \quad \mathbf{n}_{ij} \neq \mathbf{n}_{ik}. \quad (3.21)$$

Multi-point flux approximation (MPFA) schemes is a class of finite volume methods that aims to resolve the shortcomings of TPFA. The basic idea is to approximate the integrated flux,  $u_{ij}$ , by more than two cell pressures. Several MPFA schemes are presented, e.g., the O-method [17, 18].

### 3.2.2 Classical finite element method

The weak formulation of the boundary value problem (3.10) and (3.12) is obtained by multiplying (3.10) with a test function  $v \in H^1(\Omega)$ , integrate over  $\Omega$  and apply Greens formula. Find  $p \in H^1(\Omega)$  such that

$$a(p, v) = l(v), \quad \forall v \in H^1(\Omega), \quad (3.22)$$

where

$$a(\cdot, \cdot) : H^1(\Omega) \times H^1(\Omega) \rightarrow \mathbb{R}, \quad a(u, v) = (\mathbf{K}\nabla u, \nabla v)_\Omega, \quad (3.23)$$

$$l(\cdot) : H^1(\Omega) \rightarrow \mathbb{R}, \quad l(v) = (q, v)_\Omega. \quad (3.24)$$

The classical finite element method (FEM) is obtained by restricting the weak formulation to a finite dimensional subspace  $V_h \subset H^1(\Omega)$ . Choosing  $V_h = P_r(\mathcal{K}_h)$  for  $r > 0$ , results in the continuous Galerkin FEM (CG-FEM).

**Definition 3.2** (FEM). *Find  $p_h \in V_h$  such that*

$$a(p_h, v_h) = l(v_h), \quad \forall v_h \in V_h. \quad (3.25)$$

Another variant is the isogeometric FEM [19], see also [20] for an application to Darcy flow.

### 3.2.3 Mixed finite element method

The mixed FEM is based on the mixed formulation (3.11). In contrast to classical FEM, the fluxes over element faces are considered as unknowns in addition to the pressure. Let us define the following bilinear forms:

$$b(\cdot, \cdot) : H_0^{\text{div}}(\mathcal{K}_h) \times H_0^{\text{div}}(\mathcal{K}_h) \rightarrow \mathbb{R}, \quad b(\mathbf{u}, \mathbf{v}) = (\mathbf{u}, \mathbf{K}^{-1}\mathbf{v})_{\mathcal{K}_h}, \quad (3.26)$$

$$c(\cdot, \cdot) : H_0^{\text{div}}(\mathcal{K}_h) \times L^2(\Omega) \rightarrow \mathbb{R}, \quad c(\mathbf{u}, p) = (p, \nabla \cdot \mathbf{u})_{\mathcal{K}_h}, \quad (3.27)$$

$$d(\cdot, \cdot) : H_0^{\text{div}}(\mathcal{K}_h) \times H^{\frac{1}{2}}(\mathcal{F}_h) \rightarrow \mathbb{R}, \quad d(\mathbf{u}, \pi) = (\pi, \llbracket \mathbf{u} \cdot \mathbf{n} \rrbracket)_{\mathcal{F}_h}. \quad (3.28)$$

<sup>2</sup>A parallelepiped is a three dimensional volume formed by six parallelograms.

The weak formulation is derived by multiplying (3.11) by test functions, integrate over  $\Omega$  and apply Greens formula. Find  $(\mathbf{u}, p) \in H_0^{\text{div}}(\Omega) \times L^2(\Omega)$  such that

$$b(\mathbf{u}, \mathbf{v}) - c(\mathbf{v}, p) = 0, \quad \forall \mathbf{v} \in H_0^{\text{div}}(\Omega), \quad (3.29a)$$

$$c(\mathbf{u}, v) = l(v), \quad \forall v \in L^2(\Omega). \quad (3.29b)$$

A mixed FEM (MFEM) scheme is then obtained by restricting the weak formulation to finite dimensional subspaces  $U_h \subset H_0^{\text{div}}(\Omega)$  and  $V_h \subset L^2(\Omega)$ .

**Definition 3.3** (MFEM). *Find  $(\mathbf{u}_h, p_h) \in U_h \times V_h$  such that*

$$b(\mathbf{u}_h, \mathbf{v}_h) - c(\mathbf{v}_h, p_h) = 0, \quad \forall \mathbf{v}_h \in U_h, \quad (3.30a)$$

$$c(\mathbf{u}_h, v_h) = l(v_h), \quad \forall v_h \in V_h. \quad (3.30b)$$

A popular choice is to use the Raviart–Thomas elements [21, 22]. A major drawback of mixed FEM is that it requires to solve a saddle-point problem, which leads to indefinite linear systems that require special solvers and are considered hard to solve. The mixed hybrid FEM (MHFEM) resolves this issue by enforcing flux continuity weakly through Lagrange multipliers instead of requiring  $U_h \subset H_0^{\text{div}}(\Omega)$ . The hybrid formulation goes as follows. Find  $(\mathbf{u}, p, \pi) \in H_0^{\text{div}}(\mathcal{K}_h) \times L^2(\Omega) \times H^{\frac{1}{2}}(\mathcal{F}_{h,I})$  such that

$$b(\mathbf{u}, \mathbf{v}) - c(\mathbf{v}, p) + d(\mathbf{v}, \pi) = 0, \quad \forall \mathbf{v} \in H_0^{\text{div}}(\mathcal{K}_h), \quad (3.31a)$$

$$c(\mathbf{u}, v) = l(v), \quad \forall v \in L^2(\Omega), \quad (3.31b)$$

$$d(\mathbf{u}, \mu) = 0, \quad \forall \mu \in H^{\frac{1}{2}}(\mathcal{F}_{h,I}). \quad (3.31c)$$

Observe that compared to the mixed formulation (3.29), we now have  $\mathbf{u} \in H_0^{\text{div}}(\mathcal{K}_h)$  instead of  $\mathbf{u} \in H_0^{\text{div}}(\Omega)$ , and we use broken norms in the formulation. The Lagrange multiplier  $\pi$  can be interpreted as the face pressure, and Eq. (3.31c) enforces flux continuity weakly.

Similarly as for FEM and MFEM, we formulate MHFEM by restricting the weak formulation (3.31) to finite dimensional subspaces  $U_h \subset H_0^{\text{div}}(\mathcal{K}_h)$ ,  $V_h \subset L^2(\Omega)$  and  $W_h \in H^{\frac{1}{2}}(\mathcal{F}_{h,I})$ .

**Definition 3.4** (MHFEM). *Find  $(\mathbf{u}_h, p_h, \pi_h) \in U_h \times V_h \times W_h$  such that*

$$b(\mathbf{u}_h, \mathbf{v}_h) - c(\mathbf{v}_h, p_h) + d(\mathbf{v}_h, \pi_h) = 0, \quad \forall \mathbf{v}_h \in U_h, \quad (3.32a)$$

$$c(\mathbf{u}_h, v_h) = l(v_h), \quad \forall v_h \in V_h, \quad (3.32b)$$

$$d(\mathbf{u}_h, \mu_h) = 0, \quad \forall \mu_h \in W_h. \quad (3.32c)$$

In practice, the resulting linear system is typically solved by a Schur-complement reduction.

### 3.2.4 Mimetic finite difference method

The mimetic finite difference method (MFD) [23, 24] can be seen as a finite-difference counterpart of MHFEM [15]. Observe that if we choose piecewise constant functions for the pressure and the Lagrange multipliers, i.e.,  $V_h = P_0(\mathcal{K}_h)$  and  $W_h = P_0(\mathcal{F}_h)$ , both  $c(\mathbf{u}_h, p_h)$  and  $d(\mathbf{u}_h, \pi_h)$  can be determined without an explicit representation of  $\mathbf{u}_h$  in the element interiors, only by the normal component on the element boundaries. This can be seen immediately for  $d(\mathbf{u}_h, \pi_h)$ , while we apply the divergence theorem to  $c(\mathbf{u}_h, p_h)$ , to reveal that

$$c(\mathbf{u}_h, p_h) = \sum_{K \in \mathcal{K}_h} \int_K p_h \nabla \cdot \mathbf{u}_h = \sum_{K \in \mathcal{K}_h} p_h|_K \int_{\partial K} \mathbf{u} \cdot \mathbf{n}_K. \quad (3.33)$$

Hence, to formulate the MFDM we are left with the term  $b(\mathbf{u}, \mathbf{v})$ . While MHFEM approximate this term by restricting  $H_0^{\text{div}}(\mathcal{K}_h)$  to a finite dimensional subspace, MFDM instead replaces  $b(\mathbf{u}, \mathbf{v})$  by a discrete inner-product,  $m(\cdot, \cdot)$  that acts on a finite dimensional subspace  $M_h \subset L^2(\mathcal{F}_h)$ . If we denote by  $\nu_h$  the approximation to the normal flux,  $\mathbf{u} \cdot \mathbf{n}$ , we can formulate MFDM as follows.

**Definition 3.5** (MFDM). *Find  $(\nu_h, p_h, \pi_h) \in M_h \times P_0(\mathcal{K}_h) \times P_0(\mathcal{F}_h)$  such that*

$$m(\nu_h, \psi_h) - c(\psi_h, p_h) + d(\psi_h, \pi_h) = 0, \quad \forall \psi_h \in M_h, \quad (3.34a)$$

$$c(\nu_h, v_h) = l(v_h), \quad \forall v_h \in P_0(\mathcal{K}_h), \quad (3.34b)$$

$$d(\nu_h, \mu_h) = 0, \quad \forall \mu_h \in P_0(\mathcal{F}_h). \quad (3.34c)$$

Stability and convergence of MFDM for general grids are proven in [25, 26].

### 3.2.5 Discussion

Despite its shortcomings, TPFA is the dominant method in commercial reservoir simulators due to its simplicity and computational efficiency. However, as explained earlier, TPFA is not robust with respect to the grid geometry. MPFA are more accurate than TPFA, but can be hard to implement on non-conforming grids with non-matching faces. Furthermore, MPFA are not monotone on general grids, in contrast to TPFA. MFDM is very flexible with respect to cell geometry and handles non-conforming grids in a natural way.

An advantage of FEM compared to finite volume and finite difference methods is the large amount of results on convergence and error estimates. FEM can also handle grids with degenerated cells [27, Section 3.4]. CG-FEM can be considered a simpler method than M(H)FEM as they contain fewer degrees of freedom and the elements are easier to implement. In particular, CG-FEM is attractive due to simple (dynamic) mesh adaptivity. Non-matching grids can be handled in a straight forward way, while for M(H)FEM non-matching elements must be handled by special techniques such as mortar coupling. Moreover, CG-FEM produce symmetric positive definite linear systems, which are efficient to solve. Discontinuous Galerkin FEM (DG-FEM), see e.g. [28], is an alternative method that shares many of the advantages that CG-FEM has. However, it is computationally expensive due to the large number of degrees of freedom.

Classical FEM has been applied in reservoir simulation in, e.g., [29–31], where FEM is used for the pressure problem and then coupled to a node-centered finite volume method on a dual mesh for the transport problem. It has also been used in modeling fracture propagation due to the excessive need for adaptivity in such applications, see e.g. [32–36].

All numerical methods presented in this section are locally conservative in the sense of (3.13), except for the classical FEM. This is a primary drawback of FEM, and will be further discussed in Section 3.4, where we present methods to resolve this issue.

## 3.3 Discretization scheme for the transport equation

The transport equation for a single solute (2.14) reads

$$\phi \frac{\partial c}{\partial t} + \nabla \cdot (c\mathbf{u}) = f(c), \quad (3.35)$$

where we have discarded diffusion. Typically, this equation is coupled to a pressure problem, e.g., Eq. (3.10), through the velocity  $\mathbf{u}$ , but in this section we will assume that  $\mathbf{u}$  is known. A

common discretization scheme is the finite volume method with upwind weighting. Integrating (3.35) over an  $K \in \mathcal{K}_h$  and applying the divergence theorem we get that

$$\int_K \phi \frac{\partial c}{\partial t} dx + \int_{\partial K} c \mathbf{u} \cdot \mathbf{n} ds = \int_K f(c) dx. \quad (3.36)$$

Next,  $c$  is approximated by a piecewise constant function  $c_h \in P_0(\mathcal{K}_h)$  and the boundary term is approximated by upwinding. Furthermore, we apply the implicit Euler method with step size  $\Delta t$  as the time integrator, and denote by  $c_h^n$  the approximation at the intermediate time  $t = t_n$ . This results in the following equation,

$$\frac{c_h^{n+1} - c_h^n}{\Delta t} \int_K \phi dx + \int_{\partial K} c_h^{n+1} \mathbf{u} \cdot \mathbf{n} ds = \int_K f(c_h^{n+1}) dx, \quad (3.37)$$

where the concentration on the cell boundaries are approximated by upwinding, i.e.,

$$c_h^n|_{F=\partial K \cap \partial \tilde{K}} = \begin{cases} c_h^n|_K, & \text{if } \mathbf{u} \cdot \mathbf{n}_K \geq 0, \\ c_h^n|_{\tilde{K}}, & \text{if } \mathbf{u} \cdot \mathbf{n}_K < 0. \end{cases} \quad (3.38)$$

Eq. (3.37) should hold for all  $K \in \mathcal{K}_h$ .

Low order finite volume methods as described above is typically used in commercial reservoir simulators [7]. One reason is that reservoir simulation is typically performed on quite coarse grids with high uncertainty in the material properties. Hence, higher order methods may not pay off. Low-order methods are also quite robust and easy to implement. We mention that the above scheme also can be formulated as a lowest order discontinuous Galerkin scheme, see Paper III for details.

Regarding time integration, the implicit Euler method is known to cause significant numerical diffusion. The explicit Euler method is less diffusive, but requires very small time steps to obtain stability in terms of a CFL condition. Higher order methods, see e.g. [37], can be used to reduce diffusion and at the same time allow for large time steps.

### 3.4 Local conservation of mass

Assuming incompressible flow, the conservation equation for single-phase flow, Eq. (2.10), and multiphase flow, Eq. (2.27), can be written as

$$\nabla \cdot \mathbf{u} = q, \quad \text{in } \Omega, \quad (3.39)$$

where  $\mathbf{u}$  denotes either the single-phase fluid velocity, Eq. (2.2), or the global velocity, Eq. (2.26). If we integrate the conservation equation over an element  $K \in \mathcal{K}_h$  and apply the divergence theorem, we get

$$\int_{\partial K} \mathbf{u} \cdot \mathbf{n}_K ds = \int_K q dx. \quad (3.40)$$

This equation is interpreted as discrete local conservation. We can also express the integral over  $\partial K$  as a sum over the faces of  $K$ ,

$$\sum_{F \in \partial K} \int_F \mathbf{u} \cdot \mathbf{n}_F (\mathbf{n}_K \cdot \mathbf{n}_F) ds = \int_K q dx, \quad (3.41)$$

where  $\mathbf{n}_K \cdot \mathbf{n}_F = \pm 1$  dependent on the orientation of  $F$ . In this thesis we make the following definition of local conservation.

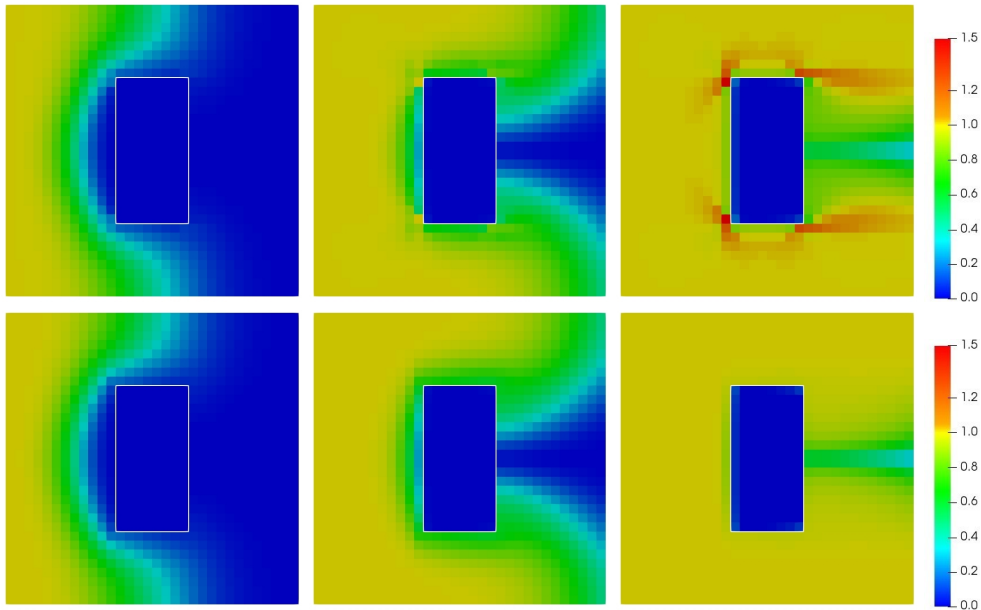


Fig. 3.1: Numerical example illustrating the effect of locally conservative velocity. A concentration of 1 flows into a domain with a low permeable barrier (depicted by the white line). The top and bottom rows display, respectively, the concentration solution with non-conservative and conservative fluxes at  $t = 0.5, 1.0, 2.0$  (from left to right). For the case with non-conservative fluxes, oscillations and unphysical solutions ( $c > 1$ ) are encountered, in particular close to the heterogeneity.

**Definition 3.6** (Local conservation). *Let  $U \in L^2(\mathcal{F}_h)$  be an approximation to the flux (normal velocity)  $\mathbf{u} \cdot \mathbf{n}_F$ , where  $\mathbf{u}$  is the solution to (3.39). We say that  $U$  is locally conservative if (3.41) holds for every  $K \in \mathcal{K}_h$ , i.e., if*

$$\sum_{F \in \partial K} \int_F U(\mathbf{n}_K \cdot \mathbf{n}_F) ds = \int_K q dx, \quad \forall K \in \mathcal{K}_h. \quad (3.42)$$

Moreover, a numerical method is locally conservative if it produces a velocity approximation whose normal component over faces  $F \in \mathcal{F}_h$  satisfies (3.42).

Local conservation is important by several reasons. Firstly, a locally conservative method produces an approximation that obeys the underlying differential operator, that is, the divergence operator. Furthermore, if coupled to a transport problem, e.g., Eq. (2.14), a non-conservative flux approximation would introduce spurious sources or sinks into the system. This could lead to erroneous and unphysical solutions, as demonstrated in Fig. 3.1, see also [38–40].

All methods introduced in Section 3.2 are locally conservative in terms of Definition 3.6, with the exception of CG-FEM. We remark, however, that CG-FEM is considered locally conservative in terms of a different definition, see e.g. [41]. Local conservation of CG-FEM is addressed in a series of papers, including [41–52]. CG-FEM has no degrees of freedom for the velocity, so that a velocity approximation must be derived from the pressure approximation, denoted  $p_h$ . Moreover, the gradient of  $p_h$  is not continuous across element boundaries. Thus,

a natural way to define the flux approximation is by averaging,

$$\mathbf{u}_h = -\mathbf{K}\nabla p_h, \quad \text{in } K \in \mathcal{K}_h, \quad (3.43)$$

$$U_h = \{\{\mathbf{u}_h \cdot \mathbf{n}_F\}\}, \quad \text{on } F \in \mathcal{F}_h, \quad (3.44)$$

Different kinds of averaging, e.g., harmonic averaging with respect to the permeability, may be applied, but nevertheless, local conservation in terms of Definition 3.6 is in general not satisfied.

### 3.4.1 Postprocessing of non-conservative fluxes

Methods for computing locally conservative fluxes from CG-FEM models have been studied for almost half a century. Optimal postprocessing for one-dimensional models was studied by [53] and generalized by [54]. Methods for approximating fluxes on the domain boundary for multi-dimensional problems based on the work by [55] were analyzed by [56]. Furthermore, postprocessing on element boundaries for multi-dimensional problems was studied by [57] for error estimation purposes. Existence of such fluxes for general FEM including 1-irregular meshes with hanging nodes<sup>3</sup> was proved in [42]. Furthermore, superconvergence of recovered gradients of linear FEM for elliptic and parabolic problems was considered by [58, 59].

In Paper II of this thesis we present a method that is based on [45] and [46] for the elliptic problem (3.39). In both papers a piecewise constant correction term is added to the non-conservative flux approximation. It can be viewed as a minimization problem such that the correction is minimized in the  $L^2$  norm. This ensures that the postprocessed flux has the same order of convergence as the original flux approximation. Such postprocessing methods are applied in a series of recent works [60–63].

Over the last few years, several noteworthy contributions have been made [48–52]. The methods by [48–50] are based on solving local Neumann problems on each element. However, it produces locally conservative fluxes on a vertex centered dual mesh, and is hence not applicable if one wants to solve the transport problem on the same mesh as was used for the pressure problem. In [51] a local postprocessing approach for both conforming, non-conforming and discontinuous finite elements on triangular meshes are presented. The fluxes are  $H_0^{\text{div}}(\Omega)$ -conforming and have optimal error estimate. Later, [52] proposed a local postprocessing method where the finite element solution is postprocessed such that the new solution satisfies Darcy’s law strongly. This method is also only defined for triangles (2D) or tetrahedrons (3D). Finally, we mention that an alternative to postprocessing based on enrichment of CG-FEM was presented in [38] for elliptic problems, and extended to parabolic problems in [39] and to two-phase flow with capillary pressure in [64].

## 4 Upscaling

Upscaling of a reservoir property refers to the technique of calculating effective values of a heterogeneous volume as if the volume was homogeneous. Due to computational limitations it is not possible to include all heterogeneities into a full field simulation model. To resolve this issue, upscaling is typically used to replace a fine-scale model with a coarse model by producing effective properties for each coarse cell, see Fig. 4.1. This process may also produce less irregular grid structures. The optimal goal of upscaling is to reproduce the global flow

<sup>3</sup>1-irregular means that only one hanging node per face is allowed



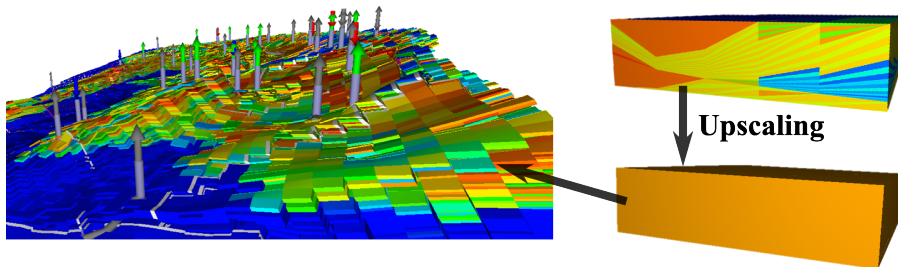


Fig. 4.1: Conceptual illustration of upscaling process. The fine scale heterogeneous (and possibly isotropic) model to the upper right is upscaled to a homogeneous anisotropic cell, which in turn is used in a larger model. The field model to the left is credited Statoil.

pattern, while at the same time reduce the computational costs. We remark, however, that this is primarily a theoretical objective since full field simulation on the fine model is seldom performed for all flow scenarios.

Additive properties like porosity and saturation are commonly upscaled by volume weighted averaging. However, for other quantities, like permeability, relative permeability and capillary pressure, it is often necessary to take fluid flow into account in order to incorporate most of the heterogeneity.

We remark that homogenization and upscaling are used interchangeably in the literature. However, homogenization is also the name of a rigorous mathematical theory for asymptotic analysis of periodic structures [65, 66]. Homogenization theory has been applied for upscaling of reservoir properties, see e.g., [67–70]. To avoid confusion, we will only use the term upscaling for the process of replacing fine scale models by effective homogeneous property values. Moreover, homogenization methods are not further considered in this thesis.

#### 4.1 Single-phase upscaling

Single-phase upscaling has been subject to extensive research over the last decades and has become an essential tool in reservoir simulation. A great variety of different methods have been developed, and we refer to [71–75] for reviews and discussions of the most common methods. For single-phase flow, porosity and permeability are the central rock properties to upscale. Porosity can be upscaled by simple volume weighted averaging, while permeability upscaling is more difficult due to its anisotropic nature. Earlier, in Section 3.2, we saw that for finite volume methods, like the two-point flux approximation, the permeability is incorporated into the transmissibility concept, cf. Eq. (3.20). Hence, instead of upscaling permeability directly, some methods upscale transmissibilities.

Upscaling methods can be classified in several ways. Firstly, we separate between *averaging methods* and *flow based methods*. Averaging methods are analytical, and thus simple and efficient. Examples of averaging methods include the harmonic and arithmetic averages, which are special cases of the more general power averaging methods [76]. However, for complex geometries, averaging is often too simple and not general enough to resolve important small-scale heterogeneities. Flow based methods, on the other hand, solve flow problems on the fine scale and use the solution to calculate the upscaled value. This gives higher computational costs compared to averaging methods, but are considered to be more accurate and robust.

Flow based methods can again be divided into two main classes. *Local methods*, e.g. [77], solves flow problems on the target coarse cell to be upscaled for, while *global methods*, e.g. [78], solve the fine scale problem on the whole domain of interest to take into account global

effects. Global methods are expected to give higher level of agreement between the simulation on the fine grid and the simulation on the coarse grid. However, the level of agreement is highly dependent on the choice of global flow problem used in the fine scale simulation. Global methods are also much more computational expensive than local methods. The major drawback of local methods is that they are dependent on the set of boundary conditions used for the local flow problems. However, they are more general in the sense that they can be used on different scales, while global methods are best suited for upscaling from a geological model to a simulation model. Local methods is also favorable for upscaling to REV's that can be used several places in the coarse model. Upscaling of every simulation cell is often not necessary and even meaningless if all parts of the reservoir do not have unique measurements. Local upscaling methods are also very easy to parallelize as each coarse grid cell can be handled individually independent on the other cells.

To try to get the best from two worlds, some hybrid methods have been presented, including extended local methods, e.g. [79–82], which consider a region of the fine scale model that is slightly larger than the target cell to be upscaled for, and quasi-global methods, e.g. [83, 84], where solutions to global coarse scale problems is used to determine the boundary conditions used for extended local methods.

In this thesis, we mainly consider local flow based upscaling. In the following subsection, we will describe in more detail how these can be formulated. As we will see later, this is also an essential tool in upscaling of two-phase properties.

#### 4.1.1 Local upscaling of permeability

Local upscaling of permeability is based on the elliptic pressure equation (2.10) over the target domain, which we denote by  $\Omega$ ,

$$-\nabla \cdot \left( \frac{\mathbf{K}}{\mu} \nabla p \right) = 0, \quad \text{on } \Omega. \quad (4.1)$$

It is assumed that  $\Omega$  is a hexahedron, where  $\partial\Omega^{\xi,i}$ , for  $\xi = x, y, z$  and  $i = 1, 2$ , denote the six boundary faces as illustrated in Fig. 4.2. Then a pressure drop,  $\Delta p_\eta$ , is imposed in the  $\eta$ -direction, for  $\eta = x, y, z$ , and the corresponding velocity solution  $\mathbf{u}_\eta$  is used to calculate the upscaled permeability tensor,  $\tilde{\mathbf{K}}$ , in the following way,

$$\tilde{\mathbf{K}} = \begin{bmatrix} \tilde{k}_{xx} & \tilde{k}_{xy} & \tilde{k}_{xz} \\ \tilde{k}_{yx} & \tilde{k}_{yy} & \tilde{k}_{yz} \\ \tilde{k}_{zx} & \tilde{k}_{zy} & \tilde{k}_{zz} \end{bmatrix}, \quad \text{where } \tilde{k}_{\xi\eta} = \mu Q_\xi^\eta L_\eta / \Delta p_\eta, \quad \xi, \eta = x, y, z. \quad (4.2)$$

Here  $L_\eta$  is the average distance between opposite boundary faces in the  $\eta$ -direction, and  $Q_\xi^\eta$  is the net flow in the  $\xi$ -direction when the pressure drop is imposed in the  $\eta$ -direction,

$$Q_\xi^\eta = \frac{1}{2|\partial\Omega^{\xi,2}|} \int_{\Omega^{\xi,2}} \mathbf{u}_\eta \cdot \mathbf{n} \, ds - \frac{1}{2|\partial\Omega^{\xi,1}|} \int_{\Omega^{\xi,1}} \mathbf{u}_\eta \cdot \mathbf{n} \, ds. \quad (4.3)$$

As mentioned earlier, the upscaled permeability is dependent on the choice of boundary conditions for the flow problem (4.1). Three sets of boundary conditions (BCs) have been commonly used. *Fixed* BCs use  $p = 1$  on  $\partial\Omega^{\eta,1}$ ,  $p = 0$  on  $\partial\Omega^{\eta,2}$ , and use no-flow conditions (homogeneous Neumann) on the other boundaries. This discard cross-directional flow, so that the upscaled permeability is diagonal. An alternative approach described in [75] yields a full tensor also with fixed BCs. *Linear* BCs also use  $p = 1$  on  $\partial\Omega^{\eta,1}$  and  $p = 0$  on  $\partial\Omega^{\eta,2}$ , but use a linear decreasing Dirichlet condition on the other boundaries. This results in a full upscaled permeability tensor, but may fail to be symmetric and positive definite. The

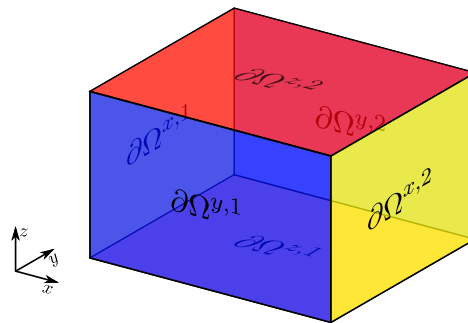


Fig. 4.2: Naming convention for the six faces of a hexahedron.

alternative aforementioned technique for fixed BCs can be applied to the case with linear BCs as well, resulting in a positive definite tensor. *Periodic* BCs [85] enforce periodicity of the normal velocity,  $\mathbf{u} \cdot \mathbf{n}$ , on opposite boundaries ( $\partial\Omega^{\xi,1}$  and  $\partial\Omega^{\xi,2}$ , for  $\xi = x, y, z$ ), and a unit pressure drop in the  $\eta$ -direction. This results in a full tensor that is symmetric and positive definite.

## 4.2 Two-phase upscaling

For two-phase flow one needs to upscale relative permeability curves, and possibly also capillary pressure curves dependent on the flow regime, in addition to porosity and permeability. Two-phase upscaling is also studied to a large extent, and we refer to [75, 86–89] for review papers. Upscaling of two-phase properties is much more complex than single-phase upscaling, because of the saturation dependency and the combination of capillary, viscous and gravitational forces. For instance, capillary trapping may occur due to heterogeneities normal to the flow direction, see e.g. [90–92], for homogenization techniques to include such effects.

There are roughly two classes of upscaling methods for two-phase flow. *Dynamic methods* (also referred to as *pseudoization methods*), can be characterized as global in the sense that they compute the solution on the whole fine scale grid, and calculate pseudorelative permeabilities based on this solution. Two early and central contributions to this class of methods are [93, 94], while newer contributions include [88, 95–98]. The other class of two-phase upscaling methods is *steady-state upscaling*, which is further introduced in the next section.

### 4.2.1 Steady-state upscaling

In steady-state upscaling, one consider the incompressible immiscible two-phase equations (2.24) at steady-state. If one further discard gravity and wells, we are left with the following equation for each phase  $\alpha$ ,

$$\nabla \cdot \left( \frac{k_{r\alpha} \mathbf{K}}{\mu_\alpha} \nabla p_\alpha \right) = 0. \quad (4.4)$$

The relative permeabilities,  $k_{r\alpha}$ , are saturation dependent, but at steady-state the saturation is constant in time. Hence, if we assume that the saturation distribution is known, Eq. (4.4) is equivalent to the single-phase equation (4.1) that was used for single-phase upscaling, but where  $\mathbf{K}$  is replaced by the phase permeability  $\mathbf{K}_\alpha = k_{r\alpha} \mathbf{K}$ . This means that we can use the single-phase upscaling method described earlier (Eq. (4.2)) to calculate the upscaled phase permeability  $\tilde{\mathbf{K}}_\alpha$ . The upscaled relative permeability,  $\tilde{\mathbf{K}}_{r\alpha}$ , can then be derived by multiplying

by the inverse of the upscaled permeability, i.e.,  $\tilde{\mathbf{K}}_{r\alpha} = \tilde{\mathbf{K}}_{\alpha}\tilde{\mathbf{K}}^{-1}$ . Observe that the upscaled relative permeability is a tensor. The upscaled relative permeability is valid for the upscaled phase saturation, which is simply calculated by a volume weighted average of the fine scale saturation distribution. By repeating this procedure for several different saturation distributions and for both phases, one obtain the desired upscaled relative permeability curves.

In the previous paragraph we assumed that the saturation distribution is known. There are several ways to find this. The most general approach is to solve the time-dependent equation (2.24) until a steady-state saturation solution is obtained. This is typically computationally expensive compared to the single-phase upscaling step and the saturation solution is dependent on the initial and boundary conditions used. A pressure drop is enforced in one of the principal directions, and it is well-known that the saturation distribution, and thus also the upscaled value, is dependent on the flow rate that this pressure drop induce [99–103].

Two simpler alternatives to obtain the saturation distribution is commonly used. The first is to consider the capillary limit, where gravitational and viscous forces are neglected. The second alternative is to consider the viscous limit, where gravitational and capillary forces are neglected and where one additionally assumes constant fractional flow. In these two limits, the saturation distribution can be calculated analytically. The capillary limit approach also defines a natural way to upscale capillary pressure curves. It is expected that the capillary limit is valid for small flow rates, while the viscous limit is valid for high flow rates.

An early reference to steady-state upscaling can be found in [104]. Later, it was further studied and discussed in a wide range of publications including [99–101, 105–108] and in more recent publications [10, 102, 103, 109, 110]. Furthermore, steady-state upscaling was extended to polymer flooding in [111].

#### 4.2.2 Multiscale methods

Multiscale methods, e.g., [112–114], is another approach to resolve fine scale heterogeneities. It is not an upscaling method, but we mention it here as it can be used instead of upscaling in some cases. The main idea of multiscale methods is to solve the global flow problem on a coarse grid, but where the local discrete approximation spaces are constructed in such a way that fine-scale heterogeneity is accounted for. In a finite element setting, this means that the basis functions are computed numerically by solving local flow problems on the coarse cell. A goal of multiscale methods is to be as efficient as applying classical upscaling methods, while at the same time produce a detailed and conservative velocity approximation on the fine grid [15]. Multiscale methods is an active field of research, and for newer contributions we mention [115–126]. For further discussion of advantages and disadvantages of using multiscale methods instead for upscaling, we refer to [8].

## 5 Flow and transport in fractured porous media

A fracture can be characterized as separation of a material into two or multiple pieces as a result of mechanical failure. Fractures in porous media occur naturally as a consequence of geological activity, or can be induced by human activity, e.g., in hydraulic fracturing, which is a technique to stimulate fluid flow in low permeable reservoir zones. Fractures divide the porous media into several domains that are commonly referred to as the matrix. The material properties are typically discontinuous at the fracture-matrix interface. In general, the conductivity can be both orders of magnitude higher and lower than the surrounding matrix. Accurate simulation

of fluid flow through fractured porous media is paramount in both cases, as they either serve as preferential paths or barriers for the fluid flow. However, modeling fluid flow in fractured media is complicated by several reasons. First of all, the fracture aperture (width) is typically several orders of magnitude smaller than any other characteristic sizes in the reservoir model. Secondly, the high contrast in conductivity often results in a big difference in the time-scales for the flow processes.

Flow and transport in fractured porous media is a complex problem, and we refer to [127–130] for more comprehensive presentations than the limited version given below. In the following, we will first write out the basic equations governing fluid flow in fractured porous media (Section 5.1), before we introduce different model concepts for incorporating fracture flow (Section 5.2). In particular, we will describe lower-dimensional discrete fracture-matrix models (Section 5.3), which are considered in Paper III.

## 5.1 Governing equations

Throughout this thesis, we assume that fluid flow in the fractures also are governed by Darcy's law, Eq. (2.2). This is a common assumption when the fractures are filled with debris, but it is not always a good approximation [127]. An alternative approach is to apply Forchheimer's law in the fractures [131, 132]. Under the assumption of Darcy flow, flow in fractured porous media is governed by the same type of equations as was introduced in Section 2. This means that the same set of equations apply to each of the subdomains, one for the fractures and one for each matrix domain separated by fractures. These equations are then accompanied by conditions imposing continuity across the fracture-matrix interfaces.

As flow model, we consider incompressible single-phase flow, Eq. (2.10), coupled to the transport model for a solute, Eq. (2.14). We will furthermore discard gravity. Consider a domain  $\Omega \subset \mathbb{R}^d$ ,  $d = 2, 3$ , and denote by  $\Omega_f \subset \Omega$  a single fracture cutting the domain into two disjoint subdomains,  $\Omega_1$  and  $\Omega_2$ , such that  $\bar{\Omega}_1 \cup \bar{\Omega}_2 = \bar{\Omega} \setminus \Omega_f$ , see Fig. 5.1a. Moreover  $\Gamma_i = \partial\Omega_f \cap \partial\Omega_i$ ,  $i = 1, 2$ , denote the interfaces between the fracture domain and the matrix domains. The governing equations for this system can be formulated as follows,

$$-\nabla \cdot (\mathbf{K}\nabla p) = q, \quad \text{in } \Omega, \quad (5.1a)$$

$$p = 0, \quad \text{on } \partial\Omega, \quad (5.1b)$$

$$[[p]] = 0, \quad \text{on } \Gamma_1 \cup \Gamma_2, \quad (5.1c)$$

$$[[\mathbf{K}\nabla p \cdot \mathbf{n}]] = 0, \quad \text{on } \Gamma_1 \cup \Gamma_2, \quad (5.1d)$$

where  $\mathbf{K} = \mathbf{K}_i$  in  $\Omega_i$  and  $q = q_i$  in  $\Omega_i$ , for  $i = 1, 2, f$ . Furthermore,  $[[\cdot]]$  denotes the jump operator on  $\Gamma_i$ , defined in a similar way as in Eq. (3.7). For simplicity, we have assumed homogeneous Dirichlet conditions (Eq. (5.1b)). Moreover, Eq. (5.1c) and (5.1d) enforce continuity of pressure and normal velocity at the fracture-matrix interfaces. These are the basic equations describing incompressible single-phase flow in fractured porous media. However, as discussed later, one seldom work directly with these equations, but they constitute the basis for deriving other fracture models.

The transport problem can be formulated analogously,

$$\phi \frac{\partial c}{\partial t} + \nabla \cdot (\mathbf{u}c) = f, \quad \text{in } \Omega \times (0, T), \quad (5.2a)$$

$$[[\mathbf{u}c \cdot \mathbf{n}]] = 0, \quad \text{on } (\Gamma_1 \cup \Gamma_2) \times (0, T), \quad (5.2b)$$

$$[[c]] = 0, \quad \text{on } (\Gamma_1 \cup \Gamma_2) \times (0, T), \quad (5.2c)$$

where  $\phi = \phi_i$  in  $\Omega_i$ , for  $i = 1, 2, f$ .

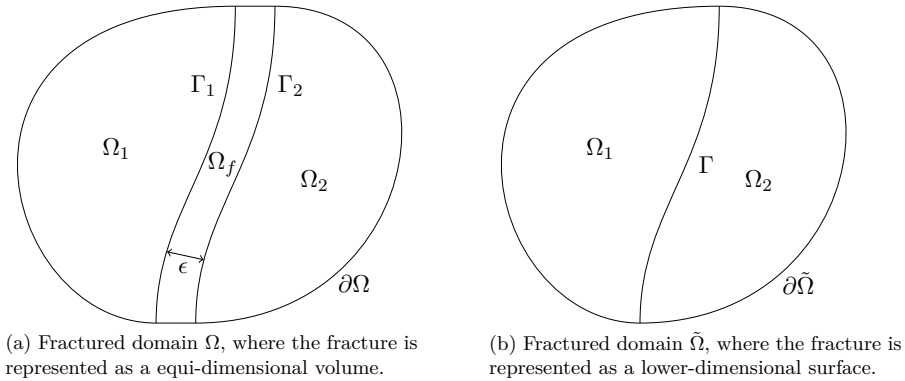


Fig. 5.1: Conceptual illustration of different fracture models.

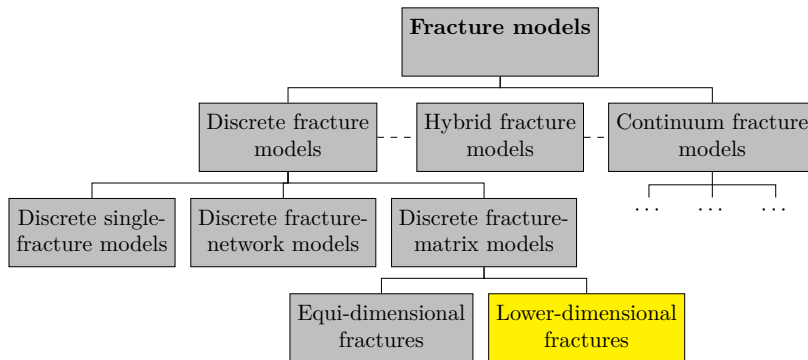


Fig. 5.2: Tree of fracture models. The dots below "Continuum fracture models" emphasize that a large variety of such models exists, see e.g. [134]. The model considered in Section 5.3 and in Paper III is highlighted.

The *local cubic law* relates the fracture permeability to the fracture width,  $\epsilon$ , by the relation  $\mathbf{K}_f = \frac{\epsilon^2}{12}$ . It is derived by solving Navier–Stokes' equation between two parallel plates and then comparing the averaged velocity with Darcy's law. We refer to [133] for a more detailed derivation and a discussion on the validity. In the following, we will not restrict the discussion to any permeability model such as the local cubic law, but continue to use the more general formulation above.

## 5.2 Discrete versus continuum fracture models

There are two main approaches to model fluid flow in fractured materials: *discrete fracture models* and *continuum fracture models*. Discrete fracture models explicitly represent the individual fractures in the model, while continuum models take fracture flow into account by homogenization or upscaling. *Hybrid models*, where only the most dominant fractures are explicitly represented, are also developed. An overview of the different models with subcategories are given by [134]. Fig. 5.2 summarize the classification of models introduced in this section.

*Discrete fracture models* represent the most accurate method to study flow in fractured materials. However, they are computationally expensive and may require large amount of data to represent the fracture network. Furthermore, mesh generation can be complex since the

fractures needs to be explicitly represented in the mesh for many such models.

Discrete fracture models can be divided into three subclasses. The first is *discrete single-fracture* models, where a single well-defined fracture is considered. Such models are used for more fundamental studies of fracture flow and are used on very fine scales. Secondly, there are *discrete fracture-network* models that only consider fluid flow in the fractures, and thus neglect exchange of fluids between fractures and the matrix. Lastly, there are *discrete fracture-matrix* (DFM<sup>1</sup>) models, where flow takes part both in the fracture network and in the matrix. DFM models can again be realized through the *equi-dimensional* approach (DFM-E), where fractures and matrix are represented by volumes of the same dimension, or the *lower-dimensional* (mixed-dimensional) approach (DFM-L), where fractures are represented as lower-dimensional surfaces embedded in the matrix domain, see Fig. 5.1. The main advantages of DFM-L are easier mesh generation and shorter computation times. DFM-E would require either very small or highly anisotropic grid cells in the vicinity of fractures, but can be an alternative if more accurate solutions are desired, see e.g. [135].

Continuum fracture models are typically used on a larger scale than discrete fracture models. On the field scale, it is not possible due to computational limitations to represent fractures explicitly. A variety of different models have been developed, and we refer to [134] for an overview, and to references therein for more details. A commonly used model in commercial simulators is the *double-porosity, single-permeability* models originally developed by [136, 137]. The main advantage of continuum fracture models is that they are computationally more efficient than discrete fracture models, so that full field simulations can be performed. However, determining effective flow properties through homogenization or upscaling is a difficult task, c.f., the discussion in Section 4. Continuum models are also based on the assumption that representative elementary volumes (REVs) can be identified on the scale of interest. Identifying REVs for fractured porous media is typically more difficult than for porous media without fractures (on the scale of interest) [138], or even not possible.

The choice of model concept is particularly dependent on the scale of interest, as summarized in Fig. 5.3. As a final remark to this discussion, we mention that fractures are present on every (macroscopic) scale of a reservoir. Hence, homogenization or upscaling is inherent also for DFM models, since we are not able to represent every tiny little fracture. In DFM models one typically only considers the most dominant fractures. With this perspective, every DFM model can be viewed as a hybrid model. In the following, we will, however, assume that we are given a set of fractures, and that the effective properties of the matrix is known. Moreover, we point out that DFM models can be used in an upscaling framework to solve local fine-scale problems, whose solution can be used to calculate effective values as described in Section 4. DFM-L models is an essential part of Paper III, and hence we continue the discussion of these in the next section.

### 5.3 Lower-dimensional discrete fracture-matrix models

Lower-dimensional models (also denoted mixed-dimensional and reduced models) are obtained by averaging the governing equations, e.g., Eq. (5.1) and (5.2), across the fractures, see further details below. A model for high permeable fractures was presented in [140, 141], where the flow equations are written in mixed form and then averaged over the fracture interface with the assumption of a continuous pressure. To also allow for low permeable fracture, this model was generalized in [142, 143], where Robin type of conditions on the pressure at the fracture interface are enforced rather than continuous pressure. Newer studies of such models can

<sup>1</sup>The abbreviation DFM is confusingly used both for *discrete fracture models* and *discrete fracture-matrix* in the literature. We only use the latter.

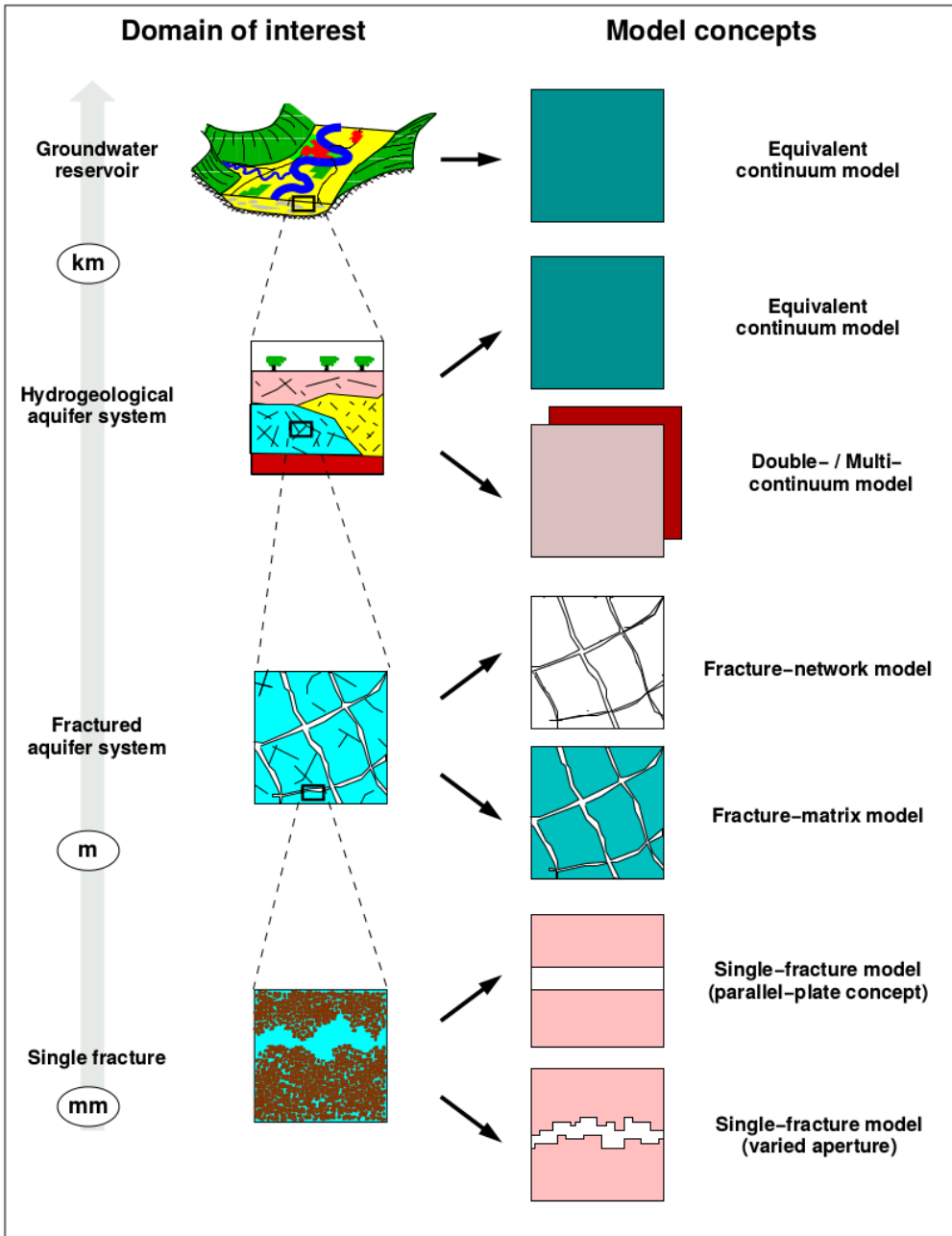


Fig. 5.3: Schematic figure of the relation between model concepts and scales of the domain of interest (after [139]).



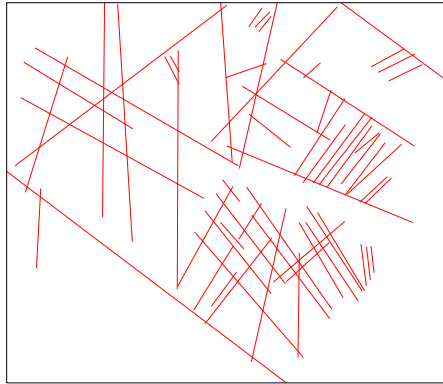


Fig. 5.4: Complex fracture network introduced as a benchmark problem in [178]. The fracture geometry represents a real set of fractures from an interpreted outcrop in the Sotra island, near Bergen in Norway.

be found in, e.g., [144–149]. The model in [140, 141] was extended by [150, 151] to curved fractures, and also generalized to allow for a non-zero pressure-jump at the interface [151].

A wide range of numerical methods for solving the lower-dimensional problem have been formulated. We mention for instance finite element methods [143, 152, 153], finite volume methods [144, 154–156], discontinuous Galerkin methods [157], mimetic finite difference methods [158, 159] and virtual element methods [160]. All of these require conforming mesh across the fracture interface. Furthermore, mortar coupling has been used to allow for non-conforming meshes, see e.g. [145, 149]. Fully non-conforming methods, i.e., schemes that allows the fracture to cut through the mesh, have been realized through extended finite elements [147, 151, 161–166].

Another approach where fractures are allowed to cut arbitrarily through the higher dimensional mesh is the embedded DFM (EDFM) model introduced by [167], see also [168–172] for newer contributions. EDFM models are based on the two-point flux approximation (TPFA; see Section 3.2), where the fracture-fracture and fracture-matrix transmissibilities are approximated from geometrical quantities. These methods are limited to study high permeability fractures, but the newly introduced projected-based EDFM (pEDFM) [173, 174] extends EDFM to also handle low permeable fractures. We also mention that EDFM has been applied to upscaling of fractured reservoirs [175, 176] and in multiscale methods [124, 177]. A benchmark study of several DFM models for incompressible single-phase flow was conducted in [178].

Common for the EDFM methods mentioned above is that the fracture pressure is represented on lower dimensional elements. An alternative is the recently introduced embedded finite element method (EFEM) presented by [179], where the fracture pressure is represented by the restriction of the higher dimensional elements. The pressure continuity on the fracture interface makes it possible to use continuous elements. However, the jump in the pressure gradient across fracture interfaces causes a loss in the regularity of the solution close to the fractures. Optimal convergence is instead realized through a priori mesh refinement in the vicinity of the fractures. EFEM is a novel approach to handle complex fracture geometry, see Fig. 5.4 for an example. We also mention that embedded surfaces may be handled by the CutFEM technology, see [180] for a general introduction and [181] for an application to a convection problem in a fractured domain.

Paper III is based on the lower-dimensional fracture model presented in [151] for the pressure problem (5.1). The transport problem (5.2) is also modeled by a lower-dimensional model, see e.g. [141, 160, 163]. In the following sections, we explain briefly how these are derived.

### 5.3.1 Lower-dimensional pressure problem

Let  $\epsilon$  be the fracture width and assume that  $\Omega_f$  can be described by its mid-curve  $\Gamma$  such that

$$\Omega_f = \left\{ \mathbf{x} \in \mathbb{R}^d : \mathbf{x} = \boldsymbol{\xi} + \epsilon l \mathbf{n}(\boldsymbol{\xi}), \boldsymbol{\xi} \in \Gamma, -\frac{1}{2} < l < \frac{1}{2} \right\}. \quad (5.3)$$

For simplicity we assume that the fracture permeability is isotropic, i.e.,  $\mathbf{K}_f = k_f \mathbf{I}$ , and furthermore, that it can be expressed as  $k_f = \frac{1}{\epsilon} k_\Gamma$  with  $k_\Gamma$  independent on  $\epsilon$ . A lower-dimensional model is then obtained in [151] by considering the weak formulation of Eq. (5.1) and passing  $\epsilon$  to 0 (or equivalently passing  $k_f$  to  $\infty$ ). The resulting variational problem can be written as the following boundary value problem over the domain  $\tilde{\Omega} = \Omega_1 \cup \Gamma \cup \Omega_2$  (see Fig. 5.1b),

$$-\nabla \cdot (\mathbf{K} \nabla p) = q, \quad \text{in } \Omega^1 \cup \Omega^2, \quad (5.4a)$$

$$-\nabla_\Gamma \cdot (k_\Gamma \nabla_\Gamma p) = q_\Gamma + \llbracket (\mathbf{K} \nabla p) \cdot \mathbf{n} \rrbracket, \quad \text{on } \Gamma, \quad (5.4b)$$

$$p = 0, \quad \text{on } \partial\Omega, \quad (5.4c)$$

$$\llbracket p \rrbracket = 0, \quad \text{on } \Gamma. \quad (5.4d)$$

Here  $\nabla_\Gamma = \mathbf{P} \nabla$  is the tangential gradient operator with  $\mathbf{P} = \mathbf{I} - \mathbf{n} \otimes \mathbf{n}$ , and  $q_\Gamma$  results from integrating  $q_f$  along line segments through  $\Omega_f$  normal to  $\Gamma$ . Observe that Eq. (5.4b) governs conservation of mass in the fracture interface  $\Gamma$ , where the jump in normal flux across  $\Gamma$  can be interpreted as a source term. We remark that this model is only valid for high permeable fractures. Furthermore, the model by [142, 143] can be written in a similar way, but where the pressure in the fracture is represented by its own function and the condition (5.4d) is replaced by Robin type conditions.

### 5.3.2 Lower-dimensional transport problem

Consider next the transport equation (5.2). A lower-dimensional model is derived in [163] by averaging the equations across the fracture domain  $\Omega_f$ . This result in the following mixed-dimensional model equations,

$$\phi \frac{\partial c}{\partial t} + \nabla \cdot (\mathbf{u} c) = f, \quad \text{in } (\Omega^1 \cup \Omega^2) \times (0, T), \quad (5.5)$$

$$\epsilon \phi_f \frac{\partial c_f}{\partial t} + \nabla_\Gamma \cdot (c_f \mathbf{u}_f) = f_\Gamma + \llbracket \mathbf{u} \cdot \mathbf{n} c^* \rrbracket \quad \text{on } \Gamma \times (0, T), \quad (5.6)$$

where  $c_f$  and  $\mathbf{u}_f$  are the concentration and velocity in the fracture, respectively. The term  $\llbracket \mathbf{u} \cdot \mathbf{n} c^* \rrbracket$  is a coupling term that models flow between the fracture and matrix. It is defined as

$$\llbracket \mathbf{u} \cdot \mathbf{n} c^* \rrbracket = \sum_{i=1}^2 \mathbf{u}_i \cdot \mathbf{n}_i c_i^*, \quad c_i^* = \begin{cases} c_i, & \text{if } \mathbf{u}_i \cdot \mathbf{n}_i \geq 0, \\ c_f, & \text{if } \mathbf{u}_i \cdot \mathbf{n}_i < 0. \end{cases} \quad (5.7)$$

where  $\mathbf{u}_i$  and  $c_i$  denotes, respectively, the velocity and concentration in  $\Omega_i$ ,  $i = 1, 2$ , and  $\mathbf{n}_i$  denotes the unit normal pointing out of  $\Omega_i$ .

## 6 Summary of papers

We close Part I of this thesis by summarizing each of the three papers contained in Part II. The intention is to highlight the main contributions and novelties of each paper, and describe how they contribute to the main objective expressed in Section 1.

## Paper I: Rate dependency in steady-state upscaling

Steady-state upscaling (see Section 4.2) is a local flow-based method for upscaling relative permeability and capillary pressure curves for two-phase flow. A key ingredient is to determine the fine-scale saturation distribution in the target coarse cell that is to be upscaled. If we neglect gravity, then capillary and viscous forces are the acting forces on the fluids, and hence, the saturation distribution is dependent on the balance of these forces. Capillary forces are dominant for high flow rates or on small-scale heterogeneities, while viscous forces are dominant for low flow rates or on larger scales. This rate dependency is addressed in Paper I.

The capillary and viscous limits are defined as the flow scenarios when the flow rate tends to 0 and  $\infty$ , respectively. In these two limits, the saturation distribution can be determined analytically from fluid and rock data, that is, without flow simulations. These approaches are denoted capillary limit (CL) and viscous limit (VL) upscaling in the following. For intermediate flow rates, however, one needs to solve local flow problems on the fine scale model to find the steady-state saturation distribution. This is computationally much more expensive than the limiting cases. Motivated by this discussion, the main objectives of this work was to

- (I) Study the rate dependency of the upscaled relative permeability curves.
- (II) Establish a static measure of the balance between capillary and viscous forces in a reservoir model, that can be used to determine a priori if CL or VL upscaling is appropriate.
- (III) Validate capillary and viscous limit upscaling by comparing simulation results on a fine-scale and an upscaled coarser model of a representative reservoir.

In particular we considered fluvial depositional systems on the field scale, which are interesting in an upscaling point of view because of their heterogeneity structure and unknown balance between capillary and viscous forces. Contributions to the above identified objectives would increase the knowledge and robustness of steady-state upscaling, which is already being used by oil and gas companies.

Objective (I) was pursued by applying steady-state upscaling to synthetic and realistic models. Both CL and VL upscaling, and general rate-dependent upscaling was considered. The following important observations were made:

- For all models, rate-dependent upscaling converged<sup>1</sup> to CL upscaling as the flow rate tends to zero, and to VL upscaling as the flow rate tends to infinity. The transition from CL to VL upscaling typically occurs over several orders of magnitude of the flow rate, and the difference between CL and VL upscaling is significant (more than 25% in relative difference is not uncommon).
- The convergence is monotone in most cases, but for models containing high permeability rock with non or poor connectivity, we may have non-monotone convergence. Such observations are important because they gain insight to when CL and VL upscaling can be used as upper and lower bounds.

These observations are in accordance with the results in [102, 103], which also studied the transition from CL to VL upscaling. However, a novelty of our study is that we consider realistic three-dimensional models on corner-point grids.

Our contribution to resolve the issue of objective (II) is a scale-dependent capillary number,  $\mathcal{N}$ , which was shown to better predict the balance between capillary and viscous forces in our models compared to the traditional capillary number (see e.g. [4]). For most of the models considered,  $\mathcal{N} \sim 1$  for a flow rate in the interval between capillary and viscous dominated flow.

<sup>1</sup>Remark that by *convergence* we do not refer to a strict mathematical definition in this setting

However, it turned out to be a difficult task to define a static measure that is able to predict the rate balance for general models.

To address objective (III), we considered a representative fluvial reservoir model taken from a field on the Norwegian Continental Shelf. Water flooding was induced by an injector–producer pair of wells. A fine-scale model was upscaled to a coarser model by means of CL and VL upscaling. Simulations on the fine-scale model demonstrated that this model is viscous dominated for realistic injection rates. This was also supported by the value of  $\mathcal{N}$ . Comparison, in terms of water cut (ratio of water produced) and visual observation of the saturation solution, between the fine-scale simulation and simulation on the upscaled model suggested that VL upscaling is most appropriate in this scenario. Furthermore, the effect of upscaling (absolute) permeability was demonstrated to have a significant effect on the results.

## Paper II: Postprocessing of non-conservative flux for compatibility with transport in heterogeneous media

This paper addresses postprocessing of non-conservative fluxes, cf. Section 3.4. As model problem we consider slightly compressible single-phase flow, Eq. (2.8), coupled to transport of a solute, Eq. (2.11). We present a sequential solver, where a linear finite element method (CG-FEM) is used for the pressure equation, and a discontinuous Galerkin FEM is used for the transport equation. The novelty of this work is the development of a postprocessing method that calculate locally conservative fluxes from the CG-FEM solution.

The postprocessing method is based on the earlier work of [45] and [46], where a piecewise constant correction term is added to the original flux. The correction is chosen such that it is minimized in the standard  $L^2$  norm. There are two central novelties of our method compared to [45, 46]:

- The correction is minimized in a weighted  $L^2$  norm rather than the standard  $L^2$  norm. This gives better control of the relative correction on each face. It is demonstrated that choosing weights equal to the effective face permeability (harmonic average), better preserves low permeable interfaces.
- The method is extended to the time dependent flow model, that is, we allow for a slightly compressible fluid.

Uniqueness and preservation of convergence order for the postprocessed flux was proven in [45, 46], and these proofs are generalized in our work to also hold under the two extensions listed above. A range of numerical examples demonstrate the abilities and properties of our method.

Compared to other recent contributions, e.g. [48–52], our postprocessing method has the main advantage that it handles heterogeneities on a large class of meshes, including general polygonal (2D) or polyhedral (3D) meshes with hanging nodes. The method by [48–50] produces fluxes that are locally conservative on a vertex centered dual mesh, while the methods in [51, 52] are presented for triangular (2D) or tetrahedral (3D) meshes. In terms of computational complexity, our method is global in the sense that a system of  $N$  linear equations has to be solved, where  $N$  is the total number of elements. In contrast the methods in [48–52] are local in the sense that only small localized problems on each element has to be solved. Local methods are expected to be computationally more efficient.

In addition to the aforementioned contributions, this paper contains the following aspects:

- The importance of locally conservative fluxes is demonstrated by comparing solutions to the transport problem where both non-conservative and conservative fluxes are used.

- Different approaches to approximate the fluxes on the domain boundary are tested, including a flux recovery technique on the Dirichlet boundary, see e.g. [41, 43, 44, 55, 182–184]. However, only small effects were observed.
- The sequential solution approach was applied to a representative 3D model based on the SPE-10 case presented in [185].
- Computational complexity of the postprocessing method is reported in terms of computation time and condition numbers. For the SPE-10 model the additional cost (relative to the CG-FEM solver) was 10–30% depending on model parameters.

As a final remark, we mention that our postprocessing method is general also in the sense that it takes as input any flux approximation, not restricted to non-conservative fluxes from classical FEM, but may also originate from other non-conservative numerical schemes or even measurements. For instance, it was recently used in combination with the virtual element method [186], and for modeling fracture flow, see Paper III. Other examples where it *could* be utilized is in modeling of coupled flow and fracture propagation, see e.g. [36], and to transfer velocity solutions to a different mesh, see [46].

### **Paper III: A simple embedded discrete fracture-matrix model for coupled flow and transport problems in porous media**

The main topic of this paper is flow and transport in fractured porous media. Fractures are modeled explicitly as lower-dimensional surfaces embedded in the surrounding matrix as discussed in Section 5.3. We only consider fractures with high permeability relative to the matrix, and aim for a simple low-order scheme that can handle complex fracture geometry and networks, e.g., as depicted in Fig. 5.4. As flow model we consider incompressible single-phase flow coupled to transport of a concentration. For the flow problem we apply the asymptotic model derived by [150, 151] and extended to bifurcating and intersecting fractures in [179]. The transport problem is modeled by a mixed-dimensional model studied in, e.g. [141, 160, 163].

In this paper we apply a sequential solution scheme for the coupled problem. We solve the flow equations by an embedded finite element method (EFEM) [179], and couple it to a finite volume method for the transport equations. The main novelties of this paper are twofold:

- (I) We present a velocity model to calculate flux approximations from the EFEM pressure solution. The postprocessing method from Paper II is adapted and applied to ensure local conservation.
- (II) We develop a non-standard low-order finite volume method with upwinding that is compatible with EFEM in the sense that the same mesh can be applied, so that the flexibility with respect to fracture geometry is retained for the coupled scheme.

A key ingredient in EFEM is that the pressure is restricted to be continuous across the fractures, so that the fracture solution can be represented as the restriction of the higher dimensional basis functions. A similar approach is not valid for the transport problem since we can not expect the concentration to be continuous across the fracture. Still, we do not want to represent the fracture solution by its own lower-dimensional field. Instead, we represent the fracture solution by the elements that are cut by the fractures. Moreover, the coupling term that models flow between the fractures and matrix, is approximated by evaluating the flux on the boundary of the fracture elements, rather than on the fracture interface.

The resulting coupled scheme is easy to formulate and implement even for problems with complex fracture networks. For optimal accuracy of the pressure solution, a priori local refinement in the vicinity of the fractures is required [179]. We demonstrate the ability of the

---

presented methods on both synthetic and representative problems with increasing complexity of the fracture network. The results are promising and show that we are able to study flow problems in highly fractured porous media, e.g., the case depicted in Fig. 5.4. We also follow up a recent benchmark study [178] for incompressible single-phase flow and evaluate EFEM on a selection of these benchmark problems. Our results are in good agreement with the results in [178] and in some cases EFEM is most accurate.

This paper presents a novel alternative to existing lower-dimensional DFM models, see e.g. [143–145, 147, 149, 151–162, 164–174], especially for problems where simple meshing is important and where a low order method is appropriate in terms of accuracy. It may be applied to study characteristics of flow and transport in fractured porous media, or as part of an upscaling framework.

## A Open-source simulation software

Most of the computer implementations and simulation software used in this thesis are available under an open licence. The only exception is the field simulations in Paper I where the commercial simulator ECLIPSE 100<sup>1</sup> was used. Furthermore, many of the geological models are also freely available under an open license, with the exception of some reservoir models in Paper I. This makes it possible to reproduce most of the results from this thesis, and also further develop the computer methods.

The upscaling results of Paper I are obtained by codes from the upscaling module of the Open Porous Media (OPM) project. Documentation and building instructions for these codes are found at <https://opm-project.org>, while the source code is available on GitHub, see <https://github.com/OPM>. OPM depends on the open-source library DUNE [187].

Regarding Paper II and III, all results are obtained from a personal code base, which is now also freely available on GitHub, see <https://github.com/laods/efsim>. The implementations are based on the open-source finite element library deal.II [188]. Building and user instructions are available in the README file in the base directory.

---

<sup>1</sup>Reservoir simulation software from Schlumberger™

## Bibliography

- [1] Peaceman, D.W. *Fundamentals of numerical reservoir simulation*. Elsevier, Amsterdam, 1977.
- [2] Aziz, K. and Settari, A. *Petroleum reservoir simulation*. Elsevier, London and New York, 1979.
- [3] Chavent, G. and Jaffre, J. *Mathematical Models and Finite Elements for Reservoir Simulation*. Studies in Mathematics and Its Applications. Elsevier, 1986.
- [4] Bear, J. *Dynamics of fluids in porous media*. Dover, New York, 1988.
- [5] Lake, L.W. *Enhanced oil recovery*. Prentice-Hall, Englewood Cliffs, NJ, 1989.
- [6] Chen, Z., Huan, G., and Ma, Y. *Computational methods for multiphase flows in porous media*. SIAM, 2006.
- [7] Aarnes, J.E., Gimse, T., and Lie, K.A. An introduction to the numerics of flow in porous media using Matlab. In *Geometric Modelling, Numerical Simulation, and Optimization*, pp. 265–306. Springer, 2007.
- [8] Aarnes, J.E., Kippe, V., Lie, K.A., and Rustad, A.B. Modelling of multiscale structures in flow simulations for petroleum reservoirs. In *Geometric Modelling, Numerical Simulation, and Optimization*, pp. 307–360. Springer, 2007.
- [9] Kløv, T., Øren, P.E., Stensen, J.Å., Lerdahl, T.R., Berge, L.I., Bakke, S., Boassen, T., and Virnovsky, G. Pore-to-field scale modeling of WAG. In *SPE Annual Technical Conference and Exhibition*, pp. 5–8. Denver, Colorado, October 2003.
- [10] Lerdahl, T.R., Rustad, A.B., Theting, T., Stensen, J.Å., Øren, P.E., Bakke, S., Boassen, T., and Palatnik, B. Pore- to field-scale multi-phase upscaling for IOR. In *67th EAGE Conference & Exhibition*. Madrid, Spain, June 2005.
- [11] Nordahl, K. and Ringrose, P.S. Identifying the representative elementary volume for permeability in heterolithic deposits using numerical rock models. *Mathematical Geosciences*, 40(7):753, 2008.
- [12] Nordahl, K., Messina, C., Berland, H., Rustad, A.B., and Rimstad, E. Impact of multiscale modelling on predicted porosity and permeability distributions in the fluvial deposits of the Upper Lunde Member (Snorre Field, Norwegian Continental Shelf). *Geological Society, London, Special Publications*, 387(1):85–109, 2014.
- [13] Øren, P.E., Bakke, S., and Arntzen, O.J. Extending predictive capabilities to network models. *SPE Journal*, 3(04):324–336, 1998.
- [14] Mishra, S., Brigham, W.E., and Orr Jr., F.M. Tracer- and pressure-test analysis for characterization of areally heterogeneous reservoirs. *SPE Formation Evaluation*, pp. 45–54, March 1991.
- [15] Aarnes, J.E., Krogstad, S., and Lie, K.A. Multiscale mixed/mimetic methods on corner-point grids. *Computational Geosciences*, 12(3):297–315, 2008.
- [16] Ponting, D.K. Corner point geometry in reservoir simulation. In *1st European Conference on Mathematics of Oil Recovery*, pp. 45–65. Oxford, 1989.



- [17] Aavatsmark, I., Barkve, T., Bøe, O., and Mannseth, T. Discretization on unstructured grids for inhomogeneous, anisotropic media. Part I: Derivation of the methods. *SIAM Journal on Scientific Computing*, 19(5):1700–1716, 1998.
- [18] Aavatsmark, I., Barkve, T., Bøe, O., and Mannseth, T. Discretization on unstructured grids for inhomogeneous, anisotropic media. Part II: Discussion and numerical results. *SIAM Journal on Scientific Computing*, 19(5):1717–1736, 1998.
- [19] Hughes, T.J.R., Cottrell, J.A., and Bazilevs, Y. Isogeometric analysis: CAD, finite elements, NURBS, exact geometry and mesh refinement. *Computer Methods in Applied Mechanics and Engineering*, 194(39-41):4135–4195, 2005.
- [20] Bekele, Y.W., Kvamsdal, T., Kvarving, A.M., and Nordal, S. Adaptive isogeometric finite element analysis of steady-state groundwater flow. *International Journal for Numerical and Analytical Methods in Geomechanics*, 40(5):738–765, 2015.
- [21] Raviart, P.A. and Thomas, J.M. A mixed finite element method for 2-nd order elliptic problems. In *Mathematical aspects of finite element methods*, pp. 292–315. Springer, 1977.
- [22] Nédélec, J.C. Mixed finite elements in  $\mathbb{R}^3$ . *Numerische Mathematik*, 35(3):315–341, 1980.
- [23] Brezzi, F., Lipnikov, K., Shashkov, M., and Simoncini, V. A new discretization methodology for diffusion problems on generalized polyhedral meshes. *Computer Methods in Applied Mechanics and Engineering*, 196(37-40):3682–3692, 2007.
- [24] Brezzi, F., Lipnikov, K., and Simoncini, V. A family of mimetic finite difference methods on polygonal and polyhedral meshes. *Mathematical Models and Methods in Applied Sciences*, 15(10):1533–1551, 2005.
- [25] Brezzi, F., Lipnikov, K., and Shashkov, M. Convergence of the mimetic finite difference method for diffusion problems on polyhedral meshes. *SIAM Journal on Numerical Analysis*, 43(5):1872–1896, 2005.
- [26] Brezzi, F., Lipnikov, K., and Shashkov, M. Convergence of mimetic finite difference method for diffusion problems on polyhedral meshes with curved faces. *Mathematical Models and Methods in Applied Sciences*, 16(02):275–297, 2006.
- [27] Hughes, T.J. *The finite element method: linear static and dynamic finite element analysis*. Dover Publications, Mineola, NY, 2000.
- [28] Rivière, B., Wheeler, M.F., and Girault, V. Improved energy estimates for interior penalty, constrained and discontinuous Galerkin methods for elliptic problems. Part I. *Computational Geosciences*, 3(3-4):337–360, 1999.
- [29] Geiger, S., Matthäi, S.K., Niessner, J., and Helmig, R. Black-oil simulations for three-component, three-phase flow in fractured porous media. *SPE Journal*, 14(02):338–354, 2009.
- [30] Matthai, S.K., Mezentsev, A.A., and Belayneh, M. Finite element–node-centered finite-volume two-phase-flow experiments with fractured rock represented by unstructured hybrid-element meshes. *SPE Reservoir Evaluation & Engineering*, 10(06):740–756, 2007.

- [31] Nick, H. and Matthäi, S. Comparison of three FE-FV numerical schemes for single- and two-phase flow simulation of fractured porous media. *Transport in Porous Media*, 90(2):421–444, 2011.
- [32] Miehe, C., Welschinger, F., and Hofacker, M. Thermodynamically consistent phase-field models of fracture: Variational principles and multi-field FE implementations. *International Journal for Numerical Methods in Engineering*, 83(10):1273–1311, 2010.
- [33] Borden, M.J., Hughes, T.J., Landis, C.M., and Verhoosel, C.V. A higher-order phase-field model for brittle fracture: Formulation and analysis within the isogeometric analysis framework. *Computer Methods in Applied Mechanics and Engineering*, 273:100–118, 2014.
- [34] Heister, T., Wheeler, M.F., and Wick, T. A primal-dual active set method and predictor-corrector mesh adaptivity for computing fracture propagation using a phase-field approach. *Computer Methods in Applied Mechanics and Engineering*, 290:466–495, 2015.
- [35] Wick, T., Singh, G., and Wheeler, M.F. Fluid-filled fracture propagation with a phase-field approach and coupling to a reservoir simulator. *SPE Journal*, 21(03):981–999, 2016.
- [36] Lee, S., Wheeler, M.F., and Wick, T. Iterative coupling of flow, geomechanics and adaptive phase-field fracture including level-set crack width approaches. *Journal of Computational and Applied Mathematics*, 314:40–60, 2017.
- [37] Matthäi, S.K., Nick, H.M., Pain, C., and Neuweiler, I. Simulation of solute transport through fractured rock: A higher-order accurate finite-element finite-volume method permitting large time steps. *Transport in Porous Media*, 83(2):289–318, 2010.
- [38] Sun, S. and Liu, J. A locally conservative finite element method based on piecewise constant enrichment of the continuous Galerkin method. *SIAM Journal on Scientific Computing*, 31(4):2528–2548, 2009.
- [39] Lee, S., Lee, Y.J., and Wheeler, M.F. A locally conservative enriched Galerkin approximation and efficient solver for elliptic and parabolic problems. *SIAM Journal on Scientific Computing*, 38(3):A1404–A1429, 2016.
- [40] Odsæter, L.H., Kvamsdal, T., and Wheeler, M.F. A postprocessing technique to produce locally conservative flux. In A. Berezovski, K. Tamm, and T. Peets, eds., *28th Nordic Seminar on Computational Mechanics*, pp. 129–132. CENS, Institute of Cybernetics at Tallinn University of Technology, Tallinn, October 2015.
- [41] Hughes, T.J., Engel, G., Mazzei, L., and Larson, M.G. The continuous Galerkin method is locally conservative. *Journal of Computational Physics*, 163(2):467–488, 2000.
- [42] Ainsworth, M. and Oden, J.T. *A posteriori error estimation in finite element analysis*. Wiley, 2000.
- [43] Kvamsdal, T. Variationally consistent postprocessing. In S. Idelsohn, E. Onate, and E. Dvorkin, eds., *Proceedings for Computational Mechanics, New Trends and Applications*. CIMNE, Barcelona, 1998.
- [44] Melbø, H. and Kvamsdal, T. Goal oriented error estimators for Stokes equations based on variationally consistent postprocessing. *Computer Methods in Applied Mechanics and Engineering*, 192(5):613–633, 2003.

- 
- [45] Larson, M.G. and Niklasson, A.J. A conservative flux for the continuous Galerkin method based on discontinuous enrichment. *Calcolo*, 41(2):65–76, 2004.
- [46] Sun, S. and Wheeler, M.F. Projections of velocity data for the compatibility with transport. *Computer Methods in Applied Mechanics and Engineering*, 195(7):653–673, 2006.
- [47] Cockburn, B., Gopalakrishnan, J., and Wang, H. Locally conservative fluxes for the continuous Galerkin method. *SIAM Journal on Numerical Analysis*, 45(4):1742–1776, 2007.
- [48] Bush, L. and Ginting, V. On the application of the continuous Galerkin finite element method for conservation problems. *SIAM Journal on Scientific Computing*, 35(6):A2953–A2975, 2013.
- [49] Deng, Q. and Ginting, V. Construction of locally conservative fluxes for high order continuous Galerkin finite element methods, 2016. ArXiv:1603.06999 [math.NA].
- [50] Deng, Q. and Ginting, V. Locally conservative continuous Galerkin FEM for pressure equation in two-phase flow model in subsurfaces. *Journal of Scientific Computing*, 74(3):1264–1285, 2016.
- [51] Becker, R., Capatina, D., and Luce, R. Local flux reconstructions for standard finite element methods on triangular meshes. *SIAM Journal on Numerical Analysis*, 54(4):2684–2706, 2016.
- [52] Zhang, S., Zhang, Z., and Zou, Q. A postprocessed flux conserving finite element solution. *Numerical Methods for Partial Differential Equations*, 33(6):1859–1883, 2017.
- [53] Wheeler, M.F. A Galerkin procedure for estimating the flux for two-point boundary value problems. *SIAM Journal on Numerical Analysis*, 11(4):764–768, 1974.
- [54] Dupont, T. A unified theory of superconvergence for Galerkin methods for two-point boundary problems. *SIAM Journal on Numerical Analysis*, 13(3):362–368, 1976.
- [55] Wheeler, J.A. Simulation of heat transfer from a warm pipeline buried in permafrost. In *74th National Meeting of the American Institute of Chemical Engineers*. New Orleans, March 1973.
- [56] Douglas Jr, J., Dupont, T., and Wheeler, M.F. A Galerkin procedure for approximating the flux on the boundary for elliptic and parabolic boundary value problems. *Revue Française d’Automatique, Informatique, Recherche Opérationnelle. Analyse Numérique*, 8(2):47–59, 1974.
- [57] Ladeveze, P. and Leguillon, D. Error estimate procedure in the finite element method and applications. *SIAM Journal on Numerical Analysis*, 20(3):485–509, 1983.
- [58] Wheeler, M.F. and Whiteman, J.R. Superconvergent recovery of gradients on subdomains from piecewise linear finite-element approximations. *Numerical Methods for Partial Differential Equations*, 3(4):357–374, 1987.
- [59] Wheeler, M.F. and Whiteman, J.R. Superconvergence of recovered gradients of discrete time/piecewise linear Galerkin approximations for linear and nonlinear parabolic problems. *Numerical Methods for Partial Differential Equations*, 10(3):271–294, 1994.

- [60] Kees, C.E., Farthing, M.W., and Dawson, C.N. Locally conservative, stabilized finite element methods for variably saturated flow. *Computer Methods in Applied Mechanics and Engineering*, 197(51):4610–4625, 2008.
- [61] Povich, T.J., Dawson, C.N., Farthing, M.W., and Kees, C.E. Finite element methods for variable density flow and solute transport. *Computational Geosciences*, 17(3):529–549, 2013.
- [62] Beirão da Veiga, L., Manzini, G., and Putti, M. Post processing of solution and flux for the nodal mimetic finite difference method. *Numerical Methods for Partial Differential Equations*, 31(1):336–363, 2015.
- [63] Scudeler, C., Putti, M., and Paniconi, C. Mass-conservative reconstruction of Galerkin velocity fields for transport simulations. *Advances in Water Resources*, 94:470–485, 2016.
- [64] Lee, S. and Wheeler, M.F. Enriched Galerkin methods for two-phase flow in porous media with capillary pressure, 2017. ArXiv:1709.01644 [math.NA].
- [65] Bensoussan, A., Lions, J.L., and Papanicolaou, G. *Asymptotic Analysis for Periodic Structures*. Elsevier Science Publishers, Amsterdam, 1978.
- [66] Jikov, V.V., Kozlov, S.M., and Oleinik, O.A. *Homogenization of differential operators and integral functionals*. Springer–Verlag, New York, 1994.
- [67] Bourgeat, A. Homogenized behavior of two-phase flows in naturally fractured reservoirs with uniform fractures distribution. *Computer Methods in Applied Mechanics and Engineering*, 47(1-2):205–216, 1984.
- [68] Hornung, U. *Homogenization and Porous Media*. Springer–Verlag, New York, 1997.
- [69] Amaziane, B., Antontsev, S., Pankratov, L., and Piatnitski, A. Homogenization of immiscible compressible two-phase flow in porous media: Application to gas migration in a nuclear waste repository. *Multiscale Modeling & Simulation*, 8(5):2023–2047, 2010.
- [70] Singh, G., Amanbek, Y., and Wheeler, M.F. Adaptive homogenization for upscaling heterogeneous porous medium. In *SPE Annual Technical Conference and Exhibition*. Society of Petroleum Engineers, 2017.
- [71] Wen, X.H. and Gómez-Hernández, J.J. Upscaling hydraulic conductivities in heterogeneous media: An overview. *Journal of Hydrology*, 183(1-2):ix–xxxii, 1996.
- [72] Christie, M.A. Upscaling for reservoir simulation. *Journal of Petroleum Technology*, 48(11):1004–1010, 1996.
- [73] Renard, P. and De Marsily, G. Calculating equivalent permeability: a review. *Advances in Water Resources*, 20(5-6):253–278, 1997.
- [74] Farmer, C.L. Upscaling: a review. *International Journal for Numerical Methods in Fluids*, 40(1-2):63–78, 2002.
- [75] Durlflosky, L.J. Upscaling and gridding of fine scale geological models for flow simulation. In *8th International Forum on Reservoir Simulation*. Iles Borromees, Italy, June 2005.
- [76] Journel, A.G., Deutsch, C., and Desbarats, A.J. Power averaging for block effective permeability. In *SPE California Regional Meeting*. Society of Petroleum Engineers, 1986.

- [77] Durlofsky, L.J. Numerical calculation of equivalent grid block permeability tensors for heterogeneous porous media. *Water Resources Research*, 27(5):699–708, 1991.
- [78] White, C.D. and Horne, R.N. Computing absolute transmissibility in the presence of fine-scale heterogeneity. In *SPE Symposium on Reservoir Simulation*. Society of Petroleum Engineers, 1987.
- [79] Holden, L. and Lia, O. A tensor estimator for the homogenization of absolute permeability. *Transport in Porous Media*, 8(1):37–46, 1992.
- [80] Nielsen, B.F. and Tveito, A. An upscaling method for one-phase flow in heterogeneous reservoirs. A weighted output least squares (WOLS) approach. *Computational Geosciences*, 2(2):93–123, 1998.
- [81] Holden, L. and Nielsen, B.F. Global upscaling of permeability in heterogeneous reservoirs; The output least squares OLS method. *Transport in Porous Media*, 40(2):115–143, 2000.
- [82] Wen, X.H., Durlofsky, L.J., and Edwards, M.G. Use of border regions for improved permeability upscaling. *Mathematical Geology*, 35(5):521–547, 2003.
- [83] Chen, Y., Durlofsky, L.J., Gerritsen, M., and Wen, X.H. A coupled local–global upscaling approach for simulating flow in highly heterogeneous formations. *Advances in Water Resources*, 26(10):1041–1060, 2003.
- [84] Chen, Y. and Durlofsky, L.J. Adaptive local–global upscaling for general flow scenarios in heterogeneous formations. *Transport in porous Media*, 62(2):157–185, 2006.
- [85] Durlofsky, L.J. Numerical calculation of equivalent grid block permeability tensors for heterogeneous porous media. *Water Resources Research*, 27(5):699–708, 1991.
- [86] Barker, J.W. and Thibeau, S. A critical review of the use of pseudorelative permeabilities for upscaling. *SPE Reservoir Engineering*, 12(2):138–143, 1997.
- [87] Christie, M.A. Flow in porous media — scale up of multiphase flow. *Current Opinion in Colloid & Interface Science*, 6(3):236–241, 2001.
- [88] Darman, N.H., Pickup, G.E., and Sorbie, K.S. A comparison of two-phase dynamic upscaling methods based on fluid potentials. *Computational Geosciences*, 6(1):5–27, 2002.
- [89] Durlofsky, L.J. and Chen, Y. Uncertainty quantification for subsurface flow problems using coarse-scale models. In *Numerical Analysis of Multiscale Problems*, pp. 163–202. Springer, 2012.
- [90] van Duijn, C.J., Mikelic, A., and Pop, I.S. Effective equations for two-phase flow with trapping on the micro scale. *SIAM Journal on Applied Mathematics*, 62(5):1531–1568, 2002.
- [91] van Duijn, C.J., Eichel, H., Helmig, R., and Pop, I.S. Effective equations for two-phase flow in porous media: the effect of trapping on the microscale. *Transport in Porous Media*, 69(3):411–428, 2007.
- [92] van Duijn, C.J., Cao, X., and Pop, I.S. Two-phase flow in porous media: dynamic capillarity and heterogeneous media. *Transport in Porous Media*, 114(2):283–308, 2016.

- [93] Jacks, H.H., Smith, O.J.E., and Mattax, C.C. The modeling of a three-dimensional reservoir with a two-dimensional reservoir simulator-the use of dynamic pseudo functions. *SPE Journal*, 13(03):175–185, 1973.
- [94] Kyte, J.R. and Berry, D.W. New pseudo functions to control numerical dispersion. *SPE Journal*, 15(04):269–276, 1975.
- [95] Stone, H.L. Rigorous black oil pseudo functions. In *SPE Symposium on Reservoir Simulation*. Society of Petroleum Engineers, 1991.
- [96] Christie, M.A., Mansfield, M., King, P.R., Barker, J.W., and Culverwell, I.D. A renormalisation-based upscaling technique for WAG floods in heterogeneous reservoirs. In *SPE Reservoir Simulation Symposium*. Society of Petroleum Engineers, 1995.
- [97] Barker, J.W. and Dupouy, P. An analysis of dynamic pseudo-relative permeability methods for oil-water flows. *Petroleum Geoscience*, 5(4):385–394, 1999.
- [98] Zhang, P., Pickup, G.E., and Christie, M.A. A new method for accurate and practical upscaling in highly heterogeneous reservoir models. In *International Oil & Gas Conference and Exhibition*. Society of Petroleum Engineers, Beijing, China, December 2006.
- [99] Ekrann, S., Dale, M., Langaas, K., and Mykkeltveit, J. Capillary limit effective two-phase properties for 3D media. In *European 3-D Reservoir Modelling Conference*. Society of Petroleum Engineers, 1996.
- [100] Kumar, A., Farmer, C.L., Jerauld, G.R., and Li, D. Efficient upscaling from cores to simulation models. In *SPE Annual Technical Conference and Exhibition*, pp. 257–272. San Antonio, Texas, October 1997.
- [101] Ekrann, S. and Aasen, J.O. Steady-state upscaling. *Transport in Porous Media*, 41(3):245–262, 2000.
- [102] Virnovsky, G.A., Friis, H.A., and Lohne, A. A steady-state upscaling approach for immiscible two-phase flow. *Transport in Porous Media*, 54(2):167–192, 2004.
- [103] Lohne, A., Virnovsky, G.A., and Durlofsky, L.J. Two-stage upscaling of two-phase flow: From core to simulation scale. *SPE Journal*, 11(03):304–316, 2006.
- [104] Smith, E.H. The influence of small-scale heterogeneity on average relative permeability. In L.W. Lake, H.B. Carroll, and T.C. Wesson, eds., *Reservoir Characterization II*. Academic Press, Waltham, 1991.
- [105] Kumar, A.T.A. and Jerauld, G.R. Impacts of scale-up on fluid flow from plug to gridblock scale in reservoir rock. In *SPE/DOE Improved Oil Recovery Symposium*. Society of Petroleum Engineers, 1996.
- [106] Pickup, G.E. and Sorbie, K.S. The scaleup of two-phase flow in porous media using phase permeability tensors. *SPE Journal*, 1(04):369–382, 1996.
- [107] Pickup, G.E. and Stephen, K.D. An assessment of steady-state scale-up for small-scale geological models. *Petroleum Geoscience*, 6(3):203–210, 2000.
- [108] Pickup, G., Ringrose, P.S., and Sharif, A. Steady-state upscaling: From lamina-scale to full-field model. *SPE Journal*, 5(02):208–217, 2000.

- 
- [109] Jonoud, S. and Jackson, M.D. New criteria for the validity of steady-state upscaling. *Transport in Porous Media*, 71(1):53–73, 2008.
- [110] Hilden, S.T. and Berg, C.F. An analysis of unsteady flooding processes: Varying force balance and the applicability of steady-state upscaling. *Transport in Porous Media*, 115(1):125–152, 2016.
- [111] Hilden, S.T., Lie, K.A., and Raynaud, X. Steady state upscaling of polymer flooding. In *ECMOR XIV-14th European Conference on the Mathematics of Oil Recovery*. Catania, Sicily, Italy, September 2014.
- [112] Chen, Z. and Hou, T. A mixed multiscale finite element method for elliptic problems with oscillating coefficients. *Mathematics of Computation*, 72(242):541–576, 2003.
- [113] Jenny, P., Lee, S., and Tchelepi, H.A. Multi-scale finite-volume method for elliptic problems in subsurface flow simulation. *Journal of Computational Physics*, 187(1):47–67, 2003.
- [114] Aarnes, J.E. On the use of a mixed multiscale finite element method for greater flexibility and increased speed or improved accuracy in reservoir simulation. *Multiscale Modeling & Simulation*, 2(3):421–439, 2004.
- [115] Hajibeygi, H. and Jenny, P. Multiscale finite-volume method for parabolic problems arising from compressible multiphase flow in porous media. *Journal of Computational Physics*, 228(14):5129–5147, 2009.
- [116] Lunati, I., Tyagi, M., and Lee, S.H. An iterative multiscale finite volume algorithm converging to the exact solution. *Journal of Computational Physics*, 230(5):1849–1864, 2011.
- [117] Wheeler, M.F., Xue, G., and Yotov, I. A multiscale mortar multipoint flux mixed finite element method. *ESAIM: Mathematical Modelling and Numerical Analysis*, 46(4):759–796, 2012.
- [118] Efendiev, Y., Galvis, J., and Hou, T.Y. Generalized multiscale finite element methods (GMsFEM). *Journal of Computational Physics*, 251:116–135, 2013.
- [119] Hajibeygi, H. and Tchelepi, H.A. Compositional multiscale finite-volume formulation. *SPE Journal*, 19(02):316–326, 2014.
- [120] Wang, Y., Hajibeygi, H., and Tchelepi, H.A. Algebraic multiscale solver for flow in heterogeneous porous media. *Journal of Computational Physics*, 259:284–303, 2014.
- [121] Møyner, O. and Lie, K.A. A multiscale two-point flux-approximation method. *Journal of Computational Physics*, 275:273–293, 2014.
- [122] Møyner, O. and Lie, K.A. A multiscale restriction-smoothed basis method for high contrast porous media represented on unstructured grids. *Journal of Computational Physics*, 304:46–71, 2016.
- [123] Møyner, O. and Lie, K.A. A multiscale restriction-smoothed basis method for compressible black-oil models. *SPE Journal*, 21(06):2–079, 2016.
- [124] Shah, S., Møyner, O., Tene, M., Lie, K.A., and Hajibeygi, H. The multiscale restriction smoothed basis method for fractured porous media (F-MsRSB). *Journal of Computational Physics*, 318:36–57, 2016.

- [125] Chung, E., Efendiev, Y., and Hou, T.Y. Adaptive multiscale model reduction with generalized multiscale finite element methods. *Journal of Computational Physics*, 320:69–95, 2016.
- [126] Singh, G., Leung, W., and Wheeler, M.F. Multiscale methods for model order reduction of non linear multiphase flow problems, 2018. ArXiv:1803.03721 [math.NA].
- [127] Berkowitz, B. Characterizing flow and transport in fractured geological media: A review. *Advances in Water Resources*, 25(8-12):861–884, 2002.
- [128] Neuman, S.P. Trends, prospects and challenges in quantifying flow and transport through fractured rocks. *Hydrogeology Journal*, 13(1):124–147, 2005.
- [129] Dietrich, P., Helmig, R., Sauter, M., Hötzl, H., Köngeter, J., and Teutsch, G. *Flow and transport in fractured porous media*. Springer, 2005.
- [130] Sahimi, M. *Flow and Transport in Porous Media and Fractured Rock. From Classical Methods to Modern Approaches*. Wiley-VCH, second, revised and enlarged edition, 2011.
- [131] Frih, N., Roberts, J.E., and Saada, A. Modeling fractures as interfaces: a model for Forchheimer fractures. *Computational Geosciences*, 12(1):91–104, 2008.
- [132] Knabner, P. and Roberts, J.E. Mathematical analysis of a discrete fracture model coupling Darcy flow in the matrix with Darcy–Forchheimer flow in the fracture. *ESAIM: Mathematical Modelling and Numerical Analysis*, 48(5):1451–1472, 2014.
- [133] Oron, A.P. and Berkowitz, B. Flow in rock fractures: The local cubic law assumption reexamined. *Water Resources Research*, 34(11):2811–2825, 1998.
- [134] Tatomir, A.B. *From Discrete to Continuum Concepts of Flow in Fractured Porous Media*. Ph.D. thesis, Universität Stuttgart, 2012.
- [135] Eikemo, B., Lie, K.A., Eigestad, G.T., and Dahle, H.K. Discontinuous Galerkin methods for advective transport in single-continuum models of fractured media. *Advances in Water Resources*, 32(4):493–506, 2009.
- [136] Barenblatt, G., Zheltov, I.P., and Kochina, I. Basic concepts in the theory of seepage of homogeneous liquids in fissured rocks [strata]. *Journal of Applied Mathematics and Mechanics*, 24(5):1286–1303, 1960.
- [137] Warren, J.E. and Root, P.J. The behavior of naturally fractured reservoirs. *SPE Journal*, 1963.
- [138] Bear, J., Tsang, C.F., and De Marsily, G. *Flow and Contaminant Transport in Fractured Rock*. Academic Press, San Diego, CA, 1993.
- [139] Assteerawatt, A. *Flow and Transport Modelling of Fractured Aquifers based on a Geostatistical Approach*. Ph.D. thesis, Universität Stuttgart, 2008.
- [140] Alboin, C., Jaffré, J., Roberts, J.E., Wang, X., and Serres, C. Domain decomposition for some transmission problems in flow in porous media. In *Numerical Treatment of Multiphase Flows in Porous Media*, pp. 22–34. Springer, 2000.



- [141] Alboin, C., Jaffré, J., Roberts, J.E., and Serres, C. Modeling fractures as interfaces for flow and transport in porous media. In Z. Chen and R.E. Ewing, eds., *Fluid Flow and Transport in Porous Media: Mathematical and Numerical Treatment*, volume 295 of *Contemporary Mathematics*, pp. 13–24. AMS, 2002.
- [142] Faille, I., Flauraud, E., Nataf, F., Pégaz-Fiornet, S., Schneider, F., and Willien, F. A new fault model in geological basin modelling. Application of finite volume scheme and domain decomposition methods. In *Finite volumes for complex applications*, volume 3, pp. 543–550. 2002.
- [143] Martin, V., Jaffré, J., and Roberts, J.E. Modeling fractures and barriers as interfaces for flow in porous media. *SIAM Journal on Scientific Computing*, 26(5):1667–1691, 2005.
- [144] Angot, P., Boyer, F., and Hubert, F. Asymptotic and numerical modelling of flows in fractured porous media. *ESAIM: Mathematical Modelling and Numerical Analysis*, 43(2):239–275, 2009.
- [145] Frih, N., Martin, V., Roberts, J.E., and Saâda, A. Modeling fractures as interfaces with nonmatching grids. *Computational Geosciences*, 16(4):1043–1060, 2012.
- [146] Formaggia, L., Fumagalli, A., Scotti, A., and Ruffo, P. A reduced model for Darcy’s problem in networks of fractures. *ESAIM: Mathematical Modelling and Numerical Analysis*, 48(4):1089–1116, 2014.
- [147] Schwenck, N., Flemisch, B., Helmig, R., and Wohlmuth, B.I. Dimensionally reduced flow models in fractured porous media: crossings and boundaries. *Computational Geosciences*, 19(6):1219–1230, 2015.
- [148] Faille, I., Fumagalli, A., Jaffré, J., and Roberts, J.E. Model reduction and discretization using hybrid finite volumes for flow in porous media containing faults. *Computational Geosciences*, 20(2):317–339, 2016.
- [149] Boon, W.M., Nordbotten, J.M., and Yotov, I. Robust discretization of flow in fractured porous media, 2016. ArXiv:1601.06977 [math.NA].
- [150] Morales, F. and Showalter, R.E. The narrow fracture approximation by channeled flow. *Journal of Mathematical Analysis and Applications*, 365(1):320–331, 2010.
- [151] Capatina, D., Luce, R., El-Otmany, H., and Barrau, N. Nitsche’s extended finite element method for a fracture model in porous media. *Applicable Analysis*, 95(10):2224–2242, 2016.
- [152] Angot, P. A model of fracture for elliptic problems with flux and solution jumps. *Comptes Rendus Mathématique*, 337(6):425–430, 2003.
- [153] Karimi-Fard, M. and Firoozabadi, A. Numerical simulations of water injection in fractured media using the discrete-fracture model and the Galerkin method. *SPE Reservoir Evaluation & Engineering*, 6(02):117–126, 2003.
- [154] Reichenberger, V., Jakobs, H., Bastian, P., and Helmig, R. A mixed-dimensional finite volume method for two-phase flow in fractured porous media. *Advances in Water Resources*, 29(7):1020–1036, 2006.

- [155] Brenner, K., Hennicker, J., Masson, R., and Samier, P. Gradient discretization of hybrid-dimensional Darcy flow in fractured porous media with discontinuous pressures at matrix–fracture interfaces. *IMA Journal of Numerical Analysis*, 37(3):1551–1585, 2016.
- [156] Karimi-Fard, M. and Durlofsky, L.J. A general gridding, discretization, and coarsening methodology for modeling flow in porous formations with discrete geological features. *Advances in Water Resources*, 96:354–372, 2016.
- [157] Antonietti, P.F., Facciola, C., Russo, A., and Varani, M. Discontinuous Galerkin approximation of flows in fractured porous media on polytopic grids. Technical Report 55, MOX, Politecnico di Milano, 2016.
- [158] Antonietti, P.F., Formaggia, L., Scotti, A., Verani, M., and Verzott, N. Mimetic finite difference approximation of flows in fractured porous media. *ESAIM: Mathematical Modelling and Numerical Analysis*, 50(3):809–832, 2016.
- [159] Scotti, A., Formaggia, L., and Sottocasa, F. Analysis of a mimetic finite difference approximation of flows in fractured porous media. *ESAIM: Mathematical Modelling and Numerical Analysis*, 2017.
- [160] Fumagalli, A. and Keilegavlen, E. Dual virtual element methods for discrete fracture matrix models, 2017. ArXiv:1711.01818 [math.NA].
- [161] D’Angelo, C. and Scotti, A. A mixed finite element method for Darcy flow in fractured porous media with non-matching grids. *ESAIM: Mathematical Modelling and Numerical Analysis*, 46(2):465–489, 2012.
- [162] Huang, H., Long, T.A., Wan, J., and Brown, W.P. On the use of enriched finite element method to model subsurface features in porous media flow problems. *Computational Geosciences*, 15(4):721–736, 2011.
- [163] Fumagalli, A. and Scotti, A. A reduced model for flow and transport in fractured porous media with non-matching grids. In *Numerical Mathematics and Advanced Applications 2011*, pp. 499–507. Springer, 2013.
- [164] Fumagalli, A. and Scotti, A. A numerical method for two-phase flow in fractured porous media with non-matching grids. *Advances in Water Resources*, 62:454–464, 2013.
- [165] Fumagalli, A. and Scotti, A. An efficient XFEM approximation of Darcy flows in arbitrarily fractured porous media. *Oil & Gas Science and Technology—Revue d’IFP Energies nouvelles*, 69(4):555–564, 2014.
- [166] Del Pra, M., Fumagalli, A., and Scotti, A. Well posedness of fully coupled fracture/bulk Darcy flow with XFEM. *SIAM Journal on Numerical Analysis*, 55(2):785–811, 2017.
- [167] Li, L. and Lee, S.H. Efficient field-scale simulation of black oil in a naturally fractured reservoir through discrete fracture networks and homogenized media. *SPE Reservoir Evaluation & Engineering*, 11(04):750–758, 2008.
- [168] Hajibeygi, H., Karvounis, D., and Jenny, P. A hierarchical fracture model for the iterative multiscale finite volume method. *Journal of Computational Physics*, 230(24):8729–8743, 2011.

- [169] Moinfar, A., Varavei, A., Sepehrnoori, K., and Johns, R.T. Development of an efficient embedded discrete fracture model for 3D compositional reservoir simulation in fractured reservoirs. *SPE Journal*, 19(02):289–303, 2014.
- [170] Panfili, P., Cominelli, A., and Scotti, A. Using embedded discrete fracture models (EDFMs) to simulate realistic fluid flow problems. In *Second EAGE workshop on naturally fractured reservoirs*. Muscat, Oman, 2013.
- [171] Panfili, P. and Cominelli, A. Simulation of miscible gas injection in a fractured carbonate reservoir using an embedded discrete fracture model. In *Abu Dhabi International Petroleum Exhibition and Conference*. Society of Petroleum Engineers, 2014.
- [172] de Araujo Cavalcante Filho, J.S., Shakiba, M., Moinfar, A., and Sepehrnoori, K. Implementation of a preprocessor for embedded discrete fracture modeling in an IMPEC compositional reservoir simulator. In *SPE Reservoir Simulation Symposium*. Society of Petroleum Engineers, 2015.
- [173] Tene, M., Bosma, S.B., Al Kobaisi, M.S., and Hajibeygi, H. Projection-based embedded discrete fracture model (pEDFM). *Advances in Water Resources*, 105:205–216, 2017.
- [174] Jiang, J. and Younis, R.M. An improved projection-based embedded discrete fracture model (pEDFM) for multiphase flow in fractured reservoirs. *Advances in Water Resources*, 109:267–289, 2017.
- [175] Fumagalli, A., Pasquale, L., Zonca, S., and Micheletti, S. An upscaling procedure for fractured reservoirs with embedded grids. *Water Resources Research*, 52(8):6506–6525, 2016.
- [176] Fumagalli, A., Zonca, S., and Formaggia, L. Advances in computation of local problems for a flow-based upscaling in fractured reservoirs. *Mathematics and Computers in Simulation*, 137:299–324, 2017.
- [177] Tene, M., Al Kobaisi, M.S., and Hajibeygi, H. Multiscale projection-based embedded discrete fracture modeling approach (F-AMS-pEDFM). In *ECMOR XV-15th European Conference on the Mathematics of Oil Recovery*. 2016.
- [178] Flemisch, B., Berre, I., Boon, W., Fumagalli, A., Schwenck, N., Scotti, A., Stefansson, I., and Tatomir, A. Benchmarks for single-phase flow in fractured porous media. *Advances in Water Resources*, 111:239–258, 2018.
- [179] Burman, E., Hansbo, P., and Larson, M.G. A simple finite element method for elliptic bulk problems with embedded surfaces, 2017. ArXiv: 1709.00972 [math.NA].
- [180] Burman, E., Claus, S., Hansbo, P., Larson, M.G., and Massing, A. CutFEM: Discretizing geometry and partial differential equations. *International Journal for Numerical Methods in Engineering*, 104(7):472–501, 2015.
- [181] Burman, E., Hansbo, P., Larson, M.G., and Larsson, K. Cut finite elements for convection in fractured domains, 2018. ArXiv:1801.06103 [math.NA].
- [182] Carey, G.F. Derivative calculation from finite element solutions. *Computer Methods in Applied Mechanics and Engineering*, 35(1):1–14, 1982.
- [183] Carey, G.F., Chow, S.S., and Seager, M.K. Approximate boundary-flux calculations. *Computer Methods in Applied Mechanics and Engineering*, 50(2):107–120, 1985.

- 
- [184] Pehlivanov, A.I., Lazarov, R.D., Carey, G.F., and Chow, S.S. Superconvergence analysis of approximate boundary-flux calculations. *Numerische Mathematik*, 63(1):483–501, 1992.
- [185] Christie, M.A. and Blunt, M.J. Tenth SPE comparative solution project: A comparison of upscaling techniques. In *SPE Reservoir Simulation Symposium*. Society of Petroleum Engineers, 2001.
- [186] Klemetsdal, Ø.S., Berge, R.L., Lie, K.A., Nilsen, H.M., and Møyner, O. Unstructured gridding and consistent discretizations for reservoirs with faults and complex wells. In *SPE Reservoir Simulation Conference*. Society of Petroleum Engineers, February 2017.
- [187] Blatt, M., Burchardt, A., Dedner, A., Engwer, C., Fahlke, J., Flemisch, B., Gersbacher, C., Gräser, C., Gruber, F., and Grüninger, C. The distributed and unified numerics environment, version 2.4. *Archive of Numerical Software*, 4(100):13–29, 2016.
- [188] Bangerth, W., Hartmann, R., and Kanschat, G. deal.ii—a general-purpose object-oriented finite element library. *ACM Transactions on Mathematical Software*, 33(4), 2007.



**Part II**

**Research papers**



## **Paper I**

### **Rate dependency in steady-state upscaling**

Odsæter, L.H., Berg, C.F., and Rustad, A.B.

*Transport in Porous Media*, 110(3):565–589, 2015





## Rate Dependency in Steady-State Upscaling

Lars Hov Odsæter<sup>1</sup>  · Carl Fredrik Berg<sup>2</sup> ·  
Alf Birger Rustad<sup>2</sup>

Received: 26 November 2014 / Accepted: 4 September 2015 / Published online: 21 September 2015  
© The Author(s) 2015. This article is published with open access at Springerlink.com

**Abstract** Steady-state upscaling of relative permeability is studied for a range of reservoir models. Both rate-dependent upscaling and upscaling in the capillary and viscous limits are considered. In particular, we study fluvial depositional systems, which represent a large and important class of reservoirs. Numerical examples show that steady-state upscaling is rate dependent, in accordance with previous work. In this respect we introduce a scale-dependent capillary number to estimate the balance between viscous and capillary forces. The difference between the limit solutions can be large, and we show that the intermediate flow rates can span several orders of magnitude. This substantiate the need for rate-dependent steady-state upscaling in a range of flow scenarios. We demonstrate that steady-state upscaling converges from the capillary to the viscous limit solution as the flow rate increases, and we identify a simple synthetic model where the convergence fails to be monotone. Two different sets of boundary conditions were tested, but had only minor effects on the presented reservoir models. Finally, we demonstrate the applicability of steady-state upscaling by performing dynamic flow simulation at the reservoir scale, both on fine-scaled and on upscaled models. The considered model is viscous dominated for realistic flow rates, and the simulation results indicate that viscous limit upscaling is appropriate.

**Keywords** Steady-state upscaling · Relative permeability · Capillary limit · Viscous limit · Capillary number

---

✉ Lars Hov Odsæter  
lars.odsater@math.ntnu.no

Carl Fredrik Berg  
carlpaatur@hotmail.com

Alf Birger Rustad  
abir@statoil.com

<sup>1</sup> Department of Mathematical Sciences, NTNU Norwegian University of Science and Technology, Alfred Getz' vei 1, 7491 Trondheim, Norway

<sup>2</sup> Statoil R&D Center, Arkitekt Ebbels veg 10, Rotvoll, 7053 Trondheim, Norway

## 1 Introduction

Hydrocarbon reservoirs are generally heterogeneous on different length scales (Kløyv et al. 2003; Lerdahl et al. 2005; Aarnes et al. 2007). Due to computational limitations, it is not always possible to include important heterogeneities into a full field reservoir simulation. Nevertheless, small-scale heterogeneities may be important for the global flow and therefore should be taken into account. Upscaling is a well-known technique in this respect, see, e.g. Durlofsky (2005) for an overview of different upscaling methods. The overall goal for all methods is to replace a fine-scale model with a coarse model by producing effective properties for each coarse cell. For upscaling of nonbulk flow properties like permeability and relative permeability, one may divide upscaling into two main classes. These are averaging methods and flow-based methods. The latter are regarded to be more accurate, but they are also computationally more demanding as they require solutions to flow equations. Furthermore, one can roughly divide the flow-based methods into local and global methods. Global methods, see, e.g. Kyte and Berry (1975) and Zhang et al. (2006), require solutions to the full fine-scale model, while local methods only consider the fine-scale region corresponding to the target coarse cell. Noting that this is a simplified view, there are also combinations of the two. Global methods typically address the common task of upscaling from a geo-cellular model to a simulation model. Local methods are more generic in nature and are convenient for determining effective flow properties for rock types or facies in geo-cellular models, see, e.g. Pickup and Stephen (2000), Kløyv et al. (2003), Rustad et al. (2008) and Nordahl et al. (2014).

The work presented here can be seen as a continuation of the work in Nordahl et al., with a focus on multiphase flow parameters. More precisely, we investigate the effects of sedimentary heterogeneity on oil–water relative permeability. Our approach is based on steady-state upscaling, a local upscaling method which has been subject to extensive research over the last 20 years, see, e.g. Smith (1991), Ekrann et al. (1996), Kumar et al. (1997), Ekrann and Aasen (2000), Pickup et al. (2000), Lohne et al. (2006) and Jonoud and Jackson (2008). As most literature, we consider incompressible, immiscible two-phase flow and neglect gravity. From the geological perspective we focus on fluvial depositional systems. These are particularly interesting from an upscaling point of view because of their heterogeneity structure. Fluvial systems typically consist of channels, crevasses and background. The channels are typically highly permeable, with an internal depth trend. Crevasses typically have lower permeability, but still contribute significantly to flow and volume. The background material is typically tight with little or no permeability. While channels can be around five meters tall (depending on the size of the depositional system), they can meander and erode into each other, stacking in complex patterns. Crevasses may be less than a meter tall. Hence, we have extreme contrast between reservoir properties at the scale of several meters, with a geometry we cannot represent in current full field simulation models. That is, the finest grid resolution we realistically can run full field flow simulations on is typically not able to represent the geometry of the main sedimentary heterogeneities of fluvial reservoirs. Moreover, fluvial reservoirs are among the most common depositional systems found in reservoirs.

For any type of flow-based upscaling method, the imposed boundary conditions can have an important effect on the upscaling results. This is one of the aspects that make upscaling ambiguous and a difficult exercise. Moreover, disregarding gravity, the viscous and capillary forces are the acting forces on the fluids in a reservoir. The results from steady-state upscaling is known to be rate dependent due to the balance of these two forces (Ekrann et al. 1996; Kumar et al. 1997; Ekrann and Aasen 2000; Virnovsky et al. 2004; Lohne et al. 2006). Capillary forces dominate for small flow rates or on small-scale heterogeneities, while viscous forces dominate

for high flow rates or on larger scales. Hence, as the flow rate tends to zero, it is expected that the viscous forces can be neglected. Similarly, for high flow rates it is expected that capillary forces can be neglected. These limits are referred to as the capillary and viscous limits, respectively, and they are interesting since they are computationally less demanding. However, these limits are only encountered in practice at some scales and some parts of the reservoir.

The effect of small-scale heterogeneities on relative permeability, typically heterolithic reservoir zones, has been studied before (e.g., [Rustad et al. \(2008\)](#)). Two important publications where the transition between capillary and viscous forces are studied are found in [Virnovsky et al. \(2004\)](#) and [Lohne et al. \(2006\)](#). There is a couple of differences to note between the work presented here and in [Virnovsky et al. \(2004\)](#) and [Lohne et al. \(2006\)](#). The first is that the steady-state simulations done here are on three-dimensional models with corner-point grids. This enables the use of the ReservoirStudio software<sup>1</sup> providing realistic models of heterogeneity at a scale where the balance between capillary and viscous forces is unclear. Secondly, all upscaling in this work are performed with codes from the Open Porous Media project (OPM),<sup>2</sup> and are freely available under the GNU GPL license. However, models and geomodelling packages are still unfortunately proprietary and hence not easy to reproduce results from.

It would be valuable to be able to decide whenever the capillary or viscous limits are fair approximations for steady-state flow. A recent work ([Jonoud and Jackson 2008](#)) addresses this problem, but originally for two-dimensional models. Although it might be possible to extend their method to three dimensions, the ambiguity that is present for two-dimensional models is even more involved when moving to three dimensions. Our contribution to this problem is a scale-dependent capillary number, which is shown to better predict the balance between capillary and viscous forces in our models compared to the traditional capillary number. For the reservoirs considered herein, heterogeneity typically introduces large differences in capillary pressure compared to capillary pressure gradients from saturation distribution inside a single rock type. For this reason, we restrict our attention to models with several rock types.

This paper is outlined as follows. We start by presenting the governing flow equations in Sect. 2. Thereafter, in Sect. 3, we explain steady-state upscaling in more detail. In particular, we discuss and define appropriate boundary conditions for the steady-state flow equations. We also describe the capillary and viscous limit approaches. In Sect. 4 we introduce a dimensionless scale-dependent capillary number to represent the capillary and viscous force balance in our models. The aim is to be able to predict when steady-state upscaling differs from its capillary and viscous limits. In Sect. 5 we test the steady-state upscaling approaches on a variety of reservoir models, both synthetic and realistic. The overall goal of this section is to get a better understanding of steady-state upscaling and to address the main advantages and challenges. We show how the results depend on the flow rate and on the choice of boundary conditions. In the last part, we consider a larger fluvial reservoir model similar to those considered in [Nordahl et al. \(2014\)](#). The aim is to study how well steady-state upscaling is able to reproduce fine-scale flow pattern and production data in a dynamic flow scenario. Finally, in Sect. 6, we discuss the results of this work and make the final conclusions.

## 2 Flow Equations

In this section we present the governing equations for incompressible immiscible two-phase flow in porous media. Let oil ( $o$ ) and water ( $w$ ) denote the two phases  $p$ . The equation of

<sup>1</sup> ReservoirStudio™ is a proprietary software from Geomodeling, [www.geomodeling.com](http://www.geomodeling.com).

<sup>2</sup> The Open Porous Media project, <http://www.opm-project.org>.

continuity reads

$$\phi \frac{\partial S_p}{\partial t} = -\nabla \cdot \mathbf{u}_p, \quad p = o, w, \quad (1)$$

where  $\phi = \phi(\mathbf{x})$  is the porosity at position  $\mathbf{x} = (x, y, z)$ , while  $S_p = S_p(\mathbf{x}, t)$  and  $\mathbf{u}_p = \mathbf{u}_p(\mathbf{x}, t)$  are the saturation and velocity, respectively, at position  $\mathbf{x}$  and time  $t$ . We assume Darcy flow, i.e.,

$$\mathbf{u}_p = -\frac{\mathbf{K}k_{rp}}{\mu_p} \nabla p_p, \quad p = o, w, \quad (2)$$

where we have neglected gravity. Furthermore,  $\mathbf{K} = \mathbf{K}(\mathbf{x})$  is the absolute permeability tensor, and  $k_{rp} = k_{rp}(\mathbf{x}, S_w)$ ,  $\mu_p$  and  $p_p = p_p(\mathbf{x}, t)$  are the relative permeability, viscosity and pressure of phase  $p$ , respectively. If we further introduce the mobility of phase  $p$ ,

$$\lambda_p = \lambda_p(\mathbf{x}, S_w) = \frac{k_{rp}(\mathbf{x}, S_w)}{\mu_p}, \quad (3)$$

and combine Eqs. (1) and (2), we get

$$\phi \frac{\partial S_p}{\partial t} = \nabla \cdot [\mathbf{K}\lambda_p \nabla p_p], \quad p = o, w. \quad (4)$$

To complete the system of equations, we have that

$$S_w + S_o = 1, \quad \text{and} \quad (5)$$

$$p_o - p_w = p_c, \quad (6)$$

where  $p_c = p_c(\mathbf{x}, S_w)$  is the capillary pressure. In total we have four equations, Eqs. (4–6), and four unknowns,  $S_p$  and  $p_p$ , for  $p = o, w$ .

We follow the approach of [Chavent and Jaffre \(1986\)](#) and introduce a global pressure  $p$ , defined as

$$p = p_o - \hat{p}, \quad \hat{p}(S_w) = \int_1^{S_w} f_w(\xi) \frac{\partial p_c}{\partial S_w}(\xi) d\xi,$$

where  $f_w(S_w) = \frac{\lambda_w(S_w)}{\lambda(S_w)}$  is the fractional flow of water and  $\lambda = \lambda_w + \lambda_o$  is the total mobility. We can now rewrite the coupled system of Eqs. (4–6) as

$$\nabla \cdot \mathbf{u} = 0, \quad \mathbf{u} = -\mathbf{K}\lambda \nabla p, \quad (7)$$

$$\phi \frac{\partial S_w}{\partial t} + \nabla \cdot [f_w(\mathbf{u} + \mathbf{K}\lambda_o \nabla p_c)] = 0. \quad (8)$$

The pressure equation (Eq. (7)) is elliptic, while the transport equation (Eq. (8)) is parabolic or hyperbolic dependent on the ratio between the terms. The equations are nonlinearly coupled due to the pressure dependency in  $u$  and the saturation dependency in  $\lambda_p$  and  $p_c$ .

When deriving the pressure equation, it is assumed that the capillary pressure  $p_c$  is a monotone function of  $S_w$  only, thus independent on the spatial position. In general, this assumption is not satisfied, but we believe that the introduced error is small. Testing and comparison with a fully implicit solver substantiate this.

At steady state,  $\frac{\partial S_p}{\partial t} = 0$ , so Eq. (4) reduces to

$$\nabla \cdot [\mathbf{K}\lambda_p \nabla p_p] = 0. \quad (9)$$

Furthermore, the system (7, 8) can at steady state be written as

$$\mathbf{u} \cdot \nabla f_w + \nabla \cdot (\mathbf{K}\lambda_o f_w \nabla p_c) = 0. \quad (10)$$

### 3 Steady-State Upscaling

Steady-state upscaling, see, e.g. [Ekram and Aasen \(2000\)](#), is a local upscaling method. Given a target coarse cell with fine-scale heterogeneity, we seek to find an effective (upscaled) relative permeability function as if the cell was homogeneous. Steady-state upscaling can be divided into three main steps:

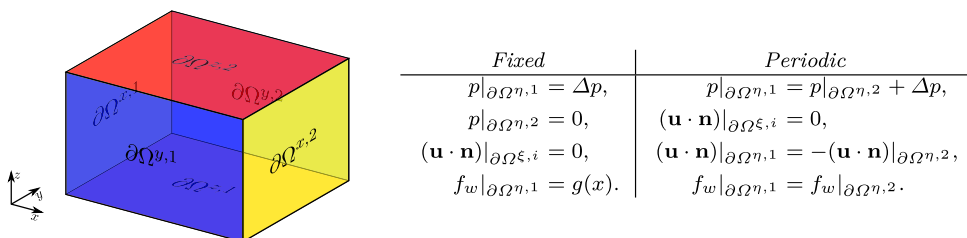
1. Calculate the fine-scale saturation distribution,  $S_w(\mathbf{x})$ , at steady state.
2. Calculate the phase permeability distribution,  $\mathbf{K}_p(\mathbf{x}, S_w) = k_{rp}(\mathbf{x}, S_w)\mathbf{K}(\mathbf{x})$ , from input data.
3. Perform single-phase upscaling on each phase separately to calculate the upscaled phase permeability tensor,  $\tilde{\mathbf{K}}_p$ .

In Step 3, single-phase upscaling corresponds to solving the steady-state equation (Eq. (9)) for each phase and then let  $\tilde{\mathbf{K}}_p$  be the phase permeability tensor which preserves the flux over each boundary face. The upscaled relative permeability tensor is now given as  $\tilde{\mathbf{K}}_p \cdot \tilde{\mathbf{K}}^{-1}$ , where  $\tilde{\mathbf{K}}$  is the upscaled (absolute) permeability tensor. The procedure above gives an upscaled relative permeability tensor valid for the upscaled water saturation,  $\tilde{S}_w$ , which is simply the volume weighted average. By varying the initial saturation and the fractional flow at inlet, one produces a sequence of upscaled tensors for different upscaled saturation points, giving an upscaled relative permeability curve. In general, Step 1 is the most demanding, as it requires a full flow simulation to reach the steady-state distribution,  $S_w(\mathbf{x})$ . However, in the capillary and viscous limits,  $S_w(\mathbf{x})$  can be calculated directly from the input data.

#### 3.1 General Steady-State Upscaling

The domain  $\Omega$  which is to be upscaled for, is assumed to be formed like a shoe-box, that is, a regular hexahedron. This is a natural assumption, as  $\Omega$  usually refers to a coarse simulation cell. Let  $\partial\Omega^{\zeta,i}$  for  $\zeta = x, y, z$  and  $i = 1, 2$  denote the six boundary faces on  $\Omega$  as illustrated in Fig. 1. To obtain the steady-state saturation distribution, we solve Eqs. (7) and (8) over the domain  $\Omega$  until steady state is reached, i.e., until the saturation distribution no longer changes with time within a given tolerance.

The flow equations must be accompanied with some appropriate boundary conditions (BCs). In this work we use two sets of BCs, denoted *fixed* and *periodic*. To induce flow, a pressure drop  $\Delta p$  is enforced in one of the Cartesian directions, hereafter denoted the pressure drop direction. For fixed BCs we set  $p = \Delta p$  and  $f_w = g(\mathbf{x})$  on inlet, and  $p = 0$  on outlet, where  $g(\mathbf{x})$  is a known function. For periodic BCs we set the flux and



**Fig. 1** Boundary conditions for the two-phase incompressible immiscible problem, Eqs. (7) and (8). To the left we see an illustration of the domain  $\Omega$  which is to be upscaled for, along with the naming conventions for the six boundary faces. To the right, precise formulations of the fixed and periodic BCs are given, where  $\eta$  denotes the pressure drop direction, and  $\xi$  denotes the two directions perpendicular to  $\eta$

the fractional flow to be periodic on inlet/outlet. This implies that what flows out at outlet flows in at inlet. A main distinction from fixed BCs is that  $f_w$  and  $p$  are allowed to vary across  $\partial\Omega$ . Furthermore, we set the pressure difference between inlet and outlet to  $\Delta p$ . For both periodic and fixed BCs we use no-flow conditions on all other boundaries. Notice that this differs from the common notion of periodic BCs, used, e.g. in [Durlafsky \(2005\)](#), as we do not induce periodic flow on boundaries parallel to the pressure drop direction. With this simplification, we neglect cross flow and our upscaled tensor will be diagonal. For reservoir models where the main heterogeneity structure is aligned with the pressure drop direction, this is a reasonable assumption.

The two sets of BCs are given explicitly in [Fig. 1](#). We let  $\mathbf{n}$  denote the outward pointing unit normal vector,  $\eta$  the pressure drop direction,  $\xi$  the two other directions, and  $f|_{\partial\Omega}$  the function  $f$  restricted to  $\partial\Omega$ . Additionally, for periodic BCs, it is necessary to specify the global pressure at one point in the domain for the system to be well-posed. Furthermore, an initial guess of the saturation distribution,  $S^0(\mathbf{x})$ , must be specified. For the periodic BCs, we use a face-to-face connection on the periodic boundaries, and we have assumed that the grids on the inlet and outlet faces match each other. This assumption is not satisfied for all realistic reservoir models, but may be overcome by mirroring the model in the pressure drop direction. Notice that with periodic BCs no fluids are allowed to enter or leave the model. Hence, the upscaled saturation at steady state is equal to the initial average saturation.

### 3.2 Capillary Limit

In the capillary limit, see, e.g. [Ekrann et al. \(1996\)](#), we neglect gravity and viscous forces. In this limit the fluid velocity vanishes, and hence [Eq. \(10\)](#) reduces to

$$\nabla \cdot (\mathbf{K}\lambda_o f_w \nabla p_c) = 0.$$

Since this should hold for the whole domain  $\Omega$  and since the product  $\mathbf{K}\lambda_o f_w$  is spatially dependent, we must require that  $\nabla p_c = 0$ , or equivalently that  $p_c$  is constant throughout the model. Thus, at a given (constant) capillary pressure,  $P_c$ , the fine-scale saturation distribution is determined by solving

$$p_c(\mathbf{x}, S_w) = P_c \tag{11}$$

for  $S_w$ . Since  $p_c(\mathbf{x}, S_w)$  is a strictly monotonically decreasing function with respect to  $S_w$ , this has a unique solution. Observe that this approach also produces an upscaled capillary pressure function,

$$\tilde{p}_c(\tilde{S}_w) = P_c. \tag{12}$$

In the following we refer to the capillary limit solution by CL.

### 3.3 Viscous Limit

In the viscous limit, see, e.g. [Ekrann and Aasen \(2000\)](#), we neglect gravity and capillary forces. Thus, [Eq. \(10\)](#) reduces to

$$\mathbf{u} \cdot \nabla f_w = 0. \tag{13}$$

This means that the fractional flow is constant along streamlines. The viscous limit solution is therefore determined by the fractional flow on the inlet boundary and is thus not unique. In general, if we know the fractional flow of water throughout the model,  $F_w(\mathbf{x})$ , we can calculate the saturation distribution by solving

$$f_w(\mathbf{x}, S_w) = F_w(\mathbf{x}) \tag{14}$$

for  $S_w$ . Under the standard assumptions that  $k_{rp} \geq 0$  for  $p = o, w$ , and that  $k_{rw}$  and  $k_{ro}$  are strictly monotonically increasing and decreasing functions with respect to  $S_w$ , respectively, it can be shown that  $f_w(\mathbf{x}, S_w)$  is a strictly monotonically increasing function with respect to  $S_w$ . Thus, Eq. (14) has a unique solution.

Calculating the streamlines for a two-phase three-dimensional problem is in general non-trivial. A class of problems for which the streamlines are identical to their single-phase counterparts has been identified (Ekrann and Aasen 2000). This class is characterized by  $\mathbf{u} \cdot \nabla \lambda = 0$ , which holds if the relative permeability curves as functions of normalized water saturation are independent on  $\mathbf{x}$ . For general problems, tracking streamlines is dependent on the discrete model, so the only steady-state viscous limit we can obtain is the one with constant fractional flow throughout the model. This is equivalent to assuming constant fractional flow on the inlet boundary. In the following, when we refer to VL we mean the viscous limit solution with constant fractional flow.

Based on the discussion above, it is necessary to have constant fractional flow on the inlet boundary if we want the general steady-state approach to converge to VL for high flow rates. For fixed BCs this is achieved by setting  $g(\mathbf{x})$  equal to the constant fractional flow that we want to upscale for, i.e.,  $g(\mathbf{x}) \equiv F_w$  cf. Figure 1. For periodic BCs the fractional flow does not necessarily converge toward a constant for high flow rates in an analytical sense. In our discretization of the fluid flow, we assume a full mixing of fluids in the grid cells. We therefore avoid mixing only when streamlines are parallel to cell boundaries. Thus, for most models, as demonstrated by numerical experiments in Sect. 5.2, we obtain constant fractional flow for high pressure drops. A layered model, as we consider in Sect. 5.1, is an example where streamlines are parallel to cell boundaries, and where the fractional flow is not necessarily constant for high pressure drops.

In contrast to the CL approach, there is no natural way of upscaling capillary pressure in the VL approach. Hence, we neglect capillary forces by letting  $p_c \equiv 0$  when considering viscous limit upscaled simulation models in Sect. 5.

## 4 Scale-dependent Capillary Number

Upscaling of two-phase flow is dependent on the balance between viscous and capillary forces. Evaluation of the force balance helps to determine which upscaling method is most appropriate. In a multiscale upscaling process, disregarding viscous forces is typically a fair approximation for models on the smallest scale (e.g., lamina scale, mm to cm), while in a full field reservoir model the impact from capillary forces is often negligible. The balance between viscous and capillary forces is thus scale dependent.

At the microscopic (interstitial) scale, the viscous–capillary force balance is traditionally described by a microscopic capillary number. There exists different forms of the capillary number, see, e.g., (Lake 1989, Tables 2, 3). Most are similar to

$$\text{Ca} = \frac{\mu u}{k_r \sigma \cos(\theta)} \simeq \frac{\mu u}{\sigma}, \quad (15)$$

where  $u$  is Darcy velocity,  $\sigma$  is the interfacial tension, and  $\theta$  is the contact angle, often set to  $0^\circ$ . The relative permeability,  $k_r$ , is often set to 1 (Dullien 1992). Observe that the capillary number, Ca, increases with increasing fluid velocity. This reflects that on the microscopic scale the capillary forces dominate for small flow rates, while viscous forces dominate for high flow rates. This transition is reflected in capillary desaturation curves, describing the relationship between residual oil saturation and the capillary number. Such capillary desaturation curves



show that below a critical capillary number the residual oil saturation remains constant, while the residual oil saturation decreases with increasing capillary numbers above the critical number (Morrow et al. 1988; Dullien 1992).

In this paper we deal with fluids and flow rates for which the capillary number is below the critical value. Thus, at the pore scale the residual oil saturation is assumed constant, and the fluid distribution will be dominated by capillary forces. Instead we are interested in the balance of viscous and capillary forces on a macroscopic (Darcy) scale. For models representing reservoir heterogeneities, individual rock types are populated with particular capillary pressure curves. Such different capillary pressure curves introduce capillary forces not represented by the traditional capillary numbers.

We seek good static approximations of the magnitudes of the viscous and capillary forces that take different capillary pressure curves into account. A characteristic magnitude of the viscous forces is given by  $|\Delta p|/L$ , where  $L$  is the length of the model in the direction of the pressure drop,  $\Delta p$ . Note that this is a static parameter for typical upscaling procedures. As the gradient of the capillary pressure is dependent on the saturation distribution, a dynamic variable, any static characteristic for the capillary forces will be an approximation. We approximate the capillary forces with an estimate of the norm of the capillary pressure gradient,

$$C = \frac{\sum_{ij} ((V_i\phi_i + V_j\phi_j)\Delta p_{c,ij}/l_{ij})}{\sum_{ij} (V_i\phi_i + V_j\phi_j)} \approx \|\nabla p_c\|, \tag{16}$$

where the sum is over neighboring cells  $ij$  with length  $l_{ij}$  between the cell centers,  $V_i$  is the volume of cell  $i$ ,  $\phi_i$  is the porosity of cell  $i$ , and  $\Delta p_{c,ij}$  is a measure of the absolute difference in capillary pressure between the neighboring cells. Hence,  $C$  is the pore volume weighted average of the estimated capillary pressure gradient,  $\Delta p_{c,ij}/l_{ij}$ , over cell interfaces. In this work we define  $\Delta p_{c,ij}$  as an integral average, such that

$$\Delta p_{c,ij} = \frac{1}{1 - \tilde{S}_{orw} - \tilde{S}_{wir} - 2\delta} \int_{\tilde{S}_{wir} + \delta}^{1 - \tilde{S}_{orw} - \delta} |p_{c,i}(S_w^{VL}) - p_{c,j}(S_w^{VL})| d\tilde{S}_w^{VL},$$

where  $S_w^{VL}$  is to be interpreted as the water saturation distribution at VL with upscaled water saturation equal to  $\tilde{S}_w^{VL}$ . Furthermore,  $p_{c,i}(S_w^{VL})$  is the capillary pressure in cell  $i$  for this saturation distribution. The endpoint saturations,  $\tilde{S}_{wir}$  and  $\tilde{S}_{orw}$ , refer to the upscaled irreducible water saturation and the upscaled residual oil saturation, respectively. The capillary pressure curves are typically very steep close to the endpoints. To obtain representative capillary pressure values, we neglect these regions when taking the integral average. We choose  $\delta$  to be

$$\delta = \epsilon(\tilde{S}_{wor} - \tilde{S}_{wir}),$$

and set  $\epsilon = 0.1$ . We report on the stability of this choice in Sect. 5.2.

A macroscopic scale-dependent capillary number,  $\mathcal{N}$ , is now defined as the fraction between viscous and capillary forces,

$$\mathcal{N} = \frac{|\Delta p|/L}{C} \approx \frac{\|\nabla p\|}{\|\nabla p_c\|}. \tag{17}$$

By using Eq. (16) as an approximation for the gradient of the capillary pressure, we neglect contributions from saturation gradients, e.g. inside a single rock type. For the fluvial reservoir type considered in this work, it is a fair assumption that differences in capillary pressure due

to heterogeneity dominate the contributions from saturation gradients, especially close to a steady-state scenario.

The variation in capillary pressures in a small-scaled model is typically at the same order as the variation in a coarser model. Hence,  $\mathcal{C}$  is typically smaller in a coarser model through the dependency on  $l_{ij}$ . The viscous pressure gradient,  $\Delta p/L$ , is on the other hand not affected by the grid size. Therefore,  $\mathcal{N}$  typically decreases with model size, reflecting that capillary forces dominate on fine-scale models, while viscous forces dominate in coarser models.

## 5 Numerical Examples

In this section we apply the steady-state upscaling methods described in Sect. 3 on a range of models, both synthetic and realistic. The purpose is to study the rate dependency in steady-state upscaling and also the impact of different boundary conditions (BCs). In the last part of this section we consider a larger representative model and test the different upscaling regimes on reservoir simulation. The aim is to see how well steady-state upscaling is able to reproduce dynamic flow on reservoir scale.

For general steady-state upscaling, the pressure and saturation equations (Eq. (7, 8)) are solved sequentially. For the elliptic pressure equation, a mimetic finite difference method (Brezzi et al. 2005) is used, while an implicit Euler method with upstream weighting of the fractional flow is used for the saturation equation. The BCs for the flow-based local single-phase upscaling correspond to the ones used to solve the two-phase equations, i.e., as seen in Fig. 1, but without the fractional flow conditions. As the initial guess we use the capillary limit distribution unless a steady-state solution to a similar problem exists. All models are represented in corner-point grids. Fluid data are listed in Table 1.

### 5.1 Synthetic Models

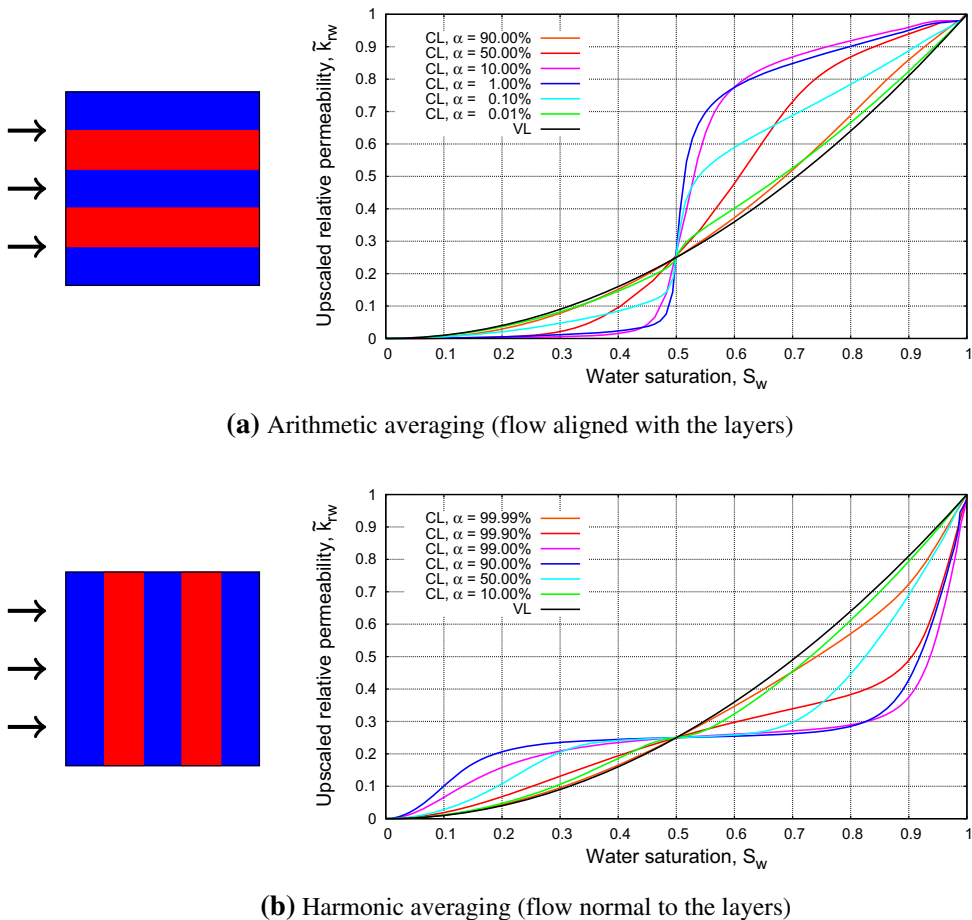
In this section we consider simple synthetic models built up of two homogeneous isotropic rocks: one high permeability rock with  $k = 1$  D (rock 1), and one low permeability rock with  $k = 1$  mD (rock 2). The porosity is 0.1 for both rocks, and we use the same relative permeability curves and Leverett J-function curve,

$$k_{rw}(S_w) = S_w^2, \quad k_{ro}(S_w) = (1 - S_w)^2, \quad J(S_w) = \frac{1}{S_w} - \frac{1}{1 - S_w}. \quad (18)$$

The capillary pressure and the Leverett J-function are related as  $p_c(S_w) = \sqrt{\phi/k}\sigma J(S_w)$ , assuming a contact angle of  $0^\circ$ . Hence, the capillary pressure curves are different in the two rocks. As the relative permeability curves are equal for oil and water, only mirrored around  $S_w = 0.5$ , we only present upscaled water curves for better readability. The results and conclusions are the same for oil curves.

**Table 1** Fluid data used for all models in this work

Parameter	Symbol	Value
Interfacial tension	$\sigma$	11 dynes/cm = 0.011 N/m
Viscosity, oil	$\mu_o$	1.78 cP = 0.00178 Pa s
Viscosity, water	$\mu_w$	0.33 cP = 0.00033 Pa s

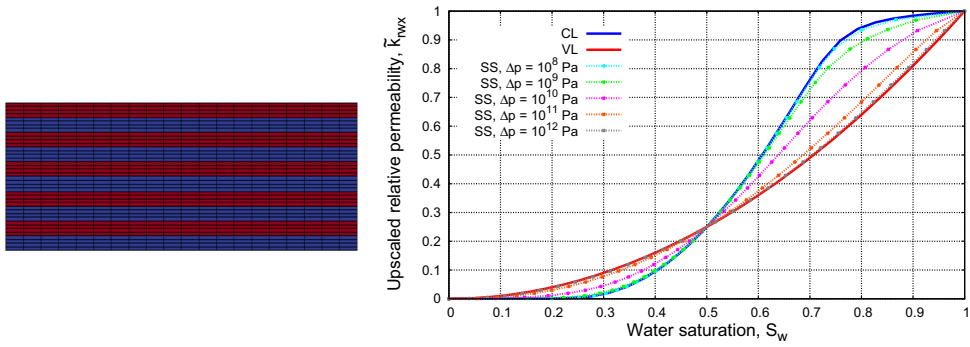


**Fig. 2** Analytic solutions for parallel models, where (a) flow is aligned with the layers, and (b) flow is normal to the layers. The volume fraction between rock 1 ( $k = 1$  D) and rock 2 ( $k = 1$  mD) is denoted  $\alpha$ . We only show water curves, as oil curves are equal, only mirrored around  $S_w = 0.5$

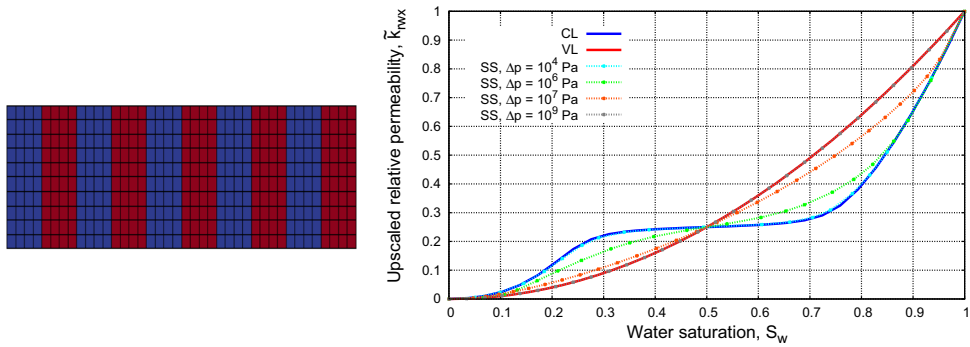
First, we consider models where the two rock types alternate in parallel layers. If the flow is aligned with the layers or if the flow is normal to the layers, we can use arithmetic or harmonic volume weighted averaging, respectively. Let  $\alpha$  denote the volume fraction between rock 1 and rock 2. Since the relative permeability curves are identical, the VL solution is independent on  $\alpha$  and is equal to the input relative permeability curve. However, due to the difference in capillary pressure, the CL solution depends on  $\alpha$ .

In Fig. 2 the analytic results for different volume fractions are displayed. For  $\alpha$  close to 0 or 100 %, the CL curves are close to the VL curves in both cases. When flow is aligned with the layers (Fig. 2a), the difference between CL and VL upscaling becomes significant at very small portions of the high permeability rock. For flow normal to the layers (Fig. 2b), the difference becomes significant for very small portions of the low permeability rock. This illustrates that even very thin high permeability channels or low permeability barriers can have large effects on the upscaling results. These results have also been used to verify our numerical upscaling routines.

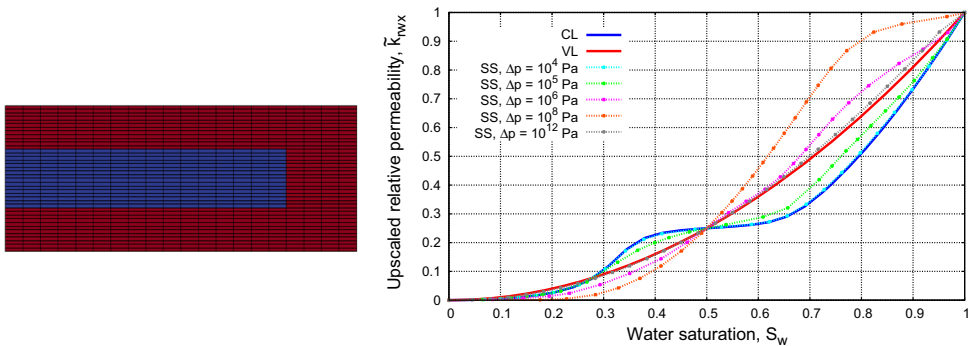
Next, we apply steady-state upscaling on the three synthetic models depicted in Fig. 3. The rock and fluid data are all the same as in the analytic examples. All models are 100 m long



(a) Flow aligned with the layers



(b) Flow normal to the layers



(c) Flow through a barrier

**Fig. 3** Synthetic test models. All models are  $100 \times 5$  m. Rock 1 (blue) has  $k = 1$  D and rock 2 (red) has  $k = 1$  mD. Results for different pressure drops and the VL and CL solutions are shown to the right. The upscaled oil curves are equal, just mirrored around  $S_w = 0.5$ . The pressure drop direction is from left to right and fixed BCs are used

and 5 m thick. We consider flow in the  $x$ -direction, that is left to right. The results with fixed BCs for different pressure drops and in CL and VL are shown in Fig. 3. Both the microscopic capillary number,  $Ca$ , and the proposed macroscopic capillary number,  $\mathcal{N}$ , are presented in Table 2.

For all models, we observe that general steady-state upscaling converges toward CL as  $\Delta p$  decreases, and toward VL as  $\Delta p$  increases. This is as expected, since for small pressure drops capillary forces manage to redistribute the fluids toward the CL, while for large enough pressure drops, the viscous forces dominate. For the two first models (Fig. 3a, b), the

**Table 2** The microscopic capillary number,  $Ca$  (Eq. (15)), interpreted as  $Ca = \frac{\mu u}{\sigma} = \frac{\bar{k} \Delta p}{\sigma L}$ , and the scale-dependent capillary number,  $\mathcal{N}$  (Eq. (17)), as functions of the global pressure drop (in Pa),  $\Delta p$ , for the three models in Fig. 3

Model	$Ca$	$\mathcal{N}$
Figure 3a	$4.5 \cdot 10^{-13} \Delta p$	$5.1 \cdot 10^{-8} \Delta p$
Figure 3b	$1.8 \cdot 10^{-15} \Delta p$	$1.0 \cdot 10^{-6} \Delta p$
Figure 3c	$4.3 \cdot 10^{-15} \Delta p$	$2.8 \cdot 10^{-7} \Delta p$

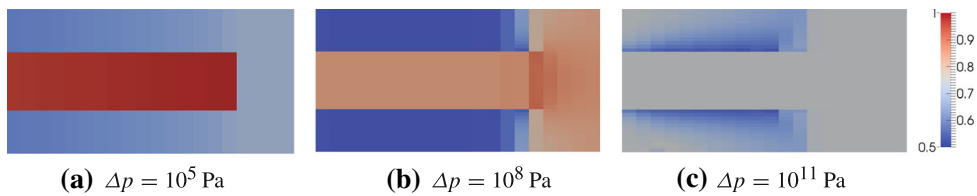
convergence from CL to VL is monotonic and the general steady-state upscaling curves are bounded by the CL and VL curves. This property does not hold for the last model (Fig. 3c), where the high permeability rock is aligned with the flow, but not percolating.

Consider the layered model (Fig. 3a). We observe that high pressure drops ( $\Delta p > 10^8$  Pa) are needed to get results different from the CL solution. First at  $\Delta p \geq 10^{12}$  Pa are the results equal to the VL solution. This is in accordance with  $\mathcal{N}$  reported in Table 2, indicating strong capillary forces. If we use periodic BCs and set the initial saturation distribution equal to the CL distribution, we will have no vertical redistribution of the fluids, and hence all streamlines will be parallel to the layers. Thus, there will be no mixing of fluids between the layers independently of the magnitude of the pressure drop. The consequence is that the steady-state saturation distribution is equal to the CL distribution for all pressure drops. Hence, the upscaled relative permeability will be rate independent. This is verified by numerical computations. The resulting upscaled relative permeability curves coincide with the CL solution with fixed BCs as seen in Fig. 3a. However, the fractional flow will be constant within each layer, and hence this solution also represents a viscous limit [recall Eq. (13)], this one in capillary equilibrium. It is important to notice that this viscous limit is *not* the same as VL (where constant fractional flow is assumed). The latter VL solution is equal to the input relative permeability curve, which again is equal to the VL solution for fixed BCs, see Fig. 3a. Thus, we have identified two viscous limit solutions that are quite different from each other. We get the same results also with other initial distributions.

Next, consider the model with a barrier (Fig. 3c). Figure 4 shows the steady-state water saturation for different pressure drops at  $\tilde{S}_w = 0.70$ : capillary dominant ( $\Delta p = 10^5$  Pa); mixed forces ( $\Delta p = 10^8$  Pa) and viscous dominant ( $\Delta p = 10^{11}$  Pa). In VL, the saturation is equal in the two rocks since the relative permeability curves are equal. For  $S_w > 0.5$ , capillary forces distribute water into the high permeability rock. This makes the barrier less permeable for water, and thus the upscaled relative permeability is lower in CL than in VL. For intermediate pressure drops, say  $\Delta p = 10^8$  Pa, capillary forces distribute water into the high permeability rock so that water flows easier there. At the same time, the pressure drop is high enough so that water flows into the low permeability rock, making the barrier more permeable for water. This is evident from Fig. 4. Overall, this results in higher upscaled water relative permeability than in VL, and explains why the convergence from CL to VL is not monotone as seen in Fig. 3c.

Upscaling of the two first models (Fig. 3a, b) correspond to arithmetic and harmonic averaging, respectively. By comparing the CL and VL results with the analytic results in Fig. 2 ( $\alpha = 50\%$ ), we see that these are equal. That the general steady-state solution converges to CL and VL serves as a verification that our upscaling routines are correct.

For the purpose of judging the balance between viscous and capillary forces in the model, the capillary number should be close to 1 at the transition between CL and VL. The micro-



**Fig. 4** Saturation distribution at steady state ( $\tilde{S}_w = 0.70$ ) for different pressure drops,  $\Delta p$ , for the barrier model in Fig. 3c. In CL the saturation is 0.95 and 0.58 in rock 1 and rock 2, respectively, and in VL the saturation is 0.70 in both rocks

scopic capillary number,  $Ca$ , is a few orders of magnitude smaller than 1 in the middle of the transition for the layered model (Fig. 3a), while it is off by many orders of magnitude for the two other models. Our proposed scale-dependent capillary number,  $\mathcal{N}$ , is about two orders of magnitude larger than 1 in the middle of the transition for the layered models (Fig. 3a, b). For the barrier model (Fig. 3c),  $\mathcal{N} \sim 1$  in the middle of the transition zone. Thus, the proposed capillary number,  $\mathcal{N}$ , better estimates the balance of the two active forces for these models. However, we are not able to tell from  $\mathcal{N}$  where the transition from CL to VL starts and ends.

## 5.2 Models Representative of Sedimentary Heterogeneity

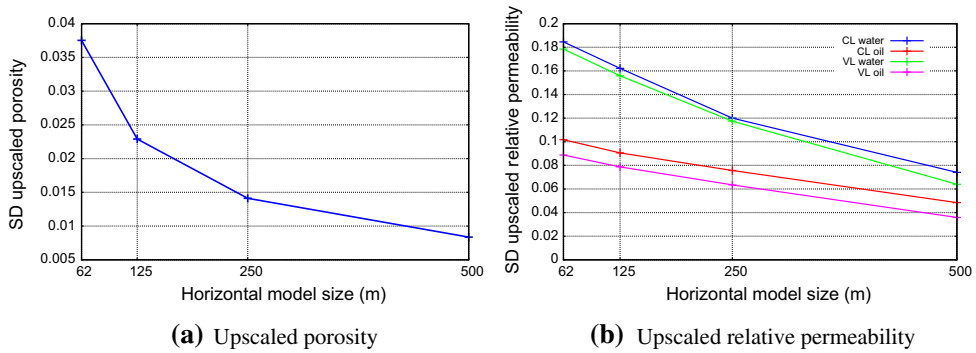
In this section we use reservoir models similar to those considered in Nordahl et al. (2014). These models represent a key heterogeneity scale for fluvial reservoirs, since the capillary or viscous dominance is unknown. Moreover, this scale includes the most important sedimentary heterogeneity for these reservoirs Nordahl et al. (2014). Generally, such reservoirs have complex geometry and anisotropic permeability spanning several orders of magnitude.

First, we consider several small sections of dimension  $100 \times 100 \times 5$  m. This is a typical size of a simulation cell, and the aim is to study steady-state upscaling on these. A wide range of sections from different sectors of the field has been examined. We therefore believe that the results and conclusions drawn are representative for this class of reservoirs. However, due to lack of space, we only present detailed results from one such section.

In the second part we consider a larger model, to represent flow within a reservoir zone. This model is large enough to represent flow between an injector and producer well pair, but still small enough to run fine-scale simulations. The aim is to study how well a coarser upscaled model captures the flow pattern and production data, with a special focus on different steady-state approaches.

### 5.2.1 REV Analysis

Local upscaling methods like the ones we study in this work are best understood by the concept of asymptotic homogenization. Multiphase flow is governed by partial differential equations, which we then seek to homogenize over a scale of heterogeneity for the material. The heterogeneity of the material gives rise to rapidly oscillating coefficients for the equations. Central to homogenization is the concept of a representative elementary volume (or element), denoted REV. In our case, an REV is the smallest volume over which a measurement can be made that is representative of the reservoir element of interest. A key reference for the REV concept in our setting is found in Bear (1972), while Nordahl et al. (2014) contains a more recent presentation. Still, we recapture here that for the REV concept to be applicable, we depend on separation of scales. That is, being able to identify volumes of investigation



**Fig. 5** Standard deviation (SD) for upscaled porosity **(a)** and upscaled relative permeability **(b)** plotted against horizontal model size for a representative sector model

where measured reservoir properties vary slowly locally. In other words, identify scales where homogenization makes sense.

For the models considered in this work, we have performed an REV analysis to identify REV for different properties. This was done by cropping the original sector model into disjoint submodels of a given size. Then each submodel was upscaled and the mean and the standard deviation (SD) of the upscaled values were calculated. This was done for different sizes of the submodels, but the ratio between the horizontal and the vertical size was kept constant at 40. Porosity, permeability and relative permeability in the two limits were considered. Porosity was upscaled with volume weighted averaging and absolute permeability with a pressure solver as explained in Sect. 3. For relative permeability we used the  $L^2$ -norm to measure the difference between two relative permeability curves, and the mean curve was interpreted as a pointwise mean. The results for porosity and relative permeability for one sector model are shown in Fig. 5.

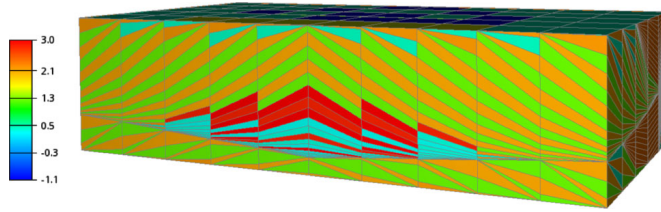
The target cell size for simulation scale is in our case approximately  $100 \times 100 \times 5$  m. Consequently, we can only expect porosity to have a separation of scales here. Permeability is not too far off, but for relative permeability we are not at a representative volume for our simulation cell size. Moreover, relative permeability is probably not at an approximate REV even within the total size of our models (i.e., a potential REV is probably at the kilometer scale here). Hence, we chose to upscale each coarse scale cell separately for our simulation models, rather than attempting rock typing with a selected set of relative permeability curves.

### 5.2.2 Steady-State Upscaling

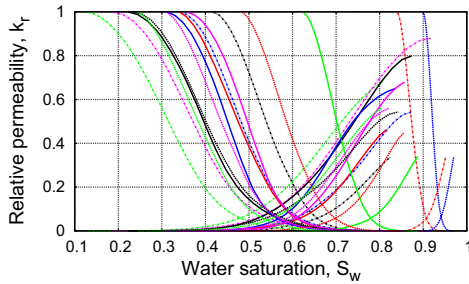
Consider the section model displayed in Fig. 6, where the horizontal permeability distribution is shown together with the input relative permeability and capillary pressure curves for the 15 different anisotropic rock types. The model contains complex geometry and the permeability spans more than 4 orders of magnitude. Each rock type has individual flow properties that are not produced from some master curve, such as J-function scaling. We see that the model is periodic in the  $x$ -direction. This is because the original model has been mirrored. Thus, we only consider flow in the  $x$ -direction. In Table 3 different pressure drops are related to the capillary numbers and typical flow rates.

The test procedure is the same as for the synthetic layered model. We perform steady-state upscaling in VL and CL, and with the general steady-state method for different pressure drops. Both fixed and periodic BCs are used. The results are given in Fig. 7.

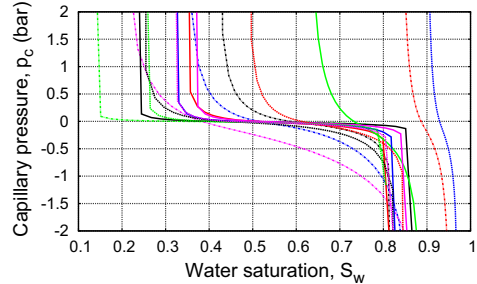




(a) Horizontal permeability distribution (mD) on logarithmic scale



(b) Input relative permeability curves



(c) Input capillary pressure curves

**Fig. 6** Realistic section model from a fluvial reservoir on the NCS represented in a corner-point grid. The original model is mirrored in the  $x$ -direction to create a periodic model. The dimension of the mirrored model is  $200 \times 100 \times 5$  m. Each of the 15 rock types have uniquely generated flow properties. All curves are cut at  $\pm 2$  bar to better see the curvature

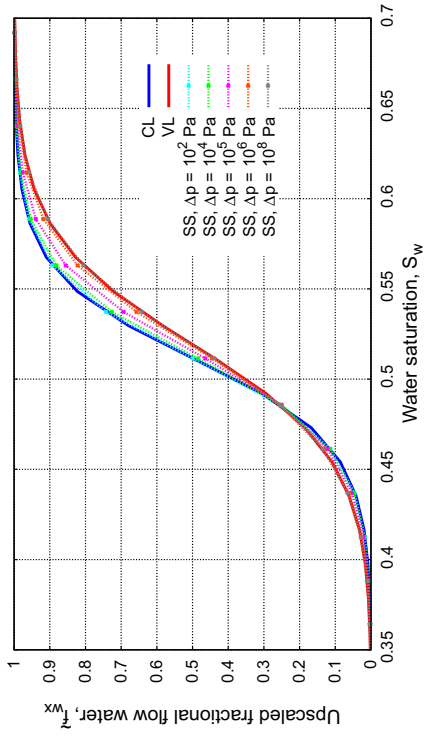
**Table 3** Pressure drop,  $\Delta p$ , related to the microscopic capillary number, Ca (Eq. (15)), interpreted as  $Ca = \frac{\mu u}{\sigma} = \frac{\tilde{k} \Delta p}{\sigma L}$ , the macroscopic capillary number,  $\mathcal{N}$  (Eq. (17)) and interstitial (pore) velocities,  $v_p = u_p / \phi$  for the realistic model in Fig. 6. We use  $k_r = 0.5$  and otherwise upscaled quantities to calculate  $v_p$

$\Delta p$ (Pa)	$\Delta p$ (bar)	Ca	$\mathcal{N}$	$v_o$ (ft/day)	$v_w$ (ft/day)
$10^2$	$10^{-3}$	$5.5 \cdot 10^{-12}$	$5.2 \cdot 10^{-5}$	$2.1 \cdot 10^{-5}$	$1.1 \cdot 10^{-4}$
$10^4$	$10^{-1}$	$5.5 \cdot 10^{-10}$	$5.2 \cdot 10^{-3}$	$2.1 \cdot 10^{-3}$	$1.1 \cdot 10^{-2}$
$10^5$	$10^0$	$5.5 \cdot 10^{-9}$	$5.2 \cdot 10^{-2}$	$2.1 \cdot 10^{-2}$	$1.1 \cdot 10^{-1}$
$10^6$	$10^1$	$5.5 \cdot 10^{-8}$	$5.2 \cdot 10^{-1}$	$2.1 \cdot 10^{-1}$	$1.1 \cdot 10^0$
$10^8$	$10^3$	$5.5 \cdot 10^{-6}$	$5.2 \cdot 10^1$	$2.1 \cdot 10^1$	$1.1 \cdot 10^2$

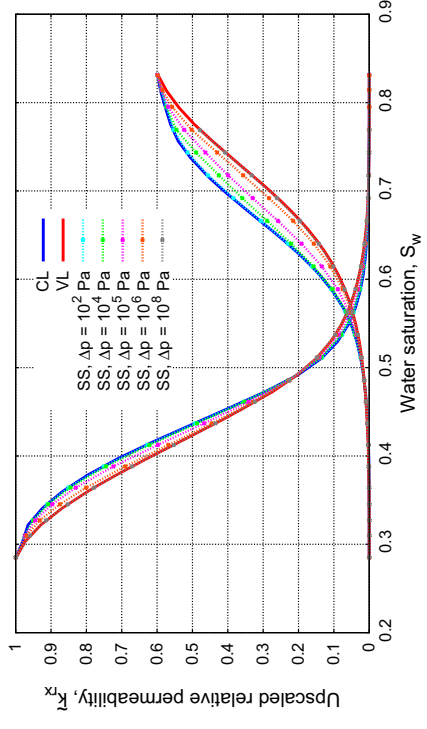
Consider the results with fixed BCs (Fig. 7a). We see that for small flow rates general steady-state upscaling coincides with CL and that the upscaled curves converge monotonically to VL as the pressure drop increases. The results with periodic BCs, see Fig. 7b, have the same behavior, and the results are very much equal. Observe that the CL and VL solutions are equal whether we use fixed or periodic BCs. The upscaled fractional flow (Fig. 7c) does also converge monotonically from CL to VL.

In Fig. 8 we see the fractional flow of water at steady state for three different pressure drops when periodic BCs are used. For a small pressure drop ( $\Delta p = 1$  Pa), the system is capillary dominated, and we see that the fractional flow is nonconstant. As we increase the pressure drop, and thus the system becomes more viscous dominated, the fractional flow becomes nearly constant at  $\Delta p = 10^8$  Pa. Hence, we have demonstrated that we converge

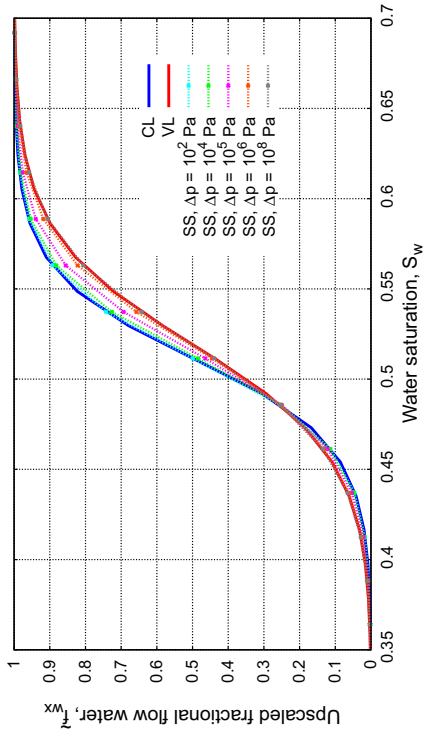




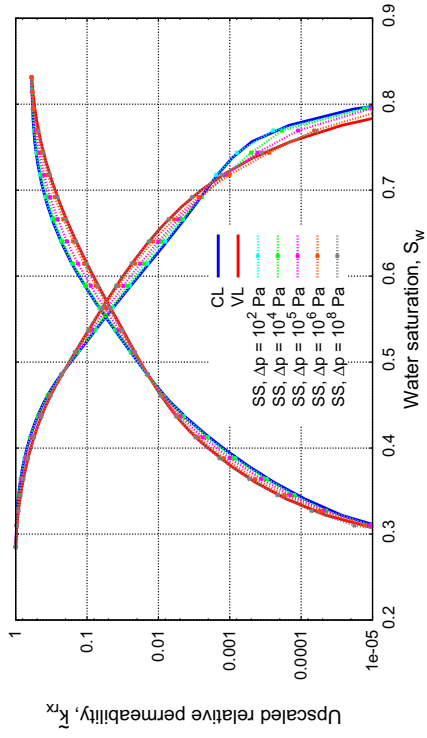
(a) Upscaled relative permeability with fixed BCs



(b) Upscaled relative permeability with periodic BCs

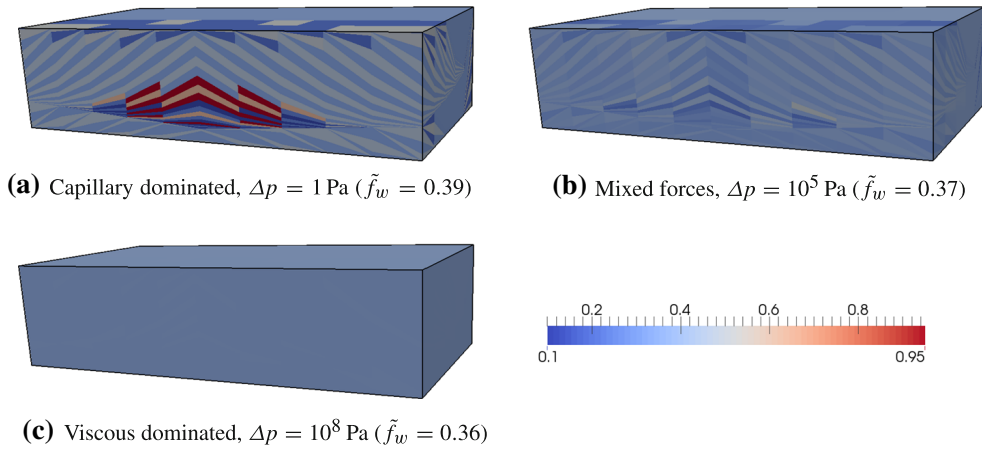


(c) Upscaled fractional flow with periodic BCs

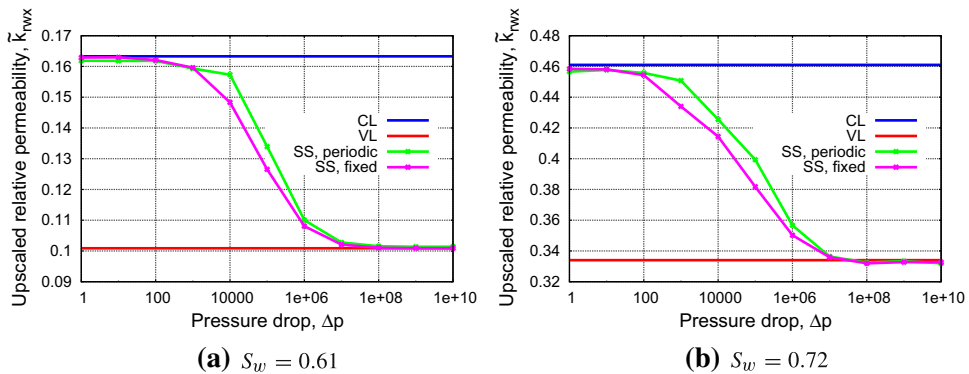


(d) Logarithmic plot of upscaled relative permeability with periodic BCs

**Fig. 7** Results from steady-state upscaling (SS) of the realistic model in Fig. 6 for different pressure drops,  $\Delta p$ , and in CL and VL. The pressure drop direction is in the  $x$ -direction



**Fig. 8** Fractional flow of water at steady state for different pressure drops,  $\Delta p$ , for the realistic model (Fig. 6). Periodic BCs are used and the average saturation is 0.5

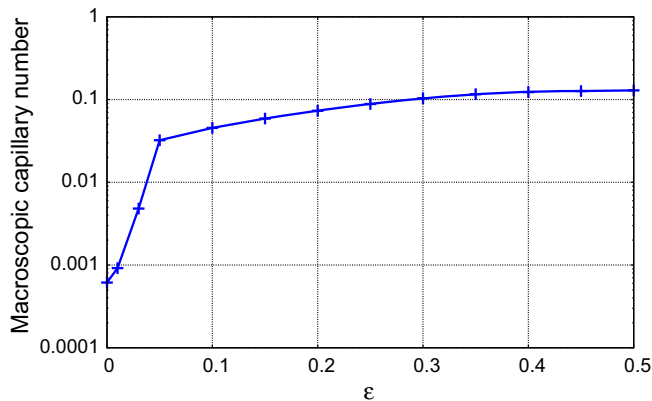


**Fig. 9** Upscaled relative permeability of water,  $\tilde{k}_{rwx}$ , is plotted against the pressure drop,  $\Delta p$ , for both fixed and periodic BCs, and at two different saturations,  $S_w = 0.61$  (a) and  $S_w = 0.72$  (b)

to VL as the pressure drop increases, even though we have not specified constant fractional flow on the inlet.

The difference between the results when using fixed and periodic BCs is illustrated in Fig. 9, where the upscaled relative permeability is plotted against the pressure drop at two different water saturations. We see that the differences are relatively small and that the transition from CL to VL occurs over approximately five orders of magnitude of the pressure drop. The results start to move away from CL at  $\Delta p \approx 100$  Pa, which corresponds to very low water flow rates around  $10^{-4}$  ft/day, and meet VL at  $\Delta p \approx 10^7$  Pa, or at water flow rates around 11 ft/day, which is about one order of magnitude larger than a typical reservoir flow rate. Furthermore, we see from Table 3 that  $\mathcal{N} \sim 1$  inside the rate-dependent interval. This is also the case for most of the other sections we have considered. However, the values of  $\mathcal{N}$  at the start- and end-points of the rate-dependent region are not the same for all models. Similar conclusions apply to the oil curves. It is evident from Table 3 that Ca fails to model the transition from CL to VL with many orders of magnitude.

Recall that the macroscopic capillary number,  $\mathcal{N}$  (Eq. (17)), is defined by taking an integral average over a range of upscaled water saturations. In Fig. 10 we have plotted  $\mathcal{N}$  against different choices of  $\epsilon$ , which is the fraction of the saturation range that is excluded at each



**Fig. 10** Plot of the macroscopic capillary number,  $\mathcal{N}$ , on a logarithmic scale, against  $\epsilon$  as defined in Sect. 4 for the realistic model in Fig. 6 with a pressure drop of  $10^5$  Pa

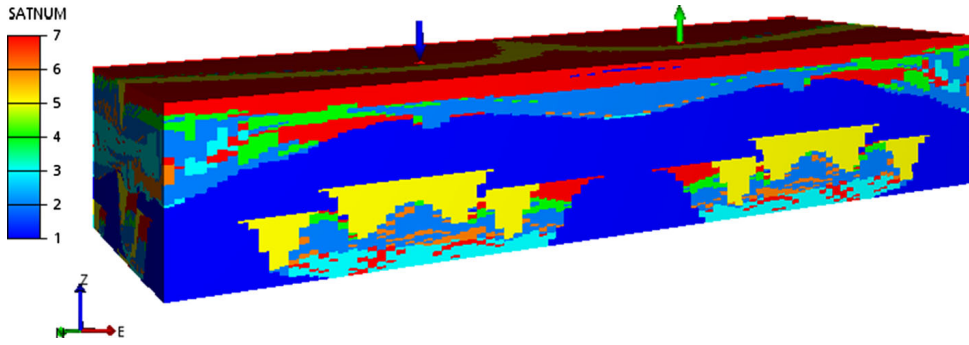
end of the integration interval. We conclude that  $\mathcal{N}$  is relatively stable with respect to  $\epsilon$  as long as  $\epsilon > 0.05$ .

### 5.2.3 Reservoir Simulation

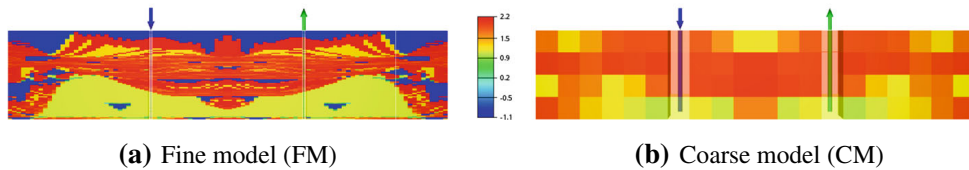
We now examine the different upscaling approaches on dynamic flow scenarios on a larger field model. A fluvial reservoir model from the NCS is represented on a regular Cartesian grid with 400,000 cells, see Fig. 11. The model is originally represented on a corner-point grid, but we have regularized it to make the simulations more efficient. The reservoir dimension is  $2000 \times 1000 \times 20$  m, and the discretization levels are 100, 50 and 80 in the  $x$ -,  $y$ - and  $z$ -directions, respectively. The model has seven different rock types, each with its unique relative permeability curve and capillary pressure curve, while porosity and permeability may vary within a rock type. The fluid data are listed in Table 1. Two vertical wells, one rate-controlled injector and one bottom hole pressure-controlled producer, are placed 700 m apart. They are placed away from the boundary, where no-flow conditions are imposed, to minimize boundary effects. The wells percolate the whole model in the  $z$ -direction and are completed in all layers. We initialize the reservoir with  $S_w = S_{wir}$ , that is the irreducible water saturation, and  $p = 200$  bar. The bottom hole pressure of the producer is kept constant at 200 bar. The injection rate is also kept constant within each simulation, but a series of scenarios with different rates are run. The start date for our simulations is October 1, 2010. As in the upscaling procedures, we disregard gravity, so that we only consider capillary and viscous forces. We use OPM for upscaling and the commercial software ECLIPSE 100<sup>3</sup> for field simulations. For the ECLIPSE runs we use the fully implicit black oil formulation with the Peaceman well model (Peaceman 1983).

The test setup is as follows. First, a fine grid simulation is performed on the original model. This is used as a reference solution. Then, we create a coarse grid and populate it with upscaled quantities. For permeability we use flow-based anisotropic local upscaling, while for relative permeability we use the steady-state upscaling techniques with periodic BCs, though restricted to the CL and VL approaches. In this way, each coarse grid cell has its unique (upscaled) relative permeability curve. We only consider isotropic relative permeability in the coarse model, that is, we use the upscaled relative permeability originating from flow in the  $x$ -direction. For other parameters, like porosity and irreducible water saturation, we

<sup>3</sup> Reservoir simulation software from Schlumberger™.



**Fig. 11** Representative fluvial reservoir model taken from a field on the NCS. The figure displays the rock type (SATNUM) distribution and the position of the wells. The dimension of the model is  $2000 \times 1000 \times 20$  m, and it is represented in a regular Cartesian grid with a total of 400,000 cells, each of dimension  $20 \times 20 \times 0.25$  m. The horizontal permeability variation for the plane intersecting the wells is displayed in Fig. 12



**Fig. 12** Horizontal permeability (logarithm) of (a) the fine model (FM), and (b) the upscaled coarse model (CMR) for the intersection parallel to the wells

use volume weighted averaging. The discretization levels in the coarse grid are 20, 10 and 4 in the  $x$ -,  $y$ - and  $z$ -directions, respectively. Thus, there is a total of 800 cells, each of size  $100 \times 100 \times 5$  m, which is the typical size of a simulation cell. Before upscaling, each coarse cell is mirrored in the  $x$ -direction. The wells in the coarse grid are placed at the same location as in the fine grid. Hereafter, we denote the coarse model by CM and the fine model by FM. Figure 12 shows profile views of the horizontal permeability for these two models. With this setup one would expect numerical dispersion due to the coarser discretization. To overcome this, we have also created a fine grid model with parameters taken from the coarse model. We denote this model the coarse model refined (CMR). For all simulations on FM we use relative permeability curves and capillary pressure curves taken from the original field model. For CM and CMR we use relative permeability upscaled in either CL or VL, and denote these realizations by CM CL, CM VL, CMR CL and CMR VL, respectively. In the VL cases, we disregard capillary forces by setting  $p_c = 0$ , while we use the upscaled capillary pressure curves produced by CL upscaling for the CL cases.

We focus our attention on two different injection rates, 20 and 200  $\text{m}^3/\text{day}$  (standard cubic meter per day). The corresponding differences in well pressures at water breakthrough for the different models are listed in Table 4. An injection rate of 200  $\text{m}^3/\text{day}$  corresponds to an average water front velocity of  $\sim 1.2$  ft/day, which is quite typical. Furthermore, the average pressure drop over each coarse cell is about  $1.4 \cdot 10^6$  Pa. Figure 13 shows a scatter plot of the macroscopic capillary number,  $\mathcal{N}$ , for all coarse cells with  $\Delta p = 1.4 \cdot 10^6$  Pa. For the majority of the coarse cells,  $\mathcal{N}$  is in the range [1, 4]. We can neither neglect capillary nor viscous forces based on these results, but they indicate stronger viscous forces than capillary forces. For an injection rate of 20  $\text{m}^3/\text{day}$ ,  $\mathcal{N}$  is about ten times lower, so we expect relatively stronger capillary forces.

**Table 4** Difference in well pressure (in bar) at water breakthrough for different models and at two different injection rates

	FM	CMR CL	CMR VL	CM CL	CM VL
20 m <sup>3</sup> /day	9.5	10.0	11.0	11.5	13.0
200 m <sup>3</sup> /day	101.0	99.0	111.0	114.0	128.0

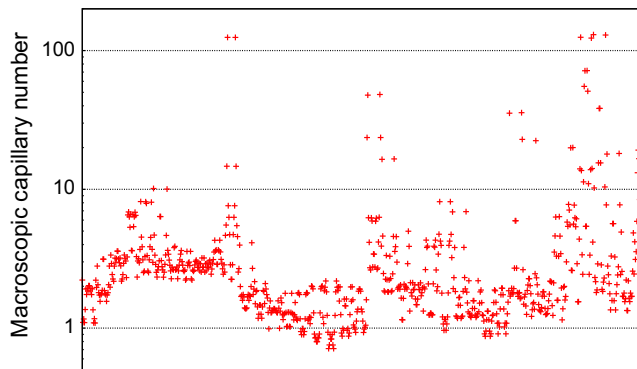
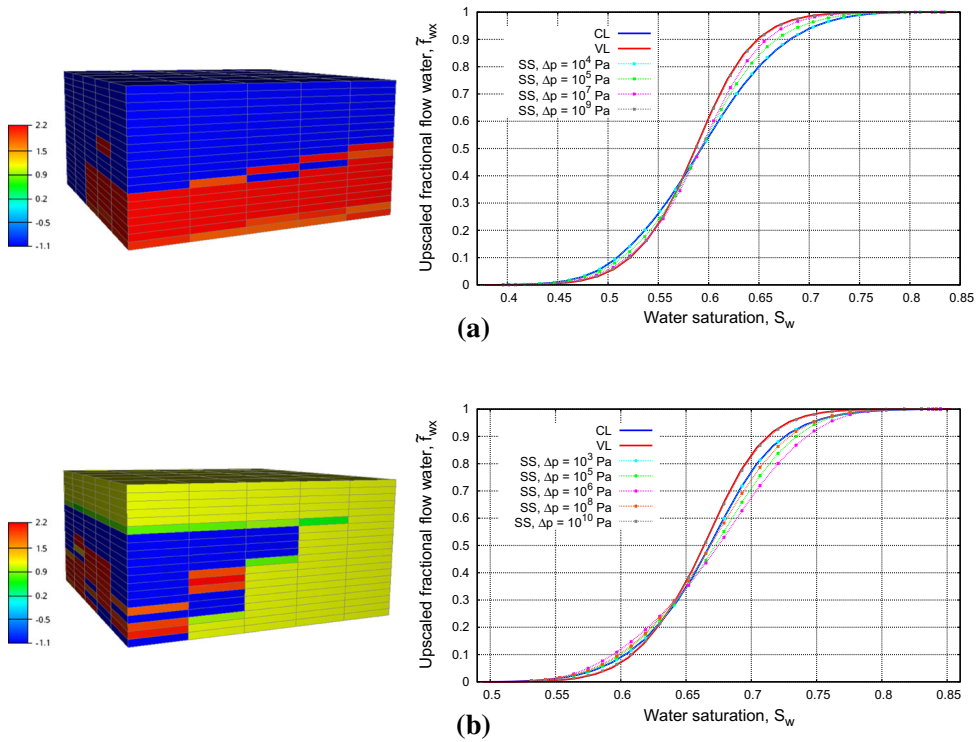
**Fig. 13** Scatter plot of the macroscopic capillary numbers  $\mathcal{N}$  for all 800 coarse cells in the simulation model. A pressure drop of 14 bar =  $1.4 \times 10^6$  Pa is used over each cell

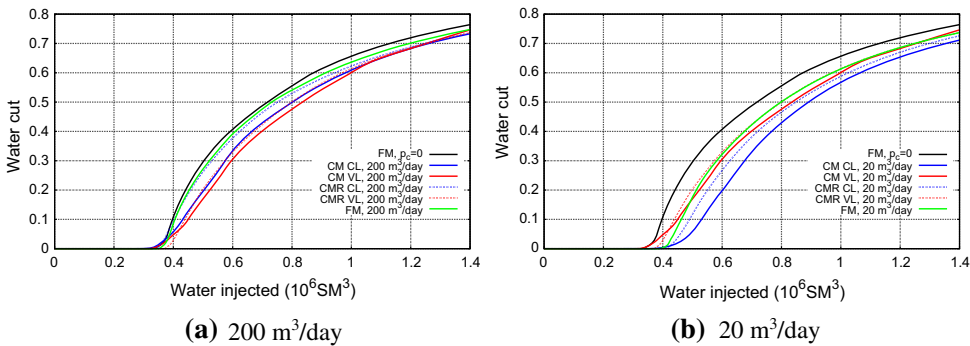
Figure 14 displays two coarse cells and their corresponding upscaled fractional flow curves. The results in Fig. 14a illustrate typical upscaled curves for the cells in the flooded region between the wells. This indicates rate sensitivity in individual coarse cells. Note that there are also cells where the rate sensitivity is less, typically in nearly homogeneous cells. Figure 14b is an example of a representative submodel where the convergence from CL to VL is not monotone. This model contains high permeability rock that only barely percolates. Compared to the results for the synthetic model with a barrier (Fig. 3c), this might explain the nonmonotonic convergence.

Before moving to the actual simulations, we make a comment on the rate dependency of the solution. Since we have an incompressible system, and if we disregard capillary forces, the water cut as function of injected water is independent on the injection rate. Specially, this means that if we use the VL approach, then all results will coincide. This motivates why we choose to plot the water cut against water injected. After all, in an incompressible system, water injected is simply time scaled by the rate.

In Fig. 15 the water cut at the producer is plotted for different models. We have also included the FM case with  $p_c = 0$ , representing the viscous limit scenario. When the injection rate is 200 m<sup>3</sup>/day (Fig. 15a), the FM result is close to the viscous limit (FM,  $p_c = 0$ ). Simulations (not shown here) indicate that capillary forces are negligible for flow rates above 50 m<sup>3</sup>/day for FM. For an injection rate of 200 m<sup>3</sup>/day the net effect of relative permeability upscaling is small, especially for the CMR cases. The difference between CL and VL upscaling is bigger when the injection rate is 20 m<sup>3</sup>/day. This is due to increased capillary forces in the model. The difference between CM and CMR is small for the VL cases. For CL upscaling the difference is bigger, and CMR gives a better match with the reference solution. This might imply that for our model the upgridding effect is more prominent in CL upscaling. For all cases, we get earlier water breakthrough for CM compared to CMR due to numerical dispersion.

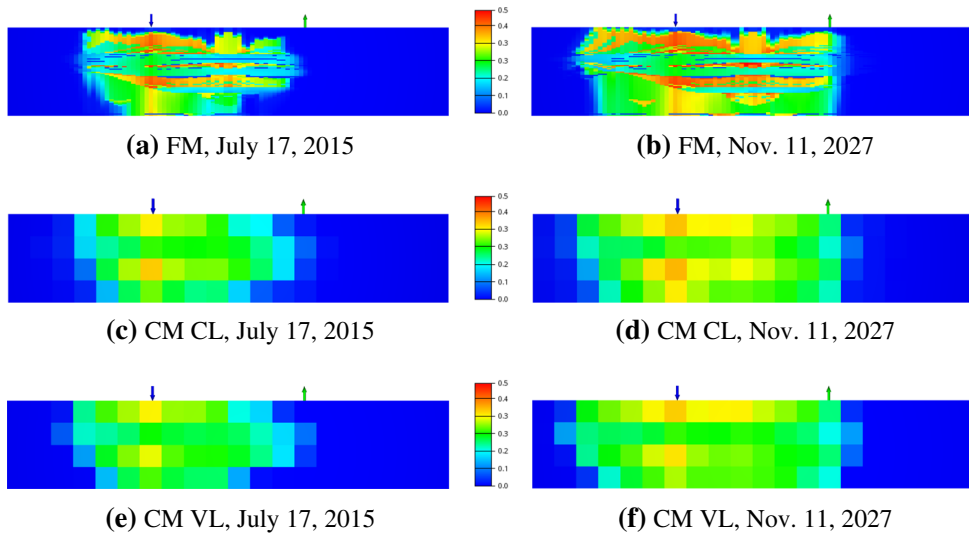


**Fig. 14** Two coarse cells from the simulation model (Fig. 12) and their upscaled fractional flow function,  $\tilde{f}_w$ , in CL and VL, and for rate-dependent flow (SS). The coloring in the left figures displays the horizontal permeability on a logarithmic scale. The cells belong to the flooded interwell region and the global flow direction is from left to right

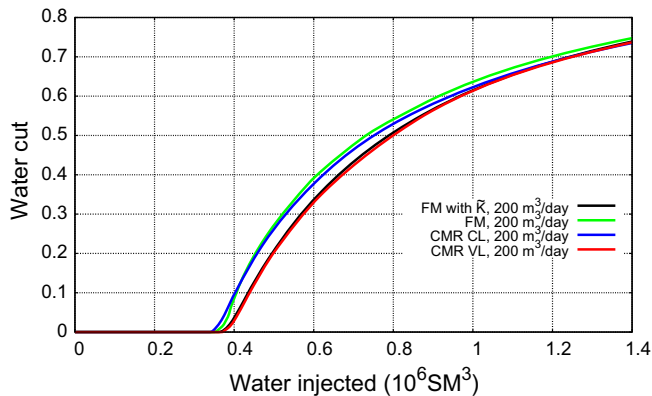


**Fig. 15** Water cut at producer as function water injected when the injection rate is  $200 \text{ m}^3/\text{day}$  (a), and  $20 \text{ m}^3/\text{day}$  (b). Results for FM, CM and CMR are shown. On the two latter we use upscaled data both in CL and in VL. A FM case with  $p_c = 0$  is also included

If we employ the theory of Welge (1952) for one-dimensional immiscible viscous displacement on the upscaled fractional flow curves in Fig. 14, we would expect earlier water breakthrough for the VL case compared to the CL case. In the viscous dominated case (Fig. 15a) the water breakthrough is similar for all cases. This might imply that the net effect of the rate sensitivity in individual coarse grid cells is small or that the theory of Welge is not appropriate for this scenario.



**Fig. 16** Difference in water saturation,  $S_w(\mathbf{x}, t) - S_w(\mathbf{x}, 0)$ , for three simulation cases at two different times and with injection rates equal to  $200 \text{ m}^3/\text{day}$ . The start date for the simulations is October 1, 2010. The results are displayed in the plane parallel to the wells

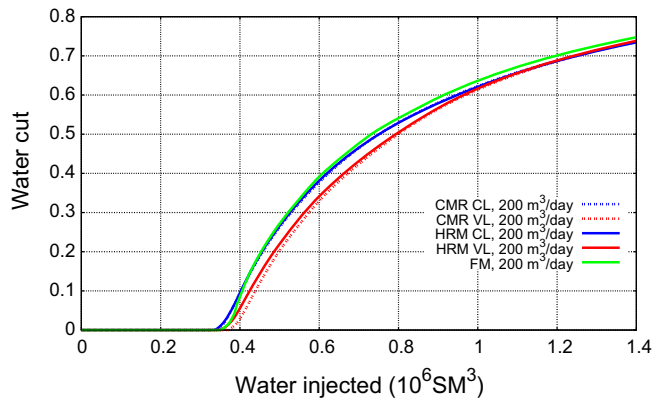


**Fig. 17** Water cut at producer as function of water injected when the injection rate is  $200 \text{ m}^3/\text{day}$ . Here we compare FM, CMR CL and CMR VL with the results from a fine model simulation where only permeability, porosity and critical saturations are upscaled (denoted FM with  $\tilde{K}$ )

Figure 16 shows, at two different times, the difference in water saturation,  $S_w(\mathbf{x}, t) - S_w(\mathbf{x}, 0)$ , for the three models FM, CM CL and CM VL. The coarse models are not able to capture all fine-scale variations, but the water front and the main characteristics are fairly close. There are only minor differences between the CL and VL cases visible from this figure.

To study the relative importance of permeability upscaling compared to relative permeability upscaling, the fine model was run with upscaled porosity, permeability and irreducible saturation, see Fig. 17 (denoted FM with  $\tilde{K}$ ). For this case we only compare with CMR to remove upgridding effects. We see that FM with  $\tilde{K}$  is almost identical to CMR VL, but differs from CMR CL. This is in accordance with the small capillary forces in the model and indicates that VL upscaling works fairly well. Furthermore, for this model it seems like CL upscaling works as a fortunate correction to the error introduced by permeability upscaling. This example also demonstrates that permeability upscaling is a significant source of error





**Fig. 18** Water cut at producer as function of water injected when the injection rate is  $200 \text{ m}^3/\text{day}$ . Results for the fine model (FM), the coarse model refined (CMR) and the homogeneous relative permeability model (HRM) are shown. On the two latter models we use upscaled data, both in CL and in VL

in the upscaled model. However, the CL case shows that relative permeability upscaling is about equally important.

Finally, consider CMR, but now with homogeneous relative permeability calculated by upscaling the whole model as one bulk, both in CL and in VL. All parameters other than relative permeability and capillary pressure are equal to those used in CMR. We denote this model by the homogeneous relative permeability model (HRM). In Fig. 18 the water cut for these scenarios with an injection rate of  $200 \text{ m}^3/\text{day}$  is shown together with the results from CMR and FM. We observe that the results do not differ significantly. This example illustrates that it might be possible to use homogeneous relative permeability.

## 6 Discussion and Conclusions

Steady-state upscaling has been studied on representative three-dimensional models. The correctness of the implemented upscaling procedures was demonstrated by comparing with analytic upscaling results in the capillary and viscous limits. We have further demonstrated that the general steady-state solution converges toward the capillary limit solution as the flow rate tends to zero, and conversely, that it converges toward the viscous limit solution, defined by constancy in fractional flow, as the flow rate increases. This holds for all models we have considered, except for flow along layers with periodic boundary conditions. The convergence may fail to be monotonic for some models, in accordance with results in [Virnovsky et al. \(2004\)](#). The transition from the capillary to the viscous limit solution is shown to occur over several orders of magnitude of the flow rate (or equivalently pressure drop). This substantiate the need for rate-dependent steady-state upscaling in a wide range of flow scenarios.

Numerical examples demonstrate that it is of great importance whether the model contains high permeability rock with poor connectivity. If this is present, the convergence from the capillary to viscous limit may fail to be monotonic.

A *static* dimensionless capillary number that models the force balance for *transient* flow can only be approximate. Still, our proposed scale-dependent capillary number,  $\mathcal{N}$ , gives values close to 1 in the transition from capillary to viscous dominated flow for a wide range of models. It is thus much more suitable for this purpose than the traditional (microscopic)



capillary number, Ca. Furthermore, it takes length scale into account, and it is robust and easy to calculate.

We have demonstrated that steady-state upscaling is dependent on the choice of boundary conditions (BCs). However, for the realistic section models considered here, the differences were modest. The flow rate is of much greater importance. In the capillary and viscous limits, and with a periodic reservoir model, the results are the same for these two sets of BCs. It should be noted that the differences probably would have been larger if we had considered fully periodic BCs, so that also the boundaries normal to the pressure drop direction are periodic. This is most prominent for models with layers not aligned with the global flow direction. Fully periodic BCs would furthermore produce a full upscaled tensor. An advantage of periodic BCs is that the upscaled saturation is the same at steady state as it was initially. Thus, it is easy to get upscaled relative permeabilities for a uniform distribution of upscaled saturations. One drawback with periodic BCs is that the flow rate can be significantly reduced if the model is not periodic. This is why we have chosen to always mirror the models.

Through the REV analysis for the fluvial reservoir models considered herein, we were able to identify an REV for porosity. This is in accordance with similar results in Nordahl et al. (2014). However, we were not able to identify any REV for relative permeability. This suggests that one should use unique upscaled relative permeabilities for each coarse cell.

Simulations on the reservoir scale illustrated that our model is viscous dominated for reasonable injection rates. This was also supported by our macroscopic capillary number. Taking into account the effect of permeability upscaling, viscous limit upscaling seems to be appropriate in this viscous dominated scenario.

**Acknowledgments** The research is funded by VISTA—a basic research program funded by Statoil, conducted in close collaboration with The Norwegian Academy of Science and Letters. The authors thank Statoil for giving permission to publish this work. The authors also want to thank Atgeirr Flø Rasmussen, Bård Skaflestad and Halvor Møll Nilsen, SINTEF ICT, and Håvard Berland, Statoil, for support and development of the upscaling routines in OPM, and Sindre Hilden, NTNU and SINTEF ICT, for helpful discussions. Finally, the authors are grateful for the thorough and constructive feedback from the Reviewers, which have helped to improve this paper.

**Open Access** This article is distributed under the terms of the Creative Commons Attribution 4.0 International License (<http://creativecommons.org/licenses/by/4.0/>), which permits unrestricted use, distribution, and reproduction in any medium, provided you give appropriate credit to the original author(s) and the source, provide a link to the Creative Commons license, and indicate if changes were made.

## References

- Aarnes, J.E., Kippe, V., Lie, K.-A., Rustad, A.B.: Modelling of multiscale structures in flow simulations for petroleum reservoirs. In: Geometric Modelling, Numerical Simulation, and Optimization, pp. 307–360. Springer (2007)
- Bear, J.: Dynamics of fluids in porous media. American Elsevier, Amsterdam (1972)
- Brezzi, F., Lipnikov, K., Shashkov, M.: Convergence of the mimetic finite difference method for diffusion problems on polyhedral meshes. *SIAM J Numer Anal* **43**(5), 1872–1896 (2005)
- Chavent, G., Jaffre, J.: Mathematical Models and Finite Elements for Reservoir Simulation Single Phase, Multiphase and Multicomponent Flows through Porous Media. Elsevier, Amsterdam (1986)
- Dale, M., Ekran, S., Mykkeltveit, J., Virnovsky, G.: Effective relative permeabilities and capillary pressure for one-dimensional heterogeneous media. *Transp. Porous Media* **26**(3), 229–260 (1997)
- Dullien, F.A.L.: Porous media: fluid transport and pore structure. Academic press, Waltham (1992)
- Durlofsky, L.J.: Upscaling and gridding of fine scale geological models for flow simulation. In: 8th International Forum on Reservoir Simulation, Iles Borromees (2005)
- Ekran, S., Aasen, J.O.: Steady-state upscaling. *Transp. Porous Media* **41**(3), 245–262 (2000)

- Ekrann, S., Dale, M., Langaas, K., Mykkeltveit, J.: Capillary limit effective two-phase properties for 3D media. In: European 3-D Reservoir Modelling Conference, Society of Petroleum Engineers, Stavanger. pp. 119–129 (1996)
- Jonoud, S., Jackson, M.D.: New criteria for the validity of steady-state upscaling. *Transp. Porous Media* **71**(1), 53–73 (2008)
- Kløv, T., Øren, P.E., Stensen, J.Å., Lerdahl, T.R., Berge, L.I., Bakke, S., Boassen, T., Virnovsky, G.: Pore-to-field scale modeling of WAG. In: SPE Annual Technical Conference and Exhibition, Denver. pp. 5–8 (2003)
- Kumar, A., Farmer, C.L., Jerauld, G.R., Li, D.: Efficient upscaling from cores to simulation models. In: SPE Annual Technical Conference and Exhibition, San Antonio. pp. 257–272 (1997)
- Kumar, A.T.A., Jerauld, G.R.: Impacts of scale-up on fluid flow from plug to gridblock scale in reservoir rock. In: SPE/DOE Improved Oil Recovery Symposium (Tulsa, Oklahoma), Society of Petroleum Engineers (1996)
- Kyte, J.R., Berry, D.W.: New Pseudo functions to control numerical dispersion. *SPE J.* **15**(04), 269–276 (1975)
- Lake, L.W.: Enhanced Oil Recovery, 2010th edn. Society of Petroleum Engineers, Dallas (1989)
- Lerdahl, T.R., Rustad, A.B., Theting, T., Stensen, J.Å., Øren, P.E., Bakke, S., Boassen, T., Palatnik, B.: Pore-to-field-scale multi-phase upscaling for IOR. In: 67th EAGE Conference & Exhibition, Madrid. (2005)
- Lohne, A., Virnovsky, G.A., Durlinsky, L.J.: Two-stage upscaling of two-phase flow: from core to simulation scale. *SPE J.* **11**(03), 304–316 (2006)
- Morrow, N.R., Chatzis, I., Taber, J.J.: Entrapment and mobilization of residual oil in bead packs. *SPE Reserv. Eng.* **3**(03), 927–934 (1988)
- Nordahl, K., Messina, C., Berland, H., Rustad, A.B., Rimstad, E.: Impact of multiscale modelling on predicted porosity and permeability distributions in the fluvial deposits of the Upper Lunde Member (Snorre Field, Norwegian Continental Shelf), vol. 387, Geological Society of London. <http://sp.lyellcollection.org/content/387/1/85.short> (2014)
- Peaceman, D.W.: Interpretation of well-block pressures in numerical reservoir simulation with nonsquare grid blocks and anisotropic permeability. *SPE J.* **23**(03), 531–543 (1983)
- Pickup, G., Ringrose, P.S., Sharif, A.: Steady-state upscaling: from Lamina-scale to full-field model. *SPE J.* **5**(02), 208–217 (2000)
- Pickup, G.E., Stephen, K.D.: An assessment of steady-state scale-up for small-scale geological models. *Pet. Geosci.* **6**(3), 203–210 (2000)
- Rustad, A.B., Theting, T.G., Held, R.J.: Pore space estimation, upscaling and uncertainty modelling for multiphase properties. In: Proceedings of SPE Symposium on Improved Oil Recovery, Society of Petroleum Engineers. <https://www.onepetro.org/conference-paper/SPE-113005-MS> (2008)
- Smith, E.H.: The influence of small-scale heterogeneity on average relative permeability. In: Lake, L. W., Carroll, H. B., Wesson, T. C. (eds.) Reservoir Characterization II. Academic Press, Waltham (1991)
- Virnovsky, G.A., Friis, H.A., Lohne, A.: A steady-state upscaling approach for immiscible two-phase flow. *Transp. Porous Media* **54**(2), 167–192 (2004)
- Welge, H.J.: A simplified method for computing oil recovery by gas or water drive. *J. Pet. Technol.* **4**(04), 91–98 (1952)
- Zhang, P., Pickup, G.E., Christie, M.A.: A new method for accurate and practical upscaling in highly heterogeneous reservoir models. In: International Oil and Gas Conference and Exhibition, Society of Petroleum Engineers, Beijing (2006)



## Paper II

### **Postprocessing of non-conservative flux for compatibility with transport in heterogeneous media**

Odsæter, L.H., Wheeler, M.F., Kvamsdal, T., and Larson, M.G.

*Computer Methods in Applied Mechanics and Engineering*, 315:799–830, 2017





Available online at [www.sciencedirect.com](http://www.sciencedirect.com)

ScienceDirect

Comput. Methods Appl. Mech. Engrg. 315 (2017) 799–830

Computer methods  
in applied  
mechanics and  
engineering

[www.elsevier.com/locate/cma](http://www.elsevier.com/locate/cma)

## Postprocessing of non-conservative flux for compatibility with transport in heterogeneous media

Lars H. Odsæter<sup>a,\*</sup>, Mary F. Wheeler<sup>b</sup>, Trond Kvamsdal<sup>a</sup>, Mats G. Larson<sup>c</sup>

<sup>a</sup> Department of Mathematical Sciences, NTNU Norwegian University of Science and Technology, Alfred Getz' vei 1, 7491 Trondheim, Norway

<sup>b</sup> The Institute for Computational Engineering and Sciences, The University of Texas at Austin, Austin, TX 78712, USA

<sup>c</sup> Department of Mathematics and Mathematical Statistics, Umeå University, SE-901 87 Umeå, Sweden

Received 11 May 2016; received in revised form 9 November 2016; accepted 10 November 2016

Available online 23 November 2016

---

### Highlights

- Present an order-preserving algorithm to postprocess non-conservative fluxes on a wide range of grids.
- Add a piecewise constant correction term that is minimized in a weighted  $L^2$  norm.
- Application of a weighted norm appears to give better results for high contrasts in permeability.
- Study both steady-state and dynamic flow models.
- Solve coupled flow and transport problem to demonstrate effect of postprocessing.

---

### Abstract

A conservative flux postprocessing algorithm is presented for both steady-state and dynamic flow models. The postprocessed flux is shown to have the same convergence order as the original flux. An arbitrary flux approximation is projected into a conservative subspace by adding a piecewise constant correction that is minimized in a weighted  $L^2$  norm. The application of a weighted norm appears to yield better results for heterogeneous media than the standard  $L^2$  norm which has been considered in earlier works. We also study the effect of different flux calculations on the domain boundary. In particular we consider the continuous Galerkin finite element method for solving Darcy flow and couple it with a discontinuous Galerkin finite element method for an advective transport problem.

© 2016 The Authors. Published by Elsevier B.V. This is an open access article under the CC BY-NC-ND license (<http://creativecommons.org/licenses/by-nc-nd/4.0/>).

**Keywords:** Postprocessing; Local conservation; Galerkin FEM; Darcy flow; Advective transport

---

\* Corresponding author.

E-mail address: [lars.odsater@math.ntnu.no](mailto:lars.odsater@math.ntnu.no) (L.H. Odsæter).

## 1. Introduction

In this paper we consider the following coupled flow and transport problem that arise in porous media:

$$\partial_t(\beta p) - \nabla \cdot (\mathbf{K}\nabla p) = q, \quad (1.1)$$

$$\partial_t(\phi c) + \nabla \cdot (c\mathbf{u} - \mathbf{D}\nabla c) = f. \quad (1.2)$$

Eq. (1.1), often referred to as the Darcy flow equation, governs conservation of mass for a slightly compressible single-phase fluid in a porous media. Here  $p$  represents pressure and  $\mathbf{u} = -\mathbf{K}\nabla p$  the Darcy velocity. The second equation (1.2) is known as the transport equation, and describes advective and diffusive transport of a concentration  $c$ . Such transport models are employed in modeling tracers in a porous media [1]. Choosing compatible numerical solvers for the flow and transport equations may be of importance for accuracy, stability and conservation properties [2]. Here we discuss using a continuous Galerkin (CG) finite element method for the flow equation and apply a postprocessing method to compute fluxes on element boundaries to obtain local conservation. A discontinuous Galerkin (DG) finite element method with upwinding is employed for the transport equation [3,4]. DG allows for discontinuities in the solution and has the advantages of local mass conservation, less numerical diffusion, favorable h- and p-refinement, handling of discontinuous coefficients, and efficient implementation.

CG is a well-developed numerical discretization for partial differential equations. It is numerically efficient for problems requiring dynamic grid adaptivity. It is known that CG requires postprocessing to obtain locally conservative fluxes on element boundaries [5–15]. This has been the topic also for studies of environmental modeling in bays and estuaries where CG has been employed for shallow water equations [16]. Applying non-conservative flux to the transport equation may result in non-physical concentration solutions [17,18,13].

Computing fluxes for CG models has been considered in many technical papers; we briefly describe some well known results and note that the list is incomplete. Optimal postprocessing of fluxes on element boundaries for one-dimensional problems was studied by Wheeler [19] and generalized by Dupont [20]. Douglas et al. [21] analyzed methods for approximating fluxes on the domain boundary for multi-dimensional problems based on the approach of J. Wheeler [22]. Postprocessing of locally conservative (or self-equilibrated) fluxes on element boundaries for multi-dimensional problems was studied by Ladeveze and Leguillon [23] for error estimation purposes. Ainsworth and Oden [5] proved the existence of such self-equilibrated fluxes for general CG methods including 1-irregular meshes with hanging nodes. Superconvergence of recovered gradients of linear CG approximations for elliptic and parabolic problems was treated by Wheeler and Whiteman [24,25].

For completeness we mention alternative schemes to CG for the pressure equation; mixed finite element methods [26], dual-grid and control volume methods [27], finite volume methods [28], mimetic finite difference methods [29], and DG [30]. All of these are conservative in the sense that they either are formulated in a mixed form so that locally conservative fluxes are obtained directly without the need for *any* postprocessing, or have an embedded local conservation statement in their derivation so that locally conservative fluxes can be calculated in a straightforward manner from the pressure solution. Recent papers [12,14] have observed that CG with postprocessing on the dual grid is more robust than standard control volume approaches. Here the postprocessing involves only local calculations. It is well known that for Laplace's equation, control volume and CG on the dual grid are equivalent. Lack or complexity of dynamic grid adaptivity is a disadvantage for many of the methods mentioned above. DG is promising both with respect to local conservation and dynamic grid adaptivity, but is computationally costly due to a high number of degrees of freedom. A conservative scheme based on enrichment of CG was proposed by [17] for elliptic problems and later extended to parabolic equations in [18].

The postprocessing method we propose in this paper is built upon the work of Sun and Wheeler [10] and Larson and Niklasson [9] for the steady-state flow model (Eq. (1.1) with  $\beta = 0$ ). Both of these papers present an algorithm for computing conservative fluxes on element boundaries. Here a given general non-conservative flux approximation is modified by adding piecewise constant corrections which are minimized in a given norm. The minimization requirement ensures that the postprocessed flux has the same order of convergence as the original flux. The works by [10] and [9] have strong similarities and are in fact identical under some specific choice of parameters, but have been formulated differently. While a variational formulation is used in [9], the method is presented elementwise in [10]. In this paper we present both and demonstrate the relationship between the two results. We mention that these postprocessing methods have been applied in a series of recent works [31–34].

The main novelties of our work compared to [10] and [9] are summarized below.

- The correction term is minimized in a weighted  $L^2$  norm instead of the standard  $L^2$  norm. This gives control of which faces should be weighted most. Our choice of weights corresponds to the inverse of the effective face permeability. This is shown to better preserve low permeable interfaces.
- Our method applies to a wide range of grids, including non-conforming and unstructured grids, in contrast to [10].
- The method is applied to the time dependent flow model (Eq. (1.1) with  $\beta \neq 0$ ).
- We solve the coupled problem (1.1)–(1.2) to demonstrate the importance of locally conservative flux and to illustrate the effect of some parameters of our postprocessing method.

The presented method is general in the sense that it takes as input any flux approximation, not restricted to non-conservative flux from classical CG, but may also originate from other numerical schemes, e.g. isogeometric finite elements [35], or even measurements. We remark that our method only produces conservative fluxes on element boundaries. To extend the flux to a velocity field on the element interiors one can set up a localized mixed finite element problem on each element, see [10]. We also point out that minimizing in a weighted norm was considered in [36] in an upscaling framework. However, our presentation includes error analysis, and we also study the impact of weighting on the transport problem. An alternative approach to preserve low permeable interfaces is to add a penalization step to correct the postprocessed flux [37].

This paper is outlined as follows. Section 2 provides some preliminaries, including the model equations, notational comments, conservation conditions, and discretization schemes for CG and DG. Next, in Section 3, we go into details of the postprocessing method, first for the time independent case and later extended to the general case. We formulate our approach based on a discrete divergence operator and its left inverse. Furthermore, we prove an error estimate and discuss some parameters of our method. In Section 4 we demonstrate our method with some numerical examples. Finally, in Section 5, we conclude this work.

## 2. Preliminaries

### 2.1. Model equations

We consider a coupled flow and transport problem in a bounded domain  $\Omega \subset \mathbb{R}^d$  ( $d = 2, 3$ ) and in the time interval  $[0, T]$ ,  $T > 0$ .

*Flow Equation.* For flow, we consider the linear parabolic problem

$$\partial_t(\beta p) - \nabla \cdot (\mathbf{K} \nabla p) = q, \quad (\mathbf{x}, t) \in \Omega \times (0, T]. \tag{2.1}$$

The unknown variable is the pressure  $p$ , from which the velocity  $\mathbf{u}$  is defined by  $\mathbf{u} = -\mathbf{K} \nabla p$ . The conductivity  $\mathbf{K} = \mathbf{K}(\mathbf{x})$  is the ratio between permeability and viscosity, and  $\mathbf{K}$  is assumed to be symmetric positive definite and bounded from below and above. Furthermore,  $\beta = \beta(\mathbf{x}, t)$  is a positive coefficient and  $q = q(\mathbf{x}, t)$  is a source term. In the case  $\beta = 0$ , the flow equation is elliptic and stationary. Throughout this paper we let  $\mu = 1$  for simplicity and will use the terms conductivity and permeability interchangeably.

The domain boundary  $\partial\Omega$  is divided into a Dirichlet part,  $\Gamma_D$ , and a Neumann part,  $\Gamma_N$ , such that  $\overline{\Gamma_D} \cup \overline{\Gamma_N} = \overline{\partial\Omega}$  and  $\Gamma_D \cap \Gamma_N = \emptyset$ . The boundary and initial conditions are

$$p = p_B, \quad (\mathbf{x}, t) \in \Gamma_D \times (0, T], \tag{2.2a}$$

$$\mathbf{u} \cdot \mathbf{n} = -\mathbf{K} \nabla p \cdot \mathbf{n} = u_B, \quad (\mathbf{x}, t) \in \Gamma_N \times (0, T], \tag{2.2b}$$

$$p = p_0, \quad (\mathbf{x}, t) \in \Omega \times \{0\}, \tag{2.2c}$$

where  $\mathbf{n}$  is the outward unit normal vector on  $\partial\Omega$  and  $p_B = p_B(\mathbf{x}, t)$ ,  $u_B = u_B(\mathbf{x}, t)$  and  $p_0 = p_0(\mathbf{x})$  are known functions.

*Transport Equation.* The model equation for transport is the time dependent advection–diffusion equation,

$$\partial_t(\phi c) + \nabla \cdot (\mathbf{u}c - \mathbf{D} \nabla c) = f, \quad (\mathbf{x}, t) \in \Omega \times (0, T]. \tag{2.3}$$

The unknown variable is the concentration  $c$ . Furthermore,  $\phi = \phi(\mathbf{x})$  is the porosity (fraction of void volume) and  $\mathbf{D} = \mathbf{D}(\mathbf{x}, c)$  is the diffusion/dispersion tensor. The right hand side  $f = f(\mathbf{x}, t)$  is a source term, and when coupled



with the flow equation (2.1), it is usually interpreted as  $f = qc^*$ , where  $c^*$  denotes the upstream concentration, so that

$$qc^* = \begin{cases} qc, & \text{if } q \leq 0, \\ qc_w, & \text{if } q > 0, \end{cases} \tag{2.4}$$

where  $c_w = c_w(\mathbf{x}, t)$  denotes the source (well) concentration.

The boundary is divided into an inflow boundary,  $\Gamma_{in} = \{\mathbf{x} \in \partial\Omega : \mathbf{u} \cdot \mathbf{n} < 0\}$ , and an outflow/no-flow boundary,  $\Gamma_{out} = \{\mathbf{x} \in \partial\Omega : \mathbf{u} \cdot \mathbf{n} \geq 0\}$ . Let  $c_B = c_B(\mathbf{x}, t)$  denote the inflow concentration on  $\Gamma_{in}$  and  $c_0 = c_0(\mathbf{x})$  the initial concentration. The boundary and initial conditions are given as

$$(\mathbf{u}c - \mathbf{D}\nabla c) \cdot \mathbf{n} = c_B \mathbf{u} \cdot \mathbf{n}, \quad (\mathbf{x}, t) \in \Gamma_{in} \times (0, T], \tag{2.5a}$$

$$(-\mathbf{D}\nabla c) \cdot \mathbf{n} = 0, \quad (\mathbf{x}, t) \in \Gamma_{out} \times (0, T], \tag{2.5b}$$

$$c = c_0, \quad (\mathbf{x}, t) \in \Omega \times \{0\}. \tag{2.5c}$$

In this work, we will focus on advection dominated flow and disregard diffusion by setting  $\mathbf{D} = 0$ .

### 2.2. Notation

*Discretization of the Domain.* Let  $\mathcal{E}_h$  be a partition of  $\Omega$  into triangles or quadrilaterals ( $d = 2$ ), or tetrahedra, prisms or hexahedra ( $d = 3$ ). We denote by  $E_i \in \mathcal{E}_h$ , for  $i = 1, 2, \dots, N$ , the  $N$  elements of the partition, and let  $h_i$  be the diameter of  $E_i$ . We assume  $\mathcal{E}_h$  to be regular in the sense that all elements are convex and that there exists  $\rho > 0$  such that each element  $E_i$  contains a ball of radius  $\rho h_i$  in its interior. Furthermore,  $\mathcal{E}_h$  should be quasi-uniform, i.e., there is a  $\tau > 0$  such that  $\frac{h_i}{h_j} \leq \tau$  for all  $E_i, E_j \in \mathcal{E}_h$ , where  $h$  is the maximum diameter of all elements. Notice that we allow for elements of mixed type and non-matching grids (hanging nodes).

We denote by  $\mathcal{F}_{h,I}$  the set of all interior edges ( $d = 2$ ) or faces ( $d = 3$ ), i.e.,

$$\mathcal{F}_{h,I} = \{F \in \mathbb{R}^{d-1} : F = E_i \cap E_j, E_i \in \mathcal{E}_h, E_j \in \mathcal{E}_h, E_i \neq E_j\}. \tag{2.6}$$

For simplicity we only use the term face in the following. Furthermore, we define  $\mathcal{F}_{h,B}$  as the set of all element faces that intersect with  $\partial\Omega$ . We assume that each face in  $\mathcal{F}_{h,B}$  is either completely on the Dirichlet or Neumann part of the boundary, such that  $\mathcal{F}_{h,B}$  can be decomposed into  $\mathcal{F}_{h,D}$  and  $\mathcal{F}_{h,N}$ , i.e., the sets of faces on the Dirichlet and Neumann boundary, respectively. Analogously, let  $\mathcal{F}_{h,out}$  and  $\mathcal{F}_{h,in}$  be the sets of faces on  $\mathcal{F}_{out}$  and  $\mathcal{F}_{in}$ , respectively. Next, let  $\mathcal{F}_h = \mathcal{F}_{h,I} \cup \mathcal{F}_{h,B}$ . For each face  $F \in \mathcal{F}_h$  we choose a unit normal vector  $\mathbf{n}_F$ .<sup>1</sup> The unit normal vector on  $F \in \mathcal{F}_{h,B}$  is chosen to coincide with the outward unit normal vector. Furthermore,  $\mathbf{n}_E$  denotes the unit normal vector pointing out of  $E$ , such that  $\mathbf{n}_E|_F = \pm \mathbf{n}_F$ .

*Piecewise Polynomial Spaces.* Let  $P_r(\mathcal{E}_h)$  be the space of piecewise polynomial functions of degree  $r$ ,

$$P_r(\mathcal{E}_h) = \{\varphi \in L^2(\Omega) : \varphi|_E \in \mathcal{Q}_r(E), E \in \mathcal{E}_h\}, \tag{2.7}$$

where  $\mathcal{Q}_r$  denotes the tensor product of polynomial spaces of degree less than or equal to  $r$  in each spatial direction.<sup>2</sup> We also need the continuous subspace of  $P_r(\mathcal{E}_h)$ ,

$$P_r^C(\mathcal{E}_h) = P_r(\mathcal{E}_h) \cap C(\Omega). \tag{2.8}$$

Furthermore, we define the space of piecewise polynomial functions on element faces as

$$P_r(\mathcal{F}_h) = \{\varphi \in L^2(\mathcal{F}_h) : \varphi|_F \in \mathcal{Q}_r(F), F \in \mathcal{F}_h\}. \tag{2.9}$$

Moreover, let  $P_r^0(\mathcal{F}_h)$  denote the subspace of  $P_r(\mathcal{F}_h)$  whose functions are zero on the Neumann boundary,

$$P_r^0(\mathcal{F}_h) = \{\varphi \in P_r(\mathcal{F}_h) : \varphi|_F = 0, F \in \mathcal{F}_{h,N}\}. \tag{2.10}$$

<sup>1</sup> This can be done by choosing  $\mathbf{n}_F$  to coincide with the outward unit normal of the element with lowest element number.

<sup>2</sup> To be rigorous,  $\mathcal{Q}_r$  is the space of functions such that when mapped to the reference element are polynomials of degree  $r$ .

**Inner Products and Norms.** We denote by  $(\cdot, \cdot)_S$  the standard  $L^2$  inner product over a domain  $S \in \mathbb{R}^d$ , or  $\langle \cdot, \cdot \rangle_S$  if  $S \in \mathbb{R}^{d-1}$ . The standard  $L^2$  norm over  $S$  is denoted  $\|\cdot\|_S$ . If  $S = \Omega$ , we write  $(\cdot, \cdot)$  or  $\|\cdot\|$  for simplicity. Furthermore, define the broken inner products and norms

$$(v, w)_{\mathcal{E}_h} = \sum_{E \in \mathcal{E}_h} (v, w)_E, \quad \|v\|_{\mathcal{E}_h}^2 = (v, v)_{\mathcal{E}_h} = \sum_{E \in \mathcal{E}_h} \|v\|_E^2, \tag{2.11}$$

$$\langle v, w \rangle_{\mathcal{F}_h} = \sum_{F \in \mathcal{F}_h} \langle v, w \rangle_F, \quad \|v\|_{\mathcal{F}_h}^2 = \langle v, v \rangle_{\mathcal{F}_h} = \sum_{F \in \mathcal{F}_h} \|v\|_F^2. \tag{2.12}$$

The measure of a domain  $S$  is denoted  $|S|$ . In particular this means that  $|F|$  is the length ( $d = 2$ ) or area ( $d = 3$ ) of a face  $F \in \mathcal{F}_h$ , while  $|E|$  is the area ( $d = 2$ ) or volume ( $d = 3$ ) of an element  $E \in \mathcal{E}_h$ .

**Average and Jump Operators.** Next, for  $s > 0$ , define

$$H^s(\mathcal{E}_h) = \left\{ \varphi \in L^2(\Omega) : \varphi|_E \in H^s(E), E \in \mathcal{E}_h \right\}. \tag{2.13}$$

Now, let  $E_i, E_j \in \mathcal{E}_h$  and  $F = \partial E_i \cap \partial E_j \in \mathcal{F}_{h,I}$  with  $\mathbf{n}_F$  exterior to  $E_i$ . Then, for  $\mathbf{v} \in (H^s(\mathcal{E}_h))^d$ ,  $s > \frac{1}{2}$ , we define the average over  $F$  as

$$\{\{\mathbf{v}\}\}_\theta = \theta_F (\mathbf{v}|_{E_i})|_F + (1 - \theta_F) (\mathbf{v}|_{E_j})|_F, \tag{2.14}$$

where  $\theta$  is a given weight with  $\theta_F = \theta|_F$  and  $0 < \theta_F < 1$ . For the standard average  $\theta = \frac{1}{2}$ , we simply write  $\{\{\mathbf{v}\}\}$ . In this work we consider weights  $\vartheta$  that depend on  $\mathbf{K}$ ,

$$\vartheta_F = \frac{\delta_{Kn}^j}{\delta_{Kn}^i + \delta_{Kn}^j}, \quad \delta_{Kn}^i = \mathbf{n}_F^\top \mathbf{K}_i \mathbf{n}_F, \tag{2.15}$$

where  $\delta_{Kn}^i$  is the normal component of  $\mathbf{K}$  across  $F$  and  $\mathbf{K}_i$  is the permeability in  $E_i$ . This choice of weights was considered by [38] for the isotropic case, and later extended to the anisotropic case in [39]. Now

$$k_e = 2\vartheta_F \delta_{Kn}^i = 2(1 - \vartheta_F) \delta_{Kn}^j = 2 \frac{\delta_{Kn}^i \delta_{Kn}^j}{\delta_{Kn}^i + \delta_{Kn}^j} \tag{2.16}$$

is the harmonic average of the normal component of  $\mathbf{K}$  along  $F$ . Observe that for isotropic permeability,  $\mathbf{K} = k\mathbb{I}$ , where  $\mathbb{I}$  is the identity matrix and  $k$  is the directional independent permeability, we have that

$$\vartheta_F = \frac{k_j}{k_i + k_j}, \quad k_e = \frac{2k_i k_j}{k_i + k_j}, \tag{2.17}$$

and it follows that

$$\{\{\mathbf{K}\nabla p\}\}_\vartheta = \frac{k_j}{k_i + k_j} k_i ((\nabla p)|_{E_i})|_F + \frac{k_i}{k_i + k_j} k_j ((\nabla p)|_{E_j})|_F = k_e \{\{\nabla p\}\}. \tag{2.18}$$

Next, for  $v \in H^s(\mathcal{E}_h)$ ,  $s > \frac{1}{2}$ , we define the jump over  $F$  as

$$\llbracket v \rrbracket = (v|_{E_i})|_F - (v|_{E_j})|_F = (v|_{E_i})|_F \mathbf{n}_{E_i} \cdot \mathbf{n}_F + (v|_{E_j})|_F \mathbf{n}_{E_j} \cdot \mathbf{n}_F. \tag{2.19}$$

For completeness, we extend the average and jump to  $F \in \mathcal{F}_{h,B}$ ,  $F \subset \partial E_i$ , by

$$\{\{\mathbf{v}\}\}_\theta = (\mathbf{v}|_{E_i})|_F, \tag{2.20}$$

$$\llbracket v \rrbracket = (v|_{E_i})|_F. \tag{2.21}$$

### 2.3. Conservation properties

**Compatibility Condition.** Consider first the case  $\beta = 0$ . If we multiply Eq. (2.1) by a test function  $\varphi$ , and then integrate and sum the result over each element  $E \in \mathcal{E}_h$ , we get that

$$(\mathbf{u}, \nabla \varphi)_{\mathcal{E}_h} + \langle \mathbf{u} \cdot \mathbf{n}, \llbracket \varphi \rrbracket \rangle_{\mathcal{F}_h} = (q, \varphi)_{\mathcal{E}_h}. \tag{2.22}$$

Let  $\mathbf{u}_h$  and  $U_h$  be approximations to  $\mathbf{u}$  in  $\mathcal{E}_h$  and  $\mathbf{u} \cdot \mathbf{n}$  on  $\mathcal{F}_h$ , respectively. Furthermore, let the space of test functions be  $P_r(\mathcal{E}_h)$ . The  $r$ th order compatibility condition for the velocity approximation reads

$$\langle \mathbf{u}_h, \nabla \varphi \rangle_{\mathcal{E}_h} + \langle U_h, \llbracket \varphi \rrbracket \rangle_{\mathcal{F}_h} = (q, \varphi)_{\mathcal{E}_h}, \quad \forall \varphi \in P_r(\mathcal{E}_h). \tag{2.23}$$

*Local Conservation.*  $U_h \in L^1(\mathcal{F}_h)$  is locally conservative if it is 0th order compatible, i.e.,

$$\langle U_h, \llbracket \varphi \rrbracket \rangle_{\mathcal{F}_h} = (q, \varphi)_{\mathcal{E}_h}, \quad \forall \varphi \in P_0(\mathcal{E}_h), \tag{2.24}$$

or, equivalently, on element form,

$$\int_{\partial E} U_h \mathbf{n}_F \cdot \mathbf{n}_E = \int_E q, \quad \forall E \in \mathcal{E}_h. \tag{2.25}$$

*Global Conservation.*  $U_h \in L^1(\mathcal{F}_h)$  is globally conservative if it satisfies (2.24) with  $\varphi = 1$ ,

$$\langle U_h, 1 \rangle_{\mathcal{F}_{h,B}} = (q, 1)_{\mathcal{E}_h}, \quad \text{or} \quad \int_{\partial \Omega} U_h = \int_{\Omega} q. \tag{2.26}$$

Global conservation follows from local conservation and flux continuity.

*Time Dependent Flow.* For  $\beta \neq 0$ , denote by  $U_h^n$  and  $p_h^n$  the flux and pressure approximation at time  $t_n$ , respectively, and let  $q^n = q(\cdot, t_n)$  and  $\beta^n = \beta(\cdot, t_n)$ . Now, local conservation is defined as

$$\langle U_h^n, \llbracket \varphi \rrbracket \rangle_{\mathcal{F}_h} = (q^n - \bar{\partial}_t(\beta^n p_h^n), \varphi)_{\mathcal{E}_h}, \quad \forall \varphi \in P_0(\mathcal{E}_h), \tag{2.27}$$

or, equivalently, on element form,

$$\int_{\partial E} U_h^n \mathbf{n}_F \cdot \mathbf{n}_E = \int_E (q^n - \bar{\partial}_t(\beta^n p_h^n)), \quad \forall E \in \mathcal{E}_h, \tag{2.28}$$

where  $\bar{\partial}_t$  is the discrete approximation to  $\partial_t$  used to solve the flow equation (2.1), e.g., for backward Euler with step size  $\Delta t$ ,  $\bar{\partial}_t p_h^n = \frac{1}{\Delta t}(p_h^n - p_h^{n-1})$ .

Global conservation is in a similar manner defined as

$$\langle U_h^n, 1 \rangle_{\mathcal{F}_{h,B}} = (q^n - \bar{\partial}_t(\beta^n p_h^n), 1)_{\mathcal{E}_h}, \quad \text{or} \quad \int_{\partial \Omega} U_h^n = \int_{\Omega} (q^n - \bar{\partial}_t(\beta^n p_h^n)). \tag{2.29}$$

### 2.4. Numerical schemes

We will briefly write down the numerical schemes used to solve the flow and transport problem. The flow equation (2.1) is solved with the continuous Galerkin (CG) finite element method, with either strong or weak enforcement of the Dirichlet conditions, while the transport equation (2.3) is solved with a discontinuous Galerkin (DG) finite element method. For time integration we use backward Euler.

*CG Scheme for the Flow Equation.* Let  $P_r^C(\mathcal{E}_h; v)$  denote the subspace of  $P_r^C(\mathcal{E}_h)$  such that the trace on  $\Gamma_D$  is equal to  $v$ ,

$$P_r^C(\mathcal{E}_h; v) = \{\varphi \in P_r^C(\mathcal{E}_h) : \varphi|_{\Gamma_D} = v\}. \tag{2.30}$$

Denote by  $\tilde{p}_B$  the projection of  $p_B$  into the polynomial space. Given  $p_h^{n-1}$  with  $p_h^0 = p_0$ , the standard CG scheme for Eq. (2.1) is to seek  $p_h^n \in P_r^C(\mathcal{E}_h; \tilde{p}_B)$  such that

$$(\beta \bar{\partial}_t p_h^n, \varphi)_{\mathcal{E}_h} + a(p_h^n, \varphi) = l(\varphi), \quad \forall \varphi \in P_r^C(\mathcal{E}_h; 0), \tag{2.31}$$

where the bilinear form  $a(p, \psi)$  and the linear functional  $l(\psi)$  are defined as follows:

$$a(p, \psi) = (\mathbf{K} \nabla p, \nabla \psi)_{\mathcal{E}_h}, \tag{2.32}$$

$$l(\psi) = (q, \psi)_{\mathcal{E}_h} - \langle \mathbf{u}_B, \psi \rangle_{\mathcal{F}_{h,N}}. \tag{2.33}$$

The energy norm associated with the discrete form (2.31) is given as

$$\|p\|_a^2 = a(p, p) = (\mathbf{K} \nabla p, \nabla p)_{\mathcal{E}_h}. \tag{2.34}$$

In the case where  $\mathbf{K}$  is the identity matrix and  $p$  is sufficiently smooth, the following error estimates hold [40],

$$\|p_h^n - p(t_n)\| \leq C(h^{r+1} + \Delta t), \quad \|p_h^n - p(t_n)\|_a \leq C(h^r + \Delta t), \tag{2.35}$$

where  $C$  is a constant independent on  $h$  and  $\Delta t$ .

Alternatively, one may impose the Dirichlet conditions weakly by adding a penalty term. Instead of (2.31) we seek  $p_h^n \in P_r^C(\mathcal{E}_h)$  such that

$$(\bar{\partial}_t(\beta^n p_h^n), \varphi)_{\mathcal{E}_h} + \tilde{a}(p_h^n, \varphi) = \tilde{l}(\varphi), \quad \forall \varphi \in P_r^C(\mathcal{E}_h), \tag{2.36}$$

where the bilinear form  $\tilde{a}(p, \psi)$  and the linear functional  $\tilde{l}(\psi)$  are defined as follows:

$$\tilde{a}(p, \psi) = (\mathbf{K}\nabla p, \nabla \psi)_{\mathcal{E}_h} + J_{D,\sigma}(p, \psi) - \langle \mathbf{K}\nabla p \cdot \mathbf{n}_F, \psi \rangle_{\mathcal{F}_{h,D}} - s_{\text{form}} \langle \mathbf{K}\nabla \psi \cdot \mathbf{n}_F, p \rangle_{\mathcal{F}_{h,D}}, \tag{2.37}$$

$$\tilde{l}(\psi) = (q, \psi)_{\mathcal{E}_h} + J_{D,\sigma}(p_B, \psi) - s_{\text{form}} \langle \mathbf{K}\nabla \psi \cdot \mathbf{n}_F, p_B \rangle_{\mathcal{F}_{h,D}} - \langle u_B, \psi \rangle_{\mathcal{F}_{h,N}}. \tag{2.38}$$

The Dirichlet penalty term  $J_{D,\sigma}(p, \psi)$  is defined as

$$J_{D,\sigma}(p, \psi) = \left\langle \frac{r^2 \sigma_F}{|F|} p, \psi \right\rangle_{\mathcal{F}_{h,D}}, \tag{2.39}$$

where the penalty parameter  $\sigma_F$  is constant on each face. In our work, we set  $s_{\text{form}} = 1$ , resulting in a symmetric formulation.

*Velocity Calculations from CG Solution.* Since  $p_h$  is only  $C^0$  continuous across element faces, the approximate velocity  $\mathbf{u}_h = -\mathbf{K}\nabla p_h$  is undefined on the faces. For this reason, we take the average value and define the velocity approximation from CG as

$$\mathbf{u}_h = -\mathbf{K}\nabla p_h, \quad \text{on } E \in \mathcal{E}_h, \tag{2.40}$$

$$U_h = \begin{cases} -\{\{\mathbf{K}\nabla p_h \cdot \mathbf{n}\}\}_\theta, & \text{on } F \in \mathcal{F}_{h,I}, \\ -\mathbf{K}\nabla p_h \cdot \mathbf{n} + \frac{r^2 \sigma_F}{|F|} (p_h - p_B), & \text{on } F \in \mathcal{F}_{h,D}, \\ u_B, & \text{on } F \in \mathcal{F}_{h,N}. \end{cases} \tag{2.41}$$

The extra penalty term on the Dirichlet boundary is added to give a globally conservative approximation when boundary conditions are imposed weakly. Notice that this term vanishes for strong boundary conditions as  $p_h = p_B$  on  $\Gamma_D$ . Global conservation for weak boundary conditions follows from (2.36) with  $\varphi = 1$ .

*Flux Recovery on Dirichlet Boundary.* The flux approximation (2.41) is not globally conservative when the boundary conditions are imposed strongly. However, there is a technique to recover globally conservative fluxes on the Dirichlet boundary [22,41–43,6–8]. This method is briefly recaptured here.

Let  $P_r^C(\mathcal{F}_{h,D}) = P_r^C(\mathcal{E}_h) \setminus P_r^C(\mathcal{E}_h; 0)$ , i.e., the space of continuous functions that are piecewise polynomials of order  $r$  with support only on elements with at least one of its faces in  $\mathcal{F}_{h,D}$ . The modified continuous Galerkin method now reads: Find  $p_h^n \in P_r^C(\mathcal{E}_h; p_B)$  and  $\mathcal{U}_h^n \in P_r^C(\mathcal{F}_{h,D})$  such that

$$-(\mathcal{U}_h^n, \varphi)_{\mathcal{F}_{h,D}} = a(p_h^n, \varphi) - l(\varphi) + (\bar{\partial}_t(\beta^n p_h^n), \varphi), \quad \forall \varphi \in P_r^C(\mathcal{E}_h). \tag{2.42}$$

We can now split this equation into two parts:

$$0 = a(p_h^n, \psi) - l(\psi) + (\bar{\partial}_t(\beta^n p_h^n), \psi), \quad \forall \psi \in P_r^C(\mathcal{E}_h; 0), \tag{2.43}$$

$$-(\mathcal{U}_h^n, \varphi)_{\mathcal{F}_{h,D}} = a(p_h^n, \varphi) - l(\varphi) + (\bar{\partial}_t(\beta^n p_h^n), \varphi), \quad \forall \varphi \in P_r^C(\mathcal{F}_{h,D}). \tag{2.44}$$

The first equation is the original problem (2.31), while the second determines  $\mathcal{U}_h^n$ , which we can use as an approximation to the flux on the Dirichlet boundary. If we assume that  $p_h^n$  is determined from (2.31) (or equivalently (2.43)), the right hand side of (2.44) is given. Global conservation of the flux  $\mathcal{U}_h^n$  follows from (2.42) with  $\varphi = 1$ .

*DG Scheme for the Transport Equation.* Given  $c_h^{n-1}$  with  $c_h^0 = c_0$ , a DG scheme with upwinding [4] for Eq. (2.3) with  $\mathbf{D} = 0$  is to seek  $c_h^n \in P_r(\mathcal{E}_h)$  satisfying

$$(\bar{\partial}_t(\phi c_h^n), \varphi)_{\mathcal{E}_h} + b(c_h^n, \varphi) = k(\varphi), \quad \forall \varphi \in P_r(\mathcal{E}_h), \tag{2.45}$$

where the bilinear form  $b(c, \psi)$  and the linear functional  $k(\psi)$  are defined as follows:

$$b(c, \psi) = -(c\mathbf{u}, \nabla\psi)_{\mathcal{E}_h} - (q^-c, \psi)_{\mathcal{E}_h} + \langle c^*\mathbf{u} \cdot \mathbf{n}_F, \llbracket \psi \rrbracket \rangle_{\mathcal{F}_{h,I}} + \langle c\mathbf{u} \cdot \mathbf{n}_F, \psi \rangle_{\mathcal{F}_{h,\text{out}}} + J_\sigma(c, \psi), \tag{2.46}$$

$$k(\psi) = (c_w q^+, \psi)_{\mathcal{E}_h} - \langle c_B \mathbf{u} \cdot \mathbf{n}_F, \psi \rangle_{\mathcal{F}_{h,\text{in}}}. \tag{2.47}$$

The interior penalty term is defined as

$$J_\sigma(c, \psi) = \left\langle \frac{r^2 \sigma_F}{|F|} \llbracket c \rrbracket, \llbracket \psi \rrbracket \right\rangle_{\mathcal{F}_{h,I}}, \tag{2.48}$$

while  $c^*$  denotes the upwind concentration, defined as

$$c^*|_F = \begin{cases} (c|_{E_i})|_F, & \text{if } \mathbf{u} \cdot \mathbf{n}_F \geq 0, \\ (c|_{E_j})|_F, & \text{if } \mathbf{u} \cdot \mathbf{n}_F < 0, \end{cases} \tag{2.49}$$

where  $\mathbf{n}_F$  is exterior to  $E_i$ . Furthermore,  $q^-$  and  $q^+$  are the negative and positive parts of the source term, respectively, i.e.

$$q^- = \min(q, 0), \quad q^+ = \max(q, 0). \tag{2.50}$$

The above scheme assumes that  $\mathbf{u}$  is known. Whenever we only have an approximation, e.g. from (2.41), we substitute  $\mathbf{u}$  by  $\mathbf{u}_h$  and  $\mathbf{u} \cdot \mathbf{n}_F$  by  $U_h$ . In this work, we only consider the lowest order method ( $r = 0$ ), for which  $\mathbf{u}$  (or an approximation to it) is not needed in the DG scheme since the first term in  $b(c, \psi)$  vanishes.

### 3. Postprocessing

In this section we will define an algorithm to postprocess a given flux approximation to obtain a locally conservative flux. In the derivation, we will assume a time independent problem ( $\beta = 0$ ), and then finally, in Section 3.6, we will show how this approach can be extended to the general case. We will start by defining a discrete divergence operator and its left inverse, and then later show how to use these to construct a locally conservative flux.

#### 3.1. A discrete divergence operator and its left inverse

*Elementwise Definitions.* Let  $D_h : L^1(\mathcal{F}_h) \rightarrow P_0(\mathcal{E}_h)$  denote the discrete divergence operator defined by

$$\int_E D_h v = \int_{\partial E} v \mathbf{n}_F \cdot \mathbf{n}_E, \quad \forall v \in L^1(\mathcal{F}_h), \quad \forall E \in \mathcal{E}_h. \tag{3.1}$$

Next, let  $D_h^\dagger : P_0(\mathcal{E}_h) \rightarrow P_0^0(\mathcal{F}_h)$  be a left inverse of  $D_h$ , i.e.,

$$\int_E v = \int_{\partial E} (D_h^\dagger v) \mathbf{n}_F \cdot \mathbf{n}_E, \quad \forall v \in P_0(\mathcal{E}_h), \quad \forall E \in \mathcal{E}_h. \tag{3.2}$$

Both  $D_h$  and  $D_h^\dagger$  are linear, and by definition,

$$D_h D_h^\dagger v = v, \quad \forall v \in P_0(\mathcal{E}_h). \tag{3.3}$$

Observe that  $D_h^\dagger$  takes functions into  $P_0^0(\mathcal{F}_h)$ , so that  $D_h^\dagger v = 0$  on  $\Gamma_N$  by definition.

*Variational Definitions.* We note that we have the following equivalent forms of (3.1) and (3.2),

$$(D_h v, w)_{\mathcal{E}_h} = \langle v, \llbracket w \rrbracket \rangle_{\mathcal{F}_h}, \quad \forall w \in P_0(\mathcal{E}_h), \tag{3.4}$$

$$(v, w)_{\mathcal{E}_h} = \langle D_h^\dagger v, \llbracket w \rrbracket \rangle_{\mathcal{F}_h}, \quad \forall w \in P_0(\mathcal{E}_h). \tag{3.5}$$

To see that our definitions are equivalent, we may first test with the characteristic function of element  $E$  to retrieve the elementwise definition from the variational formulations. Conversely we may multiply each elementwise equation with a constant and sum all the equations, and use the definition of the jump operator to conclude that the variational equations hold.

The left inverse  $D_h^\dagger$  is not uniquely defined since the dimension of  $P_0^0(\mathcal{F}_h)$  is larger than the dimension of  $P_0(\mathcal{E}_h)$ .<sup>3</sup> We may determine  $D_h^\dagger v$  uniquely for each  $v \in P_0(\mathcal{E}_h)$  by minimizing a given norm of  $D_h^\dagger v$ . We next consider minimization with respect to a weighted  $L^2$  norm.

*Minimization.* We define the weighted  $L^2$  inner product and norm as

$$\langle v, w \rangle_{\omega, \mathcal{F}_h} = \langle \omega v, w \rangle_{\mathcal{F}_h} = \sum_{F \in \mathcal{F}_h} \langle \omega v, w \rangle_F, \quad \|v\|_{\omega, \mathcal{F}_h}^2 = \langle v, v \rangle_{\omega, \mathcal{F}_h}, \tag{3.6}$$

where  $\omega|_F = \omega_F > 0$  for each  $F \in \mathcal{F}_h$  is a given bounded weight. For  $\omega = 1$ , we have the standard  $L^2$  norm.

Introducing the divergence-free subspace,  $P_{0,\text{div}}^0(\mathcal{F}_h)$ , defined by

$$P_{0,\text{div}}^0(\mathcal{F}_h) = \{v \in P_0^0(\mathcal{F}_h) : D_h v = 0\}, \tag{3.7}$$

we have the orthogonal decomposition

$$P_0^0(\mathcal{F}_h) = P_{0,\text{div}}^0(\mathcal{F}_h) \oplus P_{0,\text{div}}^{0,\perp}(\mathcal{F}_h), \tag{3.8}$$

with respect to the weighted inner product (3.6). For  $v_0 \in P_{0,\text{div}}^0(\mathcal{F}_h)$  we get from (3.4) that

$$0 = (D_h v_0, w)_{\mathcal{E}_h} = \langle v_0, \llbracket w \rrbracket \rangle_{\mathcal{F}_h} = \langle v_0, \omega^{-1} \llbracket w \rrbracket \rangle_{\omega, \mathcal{F}_h}, \quad \forall w \in P_0(\mathcal{E}_h). \tag{3.9}$$

Observe that the sum over  $\mathcal{F}_{h,N}$  vanishes as  $v_0 = 0$  on  $\mathcal{F}_{h,N}$  by definition. Hence, alternatively, we may define (3.8) by

$$P_{0,\text{div}}^{0,\perp}(\mathcal{F}_h) = \{v \in P_0^0(\mathcal{F}_h) : v = \omega^{-1} \llbracket w \rrbracket \text{ on } F \in \mathcal{F}_h \setminus \mathcal{F}_{h,N}, w \in P_0(\mathcal{E}_h)\}. \tag{3.10}$$

It follows that for  $v \in P_0(\mathcal{E}_h)$ ,

$$D_h^\dagger v = z + \omega^{-1} \llbracket y \rrbracket \in P_{0,\text{div}}^0(\mathcal{F}_h) \oplus P_{0,\text{div}}^{0,\perp}(\mathcal{F}_h), \quad \text{on } \mathcal{F}_h \setminus \mathcal{F}_{h,N}, \tag{3.11}$$

for some  $z \in P_{0,\text{div}}^0(\mathcal{F}_h)$  and  $y \in P_0(\mathcal{E}_h)$ . Recall that  $D_h^\dagger v = 0$  on  $\mathcal{F}_{h,N}$ . Using orthogonality and (3.5) we obtain

$$\begin{aligned} \langle v, w \rangle_{\mathcal{E}_h} &= \langle D_h^\dagger v, \llbracket w \rrbracket \rangle_{\mathcal{F}_h} = \langle z + \omega^{-1} \llbracket y \rrbracket, \llbracket w \rrbracket \rangle_{\mathcal{F}_h \setminus \mathcal{F}_{h,N}} \\ &= \langle z + \omega^{-1} \llbracket y \rrbracket, \omega^{-1} \llbracket w \rrbracket \rangle_{\omega, \mathcal{F}_h \setminus \mathcal{F}_{h,N}} \\ &= \langle \omega^{-1} \llbracket y \rrbracket, \omega^{-1} \llbracket w \rrbracket \rangle_{\omega, \mathcal{F}_h \setminus \mathcal{F}_{h,N}}, \quad \forall w \in P_0(\mathcal{E}_h). \end{aligned} \tag{3.12}$$

Furthermore, since

$$\|D_h^\dagger v\|_{\omega, \mathcal{F}_h}^2 = \|z + \omega^{-1} \llbracket y \rrbracket\|_{\omega, \mathcal{F}_h \setminus \mathcal{F}_{h,N}}^2 = \|z\|_{\omega, \mathcal{F}_h \setminus \mathcal{F}_{h,N}}^2 + \|\omega^{-1} \llbracket y \rrbracket\|_{\omega, \mathcal{F}_h \setminus \mathcal{F}_{h,N}}^2 \tag{3.13}$$

we see that minimizing the norm  $\|D_h^\dagger v\|_{\omega, \mathcal{F}_h}^2$  enforces  $z = 0$ .

We conclude that, subject to minimization,

$$D_h^\dagger v = \begin{cases} 0, & \text{on } \mathcal{F}_{h,N}, \\ \omega^{-1} \llbracket y \rrbracket, & \text{otherwise} \end{cases} \tag{3.14}$$

where  $y \in P_0(\mathcal{E}_h)$  is the solution to the variational problem

$$d(y, w) = (v, w)_{\mathcal{E}_h}, \quad \forall w \in P_0(\mathcal{E}_h). \tag{3.15}$$

The bilinear form  $d(y, w) : P_0(\mathcal{E}_h) \times P_0(\mathcal{E}_h) \rightarrow \mathbb{R}$  is defined as

$$d(y, w) = \langle \omega^{-1} \llbracket y \rrbracket, \omega^{-1} \llbracket w \rrbracket \rangle_{\omega, \mathcal{F}_h \setminus \mathcal{F}_{h,N}} = \langle \omega^{-1} \llbracket y \rrbracket, \llbracket w \rrbracket \rangle_{\mathcal{F}_h \setminus \mathcal{F}_{h,N}}. \tag{3.16}$$

We prove later, in Lemma 2, that (3.15) admits a unique solution. The choice of weights is discussed in Section 3.5.

<sup>3</sup> This is true for most grids, and if not, then (3.5) is sufficient.

The Operator  $D_h^\dagger D_h$ . Let  $v \in L^1(\mathcal{F}_h)$ . From the definitions (3.4) and (3.5) we have the following identity

$$\langle D_h^\dagger D_h v - v, \llbracket w \rrbracket \rangle_{\mathcal{F}_h} = 0, \quad \forall w \in P_0(\mathcal{E}_h), \tag{3.17}$$

since

$$\langle D_h^\dagger D_h v, \llbracket w \rrbracket \rangle_{\mathcal{F}_h} = (D_h v, w)_{\mathcal{E}_h} = \langle v, \llbracket w \rrbracket \rangle_{\mathcal{F}_h}. \tag{3.18}$$

Now using (3.14) we know that there is an  $y \in P_0(\mathcal{E}_h)$  such that  $D_h^\dagger D_h v = \omega^{-1} \llbracket y \rrbracket$  on  $\mathcal{F}_h \setminus \mathcal{F}_{h,N}$  (and  $D_h^\dagger D_h v = 0$  on  $\mathcal{F}_{h,N}$ ). From (3.17) it follows that

$$\begin{aligned} 0 &= \langle \omega^{-1} \llbracket y \rrbracket - v, \llbracket w \rrbracket \rangle_{\mathcal{F}_h \setminus \mathcal{F}_{h,N}} + \langle -v, \llbracket w \rrbracket \rangle_{\mathcal{F}_{h,N}} \\ &= \langle \omega^{-1} \llbracket y \rrbracket - v, \omega^{-1} \llbracket w \rrbracket \rangle_{\omega, \mathcal{F}_h \setminus \mathcal{F}_{h,N}} + \langle -v, \omega^{-1} \llbracket w \rrbracket \rangle_{\omega, \mathcal{F}_{h,N}}, \quad \forall w \in P_0(\mathcal{E}_h). \end{aligned} \tag{3.19}$$

Now, if  $v = 0$  on  $\mathcal{F}_{h,N}$ , the second term vanish. If we denote by  $L_0^1(\mathcal{F}_h)$  the subspace of  $L^1(\mathcal{F}_h)$  with functions that are zero on  $\mathcal{F}_{h,N}$ , i.e.,

$$L_0^1(\mathcal{F}_h) = \left\{ v \in L^1(\mathcal{F}_h) : v|_F = 0, F \in \mathcal{F}_{h,N} \right\}, \tag{3.20}$$

we conclude from (3.19) that the operator  $D_h^\dagger D_h : L^1(\mathcal{F}_h) \rightarrow P_0(\mathcal{F}_h)$  is the orthogonal projection of  $L_0^1(\mathcal{F}_h)$  onto the subspace  $P_{0,\text{div}}^{0,\perp}(\mathcal{F}_h)$  with respect to the weighted inner product  $\langle \cdot, \cdot \rangle_{\omega, \mathcal{F}_h}$ . In particular, it follows that

$$\|D_h^\dagger D_h\| = 1. \tag{3.21}$$

*Remark.* An alternative approach to obtain (3.14) and (3.15) is to use Lagrangian multipliers for minimizing  $\|D_h^\dagger v\|_{\omega, \mathcal{F}_h}^2$  subject to the constraints (3.5). If we let  $x = D_h^\dagger v$ , the Lagrangian reads

$$L(x, \lambda) = \frac{1}{2} \|x\|_{\omega, \mathcal{F}_h}^2 - \langle x, \llbracket \lambda \rrbracket \rangle_{\mathcal{F}_h} + (v, \lambda)_{\mathcal{E}_h}, \tag{3.22}$$

with corresponding derivative  $DL : P_0^0(\mathcal{F}_h) \times P_0(\mathcal{E}_h) \rightarrow \mathbb{R}$  given by

$$DL(x, \lambda)(\delta x, \delta \lambda) = \langle \omega x, \delta x \rangle_{\mathcal{F}_h} - \langle \delta x, \llbracket \lambda \rrbracket \rangle_{\mathcal{F}_h} + \langle x, \llbracket \delta \lambda \rrbracket \rangle_{\mathcal{F}_h} + (v, \delta \lambda)_{\mathcal{E}_h}. \tag{3.23}$$

By requiring  $DL(x, \lambda)(\delta x, \delta \lambda) = 0, \forall \delta x \in P_0(\mathcal{F}_h), \forall \delta \lambda \in P_0(\mathcal{E}_h)$ , we end up with the same result as (3.14) and (3.15).

### 3.2. Postprocessing algorithm

In the following, let  $U_h \in L^1(\mathcal{F}_h)$  be some approximation to the flux  $\mathbf{u} \cdot \mathbf{n}$  on  $\mathcal{F}_h$ . We define a residual operator,  $\mathcal{R} : L^1(\mathcal{F}_h) \rightarrow P_0(\mathcal{E}_h)$ , to measure to discrepancy from local conservation,

$$\mathcal{R}(U_h) = P_0 q - D_h U_h, \tag{3.24}$$

where  $P_0$  is the  $L^2$  projection onto  $P_0(\mathcal{E}_h)$ , i.e.,  $(P_0 q)|_E = |E|^{-1} \int_E q$ . Clearly,  $U_h$  is locally conservative if and only if  $\mathcal{R}(U_h) = 0$ , and  $U_h$  is globally conservative if and only if  $\int_\Omega \mathcal{R}(U_h) = 0$ .

The next lemma shows how the left inverse  $D_h^\dagger$  can be used to project an arbitrary flux approximation to a locally conservative flux.

**Lemma 1.** Given  $U_h \in L^1(\mathcal{F}_h)$ , the modified flux

$$V_h = U_h + D_h^\dagger(\mathcal{R}(U_h)) = U_h + D_h^\dagger(P_0 q - D_h U_h) \tag{3.25}$$

is locally conservative.

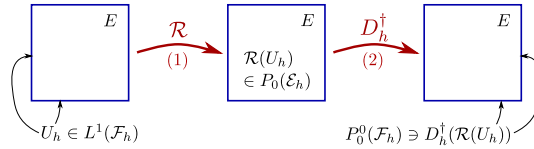


Fig. 1. Illustration of the postprocessing process. A non-conservative flux  $U_h$  is taken as input. First the operator  $\mathcal{R}$  calculates the element residuals (1). Then the operator  $D_h^\dagger$  projects the residuals onto the element faces such that the updated flux  $V_h = U_h - D_h^\dagger(\mathcal{R}(U_h))$  is locally conservative (2). This is a global process, although illustrated on a single element  $E$  here for simplicity.

**Proof.** Using the fact that  $D_h^\dagger$  is a left inverse of  $D_h$  we obtain

$$\begin{aligned}
 \mathcal{R}(V_h) &= P_0q - D_h V_h = P_0q - D_h \left( U_h + D_h^\dagger(P_0q - D_h U_h) \right) \\
 &= P_0q - D_h U_h - D_h D_h^\dagger P_0q + D_h D_h^\dagger D_h U_h \\
 &= P_0q - D_h U_h - P_0q + D_h U_h \\
 &= 0. \quad \square
 \end{aligned}
 \tag{3.26}$$

Applying (3.14) and (3.15), we may summarize the postprocessing algorithm as in the box below. The postprocessing steps and the different operators are illustrated in Fig. 1.

**Postprocessing algorithm**  
 Given  $U_h \in L^1(\mathcal{F}_h)$ , the postprocessed flux is defined as

$$V_h = U_h + D_h^\dagger(\mathcal{R}(U_h)) = \begin{cases} U_h, & \text{on } \mathcal{F}_{h,N}, \\ U_h + \omega^{-1} \llbracket y \rrbracket, & \text{on } \mathcal{F}_h \setminus \mathcal{F}_{h,N}, \end{cases}
 \tag{3.27}$$

where  $y \in P_0(\mathcal{E}_h)$  is the unique solution to

$$d(y, w) = (\mathcal{R}(U_h), w)_{\mathcal{E}_h}, \quad \forall w \in P_0(\mathcal{E}_h),
 \tag{3.28}$$

with

$$d(y, w) = \langle \omega^{-1} \llbracket y \rrbracket, \llbracket w \rrbracket \rangle_{\mathcal{F}_h \setminus \mathcal{F}_{h,N}}.
 \tag{3.29}$$

**Lemma 2.** The variational problem (3.28) has a unique solution.

**Proof.** We need to prove coercivity of the bilinear form  $d(\cdot, \cdot)$ . If  $w \in P_0(\mathcal{E}_h)$  and  $d(w, w) = \|\omega^{-1} \llbracket w \rrbracket\|_{\omega, \mathcal{F}_h} = 0$  then  $w$  is a constant function. If  $\Gamma_D$  is nonempty then  $\llbracket w \rrbracket|_F = w_F$  for  $F \subset \Gamma_D$ , so that  $w = 0$ . Otherwise, if  $\Gamma_D$  is empty, then  $w$  may be a nonzero constant  $C$ , but then the right hand side

$$(\mathcal{R}(U_h), C)_{\mathcal{E}_h} = C \int_{\Omega} \mathcal{R}(U_h) = C \left( \int_{\Omega} q - \int_{\Gamma_N} u_B \right) = 0,
 \tag{3.30}$$

since we require  $\int_{\Gamma_N} u_B = \int_{\Omega} q$  for the pure Neumann problem to be well posed. This shows uniqueness up to a constant. Since we only need the jump in  $y$ , our algorithm is well defined.  $\square$

**Matrix Formulation.** Let  $\chi_i$ , for  $i = 1, 2, \dots, N$ , denote the characteristic functions, i.e.,  $\chi_i = 1$  for  $x \in E_i$  and 0 otherwise. This is a basis for  $P_0(\mathcal{E}_h)$ , so we can write  $y = \sum_{i=1}^N y_i \chi_i$  and express the variational formulation (3.28) in matrix form

$$\mathbf{A} \mathbf{y} = \mathbf{r},
 \tag{3.31}$$



where  $\mathbf{A} \in \mathbb{R}^{N \times N}$  is the matrix with entries

$$A_{ij} = d(\chi_j, \chi_i) = \langle \omega^{-1} \llbracket \chi_j \rrbracket, \llbracket \chi_i \rrbracket \rangle_{\mathcal{F}_h} = \begin{cases} -\omega_F^{-1} |F|, & i \neq j, F = \partial E_i \cap \partial E_j, \\ \sum_{F \in \partial E_i \setminus \Gamma_N} \omega_F^{-1} |F|, & i = j. \end{cases} \tag{3.32}$$

Furthermore,  $\mathbf{y} \in \mathbb{R}^N$  is the vector with entries  $y_i$ , and  $\mathbf{r} \in \mathbb{R}^N$  is the vector of residuals, i.e., with entries

$$r_i = (\mathcal{R}(U_h), \chi_i) = \int_{E_i} q - \int_{\partial E_i} U_h \mathbf{n}_F \cdot \mathbf{n}_{E_i}. \tag{3.33}$$

Observe that  $\mathbf{A}$  is symmetric with non-zero pattern equal to the grid connectivity.

3.3. Error estimate

To measure the error on  $\mathcal{F}_h$  we introduce the face norm

$$\|v\|_{h, \mathcal{F}_h}^2 = \sum_{F \in \mathcal{F}_h} h \|v\|_F^2. \tag{3.34}$$

This norm has the advantage that  $\|1\|_{\mathcal{F}_h, h}$  is bounded as  $h \rightarrow 0$ . Furthermore, we use the notation  $x \lesssim y$  whenever there exists a positive constant  $C$  independent on  $h$  such that  $x \leq Cy$ .

**Lemma 3.** *If  $U_h$  is an approximation to the exact flux  $U = \mathbf{u} \cdot \mathbf{n}$  such that*

$$\|U - U_h\|_{h, \mathcal{F}_h} \lesssim h^s, \tag{3.35}$$

*then the local conservation residual satisfies the estimate*

$$\|\mathcal{R}(U_h)\|_{\mathcal{E}_h} \lesssim h^{s-1}, \tag{3.36}$$

*and the postprocessed locally conservative flux  $V_h$ , defined by (3.27), satisfies*

$$\|U - V_h\|_{h, \mathcal{F}_h} \lesssim h^s. \tag{3.37}$$

**Proof.** We have

$$\|\mathcal{R}(U_h)\|_{\mathcal{E}_h} = \|P_0q - D_h U_h\|_{\mathcal{E}_h} = \|D_h U - D_h U_h\|_{\mathcal{E}_h} = \|D_h(U - U_h)\|_{\mathcal{E}_h} \lesssim h^{-1/2} \|U - U_h\|_{\mathcal{F}_h}. \tag{3.38}$$

Here we have used that  $P_0q = D_h U$  and the bound  $\|D_h v\|_{\mathcal{E}_h} \lesssim h^{-1/2} \|v\|_{\mathcal{F}_h}$  which follows by setting  $w = D_h v$  in (3.4),

$$\|D_h v\|_{\mathcal{E}_h}^2 = (v, [D_h v])_{\mathcal{F}_h} \leq \|v\|_{\mathcal{F}_h} \|[D_h v]\|_{\mathcal{F}_h} \lesssim \|v\|_{\mathcal{F}_h} h^{-1/2} \|D_h v\|_{\mathcal{E}_h}. \tag{3.39}$$

In the last step we used the triangle inequality and the fact that  $\|[w]\|_{\partial E} \lesssim h^{-1/2} \|w\|_E$  for  $w \in P_0(E)$ . The bound on  $\|\mathcal{R}(U_h)\|_{\mathcal{E}_h}$  (3.36) follows since

$$\|v\|_{\mathcal{F}_h} \lesssim h^{-1/2} \|v\|_{h, \mathcal{F}_h}. \tag{3.40}$$

Furthermore, we have

$$\begin{aligned} \|U - V_h\|_{h, \mathcal{F}_h} &= \|U - (U_h + D_h^\dagger(P_0q - D_h U_h))\|_{h, \mathcal{F}_h} \\ &= \|(U - U_h) - D_h^\dagger D_h U + (D_h^\dagger D_h U_h)\|_{h, \mathcal{F}_h} \\ &\leq \|U - U_h\|_{h, \mathcal{F}_h} + \|D_h^\dagger D_h(U - U_h)\|_{h, \mathcal{F}_h} \\ &\lesssim \|U - U_h\|_{h, \mathcal{F}_h} \end{aligned} \tag{3.41}$$

where we used that  $U - U_h$  is zero on the Neumann boundary so that  $D_h^\dagger D_h$  is a projection.  $\square$

The following main result follows directly from Lemmas 1 to 3.

**Theorem 1.** *The postprocessed flux as defined by Eq. (3.27) is (i) locally conservative; (ii) uniquely defined; and (iii) has the same convergence order as the original flux.*

### 3.4. Alternative approach

An alternative approach to the one depicted above is to work on the element level. After realizing that  $D_h^\dagger v \in P_{0,\text{div}}^{0,\perp}(\mathcal{F}_h)$ , one may construct a basis for  $P_{0,\text{div}}^{0,\perp}(\mathcal{F}_h)$ . The set  $\{\varphi_i\}_{i=1}^N$ , with

$$\varphi_i = \begin{cases} -\omega_F^{-1} \mathbf{n}_F \cdot \mathbf{n}_{E_i}, & x \in F \subset \partial E_i \setminus \Gamma_N, \\ 0, & \text{otherwise,} \end{cases} \tag{3.42}$$

is a basis for  $P_{0,\text{div}}^{0,\perp}(\mathcal{F}_h)$ . We can then write

$$D_h^\dagger v = \sum_{i=1}^N \alpha_i \varphi_i. \tag{3.43}$$

From the requirement of  $D_h^\dagger$  given by (3.3), we get that

$$D_h D_h^\dagger v = D_h \left( \sum_{i=1}^N \alpha_i \varphi_i \right) = \sum_{i=1}^N \alpha_i D_h \varphi_i = v, \quad \forall v \in P_0(\mathcal{E}_h). \tag{3.44}$$

This is a linear system of  $N$  equations that uniquely determines the coefficients  $\alpha_i$  for a given  $v$ .

We remark that this is the approach presented in [10], but for the pure Dirichlet problem and only for the case where  $D_h^\dagger v$  is minimized in the standard  $L^2$  norm. The basis used in [10] is

$$\tilde{\varphi}_i = \begin{cases} -\frac{|E_i|}{|F|} \mathbf{n}_F \cdot \mathbf{n}_{E_i}, & x \in F \subset \partial E_i \\ 0, & \text{otherwise.} \end{cases} \tag{3.45}$$

One can show that this is a basis only when  $|F| = C$  for all  $F \in \mathcal{F}_h$ , i.e., when all faces are equally large.

### 3.5. Choice of weights

An important parameter in our postprocessing method is the choice of weights. Using  $\omega = 1$  will result in minimization in the standard  $L^2$  norm. This means that the correction  $D_h^\dagger(\mathcal{R}(U_h))$  will be minimized, but such that all faces are given the same weight. By choosing  $\omega \neq 1$ , we can control which faces should be weighted most in the minimization process. Our choice of weights is the inverse of the effective normal component of the permeability, i.e.,

$$\omega_F = k_e^{-1} = \frac{\delta_{Kn}^i + \delta_{Kn}^j}{2\delta_{Kn}^i \delta_{Kn}^j}, \tag{3.46}$$

where  $\delta_{Kn}^i$  was defined in Eq. (2.15).

With this choice,  $D_h^\dagger v = k_e \llbracket y \rrbracket$ , so that faces with low effective permeability will have a relatively small correction. We will reason this choice by an example. Consider two neighboring elements sharing the face  $F$  and with isotropic permeability  $k_1$  and  $k_2$ . If we fix  $k_1 = 1$ , the effective permeability will be  $k_e = 2k_2/(1 + k_2)$ . In the limit  $k_2 \rightarrow 0$ , this face should approach a no-flow interface (a Neumann type of boundary with  $u_B = \mathbf{u} \cdot \mathbf{n} = 0$ ). With the harmonic average  $\{\{\cdot\}\}_\partial$ ,  $U_h$  as defined from the CG solution, Eq. (2.41), would approach zero as desired. However, in the postprocessing step, the correction on  $F$  can be made relatively large (compared to  $U_h$ ) if  $\omega = 1$ , and thus the effect of harmonic averaging might be reduced after postprocessing. Using (3.46), we are able to preserve  $V_h \sim 0$ . The drawback is that the correction we are doing to the original flux will be larger measured in the standard  $L^2$  norm. In Section 4, we will demonstrate the effect of weighting with some numerical examples.

### 3.6. Time dependent flow

Let us now look at the case with time dependent pressure and flux, i.e.,  $\beta \neq 0$ . We need to take the compressibility (or time dependency of the pressure) into account when calculating the residual. If we discretize the flow equation

(2.1) in time, we get

$$\bar{\partial}_t(\beta^n p^n) - \nabla \cdot (\mathbf{K} \nabla p^n) = q^n, \tag{3.47}$$

where  $p^n$  and  $q^n$  are the pressure and source, respectively, at time  $t = t_n$ . Now, treating  $\bar{\partial}_t(\beta^n p^n)$  as a source term, we can extend the postprocessing method by replacing  $q$  by  $\tilde{q} = q^n - \beta \bar{\partial}_t(\beta^n p^n)$  in the above formulation. The residual operator now reads

$$\mathcal{R}(U_h^n) = P_0(q^n - \bar{\partial}_t(\beta^n p^n)) - D_h U_h^n. \tag{3.48}$$

We may now use the algorithm given by Eq. (3.27) with this extended residual operator.

For a time dependent problem, we need to perform postprocessing after each time step. However, we observe that the matrix  $\mathbf{A}$  in Eq. (3.31) is only dependent on the weights  $\omega$  and the grid. Thus, we only need to assemble  $\mathbf{A}$  whenever we alter the grid.

### 3.7. Postprocessing parameters

Given a CG pressure solution  $p_h$ , we have introduced different ways to calculate the CG flux approximation  $U_h$ . The first parameter is how we calculate the flux along the Dirichlet boundary, and the second parameter is the choice of weights  $\theta$  in the average operator. To clearly express which method we are using, we introduce the following notation:

$$\text{CG}(\alpha, \theta), \quad \alpha = \{\text{SD,WD,RD}\}, \quad \theta = \{1/2, \vartheta\}. \tag{3.49}$$

The CG flux  $U_h$  is then calculated as follows. On the internal and Neumann faces we have

$$U_h = \begin{cases} -\{\{\mathbf{K} \nabla p_h \cdot \mathbf{n}_F\}\}_\theta, & \text{on } F \in \Gamma_{h,I}, \\ u_B, & \text{on } F \in \Gamma_{h,N}. \end{cases} \tag{3.50}$$

The flux calculation on the Dirichlet boundary is given by  $\alpha$  in the following way:

- $\alpha = \text{SD}$ : CG with strong Dirichlet boundary conditions (Eq. (2.31)),

$$U_h = -\mathbf{K} \nabla p_h \cdot \mathbf{n}_F, \quad \text{on } F \in \Gamma_{h,D}. \tag{3.51}$$

- $\alpha = \text{WD}$ : CG with weak Dirichlet boundary conditions (Eq. (2.36)),

$$U_h = -\mathbf{K} \nabla p_h \cdot \mathbf{n}_F + \frac{r^2 \sigma_F}{|F|} (p_h - p_B), \quad \text{on } F \in \Gamma_{h,D}. \tag{3.52}$$

- $\alpha = \text{RD}$ : CG with strong Dirichlet boundary conditions and with recovered flux along the Dirichlet boundary (Eq. (2.44)),

$$U_h = \mathcal{U}_h, \quad \text{on } F \in \Gamma_{h,D}. \tag{3.53}$$

Furthermore, for the postprocessed flux, we have one more parameter describing which norm we are using for minimization. We use the following notation,

$$\text{PP}(\alpha, \theta, \lambda), \quad \alpha = \{\text{SD,WD,RD}\}, \quad \theta = \{1/2, \vartheta\}, \quad \lambda = \{\text{L2, wL2}\}, \tag{3.54}$$

where  $\lambda = \text{L2}$  and  $\lambda = \text{wL2}$  denotes minimization in the standard  $L^2$  norm and the weighted  $L^2$  norm, respectively. In the weighted  $L^2$  norm we use weight  $\omega = k_e^{-1}$  as described in Section 3.5. We note that the methods considered in [10] and [9] correspond to CG(SD,1/2,L2).

In the case of homogeneous permeability, the parameters  $\theta$  and  $\lambda$  are obsolete, and we simply write CG( $\alpha$ ) and PP( $\alpha$ ). In the case PP(RD,  $\cdot$ ,  $\cdot$ ), we consider the flux on the Dirichlet boundary as fixed and thus consider the postprocessing step as a pure Neumann problem.

## 4. Numerical examples

The postprocessing algorithm, along with solvers for the flow and transport equations, have been implemented. All implementations are based on the open source finite element library deal.II [44]. The numerical examples and timings

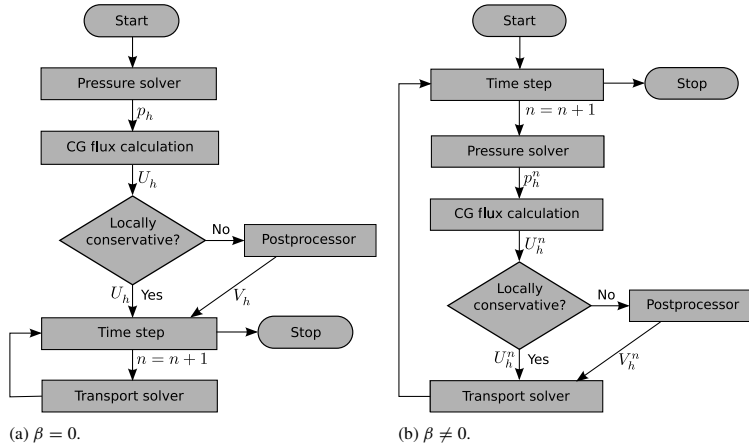


Fig. 2. Flowcharts describing the solution strategy for the elliptic case (a) and the parabolic case (b).

were performed on a single core of an Intel Xeon X7542 (2.67 GHz, 18 MB cache) with 64-bit Ubuntu 14.04 and 256 GB memory. For the flow equation we use CG with bilinear elements ( $r = 1$ ), while for the transport equation we use DG with piecewise constants ( $r = 0$ ). In this section we run a series of test cases to verify our implementations and evaluate the postprocessing algorithm. Our main objectives are to

- (i) Verify that the postprocessed flux is locally conservative on a range of grid types;
- (ii) Test if we are able to recover exact flux for a problem with analytic solution of one polynomial degree higher than the test space (expressed as an amenable *consistency condition* in [45, Section 4.1]);
- (iii) Study the effect of how flux on the Dirichlet boundary is calculated, as discussed in Section 3.7;
- (iv) Verify the error estimates given by Lemma 3;
- (v) Study the choice of weights in the average operator and the choice of norm used for minimization in the postprocessing method;
- (vi) Measure the computational complexity of the postprocessing problem compared to the flow problem.
- (vii) Demonstrate the importance of locally conservative flux when solving the transport equation.

For the latter objective, we introduce an overshoot quantity for the concentration solution  $c_h$ ,

$$\mathcal{O}(c_h) = \|\max(c_h - \bar{c}, 0) + \max(-c_h, 0)\|_{\mathcal{E}_h}, \tag{4.1}$$

where  $\bar{c}$  is the upper bound on the concentration,  $\bar{c} = \max(c_B, c_w, c_0)$ . For the incompressible flow problem ( $\beta = 0$ ), the concentration is expected to obey the maximum principle  $c \leq \bar{c}$  and be positive. Hence,  $\mathcal{O}(c_h)$  is used as a measure of the violation of these principles.

To solve the coupled flow and transport problem, Eqs. (2.1)–(2.3), we use an iterative solution technique. In each time step we first solve for pressure, then postprocess the flux if necessary, and at last solve the transport problem with the obtained flux approximation. This coupled process is illustrated by the flow chart in Fig. 2. If  $\beta = 0$ , we only need to solve for pressure and postprocess the flux once, and then do time iterations on the transport solver only. We also run cases without the postprocessing step, i.e., use  $U_h$  directly in the transport solver.

#### 4.1. Consistency tests

Our first example is a pure flow problem to examine the objectives (i)–(iii). Consider the problem

$$-\nabla \cdot (\nabla p) = 2, \quad \text{on } \Omega = (0, 1)^2, \tag{4.2a}$$

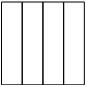

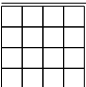
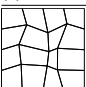
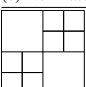
$$p = 1, \quad \text{for } x = 0, \tag{4.2b}$$

$$p = 0, \quad \text{for } x = 1, \tag{4.2c}$$

$$\mathbf{u} \cdot \mathbf{n} = 0, \quad \text{for } y = \{0, 1\}. \tag{4.2d}$$

Table 1

Consistency tests. Norm of residual and flux error before ( $U_h$ ) and after ( $V_h$ ) postprocessing for different grids and flux calculations along the Dirichlet boundary. The penalty term for CG(WD) is  $\sigma_\gamma = 10$ .

(a) Uniform 1D grid.		Method	$\ \mathcal{R}(U_h)\ _{\mathcal{E}_h}$	$\ \mathcal{R}(V_h)\ _{\mathcal{E}_h}$	$\ \mathbf{u} \cdot \mathbf{n} - U_h\ _{\mathcal{F}_h}$	$\ \mathbf{u} \cdot \mathbf{n} - V_h\ _{\mathcal{F}_h}$
	CG(SD)	0.707	2.4e-16	0.354	9.7e-16	
	CG(WD)	0.333	3.9e-17	0.118	1.2e-15	
	CG(RD)	1.2e-15	1.2e-15	1.7e-15	1.7e-15	
(b) Nonuniform 1D grid.		Method	$\ \mathcal{R}(U_h)\ _{\mathcal{E}_h}$	$\ \mathcal{R}(V_h)\ _{\mathcal{E}_h}$	$\ \mathbf{u} \cdot \mathbf{n} - U_h\ _{\mathcal{F}_h}$	$\ \mathbf{u} \cdot \mathbf{n} - V_h\ _{\mathcal{F}_h}$
	CG(SD)	0.976	2.9e-16	0.534	0.084	
	CG(WD)	0.888	9.6e-17	0.265	0.168	
	CG(RD)	0.280	6.3e-16	0.140	1.7e-15	
(c) Uniform 2D grid.		Method	$\ \mathcal{R}(U_h)\ _{\mathcal{E}_h}$	$\ \mathcal{R}(V_h)\ _{\mathcal{E}_h}$	$\ \mathbf{u} \cdot \mathbf{n} - U_h\ _{\mathcal{F}_h}$	$\ \mathbf{u} \cdot \mathbf{n} - V_h\ _{\mathcal{F}_h}$
	CG(SD)	0.707	4.6e-16	0.354	7.0e-16	
	CG(WD)	0.056	3.0e-17	0.020	1.1e-14	
	CG(RD)	2.8e-15	2.8e-15	1.4e-15	1.4e-15	
(d) Distorted 2D grid.		Method	$\ \mathcal{R}(U_h)\ _{\mathcal{E}_h}$	$\ \mathcal{R}(V_h)\ _{\mathcal{E}_h}$	$\ \mathbf{u} \cdot \mathbf{n} - U_h\ _{\mathcal{F}_h}$	$\ \mathbf{u} \cdot \mathbf{n} - V_h\ _{\mathcal{F}_h}$
	CG(SD)	0.908	1.4e-15	0.401	0.073	
	CG(WD)	0.443	7.2e-17	0.122	0.078	
	CG(RD)	0.462	6.0e-15	0.131	0.085	
(e) Nonmatching 2D grid.		Method	$\ \mathcal{R}(U_h)\ _{\mathcal{E}_h}$	$\ \mathcal{R}(V_h)\ _{\mathcal{E}_h}$	$\ \mathbf{u} \cdot \mathbf{n} - U_h\ _{\mathcal{F}_h}$	$\ \mathbf{u} \cdot \mathbf{n} - V_h\ _{\mathcal{F}_h}$
	CG(SD)	1.127	5.5e-16	0.615	0.089	
	CG(WD)	0.288	6.4e-17	0.183	0.163	
	CG(RD)	0.278	1.3e-15	0.179	0.144	

This problem has the analytical solution  $p(x, y) = 1 - x^2$ , and is essentially a one-dimensional problem. Since the permeability tensor is constant ( $\mathbf{K} = \mathbb{I}$ ), there is no effect of harmonic averaging or weighting of the  $L^2$  norm.

Results for different grids and calculations of fluxes along the Dirichlet boundary are presented in Table 1. First observe that the residual for the postprocessed flux,  $\mathcal{R}(V_h)$ , is zero in all cases. This demonstrates that  $V_h$  is locally conservative and that our postprocessing method works. For the uniform 1D grid all methods give exact solution for  $V_h$ . The flux error,  $\|\mathbf{u} \cdot \mathbf{n} - U_h\|_{\mathcal{F}_h}$ , for CG(WD) can be made arbitrarily small by increasing the penalty term  $\sigma_F$ . This illustrates some of the ambiguity with weak boundary conditions. In the limit  $\sigma_F \rightarrow \infty$ , CG(WD) and CG(RD) are equivalent. The postprocessed flux error,  $\|\mathbf{u} \cdot \mathbf{n} - V_h\|_{\mathcal{F}_h}$ , for CG(SD) and CG(WD) is non-zero for the nonuniform 1D grid because the flux  $U_h$  on the Dirichlet boundary is wrong. On this grid, CG(RD) reproduce the exact flux. For the two latter grids, the distorted and matching 2D grids, CG(SD) seems to give the best result.

We observe that for the distorted and non-matching 2D grids, we do not obtain exact fluxes for CG(RD). In Table 2 we report on the integrated flux  $\int_\gamma U_h$  along vertical mesh lines  $\gamma$ , which divides the domain  $\Omega$  in two. For the nonmatching 2D grid (Table 2(b)), we see that we recover the exact value with all methods. For the distorted 2D grid (Table 2(a)), this is only the case for CG(RD). This follows from the fact that the fluxes are globally conservative and that the integrated flux is exactly recovered along the Dirichlet boundaries [6]. Notice that for CG(SD) and CG(WD), the value of the integrated flux  $V_h$  is shifted by the same value for all  $\gamma$  (0.0033 for CG(SD) and 0.0020 for CG(WD)).

#### 4.2. Convergence tests

To verify the convergence estimates in Eq. (2.35) and Lemma 3 numerically (objective (iv)), we consider a time dependent problem with analytic solution. Let  $\Omega = (0, 1)^2$ ,  $\mathbf{K} = \mathbb{I}$ ,  $\beta = 1.0$  and  $\phi = 1.0$ . For the coupled flow and transport problem (2.1)–(2.3) we choose right hand sides and boundary conditions such that

$$p = \cos(t + x - y), \quad c = \cos(t + x - y) \tag{4.3}$$

Table 2  
Consistency tests. Integrated flux along vertical mesh lines for different flux approximations and mesh lines,  $\gamma_i$ .

(a) Distorted 2D grid.						
Flux	$\gamma_1$ ( $x = 0$ )	$\gamma_2$ ( $x \approx 0.25$ )	$\gamma_3$ ( $x \approx 0.5$ )	$\gamma_4$ ( $x \approx 0.75$ )	$\gamma_5$ ( $x = 1$ )	
Exact	$\int_{\gamma_i} \mathbf{u} \cdot \mathbf{n}$	0	0.4980	1.0850	1.4400	2
CG(SD)	$\int_{\gamma_i} U_h$	0.2551	0.5198	1.0331	1.4919	1.7196
	$\int_{\gamma_i} V_h$	0.0033	0.4947	1.0817	1.4367	1.9967
CG(WD)	$\int_{\gamma_i} U_h$	4.2e-15	0.5334	1.0330	1.4785	2
	$\int_{\gamma_i} V_h$	-0.0020	0.5001	1.0870	1.4420	2.0020
CG(RD)	$\int_{\gamma_i} U_h$	1.6e-15	0.5198	1.0331	1.4919	2
	$\int_{\gamma_i} V_h$	1.6e-15	0.4980	1.0850	1.4400	2

(b) Nonmatching 2D grid.				
Flux	$\gamma_1$ ( $x = 0$ )	$\gamma_2$ ( $x = 0.5$ )	$\gamma_3$ ( $x = 1$ )	
Exact	$\int_{\gamma_i} \mathbf{u} \cdot \mathbf{n}$	0	1	2
CG(SD)	$\int_{\gamma_i} U_h$	0.4130	1	1.5870
	$\int_{\gamma_i} V_h$	9.7e-17	1	2
CG(WD)	$\int_{\gamma_i} U_h$	1.9e-15	1	2
	$\int_{\gamma_i} V_h$	4.5e-15	1	2
CG(RD)	$\int_{\gamma_i} U_h$	8.7e-16	1	2
	$\int_{\gamma_i} V_h$	8.7e-16	1	2

are the analytic solutions. One may easily verify that  $q = 2 \cos \alpha - \sin \alpha$  and  $f = (1 + 4 \sin \alpha) \cos \alpha$  with  $\alpha = t + x - y$ . For the flow problem, we impose Dirichlet conditions on  $x = \{0, 1\}$  and Neumann conditions on  $y = \{0, 1\}$ . The numerical solution at  $t = 0.1$  on a fine grid can be viewed in Fig. 3.

First, the domain  $\Omega$  is discretized into uniform quadratic grids of size  $n \times n$  with  $n = 2^i$ ,  $i = 2, 3, 4, 5$ . Equivalently,  $h = \frac{1}{n} = 2^{-i}$ . The end time is  $T = 0.1$ , and the time step size is chosen small enough to not affect the convergence rates and is recursively refined such that  $\Delta t = \frac{1}{5 \cdot 4^{i-1}} = \frac{4}{5} h^2$ . The transport solver is run with three different flux approximations: (i) CG flux ( $U_h$ ); (ii) postprocessed CG flux ( $V_h$ ); and (iii) analytic flux ( $\mathbf{u} \cdot \mathbf{n}$ ). Dirichlet conditions are imposed strongly, CG(SD). Convergence tables for flow and transport quantities are shown in Table 3.

We observe that the error in  $p$  is of order 1 in the energy norm in accordance with the error estimate in Eq. (2.35). Furthermore, we see that the postprocessed flux,  $V_h$ , converges with order 1/2 larger than the CG flux,  $U_h$ . The residual,  $\mathcal{R}(U_h)$ , converges to zero with one order lower than  $U_h$ . These results are in accordance with Lemma 3. Finally, we observe that the residual is zero (down to machine precision) for the postprocessed flux.

For the concentration solution, all simulations converge with order 1. The differences in concentration due to different flux calculations are small in this example. However, we show later that cases involving heterogeneous permeability may result in much larger differences.

Next, the same examples were run but with Dirichlet flux recovery, CG(RD). The convergence table for flow and transport variables is displayed in Table 4. We see that the order of the error in  $U_h$  increases by 1/2 compared to CG(SD), while the residual now converges to zero with rate 1.5. This appears to be due to better flux approximation on the Dirichlet boundary as this is the only difference. The postprocessed flux has the same order as the CG flux, so the net effect is nearly the same as without Dirichlet flux recovery (cf. Table 3(a)). In the remaining examples of this work, we will therefore only consider strong Dirichlet conditions, CG(SD).

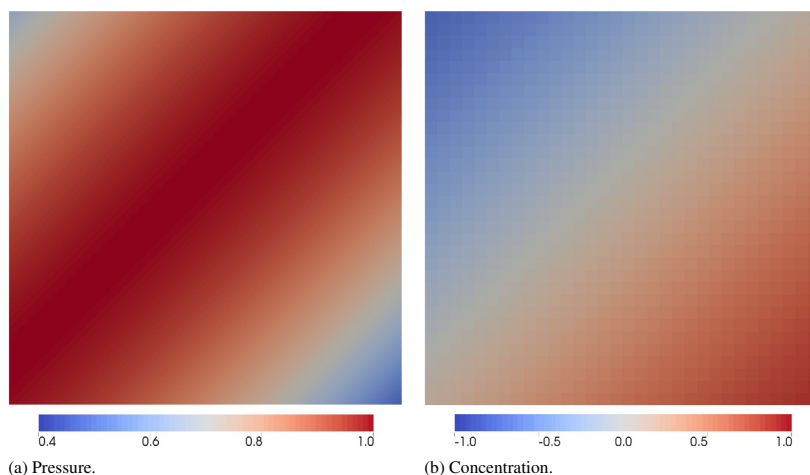


Fig. 3. Convergence tests. Pressure (a) and concentration (b) solution at  $t = 0.1$  on the finest grid level,  $1/h = 32$ . The postprocessed flux,  $V_h$ , is used in the transport solver to calculate the transport solution.

Table 3

Convergence tests. Error and convergence rates for flow variables (a) and concentration solution (b). A recursively refined quadratic grid with element size  $h$  is used. Dirichlet boundary conditions are imposed strongly, CG(SD).

(a) Flow variables.								
$1/h$	$\ p - p_h\ _a$		$\ \mathbf{u} \cdot \mathbf{n} - U_h\ _{h, \mathcal{F}_h}$		$\ \mathbf{u} \cdot \mathbf{n} - V_h\ _{h, \mathcal{F}_h}$		$\ \mathcal{R}(U_h)\ _{\mathcal{E}_h}$	
4	0.0941	–	0.08211	–	0.00809	–	0.3000	–
8	0.0470	1.00	0.02804	1.55	0.00197	2.04	0.2125	0.50
16	0.0235	1.00	0.00967	1.54	0.00049	2.00	0.1503	0.50
32	0.0117	1.00	0.00337	1.52	0.00012	2.00	0.1063	0.50
(b) Concentration solution with different flux (in parenthesis).								
$1/h$	$\ c - c_h\ _{\mathcal{E}_h}(\mathbf{u} \cdot \mathbf{n})$		$\ c - c_h\ _{\mathcal{E}_h}(U_h)$		$\ c - c_h\ _{\mathcal{E}_h}(V_h)$			
4	0.09502	–	0.09631	–	0.09507	–		
8	0.04765	1.00	0.04850	0.99	0.04766	1.00		
16	0.02385	1.00	0.02436	0.99	0.02385	1.00		
32	0.01193	1.00	0.01218	1.00	0.01193	1.00		

At last, we consider the same problem but evaluate convergence on a family of distorted and non-conforming grid. Let  $\mathcal{M}_0$  be the base grid as displayed in Fig. 4(a). Then, we iteratively refine the base grid globally by dividing each element into four by connecting midpoints of the four faces. This results in a family of refined grids,  $\mathcal{M}_i$ ,  $i = 0, 1, \dots, 4$ , where the three first grids are displayed in Fig. 4. The time steps are now  $\Delta t = \frac{1}{5.4^{i+1}}$ . Convergence results are shown in Table 5. We still observe that the order of  $V_h$  is the same as for  $U_h$ , although we have to let  $h$  be very small for the rate to converge towards 1. Notice that  $\|\mathbf{u} \cdot \mathbf{n} - V_h\|_{h, \mathcal{F}_h} < \|\mathbf{u} \cdot \mathbf{n} - U_h\|_{h, \mathcal{F}_h}$  for all cases studied in this section. This example demonstrates that our method works and that the error estimates hold for general grids.

#### 4.3. Barrier problem

In the next example we consider flow and transport through a barrier (low permeability region) and study the objectives (i), (v), (vi) and (vii). The problem is illustrated in Fig. 5. Let  $\Omega = (0, 1)^2$ ,  $\beta = 0$  and use boundary conditions

Table 4  
Convergence tests. Error and convergences rates for flow variables (a) and concentration solution (b). A recursively refined quadratic grid with element size  $h$  is used. The Dirichlet flux recovery technique, CG(RD), is used.

(a) Flow variables.									
$1/h$	$\ p - p_h\ _a$		$\ \mathbf{u} \cdot \mathbf{n} - U_h\ _{h, \mathcal{F}_h}$		$\ \mathbf{u} \cdot \mathbf{n} - V_h\ _{h, \mathcal{F}_h}$		$\ \mathcal{R}(U_h)\ _{\mathcal{E}_h}$		$\ \mathcal{R}(V_h)\ _{\mathcal{E}_h}$
4	0.0941	–	0.00965	–	0.00719	–	0.0207	–	1.6e-13
8	0.0470	1.00	0.00250	1.95	0.00160	2.17	0.0077	1.42	5.1e-13
16	0.0235	1.00	0.00064	1.97	0.00037	2.11	0.0028	1.49	7.7e-13
32	0.0117	1.00	0.00016	1.99	0.00009	2.06	0.0010	1.50	1.4e-12

(b) Concentration solution with different flux (in parenthesis).						
$1/h$	$\ c - c_h\ _{\mathcal{E}_h}(\mathbf{u} \cdot \mathbf{n})$		$\ c - c_h\ _{\mathcal{E}_h}(U_h)$		$\ c - c_h\ _{\mathcal{E}_h}(V_h)$	
4	0.09503	–	0.09514	–	0.09510	–
8	0.04765	1.00	0.04769	1.00	0.04767	1.00
16	0.02385	1.00	0.02386	1.00	0.02386	1.00
32	0.01193	1.00	0.01194	1.00	0.01193	1.00

Table 5  
Convergence tests. Error and convergences rates for flow variables (a) and concentration solution (b) for the recursively refined grids shown in Fig. 4. Dirichlet boundary conditions are imposed strongly, CG(SD).

(a) Flow variables.									
Grid	$\ p - p_h\ _a$		$\ \mathbf{u} \cdot \mathbf{n} - U_h\ _{h, \mathcal{F}_h}$		$\ \mathbf{u} \cdot \mathbf{n} - V_h\ _{h, \mathcal{F}_h}$		$\ \mathcal{R}(U_h)\ _{\mathcal{E}_h}$		$\ \mathcal{R}(V_h)\ _{\mathcal{E}_h}$
$\mathcal{M}_0$	0.08331	–	0.116103	–	0.044114	–	0.5096	–	7.3e-16
$\mathcal{M}_1$	0.04057	1.04	0.041738	1.48	0.017211	1.36	0.3153	0.69	7.1e-16
$\mathcal{M}_2$	0.02006	1.02	0.015556	1.42	0.007820	1.14	0.2233	0.50	6.9e-16
$\mathcal{M}_3$	0.00998	1.01	0.006116	1.35	0.003840	1.03	0.1585	0.49	1.0e-15
$\mathcal{M}_4$	0.00498	1.00	0.002556	1.26	0.001921	1.00	0.1122	0.50	1.4e-15
$\mathcal{M}_5$	0.00248	1.00	0.001133	1.17	0.000963	1.00	0.0793	0.50	2.4e-15
$\mathcal{M}_6$	0.00124	1.00	0.000527	1.10	0.000483	1.00	0.0560	0.50	4.6e-15

(b) Concentration solution with different flux (in parenthesis).						
Grid	$\ c - c_h\ _{\mathcal{E}_h}(\mathbf{u} \cdot \mathbf{n})$		$\ c - c_h\ _{\mathcal{E}_h}(U_h)$		$\ c - c_h\ _{\mathcal{E}_h}(V_h)$	
$\mathcal{M}_0$	0.07595	–	0.07864	–	0.07598	–
$\mathcal{M}_1$	0.03821	0.99	0.03977	0.98	0.03822	0.99
$\mathcal{M}_2$	0.01919	0.99	0.02007	0.99	0.01920	0.99
$\mathcal{M}_3$	0.00964	0.99	0.01006	1.00	0.00964	0.99

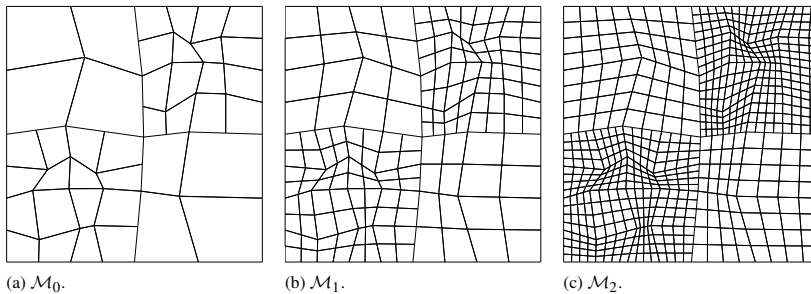


Fig. 4. Convergence tests. Base grid (left) and the first two recursively refined grids used for convergence test for distorted and non-conforming grids. All cells are divided in four in each refinement cycle.



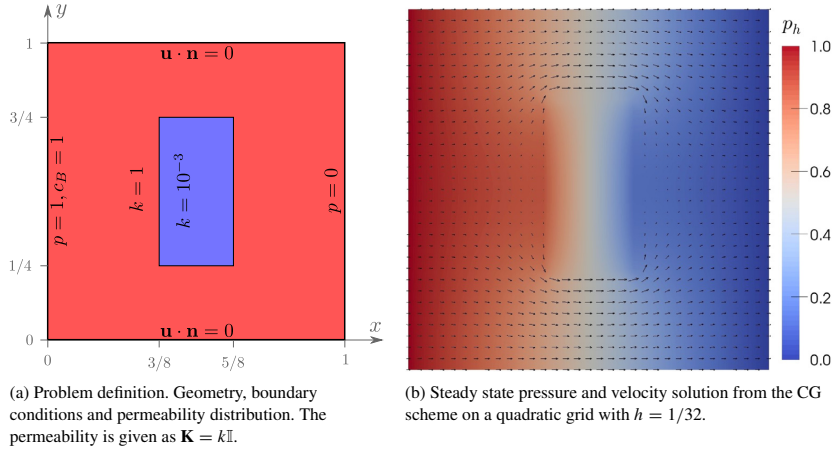


Fig. 5. Barrier problem. Problem definition (a) and numerical pressure solution (b).

Table 6

Barrier problem. Norm of residual,  $\|\mathcal{R}(\cdot)\|_{\mathcal{E}_h}$ , overshoot,  $\mathcal{O}(c_h)$ , and minimum and maximum value of concentration solution at  $t = 2$  for different flux approximations.

Method	$\ \mathcal{R}(U_h)\ _{\mathcal{E}_h}$	$\ \mathcal{R}(V_h)\ _{\mathcal{E}_h}$	$\mathcal{O}(c_h)$	$\min(c_h)$	$\max(c_h)$
CG(SD,1/2)	1.184	–	0.04107	2.1e-12	1.822
CG(SD, $\vartheta$ )	1.895	–	0.03285	3.1e-13	1.505
PP(SD,1/2,L2)	–	4.8e-16	3.2e-17	2.2e-11	1.000
PP(SD, $\vartheta$ ,L2)	–	9.7e-16	1.6e-17	1.4e-10	1.000
PP(SD, $\vartheta$ ,wL2)	–	2.7e-15	4.8e-17	3.0e-13	1.000

$p(0, y) = 1, p(1, y) = 0$  and  $\mathbf{u} \cdot \mathbf{n} = 0$  on  $y = \{0, 1\}$ . For the transport problem,  $\phi = 1, \Gamma_{in} = \{x = 0\} \cap \partial\Omega, c_B = 1$  and  $c_0 = 0$ . The steady state pressure and velocity solution from the CG scheme on a fine grid is shown in Fig. 5(b).

First, consider the case when the standard average  $\theta = 1/2$  is used for flux calculations. The concentration solution with  $\Delta t = 0.01$  at  $t = 1$  and  $t = 2$  is shown in Fig. 6, both for CG(SD,1/2) and PP(SD,1/2,L2). Furthermore, the concentration along the curve  $y = 0.735$  is plotted in the same figure. The solutions are close at  $t = 1$ , although we observe some small unphysical oscillation close to the barrier interface for CG(SD,1/2). Both solutions are in the (physical) valid range  $[0, 1]$ . However, at  $t = 2$ , CG(SD,1/2) gives an unphysical solution as  $c_h > 1.0$  in some cells and since the solution oscillates close to the barrier interface. The solution with PP(SD,1/2,L2) is in the range  $[0, 1]$  and without oscillations.

Since the contrast in permeability is three orders of magnitude, we would expect very little flow into the barrier region. However, we see from Fig. 6 that the concentration in the corners of the barrier region is rather large. To cope with this we use harmonic averaging of the permeability, thus set  $\theta = \vartheta$  in the flux averaging. Similar results as with  $\theta = 1/2$  are displayed in Fig. 7. Clearly, harmonic averaging reduces the inflow into the barrier region when we use CG flux, but still we get an unphysical solution (Figs. 7(a) and 7(d)). However, when we postprocess this flux with minimization in the standard  $L^2$  norm, the effect of harmonic averaging reduces since the concentration in the corners is now high (Figs. 7(b) and 7(e)). If we instead postprocess with minimization in the weighted  $L^2$  norm, we see that the barrier region is much less permeable (Figs. 7(c) and 7(f)). This clearly demonstrates that using the weighted  $L^2$  norm is necessary to preserve low permeable interfaces and should be used in combination with harmonic averaging of the CG flux.

The overshoot quantity,  $\mathcal{O}(c_h)$ , the minimum and maximum of  $c_h$  and the norm of the residual is reported in Table 6 for the different cases studied above. We see that for all postprocessing cases,  $\mathcal{R}(V_h)$  and  $\mathcal{O}(c_h)$  is zero down to machine precision, and that  $c_h \in [0, 1]$ . This is not satisfied with CG flux, which is not locally conservative.

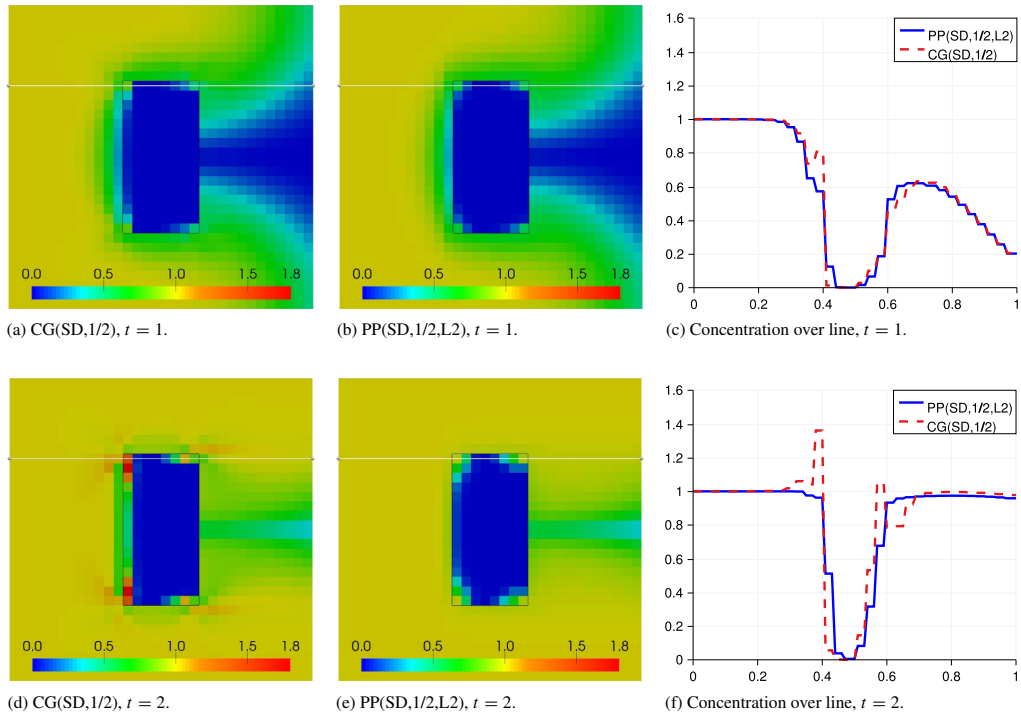


Fig. 6. Barrier problem. Concentration solution at two different times, with and without postprocessing. The standard weight  $\theta = 1/2$  is used for the average in calculations of CG flux,  $U_h$ . The solution along the white line ( $y = 0.735$ ) is plotted to the right. The low permeability region is inscribed in the black box.

Next, we compare the postprocessing step with the CG solver in terms of efficiency and computational complexity. Both the CG problem (Eq. (2.31)) and the postprocessing problem (Eq. (3.28)) are symmetric and positive definite, so we use the conjugate gradient method as linear solver. In Table 7 we report on degrees of freedom (DoF), condition number ( $\kappa$ ),<sup>4</sup> number of iterations in the linear solver (it), and the CPU time used by the linear solver (time). This is done for the CG problem and the postprocessing problem both with and without weighting for recursively refined regular Cartesian grids. We consider both the standard conjugate gradient solver and the preconditioned conjugate gradient with a symmetric successive overrelaxation preconditioner, SSOR(1.5). For all cases we use strong Dirichlet conditions and harmonic weighting of the CG flux.

Without preconditioning, we see that PP(SD,  $\vartheta$ , L2) is much less costly to solve than CG(SD,  $\vartheta$ ), both in terms of the condition number and solver time. PP(SD,  $\vartheta$ , wL2) is more expensive, and the solution time is  $\sim 70\%$  of that of CG(SD,  $\vartheta$ ). This is because weighting introduces high aspect ratios in the system matrix, see Eq. (3.32). However, if we apply a relatively simple preconditioner as SSOR, the condition numbers and solution times drop remarkably for CG(SD,  $\vartheta$ ) and PP(SD,  $\vartheta$ , wL2), such that the computational complexity of PP(SD,  $\vartheta$ , L2) and PP(SD,  $\vartheta$ , wL2) are almost similar. Still, the additional cost of the postprocessing step is significant ( $\sim 55\%$  for PP(SD,  $\vartheta$ , L2) and  $\sim 60\%$  for PP(SD,  $\vartheta$ , wL2)).

<sup>4</sup> The condition numbers are estimated by routines in the deal.II library.

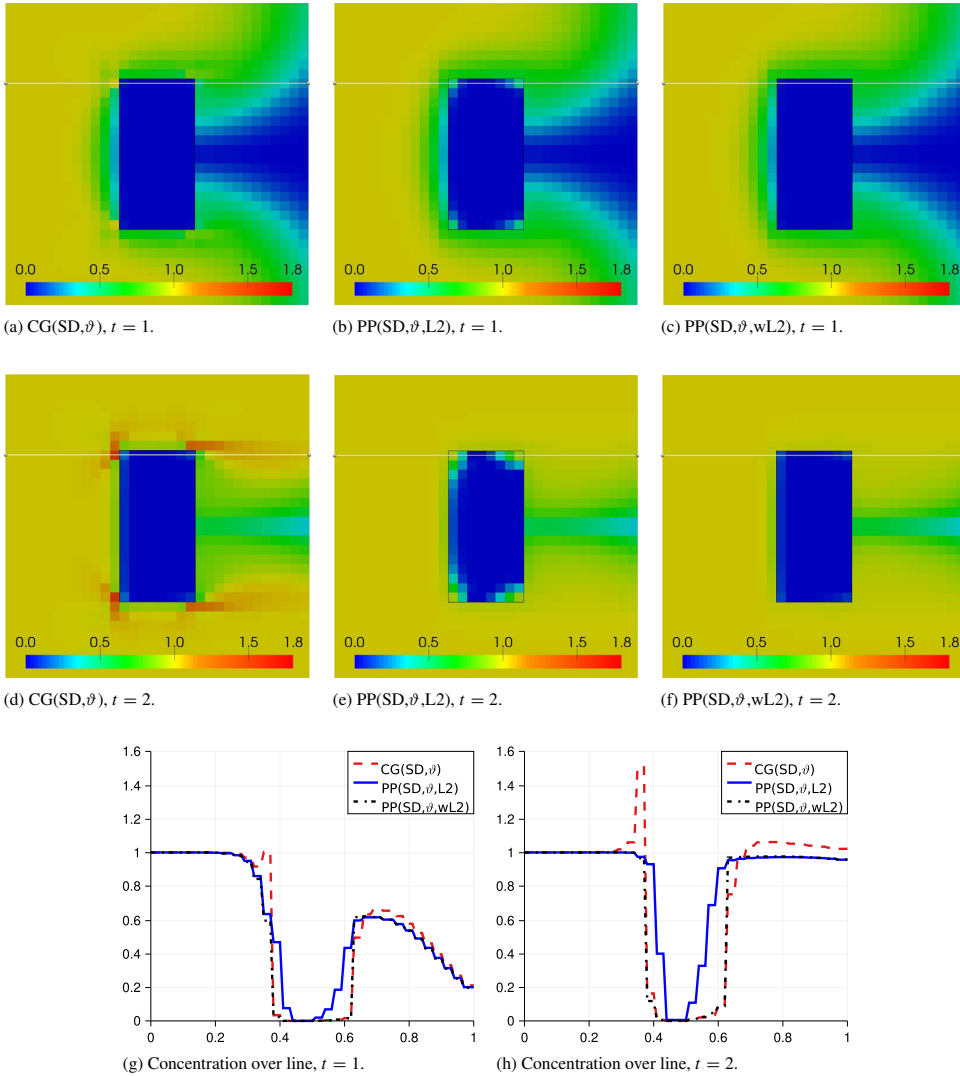


Fig. 7. Barrier problem. Concentration solution at two different times, with CG flux and postprocessed flux with the standard  $L^2$  norm and the weighted  $L^2$  norm. The harmonic weight  $\theta = \vartheta$  is used for the average in calculations of CG flux,  $U_h$ . The solution along the white line ( $y = 0.735$ ) is plotted in the bottom row. The low permeability region is inscribed in the black box.

Finally, we test the sensitivity of the computational complexity with respect to the permeability contrast. This is done by keeping the grid resolution fixed at  $1/h = 64$  and then vary the permeability in the low permeable block, denoted  $k_b$ . These results are reported in Table 8. For the case without preconditioning, we see that the condition number and linear solver time for CG(SD, $\vartheta$ ) and PP(SD, $\vartheta$ ,wL2) scale badly with the permeability contrast, whereas PP(SD, $\vartheta$ ,L2) is nearly unaffected. This is as expected since the system matrix for PP(SD, $\vartheta$ ,L2) is independent of the permeability, while for CG(SD, $\vartheta$ ) and PP(SD, $\vartheta$ ,wL2) it is not. However, if we look at the preconditioned system, we

Table 7

Barrier problem. Computational complexity for different problems; DoF: Degrees of Freedom,  $\kappa$ : condition number, it: number of iterations in linear solver, time: CPU time used by linear solver including initialization of the preconditioner (median value over 11 runs). The linear solver is the (preconditioned) conjugate gradient method with residual tolerance  $10^{-12}$ .

(a) Without preconditioning.

1/h	CG(SD, $\vartheta$ )				PP(SD, $\vartheta$ ,L2)				PP(SD, $\vartheta$ ,wL2)			
	DoF	$\kappa$	it	Time	DoF	$\kappa$	it	Time	DoF	$\kappa$	it	Time
16	289	5505	151	0.0107	256	58	40	0.0018	256	3611	136	0.0073
32	1089	21114	443	0.1039	1024	220	85	0.0136	1024	12748	416	0.0766
64	4225	83607	1203	0.4129	4096	856	163	0.0413	4096	49475	1037	0.2893
128	16641	333602	2915	3.4805	16384	3372	307	0.2758	16384	196428	2350	2.2415

(b) With SSOR(1.5) preconditioner.

1/h	CG(SD, $\vartheta$ )				PP(SD, $\vartheta$ ,L2)				PP(SD, $\vartheta$ ,wL2)			
	DoF	$\kappa$	it	Time	DoF	$\kappa$	it	Time	DoF	$\kappa$	it	Time
16	289	9.1	27	0.0040	256	11.6	25	0.0026	256	10.6	27	0.0028
32	1089	30.2	43	0.0221	1024	39.2	38	0.0125	1024	33.8	41	0.0135
64	4225	110.6	77	0.0731	4096	146.2	62	0.0375	4096	121.8	69	0.0444
128	16641	424.7	147	0.4327	16384	567.7	109	0.2116	16384	465.3	126	0.2459

Table 8

Barrier problem. Computational complexity for different problems; DoF: Degrees of Freedom,  $\kappa$ : condition number, it: number of iterations in linear solver, time: CPU time used by linear solver including initialization of the preconditioner (median value over 11 runs). The linear solver is the (preconditioned) conjugate gradient method with residual tolerance  $10^{-12}$ . The grid resolution is kept constant at  $1/h = 64$ , but the permeability in the low permeable block,  $k_b$ , is varied.

(a) Without preconditioning.

$k_b$	CG(SD, $\vartheta$ )				PP(SD, $\vartheta$ ,L2)				PP(SD, $\vartheta$ ,wL2)			
	DoF	$\kappa$	it	Time	DoF	$\kappa$	it	Time	DoF	$\kappa$	it	Time
$10^{-1}$	4225	1885	275	0.1085	4096	856	161	0.0484	4096	1331	221	0.0665
$10^{-3}$	4225	83607	1203	0.4127	4096	856	163	0.0413	4096	49475	1037	0.2875
$10^{-5}$	4225	8328390	2565	0.9362	4096	856	163	0.0375	4096	4931220	2364	0.6897

(b) With SSOR(1.5) preconditioner.

$k_b$	CG(SD, $\vartheta$ )				PP(SD, $\vartheta$ ,L2)				PP(SD, $\vartheta$ ,wL2)			
	DoF	$\kappa$	it	Time	DoF	$\kappa$	it	Time	DoF	$\kappa$	it	Time
$10^{-1}$	4225	111	77	0.0649	4096	146	61	0.0369	4096	123	68	0.0372
$10^{-3}$	4225	111	77	0.0809	4096	146	62	0.0353	4096	122	69	0.0395
$10^{-5}$	4225	111	77	0.0934	4096	146	62	0.0467	4096	122	69	0.0506

see that the effect of the permeability contrast almost vanishes. Hence, for this problem, the SSOR preconditioner is able to remove the effect of the permeability contrast on the condition number.

#### 4.4. Channel problem

To further investigate the importance of harmonic averaging (objective (v)), consider now flow and transport through a channel with corners, see Fig. 8. The problem parameters are the same as for the barrier problem, except for the permeability distribution, which now forms a channel through the domain, and the boundary concentration,  $c_B$ , which is one into the channel and zero elsewhere. The channel has permeability  $k = 1$ , while the surroundings have permeability  $k = k_s \ll 1$ , so we expect most of the flow to be in the channel. We only consider harmonic averaging ( $\theta = \vartheta$ ), but use both the standard  $L^2$  norm and the weighted  $L^2$  norm for minimization in the postprocessing method, PP(SD, $\vartheta$ ,L2) and PP(SD, $\vartheta$ ,wL2), respectively. We study the cases  $k_s = 10^{-2}$  and  $k_s = 10^{-5}$ , and set  $\Delta t = 0.005$  and  $T = 2$ .

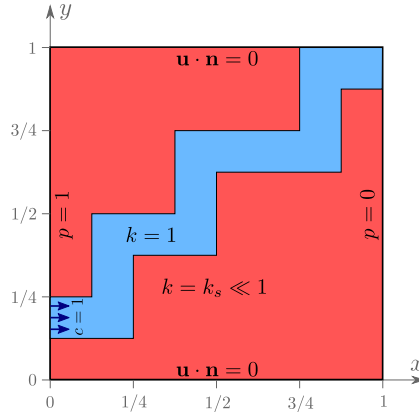


Fig. 8. Channel problem. Problem definition. Boundary conditions are  $p = 1$  on the left,  $p = 0$  on the right, and  $\mathbf{u} \cdot \mathbf{n} = 0$  on the bottom and top. The boundary concentration is  $c = 1$  into the channel only, and 0 elsewhere.

Table 9

Channel problem. Norm of residual,  $\|\mathcal{R}(\cdot)\|_{\mathcal{E}_h}$ , overshoot,  $\mathcal{O}(c_h)$ , and minimum and maximum value of concentration solution at  $t = 2$  for different flux approximations.

$k_s$	Method	$\ \mathcal{R}(U_h)\ _{\mathcal{E}_h}$	$\ \mathcal{R}(V_h)\ _{\mathcal{E}_h}$	$\mathcal{O}(c_h)$	$\min(c_h)$	$\max(c_h)$
$10^{-2}$	CG(SD, $\vartheta$ )	0.9646	–	0.05715	0	1.478
	PP(SD, $\vartheta$ ,L2)	–	3.6e-16	0	0	1.000
	PP(SD, $\vartheta$ ,wL2)	–	6.7e-16	0	0	1.000
$10^{-5}$	CG(SD, $\vartheta$ )	0.9915	–	0.06951	0	1.502
	PP(SD, $\vartheta$ ,L2)	–	4.2e-15	0	0	1.000
	PP(SD, $\vartheta$ ,wL2)	–	6.7e-16	0	0	1.000

The concentration solutions for the different scenarios are displayed in Fig. 9, and residuals, overshoot and minimum and maximum values are reported in Table 9. For  $k_s = 10^{-2}$ , we get  $c_h \gg 0$  in some areas outside but close to the channel. This seems reasonable, as the contrast in permeability is two orders of magnitude. However, for  $k_s = 10^{-5}$  the interface should be close to impermeable, and we expect very low concentrations outside the channel. For CG(SD, $\vartheta$ ), we observe that  $c_h \sim 0$  outside the channel for  $k = 10^{-5}$ , but that  $c_h > 1$  in many elements due to lack of local conservation (Figs. 9(a) and 9(d)). For the case PP(SD, $\vartheta$ ,L2), we see that the difference in solution for  $k_s = 10^{-2}$  and  $k_s = 10^{-5}$  is rather small, and that  $1 > c_h \gg 0$  for some elements outside the channel also for  $k_s = 10^{-5}$  (Figs. 9(b) and 9(e)). This is problematic, since the interface should be close to impermeable. If we instead minimize in the weighted  $L^2$  norm, PP(SD, $\vartheta$ ,wL2), we are able to resolve this issue so that the interface is close to impermeable (Figs. 9(c) and 9(f)).

The shortcoming of postprocessing with the standard  $L^2$  norm is that it does not take the permeability contrast into account. Let  $F$  be a face on the boundary of the channel. With harmonic averaging,  $U_h|_F \sim 0$ . However, in the minimization step without weighting, we allow for a flux correction that is small in absolute value compared to fluxes on faces inside the channel, but still relatively large compared to  $U_h|_F$ . Thus,  $V_h|_F$  might be orders of magnitude larger than  $U_h|_F$ , resulting in a more permeable interface. When we use the weighted  $L^2$  norm,  $F$  is given a large weight (the inverse of the effective permeability,  $k_e$ ), so that we do not allow for such large relative correction.

#### 4.5. Well pair problem

Next, we consider a simplified well scenario, and focus on objective (vii) for a problem with non-zero right hand side. Still, we let  $\beta = 0$  and  $\Omega = (0, 1)^2$ , but now  $\mathbf{K} = k\mathbb{I}$ , where  $k = 1$  if  $x \leq 0.5$  and  $k = 10^{-3}$  otherwise. Next, we model a injector/producer well pair by setting  $q = 100$  in the lower left corner and  $q = -100$  in the upper right

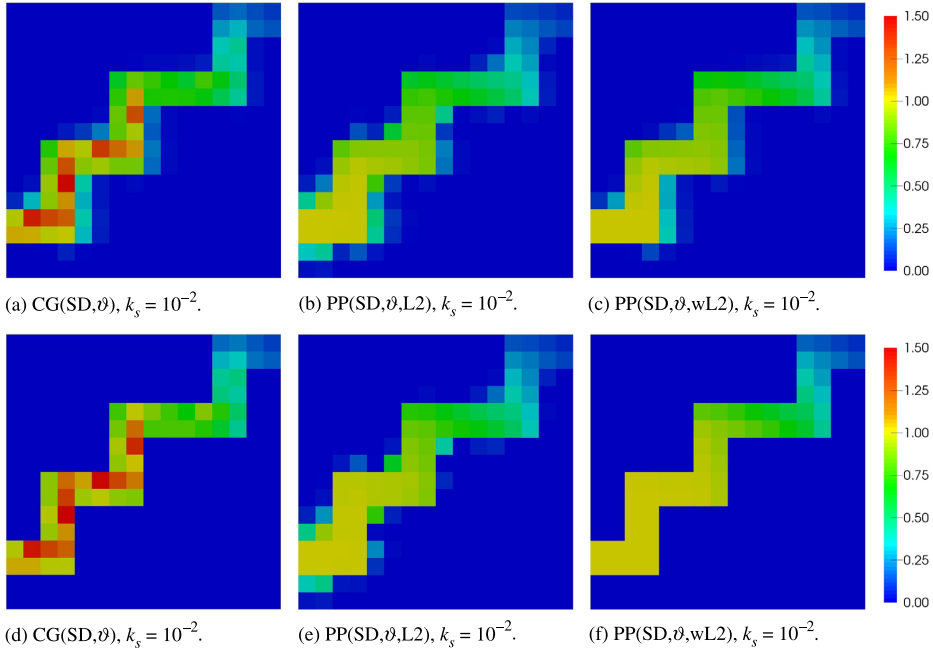


Fig. 9. Channel problem. Concentration solutions at  $t = 2$  for different flux approximations (left to right) and different permeability outside channel (top and bottom). Harmonic averaging is used for calculations of the CG flux,  $U_h$ , in all cases.

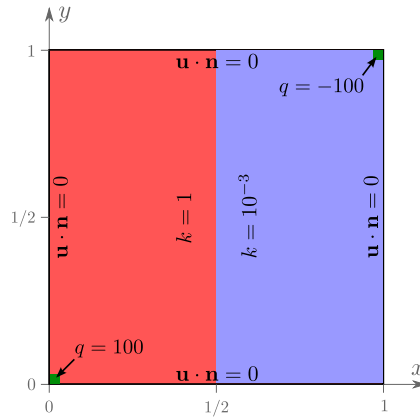


Fig. 10. Well pair problem. Problem definition. The green squares where  $q \neq 0$  in the lower left and upper right corner have size  $1/32 \times 1/32$ .

corner. See Fig. 10 for a sketch. The initial condition is  $c_0 = 0$  and the concentration of the injected fluid,  $c_w = 1.0$ . We assume a pure Neumann boundary with  $u_B = 0$ . The coupled flow and transport problem is solved on quadratic grids with  $h = \{1/16, 1/32, 1/64\}$  and  $\Delta t = 0.01$ . We only consider harmonic average in the calculations of the CG flux and use the weighted  $L^2$  norm for minimization in the postprocessing method (CG(SD, $\vartheta$ ) and PP(SD, $\vartheta$ ,wL2)).

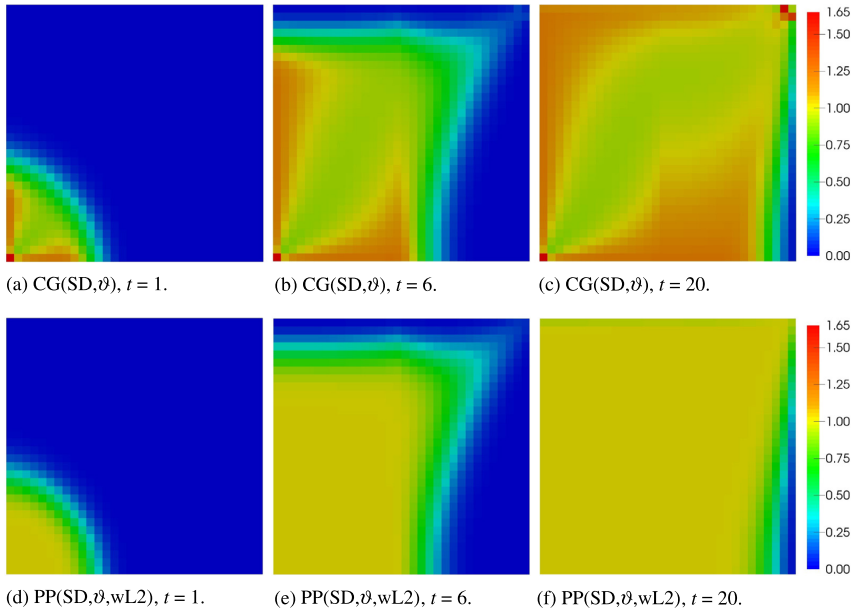


Fig. 11. Well pair problem. Concentration solution with CG flux (top row), and postprocessed flux (bottom row) at different times (left to right) on a quadratic grid with  $h = 1/32$ .

Table 10

Well pair problem. Norm of residual,  $\|\mathcal{R}(\cdot)\|_{\mathcal{E}_h}$ , overshoot,  $\mathcal{O}(c_h)$ , and minimum and maximum value of concentration solution at  $t = 10$  for different flux approximations.

$h$	Method	$\ \mathcal{R}(U_h)\ _{\mathcal{E}_h}$	$\ \mathcal{R}(V_h)\ _{\mathcal{E}_h}$	$\mathcal{O}(c_h)$	$\min(c_h)$	$\max(c_h)$
1/16	CG(SD, $\vartheta$ )	0.3162	–	0.0558	0.00508	1.217
	PP(SD, $\vartheta$ , wL2)	–	1.6e-16	0	0.00477	1.000
1/32	CG(SD, $\vartheta$ )	2.0928	–	0.0616	2.3e-5	1.652
	PP(SD, $\vartheta$ , wL2)	–	1.4e-15	1.4e-17	2.0e-5	1.000
1/64	CG(SD, $\vartheta$ )	1.5247	–	0.0102	3.9e-10	1.399
	PP(SD, $\vartheta$ , wL2)	–	1.6e-15	2.8e-15	4.2e-10	1.000

The concentration solution at different times for the grid with  $h = 1/32$  is shown in Fig. 11. The concentration is produced in the lower left corner and moves towards the source in the upper right corner. The difference between CG(SD,  $\vartheta$ ) and PP(SD,  $\vartheta$ , wL2) is significant and the maximum principle  $c_h \leq 1$  is violated for CG(SD,  $\vartheta$ ). Postprocessing is necessary to produce an acceptable concentration solution.

Similar results at  $t = 10$  for quadratic grids with  $h = \{1/16, 1/32, 1/64\}$  are shown in Fig. 12. Furthermore, residuals, overshoot and minimum and maximum values are given in Table 10. Evidently, the difference in concentration solution is smaller for smaller  $h$ . This is as expected since CG converges to the true solution, which is locally conservative. The area where  $c_h > 1$  seems to cluster around the sink and source for  $h = 1/64$ .

A quantity of interest for such well problem is the production rate at the producer,

$$PR(t) = \frac{1}{\Delta t} \int_{t-\Delta t}^t \int_{\Omega_w} qc, \tag{4.4}$$

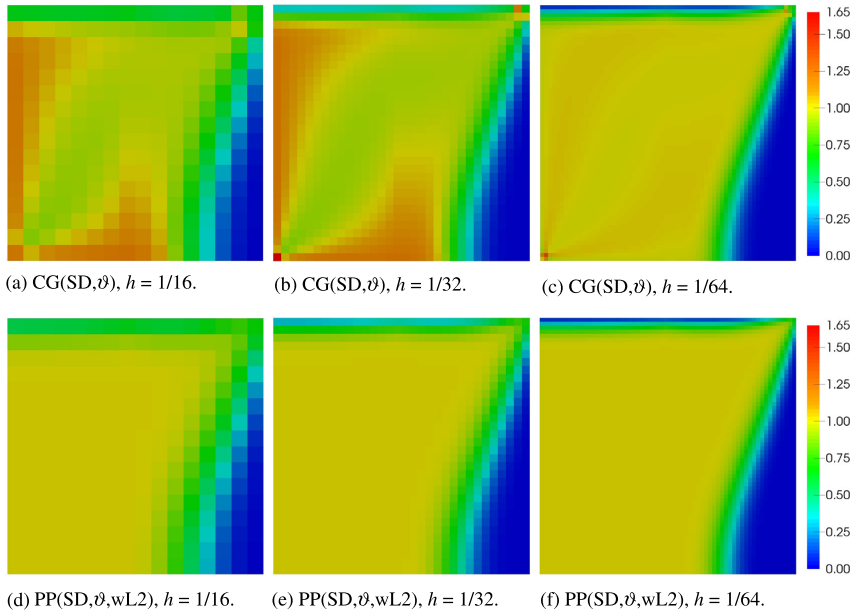


Fig. 12. Well pair problem. Concentration solution without (top row) and with (bottom row) postprocessing at  $t = 10$  on quadratic grids with different  $h$ .

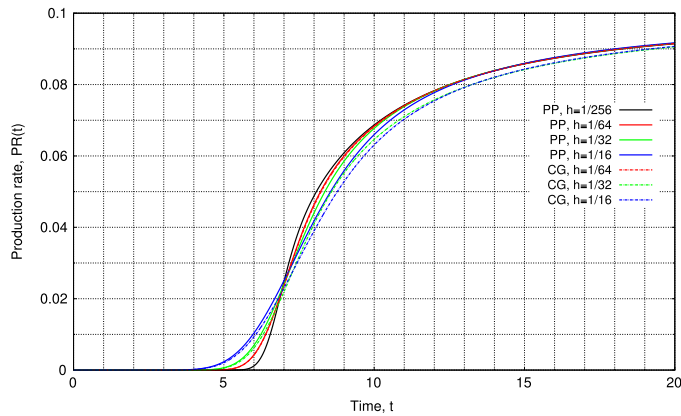


Fig. 13. Well pair problem. Production rate, PR(t), for different  $h$  and flux.

where  $\Omega_w$  is the sink part of  $\Omega$ , i.e.,  $\Omega_w = \{x \in \Omega : q(x) < 0\}$ . For this example  $\Omega_w = \left[\frac{31}{32}, 1\right]^2$ . The production rate is plotted against time for different  $h$  in Fig. 13, where a reference curve from a simulation with  $h = 1/256$  is included. Although not prominent, we see that we get different curves whether we use CG flux or postprocessed flux, and that this effect is largest for the coarsest grid. We get an earlier breakthrough (smallest  $t$  where  $PR(t) > 0$ ) for larger  $h$ . This is due to numerical dispersion.



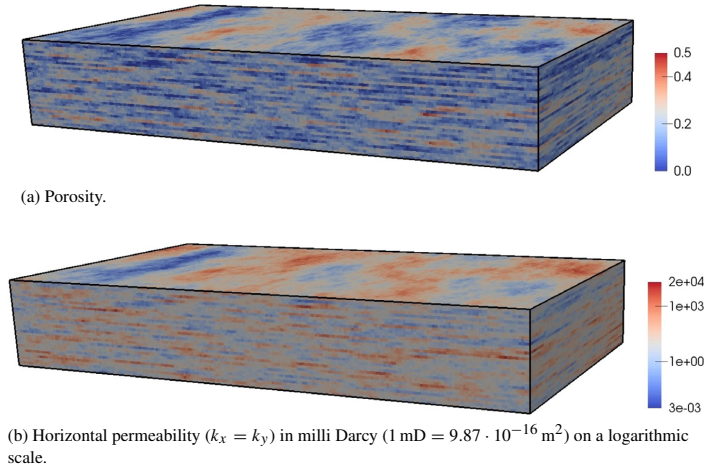


Fig. 14. SPE-10 model. Highly heterogeneous model given on a Cartesian mesh with  $220 \times 60 \times 85 = 462\,000$  regular hexahedral elements, each of size  $10 \times 20 \times 2$  feet. The model dimensions are  $2200 \times 1200 \times 170$  feet (these figures are scaled by a factor 5 in the vertical direction).

#### 4.6. SPE-10 model

Our last example is based on the SPE-10 model [46], and serves as a test problem to verify objective (i), (v), (vi) and (vii) for a realistic 3D model. The SPE-10 model was originally introduced as a benchmark problem for upscaling, but it has also been used in many studies addressing other aspects of flow in porous media. We consider the top 35 layers of the original model, representing the Tarbert formation, see Fig. 14. This model is given on a Cartesian mesh with 462 000 regular hexahedral elements. The permeability is cellwise constant and anisotropic such that the permeability tensor can be written as a diagonal tensor with entries  $k_x, k_y, k_z$  ( $k_x = k_y$ ). Observe from Fig. 14 that the model is highly heterogeneous. To work with realistic data, we will set the fluid viscosity to  $\mu = 10^{-3} \text{ Pa} \cdot \text{s}$ , in contrast to the rest of this work. We consider incompressible flow with no source ( $\beta = 0, q = 0$ ). As boundary conditions, we set  $p = 10^9 \text{ Pa}$  on the left boundary,  $p = 0$  on the right boundary, and no-flow conditions ( $\mathbf{u} \cdot \mathbf{n} = 0$ ) elsewhere. Regarding linear solver, we use the preconditioned conjugate gradient method with a general algebraic multigrid preconditioner (AMG) available through the Trilinos Project [47].

Table 11 report on the degrees of freedom (DoF), number of iterations (it), the CPU time used by the linear solver (time) and the norm of the residual, both for the CG problem and the postprocessing problem with and without the weighted norm. First observe that the residual is non-zero for the CG flux, and zero (below solver tolerance) for the postprocessed fluxes. Hence, our methods and implementations work also for this realistic 3D problem. Furthermore, we see that the computational complexity of  $\text{PP}(\text{SD}, \vartheta, \text{L2})$  is lower than  $\text{PP}(\text{SD}, \vartheta, \text{wL2})$ . This means that minimization in the weighted norm leads to worse conditioning of the system matrix. The time spent to solve  $\text{PP}(\text{SD}, \vartheta, \text{L2})$  and  $\text{PP}(\text{SD}, \vartheta, \text{wL2})$  compared to  $\text{CG}(\text{SD}, \vartheta)$  is about 9% and 30%, respectively.

To check the influence of the anisotropic permeability on the linear solver time, we run the same case but with isotropic permeability such that  $k_z = k_x (= k_y)$ . For this scenario the CPU time used by the linear solver was 20.34, 3.20 and 3.50 for  $\text{CG}(\text{SD}, \vartheta)$ ,  $\text{PP}(\text{SD}, \vartheta, \text{L2})$  and  $\text{PP}(\text{SD}, \vartheta, \text{wL2})$ , respectively. Comparing with the anisotropic case (Table 11), we observe that anisotropic permeability leads to worse conditioning for  $\text{CG}(\text{SD}, \vartheta)$  and  $\text{PP}(\text{SD}, \vartheta, \text{wL2})$ . The run time for  $\text{PP}(\text{SD}, \vartheta, \text{L2})$  is unchanged since the system matrix is independent on the permeability. With isotropic permeability, the linear solver time for  $\text{PP}(\text{SD}, \vartheta, \text{wL2})$  is about 17% of that of  $\text{CG}(\text{SD}, \vartheta)$ .

For the anisotropic case, we also consider the transport problem. We let  $c_B = 1.0$  on the inflow boundary ( $x = 0$ ) and use time steps  $\Delta t = 10^4 \text{ s}$ . The concentration solutions with  $\text{PP}(\text{SD}, \vartheta, \text{L2})$  and  $\text{PP}(\text{SD}, \vartheta, \text{wL2})$  are shown in Figs. 15 and 16, respectively. Both solutions obey the maximum principle, but we see that without weighting (Fig. 15) the vertical flow between layers with high permeability contrast is higher. Hence, the application of the weighted norm seems to better preserve low permeable interfaces. We do not display similar results for  $\text{CG}(\text{SD}, \vartheta)$  because we get a

Table 11  
 SPE-10 model. Computational complexity for different problems; DoF: Degrees of Freedom, it: number of iterations in linear solver, time: CPU time used by the linear solver including initialization of the preconditioner (median value over 11 runs). The linear solver is the conjugate gradient method with an AMG preconditioner with residual tolerance  $10^{-6}$ .

Problem	DoF	it	time	$\ \mathcal{R}\ _{\mathcal{E}_h}$
CG(SD, $\vartheta$ )	485316	105	33.58	2.5e-2
PP(SD, $\vartheta$ ,L2)	462000	10	3.14	2.0e-8
PP(SD, $\vartheta$ ,wL2)	462000	55	9.97	4.3e-8

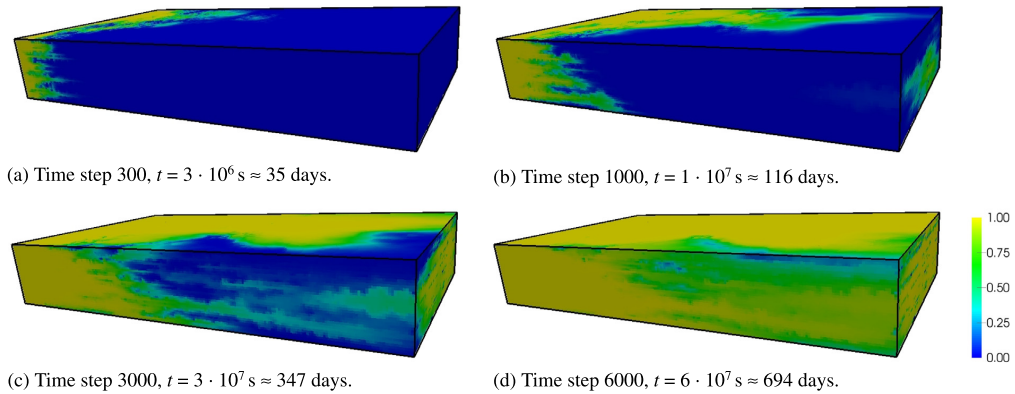


Fig. 15. SPE-10 model. Concentration solution with postprocessed flux without weighting, PP(SD, $\vartheta$ ,L2).

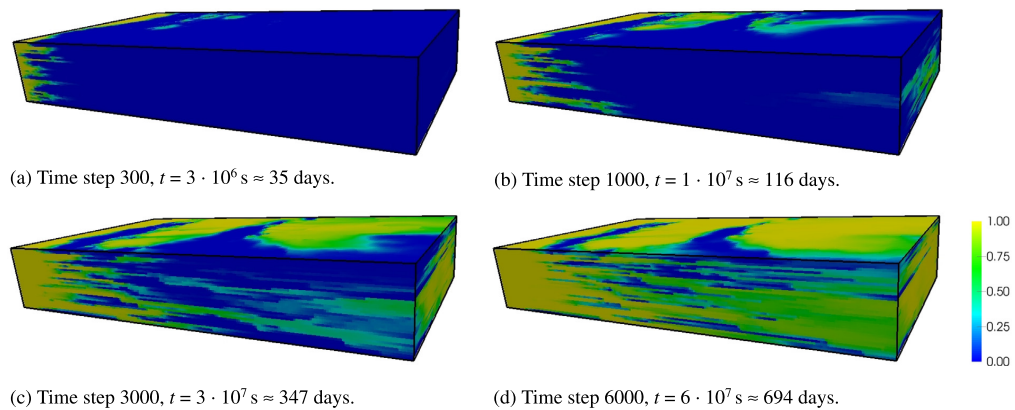


Fig. 16. SPE-10 model. Concentration solution with postprocessed flux with weighting, PP(SD, $\vartheta$ ,wL2).

totally unphysical solution. Instead, Fig. 17, shows the time evolution of  $\max(c_h)$  and  $\mathcal{O}(c_h)$  with CG(SD, $\vartheta$ ). Clearly, the maximum principle is far from satisfied.

### 5. Conclusions

Eq. (3.27), defines a general purpose postprocessing method, where a minimal piecewise constant correction term is added to the flux. Local conservation, uniqueness and preservation of convergence order are proven and summarized

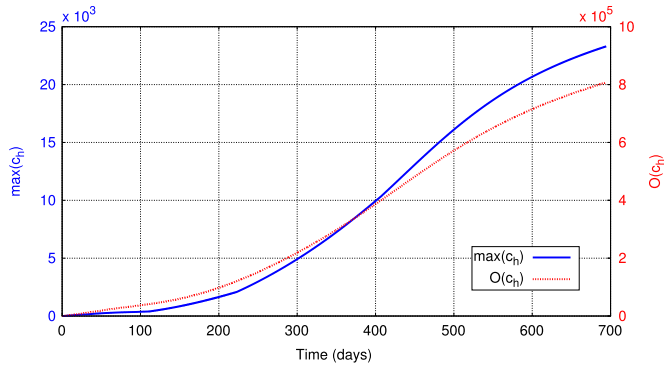


Fig. 17. SPE-10 model. Maximal concentration,  $\max(c_h)$ , and overshoot,  $O(c_h)$ , for concentration solution with CG(SD,  $\vartheta$ ). For the reference, we have  $\max(c_h) = 1.00006$  and  $O(c_h) = 0.019$  at  $t = 694$  days with PP(SD,  $\vartheta$ , wL2).

in [Theorem 1](#). Our method applies to any flux approximation in  $L^1(\mathcal{F}_h)$  and for a wide range of grids, including non-conforming and unstructured grids. It can also be used for the time dependent flow model.

Through a series of numerical examples, we have demonstrated that our method produces locally conservative flux. It is verified numerically that the postprocessed flux has the same order of convergence as the original flux. Moreover, our numerical examples clearly demonstrates the importance of locally conservative flux when coupling with a DG solver for the transport equation. Lack of local conservation may produce unphysical solutions.

The postprocessing algorithm is global in the sense that a system of  $N$  linear equations has to be solved, where  $N$  is the number of elements (or cells). However, the system matrix is symmetric and sparse and only dependent on the permeability (through the weights) and the grid. If the grid is constant or only altered occasionally, we can allow for a preconditioner that is relatively costly to initialize.

For flux approximations from CG, where the pressure gradient is discontinuous across element faces, it is favorable to use harmonic averaging to calculate the flux. A novelty of this work compared to [\[9\]](#) and [\[10\]](#) is that we minimize the correction term in a weighted  $L^2$  norm with weights equal to the inverse of the effective face permeability. This better preserves low permeable interfaces, and numerical examples demonstrate that no weighting (standard  $L^2$  norm) tends to weaken the effect of harmonic averaging.

The computational complexity of solving the linear system associated with the postprocessing step compared to that of solving the linear system for the CG problem was measured. For the synthetic 2D barrier problem, the additional cost was significant ( $\sim 60\%$ ). However, for the larger 3D SPE-10 model, the additional cost was smaller, 10%–30%, depending on anisotropy and choice of weights. This indicates that the postprocessing method is reasonable also in terms of computational efficiency. The difference in computational complexity of applying the weighted norm was small for isotropic permeability as long as an appropriate preconditioner, such as SSOR or AMG, was used. For anisotropic permeability the difference was larger. We stress that in this work we only considered general purpose preconditioners. Using a taylored preconditioner that can handle the weights better might further improve the efficiency.

Different treatment of fluxes on Dirichlet boundaries for non-Cartesian grids showed only little effect on the postprocessed flux.

## Acknowledgments

LHO thanks the Center for Subsurface Modeling at ICES, UT Austin, for hosting his research stay the first half of 2015. In particular, thanks to Gergina Pencheva, Sanghyun Lee and Prashant Mital for constructive discussions of the current work. LHO is funded by VISTA (Grant No. 6355) — a basic research program funded by Statoil, conducted in close collaboration with The Norwegian Academy of Science and Letters. MGL was supported in part by the Swedish Foundation for Strategic Research Grant No. AM13-0029 (MGL) and the Swedish Research Council Grant No 2013-4708.

## References

- [1] S. Mishra, W.E. Brigham, F.M. Orr Jr., Tracer- and pressure-test analysis for characterization of areally heterogeneous reservoirs, *SPE Formation Eval.* (1991) 45–54.
- [2] C. Dawson, S. Sun, M.F. Wheeler, Compatible algorithms for coupled flow and transport, *Comput. Methods Appl. Mech. Engrg.* 193 (23) (2004) 2565–2580.
- [3] M.F. Wheeler, An elliptic collocation-finite element method with interior penalties, *SIAM J. Numer. Anal.* 15 (1) (1978) 152–161.
- [4] S. Sun, M.F. Wheeler, Symmetric and nonsymmetric discontinuous Galerkin methods for reactive transport in porous media, *SIAM J. Numer. Anal.* 43 (1) (2005) 195–219.
- [5] M. Ainsworth, J.T. Oden, *A Posteriori Error Estimation in Finite Element Analysis*, Wiley, 2000.
- [6] T. Kvamsdal, Variationally consistent postprocessing, in: S. Idelsohn, E. Onate, E. Dvorkin (Eds.), *Proceedings for Computational Mechanics, New Trends and Applications*, CIMNE, Barcelona, 1998.
- [7] T.J. Hughes, G. Engel, L. Mazzei, M.G. Larson, The continuous Galerkin method is locally conservative, *J. Comput. Phys.* 163 (2) (2000) 467–488.
- [8] H. Melbø, T. Kvamsdal, Goal oriented error estimators for Stokes equations based on variationally consistent postprocessing, *Comput. Methods Appl. Mech. Engrg.* 192 (5) (2003) 613–633.
- [9] M.G. Larson, A.J. Niklasson, A conservative flux for the continuous Galerkin method based on discontinuous enrichment, *Calcolo* 41 (2) (2004) 65–76.
- [10] S. Sun, M.F. Wheeler, Projections of velocity data for the compatibility with transport, *Comput. Methods Appl. Mech. Engrg.* 195 (7) (2006) 653–673.
- [11] B. Cockburn, J. Gopalakrishnan, H. Wang, Locally conservative fluxes for the continuous Galerkin method, *SIAM J. Numer. Anal.* 45 (4) (2007) 1742–1776.
- [12] L. Bush, V. Ginting, On the application of the continuous Galerkin finite element method for conservation problems, *SIAM J. Sci. Comput.* 35 (6) (2013) A2953–A2975.
- [13] L.H. Odsæter, T. Kvamsdal, M.F. Wheeler, A postprocessing technique to produce locally conservative flux, in: A. Berezovski, K. Tamm, T. Peets (Eds.), *28th Nordic Seminar on Computational Mechanics, CENS*, Institute of Cybernetics at Tallinn University of Technology, Tallinn, 2015, pp. 129–132.
- [14] Q. Deng, V. Ginting, Construction of locally conservative fluxes for high order continuous Galerkin finite element methods, Preprint arXiv:1603.06999, 2016.
- [15] R. Becker, D. Capatina, R. Luce, Local flux reconstructions for standard finite element methods on triangular meshes, *SIAM J. Numer. Anal.* 54 (4) (2016) 2684–2706.
- [16] S. Chippada, C. Dawson, M. Martinez, M. Wheeler, A projection method for constructing a mass conservative velocity field, *Comput. Methods Appl. Mech. Engrg.* 157 (1) (1998) 1–10.
- [17] S. Sun, J. Liu, A locally conservative finite element method based on piecewise constant enrichment of the continuous Galerkin method, *SIAM J. Sci. Comput.* 31 (4) (2009) 2528–2548.
- [18] S. Lee, Y.-J. Lee, M.F. Wheeler, A locally conservative enriched Galerkin approximation and efficient solver for elliptic and parabolic problems, *SIAM J. Sci. Comput.* (2016).
- [19] M.F. Wheeler, A Galerkin procedure for estimating the flux for two-point boundary value problems, *SIAM J. Numer. Anal.* 11 (4) (1974) 764–768.
- [20] T. Dupont, A unified theory of superconvergence for Galerkin methods for two-point boundary problems, *SIAM J. Numer. Anal.* 13 (3) (1976) 362–368.
- [21] J. Douglas Jr., T. Dupont, M.F. Wheeler, A Galerkin procedure for approximating the flux on the boundary for elliptic and parabolic boundary value problems, *RAIRO Anal. Numér.* 8 (2) (1974) 47–59.
- [22] J.A. Wheeler, Simulation of heat transfer from a warm pipeline buried in permafrost, in: *74th National Meeting of the American Institute of Chemical Engineers*, New Orleans, March, 1973, p. 43.
- [23] P. Ladeveze, D. Leguillon, Error estimate procedure in the finite element method and applications, *SIAM J. Numer. Anal.* 20 (3) (1983) 485–509.
- [24] M.F. Wheeler, J. Whiteman, Superconvergent recovery of gradients on subdomains from piecewise linear finite-element approximations, *Numer. Methods Partial Differential Equations* 3 (4) (1987) 357–374.
- [25] M.F. Wheeler, J. Whiteman, Superconvergence of recovered gradients of discrete time/piecewise linear Galerkin approximations for linear and nonlinear parabolic problems, *Numer. Methods Partial Differential Equations* 10 (3) (1994) 271–294.
- [26] M.F. Wheeler, I. Yotov, A multipoint flux mixed finite element method, *SIAM J. Numer. Anal.* 44 (5) (2006) 2082–2106.
- [27] I. Aavatsmark, An introduction to multipoint flux approximations for quadrilateral grids, *Comput. Geosci.* 6 (3–4) (2002) 405–432.
- [28] P. Chatzipantelidis, V. Ginting, R. Lazarov, A finite volume element method for a non-linear elliptic problem, *Numer. Linear Algebra Appl.* 12 (5–6) (2005) 515–546.
- [29] F. Brezzi, K. Lipnikov, M. Shashkov, Convergence of mimetic finite difference method for diffusion problems on polyhedral meshes with curved faces, *Math. Models Methods Appl. Sci.* 16 (02) (2006) 275–297.
- [30] B. Rivière, M.F. Wheeler, V. Girault, Improved energy estimates for interior penalty, constrained and discontinuous Galerkin methods for elliptic problems. Part I, *Comput. Geosci.* 3 (3–4) (1999) 337–360.
- [31] C. Kees, M. Farthing, C. Dawson, Locally conservative, stabilized finite element methods for variably saturated flow, *Comput. Methods Appl. Mech. Engrg.* 197 (51) (2008) 4610–4625.
- [32] T. Povich, C. Dawson, M.W. Farthing, C.E. Kees, Finite element methods for variable density flow and solute transport, *Comput. Geosci.* 17 (3) (2013) 529–549.

- [33] L. Beirão da Veiga, G. Manzini, M. Putti, Post processing of solution and flux for the nodal mimetic finite difference method, *Numer. Methods Partial Differential Equations* 31 (1) (2015) 336–363.
- [34] C. Scudeler, M. Putti, C. Paniconi, Mass-conservative reconstruction of Galerkin velocity fields for transport simulations, *Adv. Water Resour.* 94 (2016) 470–485.
- [35] Y.W. Bekele, T. Kvamsdal, A.M. Kvarving, S. Nordal, Adaptive isogeometric finite element analysis of steady-state groundwater flow, *Int. J. Numer. Anal. Methods Geomech.* (2015).
- [36] X.-H. Wu, R.R. Parashkevov, M.T. Stone, S.L. Lyons, Global scale-up on reservoir models with piecewise constant permeability field, *J. Algorithms Comput. Technol.* 2 (2) (2008) 223–248.
- [37] D. Schiavazzi, *Redundant Multiresolution Uncertainty Propagation* (Ph.D. thesis), University of Padova, 2013.
- [38] E. Burman, P. Zunino, A domain decomposition method based on weighted interior penalties for advection-diffusion-reaction problems, *SIAM J. Numer. Anal.* 44 (4) (2006) 1612–1638.
- [39] A. Ern, A.F. Stephansen, P. Zunino, A discontinuous Galerkin method with weighted averages for advection–diffusion equations with locally small and anisotropic diffusivity, *IMA J. Numer. Anal.* (2008).
- [40] M.F. Wheeler, A priori L2 error estimates for Galerkin approximations to parabolic partial differential equations, *SIAM J. Numer. Anal.* 10 (4) (1973) 723–759.
- [41] G. Carey, Derivative calculation from finite element solutions, *Comput. Methods Appl. Mech. Engrg.* 35 (1) (1982) 1–14.
- [42] G. Carey, S. Chow, M. Seager, Approximate boundary-flux calculations, *Comput. Methods Appl. Mech. Engrg.* 50 (2) (1985) 107–120.
- [43] A. Pehlivanov, R. Lazarov, G. Carey, S. Chow, Superconvergence analysis of approximate boundary-flux calculations, *Numer. Math.* 63 (1) (1992) 483–501.
- [44] W. Bangerth, R. Hartmann, G. Kanschat, Deal.II—a general-purpose object-oriented finite element library, *ACM Trans. Math. Software* 33 (4) (2007).
- [45] M. Ainsworth, A. Craig, A posteriori error estimators in the finite element method, *Numer. Math.* 60 (1) (1991) 429–463.
- [46] M. Christie, M. Blunt, et al., Tenth SPE comparative solution project: A comparison of upscaling techniques, in: *SPE Reservoir Simulation Symposium*, Society of Petroleum Engineers, 2001.
- [47] M.A. Heroux, R.A. Bartlett, V.E. Howle, R.J. Hoekstra, J.J. Hu, T.G. Kolda, R.B. Lehoucq, K.R. Long, R.P. Pawlowski, E.T. Phipps, A.G. Salinger, H.K. Thornquist, R.S. Tuminaro, J.M. Willenbring, A. Williams, K.S. Stanley, An overview of the Trilinos project, *ACM Trans. Math. Software* 31 (3) (2005) 397–423.

## Paper III

**A simple embedded discrete fracture-matrix model for a coupled flow and transport problems in porous media**

Odsæter, L.H., Kvamsdal, T., and Larson, M.G.

Preprint, submitted to *Computer Methods in Applied Mechanics and Engineering*, 2018



# A simple embedded discrete fracture-matrix model for a coupled flow and transport problem in porous media

Lars H. Odsæter<sup>a,\*</sup>, Trond Kvamsdal<sup>a</sup>, Mats G. Larson<sup>b</sup>

<sup>a</sup>*Department of Mathematical Sciences, NTNU Norwegian University of Science and Technology,  
Alfred Getz' vei 1, 7491 Trondheim, Norway*

<sup>b</sup>*Department of Mathematics and Mathematical Statistics, Umeå University, SE-901 87 Umeå, Sweden*

---

## Abstract

Accurate simulation of fluid flow and transport in fractured porous media is a key challenge in subsurface reservoir engineering. Due to the high ratio between its length and width, fractures can be modeled as lower dimensional interfaces embedded in the porous rock. We apply a recently developed embedded finite element method (EFEM) for the Darcy problem. This method allows for general fracture geometry, and the fractures may cut the finite element mesh arbitrarily. We present here a velocity model for EFEM and couple the Darcy problem to a transport problem for a passive solute. The main novelties of this work is a locally conservative velocity approximation derived from the EFEM solution, and the development of a lowest order upwind finite volume method for the transport problem. This numerical model is compatible with EFEM in the sense that the same computational mesh may be applied, so that we retain the same flexibility with respect to fracture geometry and meshing. Hence, our coupled solution strategy represents a simple approach in terms of formulation, implementation and meshing. We demonstrate our model by some numerical examples on both synthetic and realistic problems, including a benchmark study for single-phase flow. Despite the simplicity of the method, the results are promising.

*Keywords:* Discrete fracture-matrix model, Embedded interface, Finite element method, Finite volume method, Porous media flow

---

## 1. Introduction

Modeling fluid flow in fractured porous media is an important yet challenging problem in subsurface engineering. Fractures are characterized as thin layers with either very high or low conductivity. They can therefore act as preferential paths or barriers and be essential to the fluid flow. The fracture width is typically several orders of magnitude smaller than any other characteristic sizes in the reservoir, and the flow rate can be orders of magnitude larger or smaller than in the surrounding matrix. This pose great challenges to the fracture model and the numerical method.

In this work we consider a discrete fracture-matrix (DFM) model, where the fractures are modeled as lower dimensional interfaces embedded in the rock matrix. We assume Darcy flow both in the matrix and the fracture, and we only consider the case where the permeability in the fractures are orders of magnitude larger than in the matrix. As flow model we consider incompressible single-phase flow governed by conservation of mass and Darcy's law. The flow problem is then coupled to a transport problem for a passive solute.

A common strategy to represent fractures in a DFM model is by averaging the governing equations across the fractures. The fracture width is then modeled as a coefficient in the equations rather than a geometrical property, and suitable coupling conditions between the fracture and matrix equations are applied. Common terminologies for such approximations are mixed-dimensional, hybrid-dimensional or reduced models. A

---

\*Corresponding author

Email address: [lars.odsater@gmail.com](mailto:lars.odsater@gmail.com) (Lars H. Odsæter)



method for the high permeability case was presented in [1, 2], where the flow equations on mixed form are averaged over the interface assuming a continuous pressure. This model was later generalized by [3] and [4] to also handle the low permeability case, where a Robin type condition on the pressure at the interface is enforced. More recent DFM models similar to [3, 4] can be found in, e.g., [5–10].

To account for more general fracture shapes, the model in [1, 2] was extended to curved fractures in [11, 12]. These models are derived by considering the asymptotic limit in the weak formulation as the fracture width tends to zero and the fracture permeability tends to infinity. In this limit, the condition of a continuous pressure follows. We mention that this model was extended to allow for pressure jumps across the interface in [12].

An embedded finite element method (EFEM) for the model in [12] was derived in [13]. Fractures are allowed to cut through the elements arbitrarily, and the fracture solution is represented by the restriction of the basis functions for the higher dimensional matrix elements. Contributions from the fracture to the fluid flow is included by superposition. A great advantage of this method is that it handles very general fracture geometry, including curved interfaces, bifurcations and intersections, and it is also easy to implement. The assumption of a continuous pressure along the fracture interface is a key ingredient as it allows for continuous elements. However, the normal flux is discontinuous across the fracture interface leading to loss of regularity, which can be resolved by local refinement close to the fractures based on an a priori error estimate. In this work, we apply EFEM for the pressure problem.

For the family of lower dimensional DFM models where the pressure is not assumed to be continuous, a great variety of numerical methods are suggested. We mention for instance finite element methods [4, 14, 15], finite volume methods [5, 16, 17], discontinuous Galerkin methods [18], mimetic finite difference methods [19, 20] and virtual element methods [21], all of which require a conforming mesh across the fracture interface. Different schemes with mortar coupling that allows for non-conforming meshes are presented in, e.g., [6, 10], but still the mesh needs to explicitly represent the fractures. Fully non-conforming discretizations have been realized through extended finite elements [8, 12, 22, 23].

The embedded DFM (EDFM) introduced by [24] is another approach where the fractures are allowed to cut arbitrarily through the higher dimensional mesh, see also [25–29] for newer contributions. EDFM is based on the two-point flux approximation (TPFA) where the fracture-fracture and fracture-matrix transmissibilities are approximated from geometrical quantities. Similar to EFEM, they are only valid for high permeability fractures, but the recently introduced projection-based EDFM (pEDFM) [30, 31] are also able to handle low permeability fractures. An important difference to EFEM is that the fractures are represented by their own lower dimensional elements along the fracture interface.

A comprehensive comparison of several DFM models for single-phase flow was conducted in a recent benchmark study [32]. We follow up on this study and evaluate EFEM on a selection of these benchmark problems.

The transport problem is also modeled by a reduced (or mixed-dimensional) model, see e.g., [2, 21, 33], where a coupling term models flow between the fracture and the matrix. We assume advection dominated flow since we are primarily interested in the coupling with the flow problem. In this work we present a novel discretization that is compatible with EFEM in the sense that the same computational mesh can be applied. This ensures that we have the same flexibility in terms of fracture geometry and meshing for the coupled solution strategy as is the case for EFEM. More specifically, we apply a zeroth order upwind finite volume method (FVM), where the fracture solution is represented by elements cut by the fracture, and where the coupling term is approximated in a non-standard way by evaluating the normal velocity (flux) on the boundary of such elements. We mention here that an alternative approach is to use the CutFEM technology, see [34] for a stationary convection problem and [35] for a general introduction to CutFEM. For compatibility of the numerical solvers, we must require the velocity approximation from the flow problem to be locally conservative. This is not directly obtained by EFEM, but is achieved through a postprocessing step [36].

We mention that combining FEM and FVM for heterogeneous and fractured porous media have been studied before, e.g., the finite element–finite volume method [37, 38], where FEM is used for the flow problem and a node-centered finite volume method is used for transport. This method was extended in [39] to allow for a discontinuous solution across interfaces for the transport problem. However, this approach requires

fractures to be aligned with element boundaries and uses a dual mesh for the transport solver.

This paper is organized as follows. In Section 2 we describe the discrete fracture-matrix models and the governing equations for the coupled flow and transport problem. Next, in Section 3, we define the numerical methods. This includes EFEM for the flow problem, FVM for the transport problem, and the velocity approximation which couples the two subproblems. In Section 4 some numerical results are presented, including a realistic problem with a complex fracture network. Finally, we make some concluding remarks in Section 5.

## 2. Model formulation

As model problem we consider incompressible single-phase flow with advective transport of a concentration in a fractured porous media. Let  $\Omega \in \mathbb{R}^d$ , with  $d = 2, 3$ , be a convex polygonal domain with an embedded interface  $\Gamma$  representing the fractures. The bulk domain  $\Omega \setminus \Gamma$  will be referred to as the matrix. We denote by  $\boldsymbol{\kappa}$  and  $\phi$  the symmetric positive definite permeability tensor and porosity of the matrix, respectively. The fracture permeability is assumed to be isotropic and is denoted  $\kappa_\Gamma$ . We denote by  $w$  and  $\phi_\Gamma$  the fracture aperture and the porosity of the fractures, respectively. Moreover,  $k_\Gamma = w\kappa_\Gamma$  is the effective (scaled by fracture aperture) fracture permeability. Next,  $q$  and  $q_\Gamma$  denotes source or sink terms in the matrix and fractures, respectively. The primary unknowns are the fluid pressure  $p$ , from which we can derive the fluid velocity  $\mathbf{u}$ , and the concentration  $c$ .

For the flow problem, the boundary  $\partial\Omega$  is partitioned into a Dirichlet and Neumann part, denoted  $\partial\Omega_D$  and  $\partial\Omega_N$ , respectively. For the transport problem, we let  $\partial\Omega_{\text{in}} := \{\mathbf{x} \in \partial\Omega | \mathbf{u} \cdot \mathbf{n} < 0\}$  denote the inflow boundary, and  $\partial\Omega_{\text{out}} := \{\mathbf{x} \in \partial\Omega | \mathbf{u} \cdot \mathbf{n} \geq 0\}$  denote the outflow boundary, where  $\mathbf{n}$  is the outward pointing unit normal.

We use the standard notation  $H^s(\omega)$  for the Sobolev space of order  $s$  on  $\omega$  with the special cases  $L^2(\omega) = H^0(\omega)$  and  $H_0^1(\Omega) = \{v \in H^1(\Omega) : v|_{\partial\Omega_D} = 0\}$ . The space of continuous functions on  $\omega$  is denoted  $C(\omega)$ . For a normed vector space  $V$ , we let  $\|\cdot\|_V$  denote the norm on  $V$ . For  $V = L^2(\omega)$ , we use the notation  $\|\cdot\|_{L^2(\omega)} = \|\cdot\|_\omega$ , and denote by  $(\cdot, \cdot)_\omega$  the  $L^2$  scalar product.

In the following, we restrict this presentation to the two dimensional case, i.e.,  $d = 2$ , but most of the theory and methods considered herein can be extended to three dimensions in a straight forward manner.

### 2.1. Fracture representation

We allow for bifurcating fractures and represent  $\Gamma$  as a graph with nodes  $\mathcal{N} = \{\mathbf{x}_i\}_{i \in I_N}$  and edges  $\mathcal{G} = \{\Gamma_j\}_{j \in I_G}$ , where  $I_N$  and  $I_G$  are finite index sets, and each  $\Gamma_j$  is a curve between two nodes with indices  $I_N(j)$ . For each  $i \in I_N$ , we let  $I_G(i)$  be the set of indices corresponding to curves for which  $\mathbf{x}_i$  is an end point. Furthermore, let  $\{\Omega_i\}_{i=1}^{n_d}$  be a partition of  $\Omega$  into  $n_d$  subdomains defined by  $\Gamma$ . See Fig. 1a.

We fix an orientation of each  $\Gamma_j$  such that the positive direction is from the node with lowest index towards the node with highest index. Then we define  $\mathbf{n}_\Gamma$  to be the unit normal on  $\Gamma$  pointing from the left side towards the right when facing the positive direction of  $\Gamma$ , see Fig 1b. For a scalar function  $v$ , possibly discontinuous at  $\Gamma$ , we define the jump as

$$[[v]] = v_+ - v_-, \quad \text{on } \Gamma, \quad (2.1)$$

where

$$v_+(\mathbf{x}) = \lim_{\epsilon \rightarrow 0^+} v(\mathbf{x} + \epsilon \mathbf{n}_\Gamma), \quad \mathbf{x} \in \Gamma, \quad (2.2)$$

$$v_-(\mathbf{x}) = \lim_{\epsilon \rightarrow 0^+} v(\mathbf{x} - \epsilon \mathbf{n}_\Gamma), \quad \mathbf{x} \in \Gamma. \quad (2.3)$$

For a vector valued function  $\mathbf{v}$ , we define the jump in the normal component across  $\Gamma$  as

$$[[\mathbf{v} \cdot \mathbf{n}]] = \mathbf{v}_+ \cdot \mathbf{n}_+ + \mathbf{v}_- \cdot \mathbf{n}_-, \quad (2.4)$$

where  $\mathbf{n}_+ = -\mathbf{n}_\Gamma$  and  $\mathbf{n}_- = \mathbf{n}_\Gamma$ .

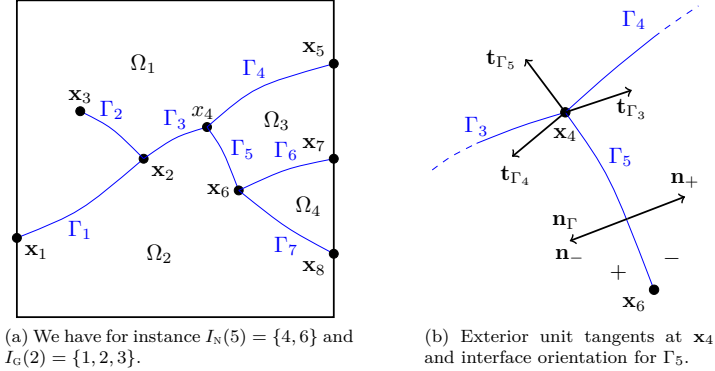


Fig. 1: Illustration of domain and fracture representation.

## 2.2. Pressure problem

The fractures are modeled as embedded surfaces with high permeability. Our model is essentially the same as the one presented in [2, 12]. It was further studied in [13], where it was extended to bifurcating cracks. The embedded model is derived as the asymptotic limit in the weak formulation as the fracture aperture goes to zero and the fracture permeability goes to infinity. We refer to [2, 12] for further details.

*Boundary value problem.* The governing equations for the pressure problem are

$$-\nabla \cdot (\boldsymbol{\kappa} \nabla p) = q, \quad \text{in } \Omega, \quad (2.5a)$$

$$-\nabla_\Gamma \cdot (k_\Gamma \nabla_\Gamma p) = q_\Gamma + \llbracket (\boldsymbol{\kappa} \nabla p) \cdot \mathbf{n} \rrbracket, \quad \text{on } \Gamma, \quad (2.5b)$$

$$\llbracket p \rrbracket = 0, \quad \text{on } \Gamma, \quad (2.5c)$$

where  $\nabla_\Gamma = \mathbf{P} \nabla$  is the tangential gradient with  $\mathbf{P} = \mathbf{I} - \mathbf{n}_\Gamma \otimes \mathbf{n}_\Gamma$ . The first equation (2.5a) is the standard Darcy equation for single-phase flow describing conservation of mass. Eq. (2.5b) governs conservation of mass in the fractures, where the last term on the right hand side represents a coupling term for the normal velocity across  $\Gamma$ . The last equation (2.5c) is another coupling term, and represents a reasonable assumption for high conductive fractures. The model can also be extended to a non-zero pressure jump [12].

We equip the governing equations with Dirichlet and Neumann boundary conditions, i.e.,

$$p = p_D, \quad \text{on } \partial\Omega_D, \quad (2.5d)$$

$$(\boldsymbol{\kappa} \nabla p) \cdot \mathbf{n} = u_N, \quad \text{on } \partial\Omega_N. \quad (2.5e)$$

Furthermore, we enforce continuity of pressure at the interface nodes,

$$p_{\Gamma_k}(x_i) = p_{\Gamma_l}(x_i), \quad \forall k, l \in I_G(i), \forall i \in I_N, \quad (2.5f)$$

and apply the Kirchhoff condition

$$\sum_{j \in I_G(i)} ((k_{\Gamma_j} \nabla_{\Gamma_j} p_{\Gamma_j}) \cdot \mathbf{t}_{\Gamma_j})|_{x_i} = 0, \quad \forall i \in I_N \setminus I_{N,N}, \quad (2.5g)$$

$$((k_{\Gamma_j} \nabla_{\Gamma_j} p_{\Gamma_j}) \cdot \mathbf{t}_{\Gamma_j})|_{x_i} = w u_N, \quad \forall i \in I_{N,N}, \quad (2.5h)$$

where  $\mathbf{t}_{\Gamma_j}$  is the exterior unit tangent to  $\Gamma_j$  (see Fig. 1b) and  $I_{N,N} \subset I_N$  is the set of indices whose corresponding nodes belong to  $\partial\Omega_N$ . We remark that Eq. (2.5g) ensures mass balance at the interface nodes, while Eq. (2.5h) is a Neumann condition for the part of  $\Gamma$  that intersects with  $\partial\Omega_N$ , and where the fracture

width  $w$  is taken into account. Observe that Eq. (2.5g) implies a homogeneous Neumann condition at the fracture tip if the tip is in the interior of  $\Omega$ . This is a natural approximation that is commonly used, see e.g., [5–7, 10].

The fluid velocity is defined by Darcy's law as  $\mathbf{u} = -\kappa \nabla p$ . We note that  $\mathbf{u}_\Gamma = -k_\Gamma \nabla_\Gamma p$  gives the flow rate through the cross section of the fracture rather than the velocity.

*Weak formulation.* We define the following function spaces,

$$V_\Gamma(\Gamma) = \{v \in C(\Gamma) : v \in H^1(\Gamma_j), \forall j \in I_G\}, \quad (2.6)$$

$$V_0(\Omega) = \{v \in H_0^1(\Omega) : v|_\Gamma \in V_\Gamma(\Gamma)\}, \quad (2.7)$$

$$V_D(\Omega; v_D) = \{v \in H^1(\Omega) : v|_{\partial\Omega_D} = v_D, v|_\Gamma \in V_\Gamma(\Gamma)\}. \quad (2.8)$$

Then multiply (2.5a) by a test function  $v \in V_0(\Omega)$ , integrate over  $\Omega$  and apply Green's formula on each subdomain  $\Omega_i$ , to obtain

$$\begin{aligned} (q, v)_\Omega &= \sum_{i=1}^{n_d} (-\nabla \cdot (\kappa \nabla p), v)_{\Omega_i} \\ &= \sum_{i=1}^{n_d} ((\kappa \nabla p, \nabla v)_{\Omega_i} - ((\kappa \nabla p) \cdot \mathbf{n}_i, v)_{\partial\Omega_i}) \\ &= (\kappa \nabla p, \nabla v)_\Omega - (\llbracket (\kappa \nabla p) \cdot \mathbf{n} \rrbracket, v)_\Gamma - (u_N, v)_{\partial\Omega_N} \\ &= (\kappa \nabla p, \nabla v)_\Omega - (q_\Gamma, v)_\Gamma - (\nabla_\Gamma \cdot (k_\Gamma \nabla_\Gamma p), v)_\Gamma - (u_N, v)_{\partial\Omega_N}. \end{aligned} \quad (2.9)$$

Notice that  $\mathbf{n}_i$  denotes the unit normal pointing out of  $\Omega_i$ . Then apply Green's formula on  $\Gamma$  and use the Kirchoff conditions, Eq. (2.5g)–(2.5h), to obtain

$$\begin{aligned} -(\nabla_\Gamma \cdot (k_\Gamma \nabla_\Gamma p), v)_\Gamma &= \sum_{j \in I_G} -(\nabla_{\Gamma_j} \cdot (k_{\Gamma_j} \nabla_{\Gamma_j} p), v)_{\Gamma_j} \\ &= \sum_{j \in I_G} (k_{\Gamma_j} \nabla_{\Gamma_j} p, \nabla_{\Gamma_j} v)_{\Gamma_j} - \sum_{j \in I_G} \sum_{i \in I_N(j)} ((k_{\Gamma_j} \nabla_{\Gamma_j} p) \cdot \mathbf{t}_{\Gamma_j}, v)_{x_i} \\ &= (k_\Gamma \nabla_\Gamma p, \nabla v)_\Gamma - \sum_{i \in I_N} \sum_{j \in I_G(i)} ((k_{\Gamma_j} \nabla_{\Gamma_j} p) \cdot \mathbf{t}_{\Gamma_j})|_{x_i} v(x_i) \\ &= (k_\Gamma \nabla_\Gamma p, \nabla v)_\Gamma - \sum_{i \in I_{N,N}} w u_N(x_i) v(x_i). \end{aligned} \quad (2.10)$$

Combing these equations we get the following weak formulation. Find  $p \in V_D(\Omega; p_D)$  such that

$$a(p, v) = l(v), \quad \forall v \in V_0(\Omega), \quad (2.11)$$

where

$$a(u, v) = (\kappa \nabla u, \nabla v)_\Omega + (k_\Gamma \nabla_\Gamma u, \nabla v)_\Gamma, \quad (2.12)$$

$$l(v) = (q, v)_\Omega + (q_\Gamma, v)_\Gamma - (u_N, v)_{\partial\Omega_N} - \sum_{i \in I_{N,N}} w u_N(x_i) v(x_i). \quad (2.13)$$

Observe that the contribution from the fractures are included by superposition, i.e., by evaluating lower dimensional integrals along  $\Gamma$ .

**Remark 2.1.** *When applying Green's formula in Eq. (2.9), we assume that there are no interfaces  $\Gamma_j$  that terminates in the interior of  $\Omega$  (as is the case for  $\Gamma_2$  in Fig. 1a). In such cases we can divide in two the domains  $\Omega_i$  with a terminating node such that the two new domains, denoted  $\Omega_{i_a}$  and  $\Omega_{i_b}$ , are separated by*

the interface with the terminating node and an artificial line connecting the terminating node with either  $\partial\Omega$  or another interface. We can then replace the contribution from  $\Omega_i$  by the sum of the contributions from  $\Omega_{ia}$  and  $\Omega_{ib}$  in Eq. (2.9). For the situation in Fig. 1a, we may for instance divide  $\Omega_1$  into two subdomains,  $\Omega_{1a}$  and  $\Omega_{1b}$ , separated by  $\Gamma_2$  and a line connecting  $\mathbf{x}_3$  with the upper left corner of  $\Omega$ . We mention that a similar approach was used in [5].

### 2.3. Transport problem

Advective transport in the fractured domain is modeled by a reduced (or mixed-dimensional) model, see e.g., [2, 21, 33],

$$\phi \frac{\partial c}{\partial t} + \nabla \cdot (\mathbf{u}c) = f(c), \quad \text{in } \Omega \times (0, T], \quad (2.14a)$$

$$w\phi_\Gamma \frac{\partial c_\Gamma}{\partial t} + \nabla_\Gamma \cdot (\mathbf{u}_\Gamma c_\Gamma) - \llbracket \mathbf{u} \cdot \mathbf{n}c^* \rrbracket = f_\Gamma(c_\Gamma), \quad \text{in } \Gamma \times (0, T], \quad (2.14b)$$

Initial and boundary conditions are given as

$$c = c_0, \quad \text{on } \Omega \times \{0\}, \quad (2.14c)$$

$$c_\Gamma = c_{\Gamma,0}, \quad \text{on } \Gamma \times \{0\}, \quad (2.14d)$$

$$c = c_B, \quad \text{on } \partial\Omega_{\text{in}} \times (0, T], \quad (2.14e)$$

$$c_\Gamma = c_{\Gamma,B}, \quad \text{on } \Gamma_{\text{in}} \times (0, T]. \quad (2.14f)$$

Here  $c_0$  and  $c_{\Gamma,0}$  are the initial concentrations in the matrix and fractures, respectively, while  $c_B$  and  $c_{\Gamma,B}$  are the inflow concentrations for the matrix and fractures, respectively. The right hand sides denote source terms, defined as

$$f(c) = \check{q}c + \hat{q}c_w = \begin{cases} qc, & \text{if } q \leq 0, \\ qc_w, & \text{if } q > 0, \end{cases} \quad (2.15a)$$

$$f_\Gamma(c_\Gamma) = \check{q}_\Gamma c_\Gamma + \hat{q}_\Gamma c_w = \begin{cases} q_\Gamma c_\Gamma, & \text{if } q_\Gamma \leq 0, \\ q_\Gamma c_w, & \text{if } q_\Gamma > 0, \end{cases} \quad (2.15b)$$

where  $\check{q} = \min(q, 0)$  and  $\hat{q} = \max(q, 0)$ , and  $c_w$  is the inflow concentration from the source term. The third term in the fracture equation (2.14b),  $\llbracket \mathbf{u} \cdot \mathbf{n}c^* \rrbracket$ , is a coupling term that models flow between the fracture and matrix. Here,  $c^*$  is interpreted as

$$c_\pm^* = \begin{cases} c_\pm, & \text{if } (\mathbf{u} \cdot \mathbf{n})_\pm \geq 0, \\ c_\Gamma, & \text{otherwise,} \end{cases} \quad \text{on } \Gamma \times (0, T]. \quad (2.16)$$

Observe that the transport problem is coupled to the pressure problem through the velocities  $\mathbf{u}$  and  $\mathbf{u}_\Gamma$ .

## 3. Numerical methods

### 3.1. Preliminaries

*Domain discretization.* Let  $\mathcal{K}_h$  be a partition of  $\Omega$ , and denote by  $K \in \mathcal{K}_h$  an element of the partition. We let  $K \in \mathcal{K}_h$  be open such that  $\bigcup_{K \in \mathcal{K}_h} \bar{K} = \bar{\Omega}$ . The diameter of  $K$  is denoted  $h_K$ , while  $h$  is the maximum diameter of all elements. We assume  $\mathcal{K}_h$  to be regular and quasi-uniform. By regular we mean that all elements are convex and that there exists  $\rho > 0$  such that each element  $K \in \mathcal{K}_h$  contains a ball of radius  $\rho h_K$  in its interior. Furthermore,  $\mathcal{K}_h$  is quasi-uniform if there exists  $\tau > 0$  such that  $h/h_K \leq \tau$  for all  $K \in \mathcal{K}_h$ .

We denote by  $\mathcal{F}_h$  the set of all element faces. This set is then divided into the set of interior faces,  $\mathcal{F}_{h,i}$ , and boundary faces,  $\mathcal{F}_{h,B}$ . We assume that each face in  $\mathcal{F}_{h,B}$  is either completely on the Dirichlet or

Neumann part of the boundary, such that  $\mathcal{F}_{h,B}$  can be split into  $\mathcal{F}_{h,D}$  and  $\mathcal{F}_{h,N}$ , i.e., the sets of faces on the Dirichlet and Neumann boundary, respectively. Similarly, let  $\mathcal{F}_{h,in}$  and  $\mathcal{F}_{h,out}$  be the set of boundary faces on the inflow and outflow boundary, respectively. For each face  $F \in \mathcal{F}_h$  we choose an orientation and let  $\mathbf{n}_F$  denote the unit normal in this direction. The unit normal vector on  $F \in \mathcal{F}_{h,B}$  is chosen to coincide with the outward unit normal. Furthermore,  $\mathbf{n}_K$  denotes the unit normal pointing out of  $K$ . We will also use the notation  $|K|$  for the measure of  $K$ , and similarly  $|F|$  for the measure of  $F$ .

For the transport solver, we further divide  $\mathcal{K}_h$  into two subsets,  $\mathcal{K}_h^M$  and  $\mathcal{K}_h^F$ , where  $\mathcal{K}_h^F$  contains all fractured cells,  $\mathcal{K}_h^F = \{K \in \mathcal{K}_h : K \cap \Gamma \neq \emptyset\}$ , and  $\mathcal{K}_h^M = \mathcal{K}_h \setminus \mathcal{K}_h^F$ , see Fig. 2a. The set of interior faces,  $\mathcal{F}_{h,i}$  are then partitioned into three subsets,  $\mathcal{F}_{h,i}^F$ ,  $\mathcal{F}_{h,i}^M$  and  $\mathcal{F}_{h,i}^{FM}$ , where  $\mathcal{F}_{h,i}^F$  are the set of faces between two fractured elements,  $\mathcal{F}_{h,i}^M$  is the set of faces between two matrix elements, and  $\mathcal{F}_{h,i}^{FM}$  are the sets of faces between a fracture and a matrix element.

**Remark 3.1.** *In the situation where  $\Gamma$  coincides with an element face  $F = \partial K_- \cap \partial K_+ \in \mathcal{F}_{h,i}$ , we need to choose which of the neighboring elements that belong to  $\mathcal{K}_h^F$ . One possibility is to choose the element for which  $\mathbf{n}_\Gamma$  is exterior, i.e.,  $K_-$ . For the numerical examples presented in Section 4 we have avoided this situation.*

*Jump and average operators.* We define the jump operator  $[\![\cdot]\!]_F$  over a face  $F \in \mathcal{F}_h$  in the same way as we did for the jump over  $\Gamma$ , see Eq. (2.1) and (2.4), where  $\mathbf{n}_F$  now defines the orientation. Furthermore, we denote by  $\{\!\{ \cdot \}\!\}_\theta$  the weighted average operator on  $F$ , defined as

$$\{\!\{ v \}\!\}_\theta = \theta_F v_- + (1 - \theta_F) v_+, \quad (3.1)$$

where  $\theta_F = \theta|_F$  and  $0 \leq \theta \leq 1$ . For  $\theta = \frac{1}{2}$  we simply write  $\{\!\{ \cdot \}\!\}$  without any subscript. For  $F \in \mathcal{F}_{h,B}$  we define the jump and average operators as the one sided value, i.e.,

$$[\![v]\!] = \{\!\{ v \}\!\}_\theta = v_-. \quad (3.2)$$

*Finite dimensional function spaces.* In our implementation we work with quadrilateral elements, but the all numerical methods can equally well be formulated on other elements, e.g., triangular. Denote by  $\hat{K} = (0, 1)^2$  the reference element with coordinates  $(\xi, \eta)$ , and by  $M_K$  the mapping from  $\hat{K}$  to  $K$ . With this, we denote by  $\hat{Q}_r(\hat{K})$  the tensor product of polynomial spaces of degree less than or equal to  $r$  in each spatial direction, i.e.,

$$\hat{Q}_r(\hat{K}) = \left\{ v \in H^1(\hat{K}) : v = \left( \sum_{i=0}^r a_i \xi^i \right) \left( \sum_{i=0}^r b_i \eta^i \right), a_i, b_i \in \mathbb{R} \right\}. \quad (3.3)$$

Next,  $Q_r(K)$  denotes the reference element functions mapped to the actual element  $K$ ,

$$Q_r(K) = \{ \hat{v} \circ M_K^{-1} : \hat{v} \in \hat{Q}_r(\hat{K}) \}. \quad (3.4)$$

We may now define the following function spaces of piecewise polynomials of order  $r > 0$ ,

$$Q_r(\mathcal{K}_h) = \{ v \in C(\Omega) : v|_K \in Q_r(K), K \in \mathcal{K}_h \}, \quad (3.5)$$

$$Q_{r,D}(\mathcal{K}_h; v_D) = \{ v \in Q_r(\mathcal{K}_h) : v|_{\partial\Omega_D} = v_D \}. \quad (3.6)$$

Moreover, we define the following spaces of piecewise constant functions ( $r = 0$ ),

$$Q_0(\mathcal{K}_h) = \{ v \in L^2(\Omega) : v|_K = a_K, a_K \in \mathbb{R}, K \in \mathcal{K}_h \}, \quad (3.7)$$

$$Q_0(\mathcal{F}_h) = \{ v \in L^2(\mathcal{F}_h) : v|_F = a_F, a_F \in \mathbb{R}, F \in \mathcal{F}_h \}. \quad (3.8)$$

Finally, we denote by  $(\cdot, \cdot)_{\mathcal{K}_h}$  and  $(\cdot, \cdot)_{\mathcal{F}_h}$  the broken  $L^2$  scalar products, i.e.,

$$(u, v)_{\mathcal{K}_h} = \sum_{K \in \mathcal{K}_h} (u, v)_K, \quad (u, v)_{\mathcal{F}_h} = \sum_{F \in \mathcal{F}_h} (u, v)_F. \quad (3.9)$$

### 3.2. Pressure problem

We follow [13] and approximate the pressure solution with piecewise bilinear functions by restricting the weak formulation (2.11) to the finite dimensional subspace  $Q_{1,D}(\mathcal{K}_h; p_D) \subset V_D(\Omega; p_D)$ . Find  $p_h \in Q_{1,D}(\mathcal{K}_h; p_D)$  such that

$$a(p_h, v) = l(v), \quad \forall v \in Q_{1,D}(\mathcal{K}_h; 0). \quad (3.10)$$

The following a priori error estimate for the pressure approximation was proved in [13]. Let  $\mathcal{N}_h(K) \subset \mathcal{K}_h$  be the set of all elements which are node neighbors of  $K$ , and let  $h_\Gamma$  denote the mesh parameter in the vicinity of  $\Gamma$  such that  $h_K \leq h_\Gamma$  for all  $K \in \mathcal{N}_h(\mathcal{K}_h^F)$ . Then it holds that

$$\|p - p_h\|_\Omega + \|p - p_h\|_\Gamma \lesssim (h_\Gamma + h^2) \left( \sum_{i=1}^{n_d} \|p\|_{H^2(\Omega_i)} \right) + h_\Gamma^2 \|p\|_{H^2(\Gamma)}. \quad (3.11)$$

As a consequence, one should refine locally around the fractures until  $h_\Gamma \sim h^2$  to obtain the optimal order of convergence in terms of  $h$ .

**Remark 3.2.** *The estimate (3.11) was proved in [13] for the simple geometry where  $\Gamma$  is a smooth embedded interface in the interior of  $\Omega$  without boundary. It can be extended to the case where  $\Gamma$  is represented as a graph. However, depending on the geometry of  $\Gamma$ , we may lose some regularity of the solution (this is especially the case for terminating nodes in the interior of  $\Omega$ , e.g.,  $\mathbf{x}_2$  in Fig. 1a), so that we must replace the term  $(h_\Gamma + h^2)$  by  $(h_\Gamma + h^s)$  for some  $s \in [1, 2]$ . Yet, the condition  $h_\Gamma \sim h^2$  is still sufficient to obtain the optimal convergence in terms of  $h$  since refinement around  $\Gamma$  also means refinement around the interface nodes.*

### 3.3. Transport problem

We approximate the concentration solution by piecewise constants  $c_h \in Q_0(\mathcal{K}_h)$ , and let  $c_h$  on  $\mathcal{K}_h^F$  represent the concentration in the fractures, and  $c_h$  on  $\mathcal{K}_h^M$  represent the concentration in the matrix. We use an upwind approximation of the concentration on element faces. The numerical scheme can be formulated as a zeroth order finite volume method (FV), or equivalently as a zeroth order Discontinuous Galerkin method (DG). We only express the FV formulation here, and refer to Appendix A.1 for the DG formulation.

*FV formulation.* We integrate the matrix equation (2.14a) over  $K \in \mathcal{K}_h^M$  to obtain the integral formulation

$$\int_K \phi \frac{\partial c}{\partial t} + \int_{\partial K} \mathbf{u} \cdot \mathbf{n}_K c = \int_K f(c), \quad K \in \mathcal{K}_h^M. \quad (3.12)$$

Similarly, for  $K \in \mathcal{K}_h^F$ , we integrate the fracture equation (2.14a) over  $K \cap \Gamma$  to obtain

$$\int_{K \cap \Gamma} w \phi_\Gamma \frac{\partial c_\Gamma}{\partial t} + \int_{\partial(K \cap \Gamma)} \mathbf{u}_\Gamma \cdot \mathbf{n}_{K \cap \Gamma} c_\Gamma - \int_{K \cap \Gamma} [\mathbf{u} \cdot \mathbf{n} c^*] = \int_{K \cap \Gamma} f_\Gamma(c_\Gamma), \quad K \in \mathcal{K}_h^F. \quad (3.13)$$

The lowest order finite volume method is then obtained by replacing  $c$  by  $c_h \in Q_0(\mathcal{K}_h)$ . We use an upwind approximation on  $\partial K$ , i.e.,

$$\mathbf{u} \cdot \mathbf{n}_K c_h|_{F=\partial K \cap \partial \tilde{K}} = \begin{cases} \mathbf{u} \cdot \mathbf{n}_K c_h|_K, & \text{if } \mathbf{u} \cdot \mathbf{n}_K \geq 0, \\ \mathbf{u} \cdot \mathbf{n}_K c_h|_{\tilde{K}}, & \text{if } \mathbf{u} \cdot \mathbf{n}_K < 0, \end{cases} \quad (3.14a)$$

where  $\tilde{K}$  is a neighbor element of  $K$ . If  $F \subset \partial K$  is a boundary face, we have

$$\mathbf{u} \cdot \mathbf{n}_K c_h|_{F=\partial K \cap \partial \Omega} = \begin{cases} \mathbf{u} \cdot \mathbf{n}_K c_h|_K, & \text{if } \mathbf{u} \cdot \mathbf{n}_K \geq 0, \\ \mathbf{u} \cdot \mathbf{n}_K c_B, & \text{if } \mathbf{u} \cdot \mathbf{n}_K < 0. \end{cases} \quad (3.14b)$$

An equivalent upwind approximation of  $c_h$  is used on  $\partial(K \cap \Gamma)$ .

Recall the definition of the vector valued jump in Eq. (2.4). The coupling term in Eq. (3.13), with  $c$  replaced by  $c_h$ , can be written as

$$\llbracket \mathbf{u} \cdot \mathbf{n} c_h^* \rrbracket = (\mathbf{u} \cdot \mathbf{n}_\Gamma c_h^*)_- - (\mathbf{u} \cdot \mathbf{n}_\Gamma c_h^*)_+, \quad \text{on } K \cap \Gamma. \quad (3.15)$$

Given a velocity approximation that is continuous in the interior of an element, we see that  $\llbracket \mathbf{u} \cdot \mathbf{n} c_h^* \rrbracket$  vanish as long as  $\Gamma$  is not aligned with the element faces. This would result in no coupling between the fracture and the matrix. To overcome this, we approximate the flow between matrix and fracture by evaluating  $(\mathbf{u} \cdot \mathbf{n}_\Gamma c_h^*)_\pm$  on the part of the element boundary that borders to matrix elements, i.e.,

$$\int_{K \cap \Gamma} \llbracket \mathbf{u} \cdot \mathbf{n} c_h^* \rrbracket \approx \sum_{\bar{K} \in \mathcal{K}_h^M} \int_{\partial \bar{K} \cap \partial K} \mathbf{u} \cdot \mathbf{n}_K c_h, \quad (3.16)$$

where the upwind scheme (3.14) applies. Since  $c_h$  on  $K \in \mathcal{K}_h^F$  represents the approximation in the fracture, (3.16) is compatible with the condition (2.16). Given the low order method, the approximation (3.16) seems reasonable when combined with local refinement around  $\Gamma$ .

We apply the implicit Euler (IE) method as time integrator. For simplicity, we use constant time steps  $\Delta t$ , and let  $c_h^n$  denote the approximation at  $t = n\Delta t$ , with  $c_h^0 = Q_0 c_0$ , where  $Q_0$  is a projection operator from  $L^2(\Omega)$  to  $Q_0(\mathcal{K}_h)$ .

To sum up, the FV-IE scheme can be formulated as follows. Find  $c_h^{n+1} \in Q_0(\mathcal{K}_h)$  such that

$$\int_K \phi \frac{c_h^{n+1} - c_h^n}{\Delta t} + \int_{\partial K} \mathbf{u} \cdot \mathbf{n}_K c_h^{n+1} = \int_K f^{n+1}(c_h^{n+1}), \quad \forall K \in \mathcal{K}_h^M, \quad (3.17a)$$

$$\begin{aligned} \int_{K \cap \Gamma} w \phi_\Gamma \frac{c_h^{n+1} - c_h^n}{\Delta t} + \int_{\partial(K \cap \Gamma)} \mathbf{u}_\Gamma \cdot \mathbf{n}_{K \cap \Gamma} c_h^{n+1} - \sum_{\bar{K} \in \mathcal{K}_h^M} \int_{\partial \bar{K} \cap \partial K} \mathbf{u} \cdot \mathbf{n}_K c_h^{n+1} \\ = \int_{K \cap \Gamma} f_\Gamma^{n+1}(c_h^{n+1}), \quad \forall K \in \mathcal{K}_h^F. \end{aligned} \quad (3.17b)$$

*Interpretation of solution.* In the numerical method,  $c|_{K \cap \Gamma}$ , for  $K \in \mathcal{K}_h^F$ , is represented by the value  $c_h|_K$ . However,  $K$  also contains subdomains belonging to the matrix, whose concentration solution we represent by the solution in the neighboring matrix elements, see Fig. 2 for an illustrative example. For a single fracture the matrix concentration in  $K$  to the left/right of  $\Gamma$  is given by the solution in the left/right-neighboring matrix elements. For cells  $K$  with intersecting or bifurcating fractures, this interpretation is slightly more complex, as  $\Gamma$  divides  $K$  into more than two subdomains. We refer to Appendix A.2 for a well-defined interpretation.

### 3.4. Velocity model

We observe from the transport model, Eq. (3.17), that we need the flux (normal velocity) over the element faces. We denote the flux by  $U$  and define it as

$$U = \begin{cases} -\kappa \nabla p \cdot \mathbf{n}_F, & \text{on } F \in \mathcal{F}_h \setminus (\mathcal{F}_{h,1}^F \cup \mathcal{F}_{h,N}^F), \\ -\frac{1}{|F|} k_\Gamma \nabla_\Gamma p \cdot \mathbf{t}_{\Gamma,F}, & \text{on } F \in \mathcal{F}_{h,1}^F, \\ u_N, & \text{on } F \in \mathcal{F}_{h,N}^F, \end{cases} \quad (3.18)$$

where  $\mathbf{t}_{\Gamma,F}$  is the unit tangent to  $\Gamma$  oriented in the same direction as  $\mathbf{n}_F$ . Recall that  $k_\Gamma = w\kappa_\Gamma$  so that  $k_\Gamma \nabla_\Gamma p \cdot \mathbf{t}_\Gamma$  gives the flow rate rather than the velocity. The reason for multiplying by  $1/|F|$  for faces  $F \in \mathcal{F}_{h,1}^F$



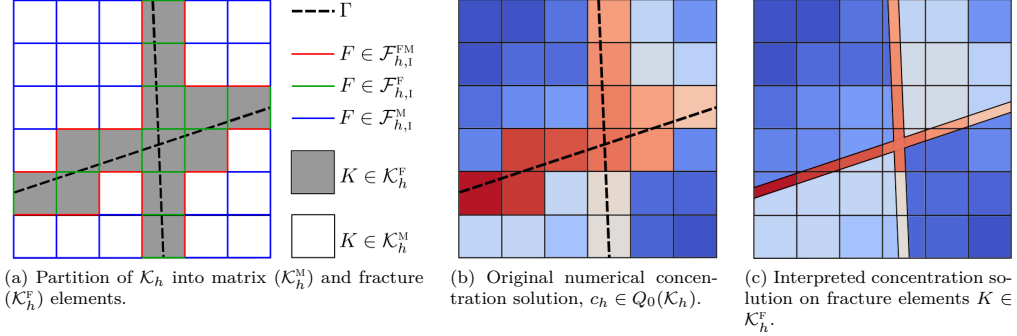


Fig. 2: Synthetic example of partition into matrix and fracture elements, and corresponding interpretation of concentration solution. The interpreted solution on interface elements  $K \cap \Gamma$  is visualized with a fixed (exaggerated) thickness.

is that we want to work directly on  $\mathcal{F}_h$  so that when  $U$  is integrated over  $F$  we get the total flow rate through  $F$ . With this definition of  $U$  we can simplify two terms in Eq. (3.17b),

$$\int_{\partial(K \cap \Gamma)} \mathbf{u}_\Gamma \cdot \mathbf{n}_{K \cap \Gamma} c_h^{n+1} - \sum_{\bar{K} \in \mathcal{K}_h^M} \int_{\partial \bar{K} \cap \partial K} \mathbf{u} \cdot \mathbf{n}_K c_h^{n+1} = \int_{\partial K} U c_h^{n+1} \mathbf{n}_K \cdot \mathbf{n}_F. \quad (3.19)$$

The term  $\mathbf{n}_K \cdot \mathbf{n}_F$  is either plus or minus 1 depending on the orientation of  $F$ .

For the coupled flow and transport problem, the velocity is derived from the pressure approximation  $p_h$ . The pressure gradient,  $\nabla p_h$ , is not continuous across element faces, so a naive flux approximation is to use the average value,

$$U_h = \begin{cases} -\{\{\kappa \nabla p_h \cdot \mathbf{n}_F\}\} \vartheta, & \text{on } F \in \mathcal{F}_h \setminus (\mathcal{F}_{h,1}^F \cup \mathcal{F}_{h,N}), \\ -\frac{1}{|F|} \{\{k_\Gamma \nabla_\Gamma p_h \cdot \mathbf{t}_\Gamma\}\}, & \text{on } F \in \mathcal{F}_{h,1}^F, \\ u_N, & \text{on } F \in \mathcal{F}_{h,N}. \end{cases} \quad (3.20)$$

Recall the definition of the average operator in Eq. (3.1). As weights we follow [36] and use weights equal to the normal component of the permeability of the neighboring cell. Hence,

$$\vartheta_F = \frac{\delta_{K_n}^+}{\delta_{K_n}^+ + \delta_{K_n}^-}, \quad \delta_{K_n}^\pm = \mathbf{n}_F \cdot (\kappa_\pm \mathbf{n}_F), \quad (3.21)$$

where  $\kappa_\pm$  are the permeabilities of the two cells sharing  $F$ . For a fractured cell we use  $\kappa = \kappa_\Gamma \mathbf{I}$ , and for  $F \in \mathcal{F}_{h,B}$ ,  $\omega|_F = 1/\delta_{K_n}^-$ . In the case of isotropic permeability, i.e.,  $\kappa = \kappa \mathbf{I}$ , observe that  $\vartheta_F = \kappa_+ / (\kappa_+ + \kappa_-)$  such that

$$U_h = -\{\{\kappa \nabla p_h \cdot \mathbf{n}_F\}\} \vartheta = -\frac{\kappa_+ \kappa_-}{\kappa_+ + \kappa_-} (\nabla p_h)_- \cdot \mathbf{n}_F - \frac{\kappa_- \kappa_+}{\kappa_+ + \kappa_-} (\nabla p_h)_+ \cdot \mathbf{n}_F = -k_e \{\{\nabla p_h \cdot \mathbf{n}_F\}\}, \quad (3.22)$$

where  $k_e = \frac{2\kappa_+ \kappa_-}{\kappa_+ + \kappa_-}$  is the effective face permeability (harmonic average).

We say that a flux approximation  $U_h$  on  $\mathcal{F}_h$  is locally conservative if

$$\int_{\partial K} U_h(\mathbf{n}_K \cdot \mathbf{n}_F) = \int_K q, \quad \forall K \in \mathcal{K}_h. \quad (3.23)$$

As reported in [36], Eq. (3.20) does not define a locally conservative flux approximation. If coupled to the transport scheme one may get unphysical solutions due to artificial sinks and sources. To deal with this, we apply the postprocessing method presented in [36]. This method was shown to preserve accuracy of the velocity solution and was demonstrated to be especially beneficial for highly heterogeneous media.

*Variationally consistent postprocessing of fluxes.* The core idea of the postprocessing method is to add a piecewise constant correction to  $U_h$  under the constraint that the correction is minimized in a weighted  $L^2$  norm,

$$\|v\|_{\omega, \mathcal{F}_h} = \sqrt{(\omega v, v)_{\mathcal{F}_h}}, \quad (3.24)$$

where  $\omega$  are positive and bounded weights. We define the weight on  $F \in \mathcal{F}_h$  as the inverse of the effective normal component of the permeability,

$$\omega|_F = \frac{\delta_{\mathcal{K}_n}^+ + \delta_{\mathcal{K}_n}^-}{2\delta_{\mathcal{K}_n}^+ \delta_{\mathcal{K}_n}^-}. \quad (3.25)$$

These weights were demonstrated to be a good choice for heterogeneous permeability as low permeable interfaces are better preserved compared to minimizing in the standard  $L^2$  norm ( $\omega = 1$ ) [36].

Next, we define a residual operator,  $\mathcal{R} : L^2(\mathcal{F}_h) \rightarrow Q_0(\mathcal{K}_h)$ , measuring the discrepancy from local conservation,

$$\mathcal{R}(U)|_K = \begin{cases} \frac{1}{|K|} (\int_K q - \int_{\partial K} U \mathbf{n}_F \cdot \mathbf{n}_K), & K \in \mathcal{K}_h^M, \\ \frac{1}{|K|} (\int_{K \cap \Gamma} q_\Gamma - \int_{\partial K} U \mathbf{n}_F \cdot \mathbf{n}_K), & K \in \mathcal{K}_h^F. \end{cases} \quad (3.26)$$

With this we define the postprocessed flux,  $V_h$ , as follows.

$$V_h = \begin{cases} U_h + \omega^{-1} \llbracket y \rrbracket, & \text{on } F \in \mathcal{F}_h \setminus \mathcal{F}_{h,N}, \\ u_N, & \text{on } F \in \mathcal{F}_{h,N}, \end{cases} \quad (3.27)$$

where  $y \in Q_0(\mathcal{K}_h)$  is the unique solution to

$$(\omega^{-1} \llbracket y \rrbracket, \llbracket w \rrbracket)_{\mathcal{F}_h \setminus \mathcal{F}_{h,N}} = (\mathcal{R}(U_h), w)_{\mathcal{K}_h}, \quad \forall w \in Q_0(\mathcal{K}_h). \quad (3.28)$$

For further details on the postprocessing method, we refer to [36].

*Coupled formulation.* Applying Eq. (3.19) and using  $V_h$  as an approximation to  $U$ , the FV-IE scheme, Eq. (3.17), can be formulated as follows. Find  $c_h^{n+1} \in Q_0(\mathcal{K}_h)$  such that

$$\int_K \phi \frac{c_h^{n+1} - c_h^n}{\Delta t} + \int_{\partial K} V_h c_h^{n+1} \mathbf{n}_K \cdot \mathbf{n}_F = \int_K f^{n+1}(c_h^{n+1}), \quad \forall K \in \mathcal{K}_h^M, \quad (3.29a)$$

$$\int_{K \cap \Gamma} w \phi_\Gamma \frac{c_h^{n+1} - c_h^n}{\Delta t} + \int_{\partial K} V_h c_h^{n+1} \mathbf{n}_K \cdot \mathbf{n}_F = \int_{K \cap \Gamma} f_\Gamma^{n+1}(c_h^{n+1}), \quad \forall K \in \mathcal{K}_h^F. \quad (3.29b)$$

Note that the second term in Eq. (3.29b) contains both the flux along the fracture and the coupling term, cf. Eq. (3.19).

#### 4. Numerical results

In this section we demonstrate the numerical methods presented in Section 3. First, in Section 4.1, we consider a pure transport problem where the velocity is given explicitly and the exact solution is known. This is to verify our transport model, Eq. (3.29), and in particular our approximation of the coupling term, see Eq. (3.16).

Next, in Section 4.2, we consider two benchmark cases for the pure pressure problem presented in [32]. The first case is a regular fracture network, while the second problem is a realistic case with a complex fracture network. The aim is to compare EFEM, Eq. (3.10), to other DFM models for single-phase flow.

Finally, in Section 4.3, we solve the coupled pressure and transport problem on the same cases as in Section 4.2. This will reveal the capabilities of our solution approach.

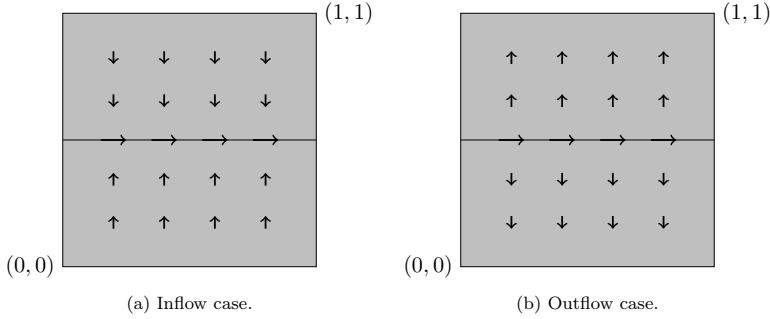


Fig. 3: Pure transport problem: Description of the two cases. Arrows describe the velocity field.

All implementation of the numerical methods are based on the open-source software deal.II [? ]. We only consider 2D problems, but our fracture model and numerical methods can be applied to 3D problems as well. All meshes are built up of quadrilateral elements. The meshes may be locally refined by recursively dividing selected elements in four, but we allow for no more than one hanging node per element face. The number of degrees of freedom are denoted  $N_{\text{dof}}$ .

#### 4.1. Pure transport problem

We consider first a pure transport problem with an explicitly given velocity field. Let  $\Omega = (0, 1)^2$  and  $\Gamma = (0, 1) \times \{0.5\}$ . The fracture velocity,  $u_\Gamma = \mathbf{u}_\Gamma \cdot (1, 0) = 10$ , and we consider two cases for the matrix velocity,  $\mathbf{u}$ . Either  $\mathbf{u} = (0, 1)$  for  $y < 0.5$  and  $\mathbf{u} = (0, -1)$  otherwise, or  $\mathbf{u} = (0, -1)$  for  $y < 0.5$  and  $\mathbf{u} = (0, 1)$  otherwise. The two cases are depicted in Fig. 3 and are denoted *inflow* and *outflow*, respectively. In both cases we set  $w = 1$  and use initial and boundary conditions  $c_0 = 0$  and  $c_B = 1$ .

The 1D advective transport equation describing the fracture concentration,  $c_\Gamma$ , is given as

$$w \frac{\partial c_\Gamma}{\partial t} + u_\Gamma \frac{\partial c_\Gamma}{\partial x} - \llbracket \mathbf{u} \cdot \mathbf{n} c^* \rrbracket = 0, \quad \text{on } \Gamma, \quad (4.1a)$$

$$c_\Gamma = 1, \quad \text{at } x = 0. \quad (4.1b)$$

For the inflow case we have  $c^* = c$ , and for the outflow case  $c^* = c_\Gamma$ . Both cases are solved on uniform  $N \times N$  meshes with time steps  $dt = 0.001$ , and the simulations are run until a steady-state solution is reached.

*Inflow case.* For the inflow case the concentration front from the top and bottom boundary moves with speed 1, so that  $\llbracket \mathbf{u} \cdot \mathbf{n} c^* \rrbracket = 2c$  with  $c = 0$  for  $t < 0.5$  and  $c = 1$  for  $t > 0.5$ . Hence, the exact solution for  $t < 0.5$  reads

$$c_\Gamma(x, t) = \begin{cases} 1, & x < \frac{u_\Gamma}{w} t, \\ 0, & x \geq \frac{u_\Gamma}{w} t. \end{cases} \quad (4.2)$$

At steady-state,  $c = 1$  in the matrix, and the exact steady-state solution is

$$c_\Gamma^{\text{ss}}(x) = 1 + \frac{2w}{u_\Gamma} x. \quad (4.3)$$

The approximation,  $c_h$ , along the fracture is plotted at  $t = 0.05$  and  $t = 1.5$  (steady-state) in Fig. 4 and compared to the exact solution.

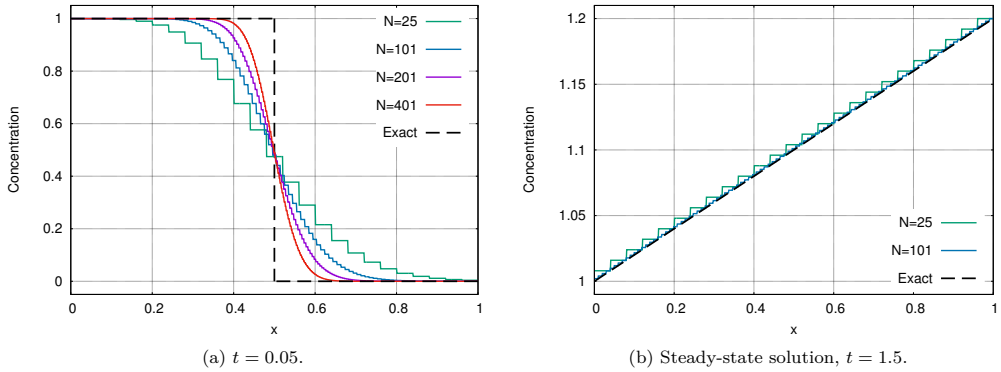


Fig. 4: Pure transport problem — inflow case: Fracture concentration on uniform  $N \times N$  meshes compared to exact solution.

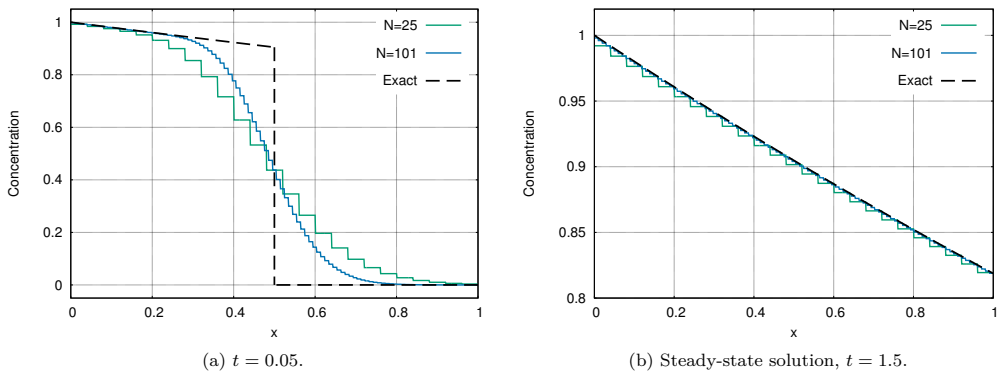


Fig. 5: Pure transport problem — outflow case: Fracture concentration on uniform  $N \times N$  meshes compared to exact solution.

*Outflow case.* For the outflow case,  $[\mathbf{u} \cdot \mathbf{n}_\Gamma c^*] = -2c_\Gamma$ , so that the exact solution reads

$$c_\Gamma(x, t) = \begin{cases} \exp\{-\frac{2}{u_\Gamma}x\}, & x < u_\Gamma t, \\ 0, & x \geq u_\Gamma t. \end{cases} \quad (4.4)$$

The approximation,  $c_h$ , along the fracture is plotted at  $t = 0.05$  and  $t = 1.5$  (steady-state) in Fig. 5 and compared to the exact solution.

We observe that we get the correct steady-state solution in both cases, and that the velocity of the concentration front is correct. Due to the low order method we get significant numerical diffusion as expected, but we see that the front gets sharper as  $N$  increases.

#### 4.2. Benchmark cases for the pure pressure problem

In this section we consider two of the benchmark cases defined in [32] for the pure pressure problem. We only consider the cases where all fractures have higher permeability than the surrounding matrix as our model only applies to such problems. We employ the exact same problem setup as [32] and compare

Table 1: List of the participating methods in the benchmark paper [32].

Method	Description
Box	Vertex-centered finite-volume method
TPFA	Control volume finite difference method with two-point flux approximation
MPFA	Control volume finite difference method with multi-point flux approximation
EDFM	Embedded discrete fracture-matrix model
Flux-Mortar	Mortar discrete fracture-matrix model
P-XFEM	Primal extended finite element method
D-XFEM	Dual extended finite element method

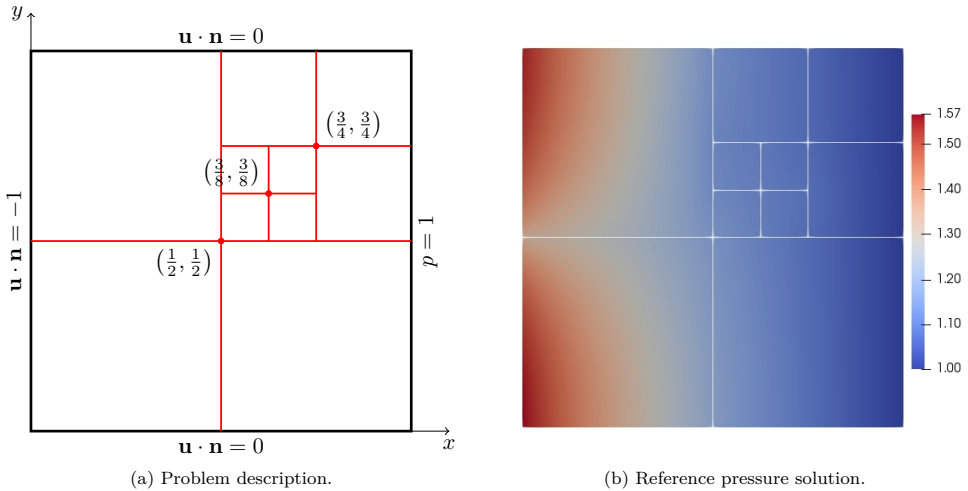


Fig. 6: Benchmark 1 (pressure problem).

our results with those given therein<sup>1</sup>. The six methods considered in this study are listed in Table 1. We only give a very brief description of these methods here, and refer to [32] and references therein for further details. Our method will be denoted EFEM.

#### 4.2.1. Benchmark 1: Regular fracture network

Benchmark 1 is a regular fracture network embedded in the unit square,  $\Omega = (0, 1)^2$ , see Fig. 6a. The top and bottom boundary faces have homogeneous Neumann conditions (no flow); the left boundary face has a constant inflow flux,  $\mathbf{u} \cdot \mathbf{n} = -1$ ; and the right boundary face has Dirichlet condition  $p_D = 1$ . The rock properties are  $\boldsymbol{\kappa} = \mathbf{I}$ ,  $\kappa_\Gamma = 10^4$  and  $w = 10^{-4}$ .

A reference solution is obtained in [32] by using a mimetic finite difference (MFD) method on a very fine reference mesh where the fractures are resolved by 10 elements in their normal direction. The reference mesh is coarser away from the fractures and has a total of 1175056 elements. Hence, the fractures are not modeled as a lower dimensional embedding, but as a continuous model with  $\boldsymbol{\kappa} = \kappa_\Gamma \mathbf{I}$  in the fracture elements. We denote by  $K_{\text{ref}}$  the reference elements and by  $p_{\text{ref}}$  the reference solution. The reference solution is displayed in Fig. 6b.

<sup>1</sup>All results reported in [32] are public available at <https://git.iws.unistuttgart.de/benchmarks/fracture-flow>.

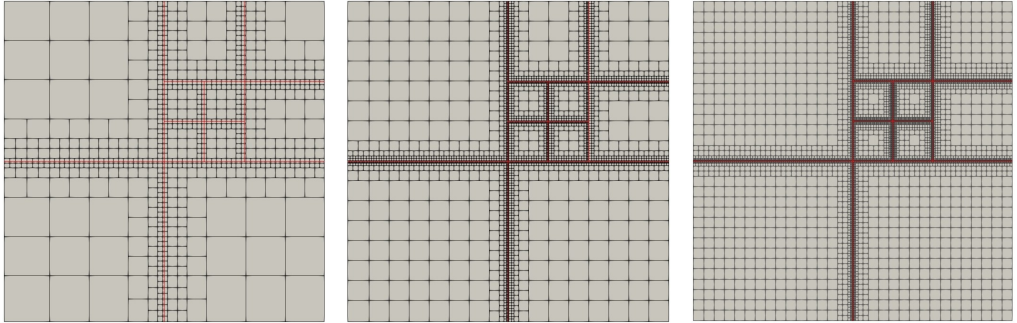


Fig. 7: Benchmark 1 (pressure problem). Locally refined meshes with  $N_{\text{dof}}$  equal to 932, 4532 and 19579, respectively. Fractures are included as red lines. We avoid fractures along element faces.

To measure the error in the pressure solution, we define two error functions,  $err_M$  and  $err_F$ , measuring the error in the matrix and fractures, respectively,

$$err_M^2 = \frac{1}{|\Omega|(\Delta p_{\text{ref}})^2} \sum_{f=K_{\text{ref}} \cap K} |f|(p_h|_{f_m} - p_{\text{ref}}|_{K_{\text{ref}}})^2 \approx \frac{1}{|\Omega|(\Delta p_{\text{ref}})^2} \|p_h - p_{\text{ref}}\|_{L^2(\Omega)}^2, \quad (4.5)$$

$$err_F^2 = \frac{1}{|\Gamma|(\Delta p_{\text{ref}})^2} \sum_{e=(K_{\text{ref}} \cap K) \cap \Gamma} |e|(p_h|_{e_m} - p_{\text{ref}}|_{K_{\text{ref}}})^2 \approx \frac{1}{|\Gamma|(\Delta p_{\text{ref}})^2} \|p_h - p_{\text{ref}}\|_{L^2(\Gamma)}^2, \quad (4.6)$$

where  $\Delta p_{\text{ref}} = \max_{\Omega} p_{\text{ref}} - \min_{\Omega} p_{\text{ref}}$  and  $f_m$  and  $e_m$  denotes the midpoints of  $f$  and  $e$ , respectively. Observe that these are  $L^2$  errors where the integrals are approximated by the midpoint rule.

We solve the pressure problem on both uniform  $N \times N$  meshes with  $N = \{19, 37, 73, 139\}$ , denoted UMRN, and three locally refined meshes, denoted LR*i*, for  $i = 1, 2, 3$ , where the local refinement is based on the a priori estimate (3.11) such that  $h_{\Gamma} \lesssim h^2$  where  $h_{\Gamma}$  is the element size in the vicinity of the fractures. The LR meshes are shown in Fig. 7. The errors are plotted against  $N_{\text{dof}}$  in Fig. 8. We see that the error for the uniform meshes has convergence order  $N_{\text{dof}}^{-1/2}$  in accordance with the error estimate, while the error is lower and converge faster for the LR meshes.

In Table 2 we compare our results with the ones reported in [32], and we observe that the results are in good agreement. Furthermore, in Fig. 9 the pressure along the lines  $y = 0.7$  and  $x = 0.5$  are plotted, similarly to the results reported in [32]. We observe a good match with the reference solution, and in particular we see that the LR mesh gives better accuracy close to the fractures.

**Remark 4.1.** We would like to point out that the error functions in [32] are defined in a similar way, but instead of using  $p_h$  directly, the projection of  $p_h$  onto piecewise constant functions on the computational mesh is used. In the case where the pressure approximation is piecewise constant this is equivalent to what we do. However, for higher order polynomial approximations, the error functions used in [32] would give unfavorable results.

#### 4.2.2. Benchmark 4: A realistic case

We consider next benchmark 4 in [32]. The geometry represents a real set of fractures from an interpreted outcrop in the Sotra island, near Bergen in Norway, see [32] for more details. For this case  $\Omega = (0, 700) \times (0, 600)$  and  $\Gamma$  is the union of 64 straight fractures in a complex pattern, see Fig. 10. The matrix permeability is set to  $\kappa = 10^{-14} \mathbf{I} \text{ m}^2$ . All fractures have permeability  $\kappa_{\Gamma} = 10^{-8} \text{ m}^2$ , and aperture  $w = 10^{-2} \text{ m}$ . We apply homogeneous Neumann boundary conditions (no flow) on the top and bottom boundary faces,  $p_D = 1013250 \text{ Pa}$  on the left face, and  $p_D = 0 \text{ Pa}$  on the right face.

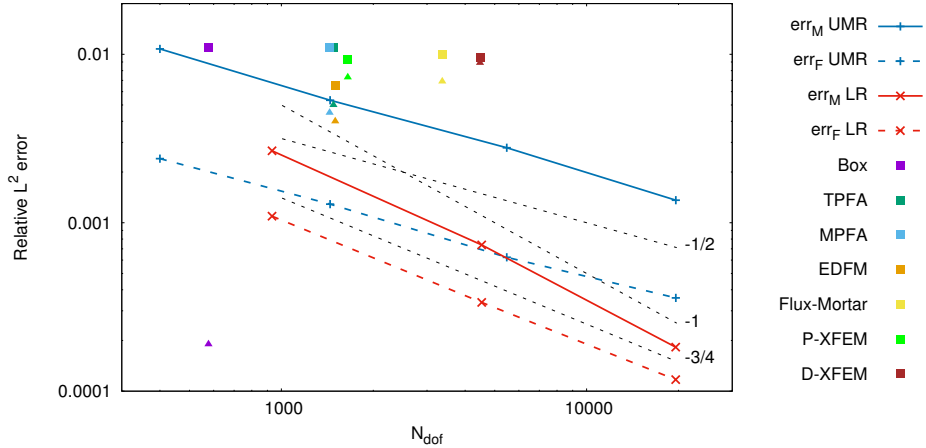


Fig. 8: Benchmark 1 (pressure problem). Errors against  $N_{\text{dof}}$ . Solid lines denote the matrix error  $err_M$ , and dashed lines denote the fracture error  $err_F$  for UMR (blue) and LR (red) meshes. Black dashed lines are straight lines of labeled slope. Filled squares and triangles denote  $err_M$  and  $err_F$ , respectively, for the methods reported in [32].

Table 2: Benchmark 1 (pressure problem). Comparison with the results in [32] for error, matrix density (nnz denotes number of non-zero entries in the system matrix) and matrix condition number. *No. of elements* for the methods in [32] are listed as matrix elements plus fracture elements. In light of Remark 4.1 we would like to point out that Box and EDFM have continuous pressure approximation, so that the errors associated with these would likely be smaller.

Method	$N_{\text{dof}}$	No. of elements	$err_M$	$err_F$	$\text{nnz}/N_{\text{dof}}^2$	$\ \cdot\ _2\text{-cond}$
EFEM UMR37	1444	1369	5.3e-3	1.3e-3	5.9e-3	3.3e4
EFEM LR1	932	757	2.7e-3	1.1e-3	7.0e-3	1.1e4
Box	577	1078 + 74	1.1e-2	1.9e-4	1.1e-2	2.2e3
TPFA	1481	1386 + 95	1.1e-2	4.4e-3	2.7e-3	4.8e4
MPFA	1439	1348 + 91	1.1e-2	4.5e-3	8.0e-3	5.8e4
EDFM	1501	1369 + 132	6.5e-3	4.0e-3	3.3e-3	5.6e4
Flux-Mortar	3366	1280 + 75	1.0e-2	6.9e-3	1.8e-3	2.4e6
P-XFEM	1650	961 + 164	9.3e-2	7.3e-3	8.0e-3	9.3e9
D-XFEM	4474	1250 + 126	9.6e-3	8.9e-3	1.3e-3	1.2e6

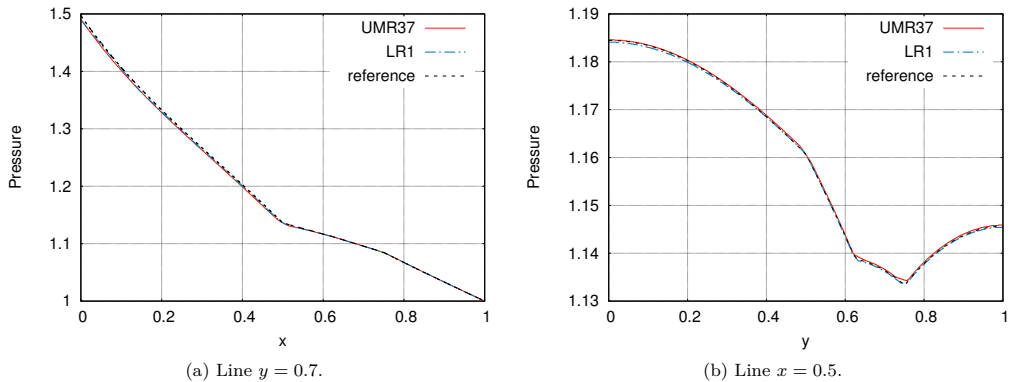


Fig. 9: Benchmark 1 (pressure problem). Pressure solution along two lines.

Table 3: Benchmark 4 (pressure problem). DoF, number of elements, matrix density (nnz denotes number of non-zero entries in the system matrix) and matrix condition number for EFEM on different meshes compared to the corresponding methods in [32]. *No. of elements* for the methods in [32] are listed as matrix elements plus fracture elements.

Method	$N_{\text{dof}}$	No. of elements	$\text{nnz}/N_{\text{dof}}^2$	$\ \cdot\ _2\text{-cond}$
EFEM $\mathcal{M}_2^2$	5349	4623	1.3e-3	3.5e5
EFEM $\mathcal{M}_2^{2,r}$	9185	7629	7.2e-4	9.3e6
EFEM $\mathcal{M}_2^4$	33337	27666	2.0e-4	1.5e7*
EFEM $\mathcal{M}_2^{4,r}$	33924	28104	1.9e-4	6.4e7*
Box	5563	10807 + 1386	1.2e-3	9.3e5
TPFA	8481	7614 + 867	4.9e-4	5.3e6
MPFA	8588	7614 + 867	1.6e-3	4.9e6
EDFM	3599	2491 + 1108	1.4e-3	4.7e6
Flux-Mortar	25258	8319 + 1317	2.0e-4	2.2e17

\* Estimate of the 1-norm condition number based on MATLABs `cond` command.

Denote by  $\mathcal{M}_0$  the  $7 \times 6$  base mesh with  $h = 100$ . Then let  $\mathcal{M}_i^j$  be the mesh where  $\mathcal{M}_0$  is first refined globally  $i$  times, and then recursively refined locally around the fractures  $j$  times. With this  $h_{\min} = 100 \cdot 2^{-(i+j)}$  and  $h_{\max} = 100 \cdot 2^{-i}$ . Some of the fractures are very close without intersecting. It is important to resolve this geometrical aspect so that each vertex patch only see one fracture unless the fractures are connected. We denote by  $\mathcal{M}_i^{j,r}$  the mesh where  $\mathcal{M}_i^j$  is further locally refined to resolve close non-connected fractures. The DoFs and number of elements are reported in Table 3, along with the corresponding numbers for the methods considered in [32]. Fig. 11 displays two of the meshes and illustrates the effect of resolving the geometry.

Fig. 12 shows the pressure approximation on four different meshes. Observe that we have some instabilities in the solution in the upper right corner that vanish as we refine. This is due to the fact that one of the fractures cuts the corner and that we have zero Dirichlet condition at the right end of this fracture. Figs. 13 and 14 plots the pressure approximation along the lines  $y = 500$  and  $x = 625$ . Results on the highly refined mesh  $\mathcal{M}_6^6$ , where all geometry is sufficiently resolved, are included as a reference solution. We clearly see the effect of resolving the geometry, and we observe similar results to the ones reported in [32].



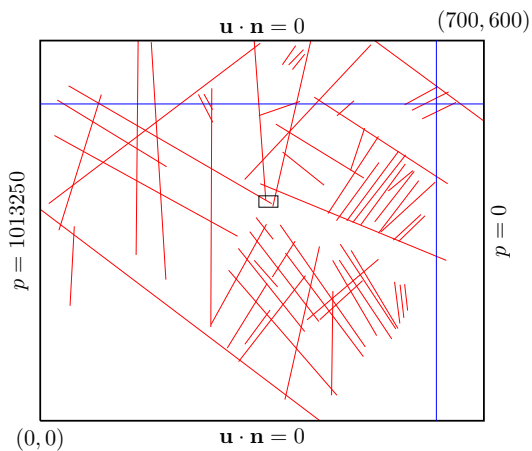


Fig. 10: Benchmark 4 (pressure problem). Problem description with boundary conditions. The red lines represent fractures, the blue lines represent the lines for which the solution is plotted along in Figs. 13 and 14, and the small black box represents the box plotted in Fig. 11.

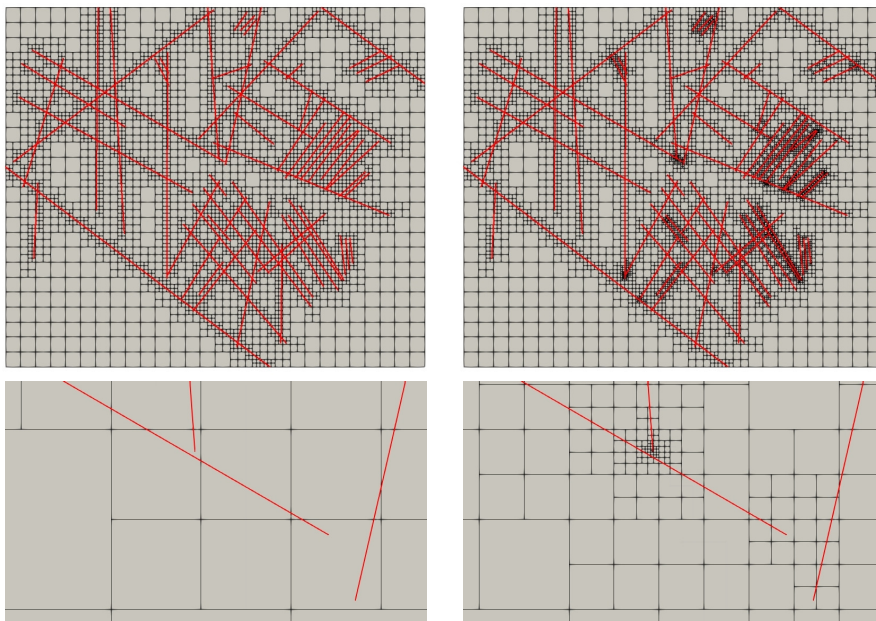


Fig. 11: Benchmark 4 (pressure problem). Computational meshes,  $\mathcal{M}_2^2$  [left] and  $\mathcal{M}_2^{2,r}$  [right]. The top row displays the whole domain  $\Omega$ , while the bottom row displays the mesh on the small rectangle in the middle of Fig. 10.

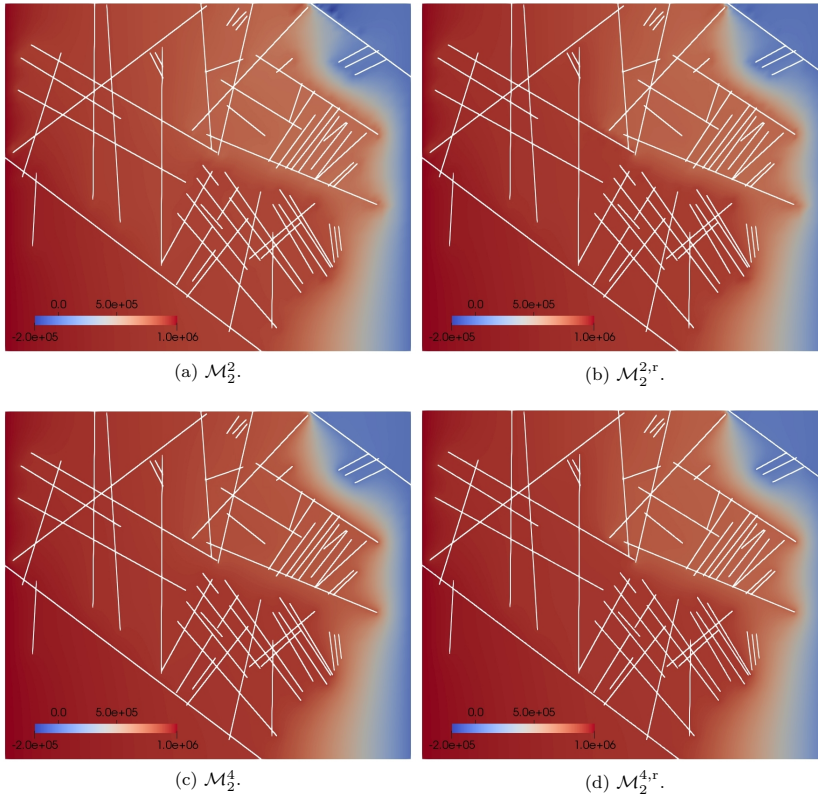


Fig. 12: Benchmark 4 (pressure problem). Pressure approximations.

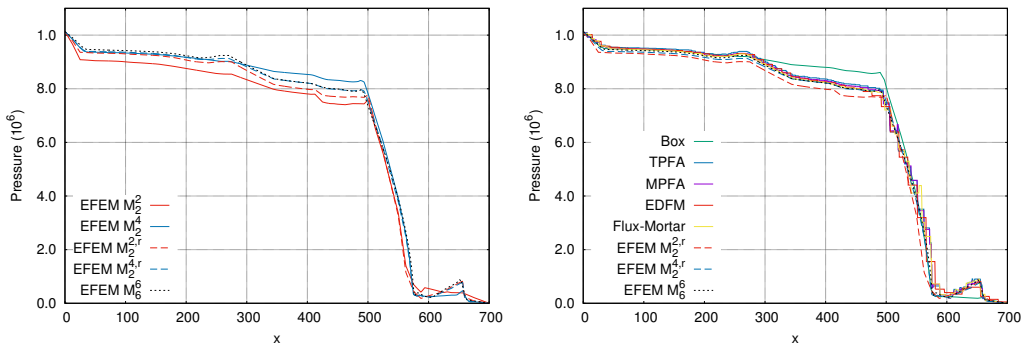


Fig. 13: Benchmark 4. Pressure solution along the line  $y = 500$ . The solution on  $\mathcal{M}_6^6$  is considered as a reference solution.

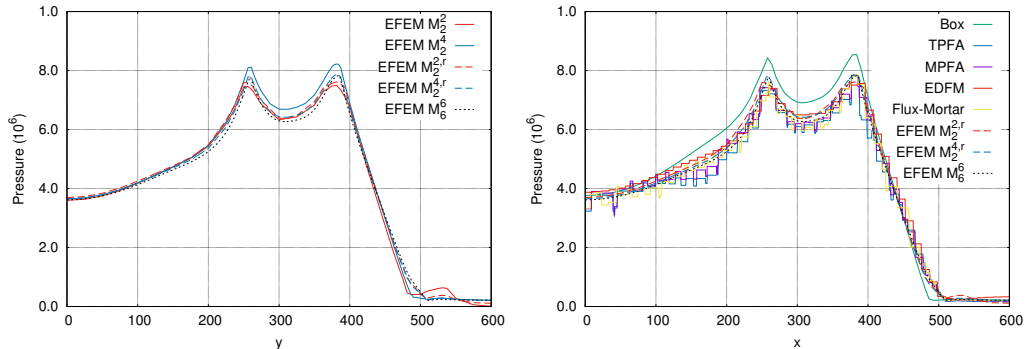


Fig. 14: Benchmark 4 (pressure problem). Pressure solution along the line  $x = 625$ . The solution on  $\mathcal{M}_6^6$  is considered as a reference solution.

### 4.3. Coupled problems

We now couple the benchmark cases with the transport problem and solve for concentration. The coupled problem was not considered in [32].

#### 4.3.1. Benchmark 1: Regular fracture network

For the transport problem we set  $c_0 = 0$ , apply a boundary concentration  $c_b = 1$  on the inflow boundary ( $x = 0$ ), and let  $T = 0.5$ . We consider the same computational meshes as for the pressure problem. In addition, we construct a reference mesh with 182674 elements where the fractures are fully resolved, i.e.,  $h = w$  at the fractures and  $h \approx 16w$  away from the fractures. A reference solution is then obtained by a standard FV method on a continuous fracture model (no lower dimensional embedding), i.e., Eq. (3.29a) with  $\mathcal{K}_h^M = \mathcal{K}_h$  and  $\boldsymbol{\kappa} = \kappa_{\Gamma} \mathbf{I}$  in the elements in the fracture domain. Time steps for the reference solution is  $\Delta t = 1 \cdot 10^{-5}$ .

Fig. 15 shows the velocity approximations in each of the six fractures for the different meshes. We see a very good agreement, in particular for the LR meshes. This is as expected since the velocity is derived from the pressure solution, which was shown earlier to have higher accuracy when refining around the fractures.

For the transport problem, we define a quantity of interest, QOI, as the flux of concentration out of the two fractures on the right boundary face,

$$\text{QOI}_1(t) = (\mathbf{u}_{\Gamma} \cdot \mathbf{nc})|_{\mathbf{x}=(1.0,0.5)}, \quad (4.7a)$$

$$\text{QOI}_2(t) = (\mathbf{u}_{\Gamma} \cdot \mathbf{nc})|_{\mathbf{x}=(1.0,0.75)}. \quad (4.7b)$$

For the reference solution, these quantities are calculated as

$$\text{QOI}_1^{\text{ref}}(t) = \int_{0.5 - \frac{w}{2}}^{0.5 + \frac{w}{2}} (\mathbf{u} \cdot \mathbf{nc})|_{x=1} dy, \quad (4.8a)$$

$$\text{QOI}_2^{\text{ref}}(t) = \int_{0.75 - \frac{w}{2}}^{0.75 + \frac{w}{2}} (\mathbf{u} \cdot \mathbf{nc})|_{x=1} dy. \quad (4.8b)$$

First, we solve the coupled problem on the four uniform meshes with  $\Delta t = 1.0 \cdot 10^{-3}$ ,  $5.0 \cdot 10^{-4}$ ,  $2.5 \cdot 10^{-4}$ , and  $1.25 \cdot 10^{-4}$ , respectively, and on the three LR meshes with  $\Delta t = 5.0 \cdot 10^{-4}$ ,  $2.5 \cdot 10^{-4}$ , and  $1.25 \cdot 10^{-4}$ , respectively. The concentration solution on the finest meshes are displayed in Figs. 16 and 17, while QOI is plotted against time for all meshes in Fig. 18.

We observe similar solutions for all meshes. At early times and in fracture 1 ( $y = 0.5$ ), we have the best results on the LR meshes. However, the LR meshes are relatively coarse in the matrix. This causes large

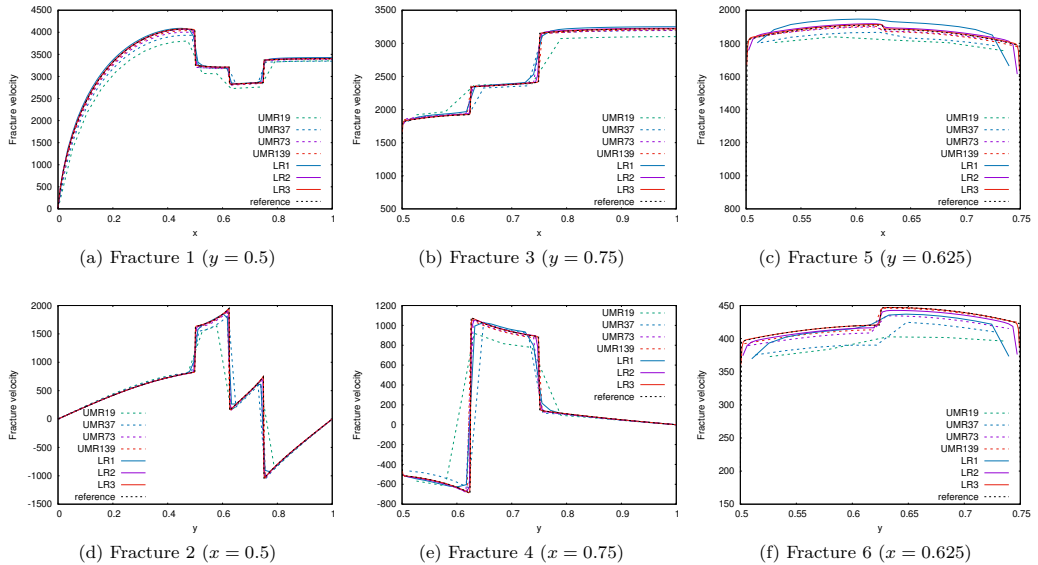


Fig. 15: Benchmark 1 (coupled problem): Fracture velocities for the different meshes.

numerical diffusion and with time the concentration front in the matrix reaches the first vertical fracture ( $x = 0.5$ ). This explains why the solution on the LR meshes becomes inaccurate at large times. A better meshing for the coupled problem would be to refine both close to the fractures and in the left half of  $\Omega$ .

At last, we ran a series of simulations on the UMR meshes with  $\Delta t = 10^{-4}$  and compared to the reference solution by a  $L^2$  norm over the fractures, see Fig. 19. We get a higher convergence than what is expected from the lowest order FV method.

#### 4.3.2. Benchmark 4: A realistic case

We now couple benchmark 4 to the transport problem, where  $c_0 = 0$  and an inflow concentration  $c_b = 1$  is set on the left boundary face. Such problem was also considered in [21], but with different permeabilities. We set the end time for the simulations to  $T = 100$  years<sup>2</sup>.

First, we set  $\Delta t = 1$  hour (36500 time steps), and consider the meshes  $\mathcal{M}_2^{d,r}$ . Concentration solutions in the fractures are displayed in Fig. 20. Furthermore, convergence of the concentration in the fractures is demonstrated in Fig. 21. Due to the high fracture permeability, nearly all transport take place in the fractures, and hence we do not display the matrix solution. We observe that we get reasonable good results even for the coarsest mesh. Furthermore, the results for  $\mathcal{M}_2^d$  clearly illustrates the importance of resolving the geometry, as the solution is far off in some of the fractures, even compared to  $\mathcal{M}_2^{d,r}$  which has much less DoFs. Convergence is rather slow due to the low order method.

Next, we ran a series of simulations on  $\mathcal{M}_2^{d,r}$  with  $\Delta t = \{20, 50, 100, 365\}$  days and compared to the solution with  $\Delta t = 1$  hour on the same mesh. The  $L^2$  error over  $\Omega$  at  $t = T$  is plotted against  $(\Delta t)^{-1}$  in Fig. 22, and we observe linear convergence in time as expected.

<sup>2</sup>1 year = 365 days.

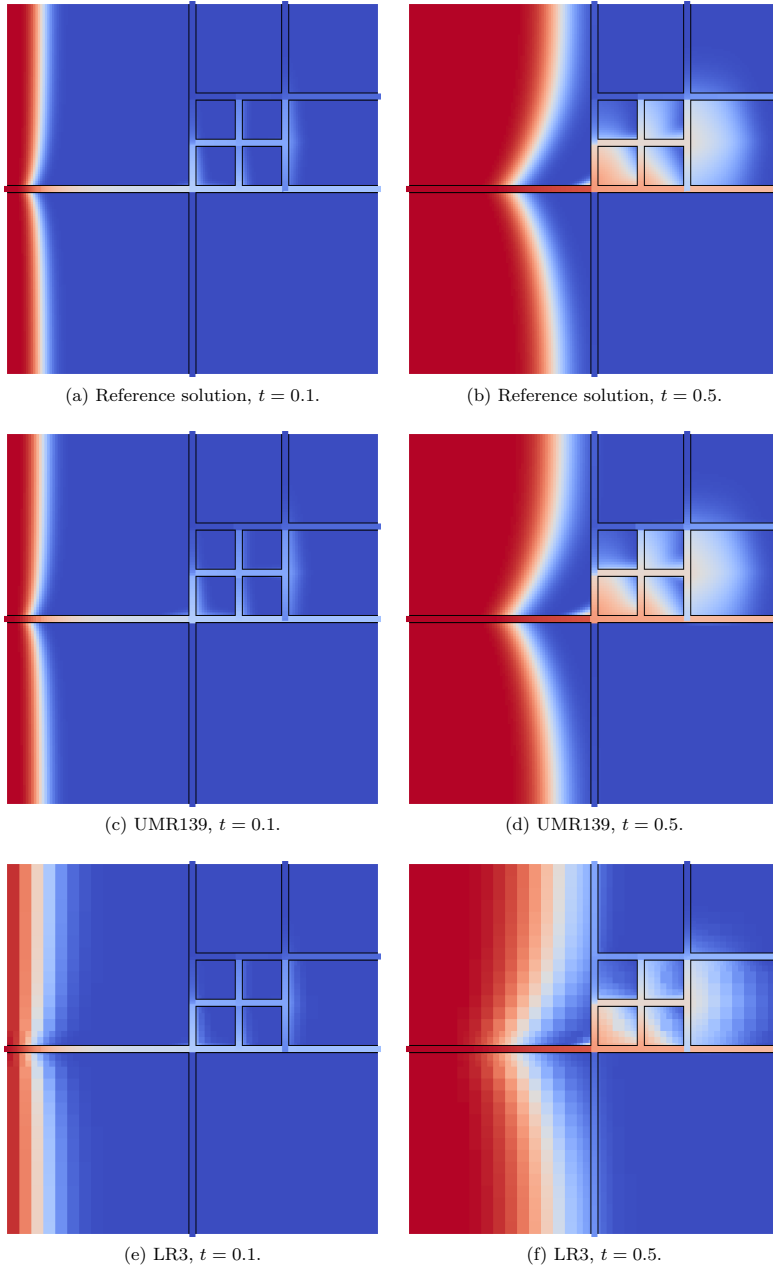


Fig. 16: Benchmark 1 (coupled problem). Concentration solution. The fractures are visualized with a fixed exaggerated width. Number of degrees of freedom,  $N_{\text{dof}}$ , is 182674 for the reference solution (continuum model), 19321 for UMR139, and 16252 for LR3.

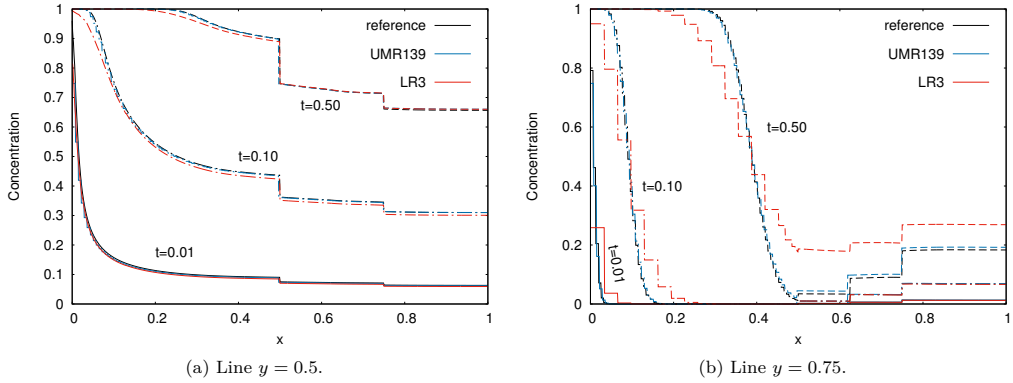


Fig. 17: Benchmark 1 (coupled problem). Concentration solution along two lines at different times.

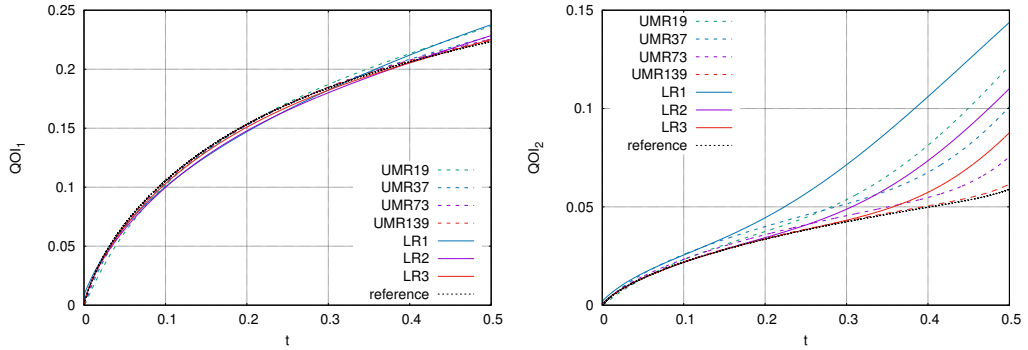


Fig. 18: Benchmark 1 (coupled problem). Quantity of interest,  $QOI_i$ ,  $i = 1, 2$ , as functions of time.

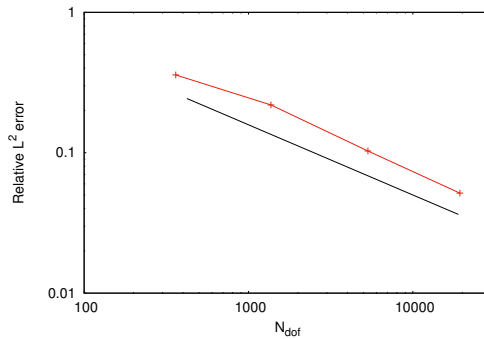


Fig. 19: Benchmark 1 (coupled problem). Relative concentration error in fractures,  $\frac{\|c_{ref} - c_h\|_{L^2(\Gamma)}}{\|c_{ref}\|_{L^2(\Gamma)}}$ , at  $t = T$  against  $N_{dof}$ . The reference solution is compared against the solution on the UMR meshes with  $\Delta t = 1 \cdot 10^{-4}$ . The black reference line has slope  $-0.5$ .

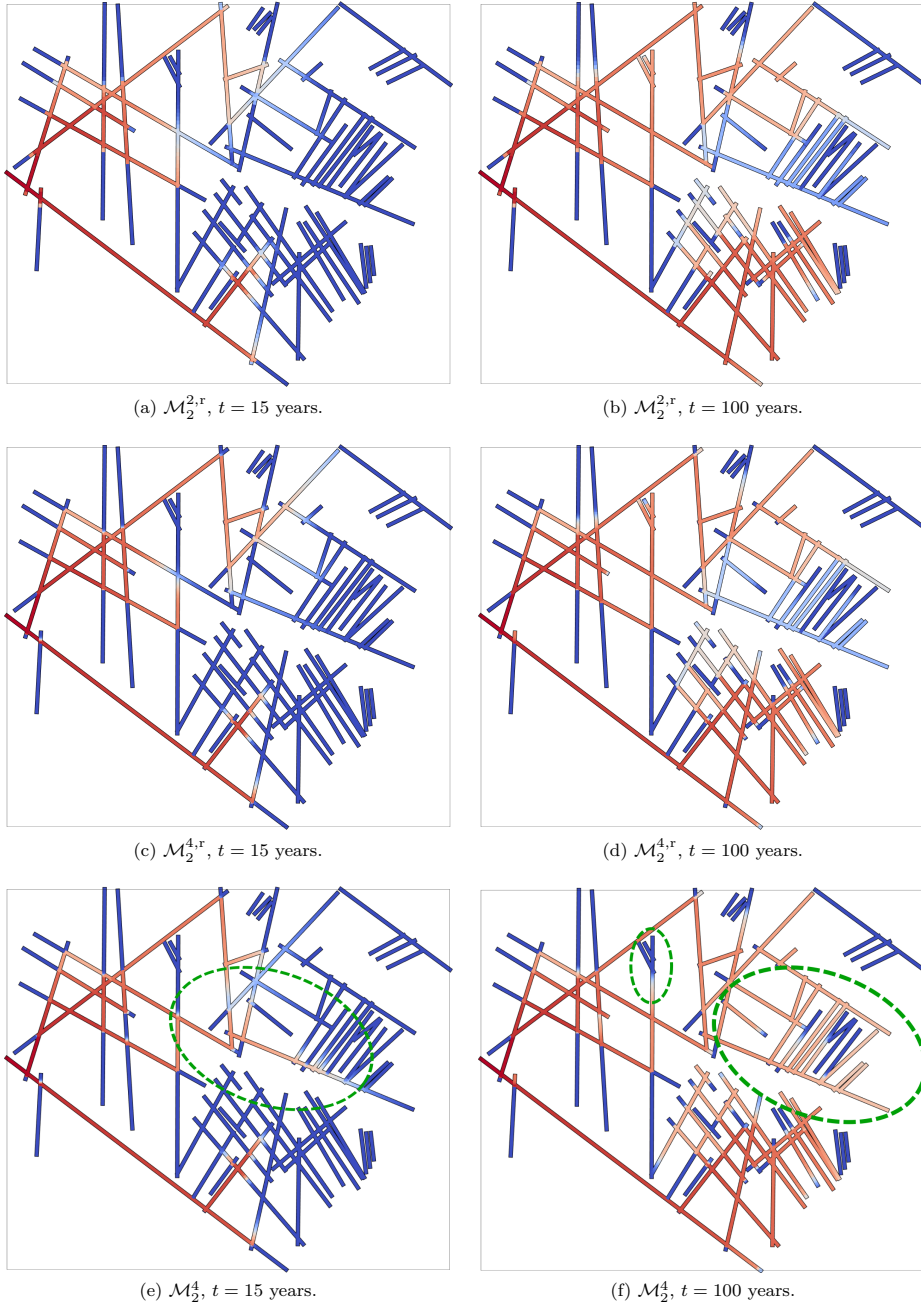


Fig. 20: Benchmark 4 (coupled problem). Concentration solutions in fractures. The fractures are displayed with a fixed (exaggerated) width. Regions where the results on the non-resolved mesh  $\mathcal{M}_2^4$  deviates substantially from the other two meshes are marked with green dashed ellipses.

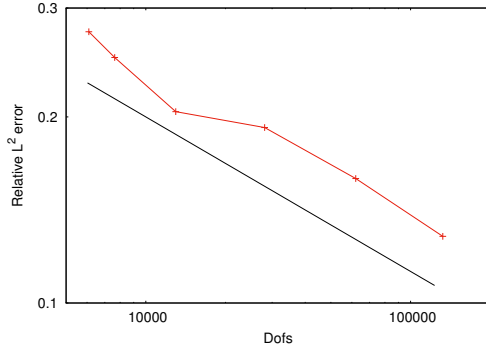


Fig. 21: Benchmark 4 (coupled problem). Relative concentration error in fractures,  $\frac{\|c_{\text{ref}} - c_h\|_{L^2(\Gamma)}}{\|c_{\text{ref}}\|_{L^2(\Gamma)}}$ , at  $t = T$  against  $N_{\text{dof}}$ . The solution on  $\mathcal{M}_2^{8,r}$  is used as reference solution,  $c_{\text{ref}}$ , and compared against the solutions on  $\mathcal{M}_2^{j,r}$  for  $j = 1, 2, \dots, 6$ . All simulations are run with  $\Delta t = 1$  day. The black reference line has slope  $-0.25$ .

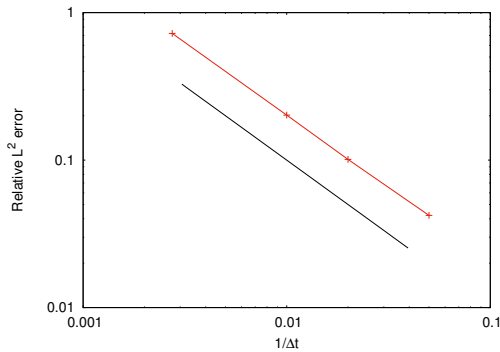


Fig. 22: Benchmark 4 (coupled problem). Relative concentration error,  $\frac{\|c_{\text{ref}} - c_h\|_{L^2(\Omega)}}{\|c_{\text{ref}}\|_{L^2(\Omega)}}$ , at  $t = T$  against  $1/\Delta t$ . All simulations are run on  $\mathcal{M}_2^{2,r}$ . The solution with  $\Delta t = 1$  hour is used as reference solution,  $c_{\text{ref}}$ , and compared to the solutions with  $\Delta t = \{20, 50, 100, 365\}$  days. The black reference line has slope  $-1$ .



## 5. Concluding remarks

This article addresses the *numerical solution of a coupled flow and transport problem* in fractured porous media, where the *fractures are modeled as lower-dimensional interfaces* embedded in the surrounding matrix. The proposed solution strategy includes three main steps: (1) Solving the flow problem with an embedded finite element method (EFEM) [13]; (2) Locally conservative flux approximation; and (3) Solving the transport problem with a non-standard lowest order finite volume (FV) method.

*The main contribution of this work is that we couple EFEM with a numerical model for the transport problem.* EFEM allows for complex fracture geometry, where the fractures can cut the elements arbitrarily, and compared to other embedded discrete fracture-matrix models, there are no lower-dimensional elements along the fractures. The numerical model for the transport problem presented in this work, aims to be as flexible as EFEM with respect to meshing. This is resolved by a lowest order upwind FV method where the fracture solution is represented by elements cut by the fracture. The main novelty in our method is how we approximate the coupling term between the matrix and the fractures.

Furthermore, this work includes the following contributions:

- We apply EFEM to realistic benchmark problems presented in [32]. Our results are in good agreement with the results in [32] and in some cases EFEM is most accurate. Applying a priori local refinement based on an estimate in [13] gives especially good results.
- To ensure locally conservative fluxes, we adapt and apply the postprocessing method presented in [36].
- We demonstrate the abilities of our coupled solution strategy by numerical examples on a realistic case with a complex fracture network.

*A main advantage of our method compared to other discrete fracture-matrix models, is the inherent simplicity*, both in terms of formulation, implementation and meshing. Despite the simplicity, the presented results are promising.

One direction for further work is to consider adaptive routines for the transport solver, perhaps looking at the space-time approach allowing for easy handling of local time refinement. Rigorous convergence proofs and error estimates for the transport solver are also desired. Moreover, one could pursue including more physics into the model, e.g., multi-phase flow. To reduce the numerical diffusion associated with the implicit Euler method, one could consider higher order time integration, e.g., [40].

## Acknowledgements

LHO is funded by VISTA (Grant No. 6355) — a basic research program funded by Statoil, conducted in close collaboration with The Norwegian Academy of Science and Letters. MGL was supported by The Swedish Foundation for Strategic Research Grant No. AM13-0029, and the Swedish Research Council Grants Nos. 2013-4708, 2017-03911. The authors appreciate the open access to the results given in the benchmark paper [32]. Furthermore, the authors thank Karl Larsson, Department of Mathematics and Mathematical Statistics, Umeå University, for his help with visualization of the results in Figs. 16 and 20.

## Appendix

### A.1. Discontinuous Galerkin formulation

We formulate here a lowest order Discontinuous Galerkin method (DG(0)) with upwinding for the transport problem, Eq. (2.14). This formulation is equivalent to the finite volume method derived in Section 3.3. We include it here for convenience of the reader more familiar with DG methods. The DG formulation is also more suitable for deriving error estimates.

We start by multiplying Eq. (2.14a) by a test function  $v$ , integrate over an element  $K \in \mathcal{K}_h^M$  and apply Greens formula to obtain

$$\int_K \phi \frac{\partial c}{\partial t} v - \int_K \mathbf{c} \mathbf{u} \cdot \nabla v + \int_{\partial K} \mathbf{u} \cdot \mathbf{n}_K c v = \int_K f(c) v, \quad K \in \mathcal{K}_h^M. \quad (\text{A.1})$$

Summing the boundary term over all  $K \in \mathcal{K}_h^M$  we get

$$\begin{aligned} \sum_{K \in \mathcal{K}_h^M} \int_{\partial K} \mathbf{u} \cdot \mathbf{n}_K c v &= - \sum_{F \in \mathcal{F}_{h,1}^M} \int_F \mathbf{u} \cdot \mathbf{n}_F c \llbracket v \rrbracket \\ &+ \sum_{F \in \mathcal{F}_{h,1}^{FM}} \int_F \mathbf{u} \cdot \mathbf{n}_{MF} c v \\ &+ \sum_{F \in \mathcal{F}_{h,\text{out}}^M} \int_F \mathbf{u} \cdot \mathbf{n}_F c v + \sum_{F \in \mathcal{F}_{h,\text{in}}^M} \int_F \mathbf{u} \cdot \mathbf{n}_F c_B v. \end{aligned} \quad (\text{A.2})$$

We have denoted by  $\mathbf{n}_{MF}$  the unit normal on  $F \in \mathcal{F}_{h,1}^{FM}$  pointing from the matrix domain towards the fracture.

Similarly, we multiply Eq. (2.14b) by a test function  $v_\Gamma$ , integrate over  $K \cap \Gamma$ , for  $K \in \mathcal{K}_h^F$ , and apply Greens formula to obtain

$$\int_{K \cap \Gamma} w \phi_\Gamma \frac{\partial c_\Gamma}{\partial t} v_\Gamma - \int_{K \cap \Gamma} c_\Gamma \mathbf{u}_\Gamma \cdot \nabla_\Gamma v_\Gamma + \int_{\partial(K \cap \Gamma)} \mathbf{u}_\Gamma \cdot \mathbf{n}_{K \cap \Gamma} c_\Gamma v_\Gamma - \int_{K \cap \Gamma} \llbracket \mathbf{u} \cdot \mathbf{n} c^* \rrbracket v_\Gamma = \int_{K \cap \Gamma} f_\Gamma(c_\Gamma) v_\Gamma. \quad (\text{A.3})$$

Again, summing the boundary term over all  $K \in \mathcal{K}_h^F$  we get

$$\begin{aligned} \sum_{K \in \mathcal{K}_h^F} \int_{\partial(K \cap \Gamma)} \mathbf{u}_\Gamma \cdot \mathbf{n}_{K \cap \Gamma} c_\Gamma v_\Gamma &= - \sum_{F \in \mathcal{F}_{h,1}^F} (\mathbf{u}_\Gamma \cdot \mathbf{t}_{\Gamma,FC\Gamma} \llbracket v_\Gamma \rrbracket) |_{F \cap \Gamma} \\ &+ \sum_{F \in \mathcal{F}_{h,\text{in}}^F} (\mathbf{u}_\Gamma \cdot \mathbf{t}_{\Gamma,FC\Gamma,B} v_\Gamma) |_{F \cap \Gamma} \\ &+ \sum_{F \in \mathcal{F}_{h,\text{out}}^F} (\mathbf{u}_\Gamma \cdot \mathbf{t}_{\Gamma,FC\Gamma} v_\Gamma) |_{F \cap \Gamma}, \end{aligned} \quad (\text{A.4})$$

where  $\mathbf{t}_{\Gamma,F}$  is the unit tangent to  $\Gamma$  oriented in the same direction as  $\mathbf{n}_F$ .

To formulate the DG method, we replace  $c$  and  $c_\Gamma$  by  $c_h \in Q_0(\mathcal{K}_h)$  and  $\varphi$  and  $\varphi_\Gamma$  by  $\varphi_h \in Q_0(\mathcal{K}_h)$ . Furthermore, we approximate the coupling term as follows,

$$\int_{K \cap \Gamma} \llbracket \mathbf{u} \cdot \mathbf{n} c_h^* \rrbracket v_h \approx \sum_{\bar{K} \in \mathcal{K}_h^M} \int_{\partial \bar{K} \cap K} (\mathbf{n}_F \cdot \mathbf{n}_K) \mathbf{u} \cdot \mathbf{n}_F c_h v_h. \quad (\text{A.5})$$

This is an equivalent approximation as Eq. (3.16). Summing this term over all  $K \in \mathcal{K}_h^F$  we get

$$\sum_{K \in \mathcal{K}_h^F} \int_{K \cap \Gamma} \llbracket \mathbf{u} \cdot \mathbf{n} c_h^* \rrbracket v_h \approx \sum_{F \in \mathcal{F}_{h,1}^{FM}} \int_F \mathbf{u} \cdot \mathbf{n}_{MF} c_h v_h. \quad (\text{A.6})$$

Adding everything up, we end up the following formulation. Find  $c_h \in Q_0(\mathcal{K}_h)$  such that

$$b(c_h, v_h) = k(v_h), \quad \forall v_h \in Q_0(\mathcal{K}_h), \quad (\text{A.7})$$

where

$$\begin{aligned} b(c, v) &= \sum_{K \in \mathcal{K}_h^M} \int_K \left( \phi \frac{\partial c}{\partial t} c v + \check{q} c v \right) + \sum_{K \in \mathcal{K}_h^F} \int_{K \cap \Gamma} \left( w \phi_\Gamma \frac{\partial c}{\partial t} v + \check{q}_\Gamma c v \right) \\ &- \sum_{F \in (\mathcal{F}_{h,1} \setminus \mathcal{F}_{h,1}^F)} \int_F \mathbf{u} \cdot \mathbf{n}_F c \llbracket v \rrbracket - \sum_{F \in \mathcal{F}_{h,1}^F} (\mathbf{u}_\Gamma \cdot \mathbf{t}_{\Gamma,FC\Gamma} \llbracket v \rrbracket) |_{F \cap \Gamma} \\ &+ \sum_{F \in \mathcal{F}_{h,\text{out}}^M} \int_F \mathbf{u} \cdot \mathbf{n}_F c v + \sum_{F \in \mathcal{F}_{h,\text{out}}^F} (\mathbf{u}_\Gamma \cdot \mathbf{t}_{\Gamma,FC\Gamma} c v) |_{F \cap \Gamma} \end{aligned} \quad (\text{A.8})$$

and

$$\begin{aligned}
k(v) &= \sum_{K \in \mathcal{K}_h^M} \int_K \hat{q} c_w v + \sum_{K \in \mathcal{K}_h^F} \int_{K \cap \Gamma} \hat{q}_\Gamma c_w v \\
&+ \sum_{F \in \mathcal{F}_{h,\text{in}}^M} \int_F \mathbf{u} \cdot \mathbf{n}_F c_B v + \sum_{F \in \mathcal{F}_{h,\text{in}}^F} (\mathbf{u}_\Gamma \cdot \mathbf{t}_{\Gamma,F} c_{\Gamma,B} v) |_{F \cap \Gamma}.
\end{aligned} \tag{A.9}$$

We have used the definition of  $f(c)$  and  $f_\Gamma(c_\Gamma)$ , see Eq. (2.15). For the concentration on faces  $F \in \mathcal{F}_h$ , we use the upwind approximation

$$\mathbf{u} \cdot \mathbf{n}_F c_h = \begin{cases} \mathbf{u} \cdot \mathbf{n}_F (c_h)_-, & \text{if } \mathbf{u} \cdot \mathbf{n}_F \geq 0, \\ \mathbf{u} \cdot \mathbf{n}_F (c_h)_+, & \text{if } \mathbf{u} \cdot \mathbf{n}_F < 0. \end{cases} \tag{A.10}$$

Applying the velocity model described by Eqs. (3.18)–(3.27), we may simplify the forms  $b(\cdot, \cdot)$  and  $k(\cdot)$  for the coupled problem by a similar approach as described by Eq. (3.19), so that

$$\begin{aligned}
b(c, v) &= \sum_{K \in \mathcal{K}_h^M} \int_K \left( \phi \frac{\partial c}{\partial t} c v + \check{q} c v \right) + \sum_{K \in \mathcal{K}_h^F} \int_{K \cap \Gamma} \left( w \phi_\Gamma \frac{\partial c}{\partial t} v + \check{q}_\Gamma c v \right) \\
&- \sum_{F \in \mathcal{F}_{h,\text{in}}^M} \int_F V_h c \llbracket v \rrbracket + \sum_{F \in \mathcal{F}_{h,\text{out}}^F} \int_F V_h c v
\end{aligned} \tag{A.11}$$

and

$$k(v) = \sum_{K \in \mathcal{K}_h^M} \int_K \hat{q} c_w v + \sum_{K \in \mathcal{K}_h^F} \int_{K \cap \Gamma} \hat{q}_\Gamma c_w v + \sum_{F \in \mathcal{F}_{h,\text{in}}^M} \int_F V_h c_B v + \sum_{F \in \mathcal{F}_{h,\text{in}}^F} \int_F V_h c_{\Gamma,B} v. \tag{A.12}$$

If we apply implicit Euler as time integrator, we end up with a scheme that is equivalent to the FV-IE scheme in Eq. (3.29).

### A.2. Interpretation of concentration solution

The numerical method given by Eq. (3.29) defines a constant solution on  $K \in \mathcal{K}_h^F$ . However,  $K$  originally contains both a fractured domain represented as a lower-dimensional interface,  $K \cap \Gamma$ , and a matrix domain  $K \setminus \Gamma$ . Let  $\{K_j\}_{j \in \{1, \dots, N_K\}}$  be a partition of  $K$  into  $N_K$  subelements defined by  $\Gamma$ . For a single fracture cutting  $K$ , we have  $n_K = 2$ , but for intersecting and bifurcating fractures in  $K$ ,  $n_K$  can be larger. For a terminating fracture, we have  $n_K = 1$ . We interpret the solution on  $K$  by assigning a constant value to each subelement  $K_j$  and one value on the fracture intersection  $K \cap \Gamma$ . Let  $\hat{c}_h$  denote the interpreted solution. Then we define

$$\hat{c}_h|_K = c_h|_K, \quad \forall K \in \mathcal{K}_h^M, \tag{A.13}$$

$$\hat{c}_h|_{K \cap \Gamma} = c_h|_K, \quad \forall K \in \mathcal{K}_h^F. \tag{A.14}$$

It is not as easy to define the interpreted solution on the fracture subelements, but the following algorithm can be used. Denote by  $\mathcal{K}_h^{M,i}$  the (non-empty) subsets of  $\mathcal{K}_h^M$  with elements contained in  $\Omega_i$ , i.e.,

$$\mathcal{K}_h^{M,i} = \{K \in \mathcal{K}_h^M : K \subset \Omega_i\}. \tag{A.15}$$

Furthermore, let  $\mathcal{K}_h^{F,i}$  be the set of all fracture subelements contained in  $\Omega_i$ , i.e.,

$$\mathcal{K}_h^{F,i} = \{K_j \in K : K_j \subset \Omega_i, K \in \mathcal{K}_h^F\}. \tag{A.16}$$

At last, denote by  $\mathcal{N}_K(F)$  the neighbor of  $K$  that shares face  $F$ .

Algorithm 1 recursively assigns values to each element  $\tilde{K} \in \mathcal{K}_h^{\text{F},i}$ . Once a value is assigned to  $\tilde{K}$ , we move  $\tilde{K}$  from  $\mathcal{K}_h^{\text{F},i}$  to  $\mathcal{K}_h^{\text{M},i}$ . In this way we mark  $\tilde{K}$  as assigned and also allow for its value to be further assigned to another neighbor in the next cycle. The algorithm works under the mild assumption that there is at least one matrix element for each subdomain, i.e., for all  $\Omega_i$ ,  $i = 1, 2, \dots, n_d$ , there is an  $K \in \mathcal{K}_h^{\text{M}}$  such that  $K \subset \Omega_i$ . Moreover, we remark that the algorithm is sensitive to the ordering of elements. We refer to Fig. 2 for an illustrative example of how this algorithm works. Finally, we emphasize that this algorithm is purely for the interpretation of the results, and not part of the numerical method.

---

**Algorithm 1:** Assigning values to fracture subelements
 

---

```

for  $i = 1, \dots, n_d$  do
  while  $\mathcal{K}_h^{\text{M},i} \neq \emptyset$  do
    for  $K \in \mathcal{K}_h^{\text{M},i}$  do
      for  $F \in \partial K$  do
         $\tilde{K} = \mathcal{N}_K(F)$ 
        if  $\tilde{K} \in \mathcal{K}_h^{\text{F},i}$  then
           $\tilde{c}_h|_{\tilde{K}} = c_h|_K$ 
           $\mathcal{K}_h^{\text{F},i} = \mathcal{K}_h^{\text{F},i} \setminus \{\tilde{K}\}$ 
           $\mathcal{K}_h^{\text{M},i} = \mathcal{K}_h^{\text{M},i} \cup \{\tilde{K}\}$ 
        end
      end
    end
  end
end
end
end

```

---

**References**

- [1] Alboin, C., Jaffré, J., Roberts, J.E., Wang, X., and Serres, C. Domain decomposition for some transmission problems in flow in porous media. In *Numerical Treatment of Multiphase Flows in Porous Media*, pp. 22–34. Springer, 2000.
- [2] Alboin, C., Jaffré, J., Roberts, J.E., and Serres, C. Modeling fractures as interfaces for flow and transport in porous media. In Z. Chen and R.E. Ewing, eds., *Fluid Flow and Transport in Porous Media: Mathematical and Numerical Treatment*, volume 295 of *Contemporary Mathematics*, pp. 13–24. AMS, 2002.
- [3] Faille, I., Flauraud, E., Nataf, F., Pégaz-Fiornet, S., Schneider, F., and Willien, F. A new fault model in geological basin modelling. Application of finite volume scheme and domain decomposition methods. In *Finite volumes for complex applications*, volume 3, pp. 543–550. 2002.
- [4] Martin, V., Jaffré, J., and Roberts, J.E. Modeling fractures and barriers as interfaces for flow in porous media. *SIAM Journal on Scientific Computing*, 26(5):1667–1691, 2005.
- [5] Angot, P., Boyer, F., and Hubert, F. Asymptotic and numerical modelling of flows in fractured porous media. *ESAIM: Mathematical Modelling and Numerical Analysis*, 43(2):239–275, 2009.
- [6] Frih, N., Martin, V., Roberts, J.E., and Saàda, A. Modeling fractures as interfaces with nonmatching grids. *Computational Geosciences*, 16(4):1043–1060, 2012.
- [7] Formaggia, L., Fumagalli, A., Scotti, A., and Ruffo, P. A reduced model for Darcy’s problem in networks of fractures. *ESAIM: Mathematical Modelling and Numerical Analysis*, 48(4):1089–1116, 2014.
- [8] Schwenck, N., Flemisch, B., Helmig, R., and Wohlmuth, B.I. Dimensionally reduced flow models in fractured porous media: crossings and boundaries. *Computational Geosciences*, 19(6):1219–1230, 2015.
- [9] Faille, I., Fumagalli, A., Jaffré, J., and Roberts, J.E. Model reduction and discretization using hybrid finite volumes for flow in porous media containing faults. *Computational Geosciences*, 20(2):317–339, 2016.
- [10] Boon, W.M., Nordbotten, J.M., and Yotov, I. Robust discretization of flow in fractured porous media, 2016. ArXiv:1601.06977 [math.NA].
- [11] Morales, F. and Showalter, R.E. The narrow fracture approximation by channeled flow. *Journal of Mathematical Analysis and Applications*, 365(1):320–331, 2010.
- [12] Capatina, D., Luce, R., El-Otmany, H., and Barrau, N. Nitsche’s extended finite element method for a fracture model in porous media. *Applicable Analysis*, 95(10):2224–2242, 2016.
- [13] Burman, E., Hansbo, P., and Larson, M.G. A simple finite element method for elliptic bulk problems with embedded surfaces, 2017. ArXiv: 1709.00972 [math.NA].

- [14] Karimi-Fard, M. and Firoozabadi, A. Numerical simulations of water injection in fractured media using the discrete-fracture model and the Galerkin method. *SPE Reservoir Evaluation & Engineering*, 6(02):117–126, 2003.
- [15] Angot, P. A model of fracture for elliptic problems with flux and solution jumps. *Comptes Rendus Mathématique*, 337(6):425–430, 2003.
- [16] Brenner, K., Hennicker, J., Masson, R., and Samier, P. Gradient discretization of hybrid-dimensional Darcy flow in fractured porous media with discontinuous pressures at matrix–fracture interfaces. *IMA Journal of Numerical Analysis*, 37(3):1551–1585, 2016.
- [17] Karimi-Fard, M. and Durlofsky, L.J. A general gridding, discretization, and coarsening methodology for modeling flow in porous formations with discrete geological features. *Advances in Water Resources*, 96:354–372, 2016.
- [18] Antonietti, P.F., Facciola, C., Russo, A., and Varani, M. Discontinuous Galerkin approximation of flows in fractured porous media on polytopic grids. Technical Report 55, MOX, Politecnico di Milano, 2016.
- [19] Antonietti, P.F., Formaggia, L., Scotti, A., Verani, M., and Verzott, N. Mimetic finite difference approximation of flows in fractured porous media. *ESAIM: Mathematical Modelling and Numerical Analysis*, 50(3):809–832, 2016.
- [20] Scotti, A., Formaggia, L., and Sottocasa, F. Analysis of a mimetic finite difference approximation of flows in fractured porous media. *ESAIM: Mathematical Modelling and Numerical Analysis*, 2017.
- [21] Fumagalli, A. and Keilegavlen, E. Dual virtual element methods for discrete fracture matrix models, 2017. ArXiv:1711.01818 [math.NA].
- [22] D’Angelo, C. and Scotti, A. A mixed finite element method for Darcy flow in fractured porous media with non-matching grids. *ESAIM: Mathematical Modelling and Numerical Analysis*, 46(2):465–489, 2012.
- [23] Huang, H., Long, T.A., Wan, J., and Brown, W.P. On the use of enriched finite element method to model subsurface features in porous media flow problems. *Computational Geosciences*, 15(4):721–736, 2011.
- [24] Li, L. and Lee, S.H. Efficient field-scale simulation of black oil in a naturally fractured reservoir through discrete fracture networks and homogenized media. *SPE Reservoir Evaluation & Engineering*, 11(04):750–758, 2008.
- [25] Hajibeygi, H., Karvounis, D., and Jenny, P. A hierarchical fracture model for the iterative multiscale finite volume method. *Journal of Computational Physics*, 230(24):8729–8743, 2011.
- [26] Moïnfar, A., Varavei, A., Sepehrnoori, K., and Johns, R.T. Development of an efficient embedded discrete fracture model for 3D compositional reservoir simulation in fractured reservoirs. *SPE Journal*, 19(02):289–303, 2014.
- [27] Panfili, P., Cominelli, A., and Scotti, A. Using embedded discrete fracture models (EDFMs) to simulate realistic fluid flow problems. In *Second EAGE workshop on naturally fractured reservoirs*. 2013.
- [28] Panfili, P. and Cominelli, A. Simulation of miscible gas injection in a fractured carbonate reservoir using an embedded discrete fracture model. In *Abu Dhabi International Petroleum Exhibition and Conference*. Society of Petroleum Engineers, 2014.
- [29] de Araujo Cavalcante Filho, J.S., Shakiba, M., Moïnfar, A., and Sepehrnoori, K. Implementation of a preprocessor for embedded discrete fracture modeling in an IMPEC compositional reservoir simulator. In *SPE Reservoir Simulation Symposium*. Society of Petroleum Engineers, 2015.
- [30] Tene, M., Bosma, S.B., Al Kobaisi, M.S., and Hajibeygi, H. Projection-based embedded discrete fracture model (pEDFM). *Advances in Water Resources*, 105:205–216, 2017.
- [31] Jiang, J. and Younis, R.M. An improved projection-based embedded discrete fracture model (pEDFM) for multiphase flow in fractured reservoirs. *Advances in Water Resources*, 109:267–289, 2017.
- [32] Flemisch, B., Berre, I., Boon, W., Fumagalli, A., Schwenck, N., Scotti, A., Stefansson, I., and Tatomir, A. Benchmarks for single-phase flow in fractured porous media. *Advances in Water Resources*, 111:239–258, 2018.
- [33] Fumagalli, A. and Scotti, A. A reduced model for flow and transport in fractured porous media with non-matching grids. In *Numerical Mathematics and Advanced Applications 2011*, pp. 499–507. Springer, 2013.
- [34] Burman, E., Hansbo, P., Larson, M.G., and Larsson, K. Cut finite elements for convection in fractured domains, 2018. ArXiv:1801.06103 [math.NA].
- [35] Burman, E., Claus, S., Hansbo, P., Larson, M.G., and Massing, A. Cutfem: Discretizing geometry and partial differential equations. *International Journal for Numerical Methods in Engineering*, 104(7):472–501, 2015.
- [36] Odsæter, L.H., Wheeler, M.F., Kvamsdal, T., and Larson, M.G. Postprocessing of non-conservative flux for compatibility with transport in heterogeneous media. *Computer Methods in Applied Mechanics and Engineering*, 315:799–830, 2017.
- [37] Geiger, S., Roberts, S., Matthäi, S., Zoppou, C., and Burri, A. Combining finite element and finite volume methods for efficient multiphase flow simulations in highly heterogeneous and structurally complex geologic media. *Geofluids*, 4(4):284–299, 2004.
- [38] Paluszny, A., Matthäi, S., and Hohmeyer, M. Hybrid finite element–finite volume discretization of complex geologic structures and a new simulation workflow demonstrated on fractured rocks. *Geofluids*, 7(2):186–208, 2007.
- [39] Nick, H. and Matthäi, S. A hybrid finite-element finite-volume method with embedded discontinuities for solute transport in heterogeneous media. *Vadose Zone Journal*, 10(1):299–312, 2011.
- [40] Matthäi, S.K., Nick, H.M., Pain, C., and Neuweiler, I. Simulation of solute transport through fractured rock: a higher-order accurate finite-element finite-volume method permitting large time steps. *Transport in Porous Media*, 83(2):289–318, 2010.